

---

**STUDIES ON SYNTHESIS AND CHARACTERIZATIONS OF  
GADOLINIUM DOPED CERIA SOLID ELECTROLYTE**

---

**A THESIS SUBMITTED TO  
SHIVAJI UNIVERSITY, KOLHAPUR**

**FOR THE DEGREE OF  
DOCTOR OF PHILOSOPHY**

**IN**

**PHYSICS**

**UNDER THE FACULTY OF  
SCIENCE**

**BY**

**Mr. MURALIDHAR GIRISH CHOURASHIYA**  
*M.Sc., CSIR-SRF-direct*

**UNDER THE GUIDANCE OF**

**Dr. LATA D. JADHAV**  
*M.Sc., Ph.D.*

---

**SCHOOL OF ENERGY STUDIES,  
DEPARTMENT OF PHYSICS,  
SHIVAJI UNIVERSITY, KOLHAPUR.**

---

**JUNE – 2009**



**STUDIES ON SYNTHESIS AND CHARACTERIZATIONS  
OF GADOLINIUM DOPED CERIA SOLID ELECTROLYTE**

A THESIS SUBMITTED TO  
**SHIVAJI UNIVERSITY, KOLHAPUR**

FOR THE DEGREE OF  
**DOCTOR OF PHILOSOPHY**

IN  
**PHYSICS**  
UNDER THE FACULTY OF  
**SCIENCE**

BY

**Mr. MURALIDHAR GIRISH CHOURASHIYA**  
*M.Sc., CSIR-SRF-direct*

UNDER THE GUIDANCE OF

**Dr. LATA D. JADHAV**  
*M.Sc., Ph.D.*

SCHOOL OF ENERGY STUDIES,  
DEPARTMENT OF PHYSICS,  
SHIVAJI UNIVERSITY, KOLHAPUR.

**JUNE – 2009**





# DECLARATION

---

*I hereby declare that the thesis entitled "Studies on synthesis and characterizations of gadolinium doped ceria solid electrolyte" completed and written by me has not previously formed the basis for the award of any Degree or Diploma or other similar title of this or any other University or examining body.*

---

*Place: Kolhapur*

*Research Student*

*Date: 15<sup>th</sup> August 2009*

---

*Mr. Muralidhar G. Chourashiya*

---



# CERTIFICATE

---

This is to certify that the thesis entitled "*Studies on synthesis and characterizations of gadolinium doped ceria solid electrolyte*", which is being submitted herewith for the award of the *degree of Doctor of Philosophy in Physics* of Shivaji University, Kolhapur is the result of the original research work completed by *Mr. Muralidhar Girish Chourashiya* under my supervision and guidance and to the best of my knowledge and belief the work embodied in this thesis has not formed earlier the basis for the award of any degree or similar title of this or any other University or examining body.

---

*Place: Kolhapur*

*Research Guide*

*Date: 15<sup>th</sup> August 2009*

---

*Dr. (Smt.) Lata D. Jadhav*

---



# ACKNOWLEDGEMENTS

---

I have great pleasure while expressing my enormous appreciation towards *Dr. (Smt.) Lata D. Jadhav*, research guide, Lecturer, Department of Physics, Rajaram College, Kolhapur for her most knowledgeable guidance together with constant encouragement at all phases of this work. The work presented here could not have been accomplished without her motivating supervision and practical admiration during the course of my research.

I am incredibly grateful to *Prof. S. H. Pawar*, Vice Chancellor, D.Y. Patil University, Kolhapur for generation of initial spark of research spirit in my academic attitude and then after for his continuous support. I express my sincere thanks to *Prof. C. H. Bhosale* and *Dr. P. S. Patil*, Department of Physics, Shivaji University, Kolhapur for his encouragement and constant support for my self-motivated research during my masters (M.Sc.). Their support even after the M.Sc. was of significant importance and helped me to be a courageous researcher. I also wish to express my thanks to *Prof. C. D. Lokhande*, Department of Physics, Shivaji University, Kolhapur for his efforts during my M.Sc. project (research guide) to bestow me the essence of research.

I am very much thankful to *Late Prof. M. K. Soudagar*, *Prof. B. K. Chougule*, former Heads and *Prof. A. V. Rao*, Head of Department of Physics, Shivaji University, Kolhapur for ~~encouragement and~~ providing the facilities to carry out the experiments and complete this work. I am also thankful to all my teachers for their guidance and help during my research work.

I am very much thankful to *Dr. (Smt.) S. R. Bhardwaj*, Head, Fuel Cell and Catalysis Section, Chemistry Division, BARC, Mumbai for



providing impedance measurement facility and to *Dr. R. N. Basu*, Head, Fuel cell and battery section, Central Glass and Ceramics Research Institute (CGCRI), Calcutta for OCV measurements. I also thank *Dr. D.M. Phase*, *Dr. V. Ganesan*, *Dr. N.P. Lalla*, *Dr. Alok Banarjee* and *Dr. R. J. Chowdhury*, faculties from UGC-DAE- Inter University Consortium (UGC-DAE-IUC), Indore for providing various synthesis and characterization facilities. I also express my thank to the engineers from respective laboratories of IUC, Indore & especially to *Mr. Vinay Ahire*, *Mr. Mohan Gangarade* and *Miss. Priti Mahajan* for their help during the measurements.

My sincere thanks to *Dr. D. D. Shivagan*, *Dr. K. M. Subhedar* and *Dr. R. S. Hyam* for their valuable suggestions during my research work. I am also grateful to all research scholars of the Physics Department, Shivaji University, Kolhapur for their help.

My special thanks are due to *staff* at *Physics*, *CFC* and *USIC* Department, Shivaji University, Kolhapur for providing me all the possible and well-timed support.

I greatly acknowledge the *Defense Research and Development Organization (DRDO)*, New Delhi, [JRF (2 years) and SRF (1.25 years)], *Council of Scientific and Industrial Research (CSIR)*, New Delhi [CSIR-SRF-direct (till date)] and *Department of Science and Technology (DST)*, New Delhi [International travel scheme] for providing me the financial assistance during the pursuit of research goals of this work.

I am indeed indebted to my *Parents*, *Brother Mantu*, *Sister Anita*, *Bhabhi Mamata* and *Putani Suhani* for their immense help at all levels with moral and social support. Their patience, care, and support throughout my studies enabled me to accomplish the research well in time.

---

***Mr. Muralidhar Girish Chourashiya***





Special thanks to...



DRDO, New Delhi



CSIR, New Delhi



DST, New Delhi

for financial assistance...





Dedicated to...

my beloved family...







*Contents of ...*

***Studies on synthesis and characterizations of gadolinium doped ceria solid electrolyte***

***Ph.D. Thesis***

*By*

**Mr. Muralidhar G. Chourashiya,**

*CSIR-SRF-direct,*

*Department of Physics,*

*Shivaji University, Kolhapur.*

*Under the Guidance of,*

**Dr. (Smt.) L.D. Jadhav,**

*Lecturer,*

*Department of Physics,*

*Rajaram College, Kolhapur*





## CONTENTS

Chapter no.	Title	Page no.
Chapter one	Introduction	1
Chapter two	Ionic conduction mechanism and electrical behavior of pure and doped ceria	37
Chapter three	Introduction to experimental techniques of synthesis and characterization	71
Chapter four	Synthesis and characterization of gadolinium doped ceria in bulk form using solid state reaction method	133
Chapter five	Synthesis and characterization of 10%Gd doped ceria (GDC10) thin films using spray pyrolysis technique	185
Chapter six	Synthesis and characterization of 10%Gd doped ceria (GDC10) thin films on ceramic substrates	219
Chapter seven	Gd doped ceria in bulk and thin film form as solid electrolyte for IT-solid oxide fuel cells	255
Chapter eight	Summary and conclusions	283
<b>APPENDIX</b>		
Appendix I-A	Powder synthesis techniques	[i]
Appendix I-B	Green body formation	[ix]
Appendix II	Some useful definitions	[xvii]
Appendix III	Standard reduction potentials–for different H <sub>2</sub> -O <sub>2</sub> chemical reactions	[xxxii]





# Chapter one

## CONTENTS

1. INTRODUCTION .....	2
1.1. Solid state ionic conductors (solid electrolytes).....	3
1.2. Oxide ion conductors (OICs).....	4
1.3. Applications of Oxide Ion Conductors:.....	7
1.4. Obstacles in commercialization of OIC devices (particularly for SOFCs) and the resolutions.....	9
1.5. Relevant literature survey.....	11
1.5.1. 8% Ytria stabilized zirconia (YSZ).....	12
1.5.2. Sc-stabilized-Zirconia, $\text{Sc}_2\text{Zr}_{1-x}\text{Zr}_x\text{O}_{3/2}$ (ScSZ).....	13
1.5.3. $\text{La}_{0.8}\text{Sr}_{0.2}\text{Ga}_{0.8}\text{Mg}_{0.2}\text{O}_8$ (LSGM).....	13
1.5.4. $\text{BaIn}_2\text{O}_7$ .....	14
1.5.5. Stabilized $\delta\text{-Bi}_2\text{O}_3$ .....	15
1.5.6. Doped ceria.....	15
1.6. Importance of pure and doped ceria.....	16
1.6.1. Gd doped ceria (GDC).....	18
1.6.2. Shortfalls in the use of GDC as solid electrolytes and the resolutions over it.....	19
1.6.3. Synthesis of GDC by the cost effective ceramic route (solid state reaction).....	21
1.6.4. GDC thin film as solid electrolyte for IT- or LT-SOFCs.....	22
1.7. Scope of research work.....	26
References:.....	29

# Chapter two

## CONTENTS

2. IONIC CONDUCTION MECHANISM AND ELECTRICAL BEHAVIOR OF PURE AND DOPED CERIA .....	38
2.1. Introduction .....	39
2.2. Ion conduction mechanisms in solid electrolytes .....	40
2.2.1. Conduction mechanisms.....	40
2.2.2. Mobile ion concentrations - doping effects.....	42
2.2.3. Ion trapping effects.....	43
2.2.4. Potential energy profile.....	44
2.2.5. The activation energy for conduction.....	45
2.2.6. Hopping rates .....	46
2.2.7. The ac conductivity spans: local motions and long range conduction.....	47
2.2.8. An example of solid electrolyte: Oxide ion conductors.....	48
2.3. Crystal structure and electrical behavior of pure and doped ceria ....	49
2.3.1. About cerium (Ce) element [5].....	49
2.3.2. Crystal structure of ceria.....	51
2.3.2.1. Fluorite structure of $\text{CeO}_2$ .....	51
2.3.2.2. Stoichiometry of fluorite structured $\text{CeO}_2$ .....	53
2.3.2.3. Holes in fluorite structured $\text{CeO}_2$ .....	53
2.3.3. Defect structure of ceria.....	55
2.3.3.1. General format of Kröger-Vink notation.....	56
2.3.3.2. Intrinsic defects (or disorders) in ceria.....	57
2.3.3.3. Extrinsic defects (disorder) in ceria.....	59
2.3.3.4. Defect concentrations in pure and doped ceria.....	61
2.3.4. Ionic conductivity in ceria and doped ceria.....	63
2.3.5. Electrical behavior of pure and doped ceria.....	66
2.3.5.1. Influence of doping.....	66
2.3.5.2. The temperature dependence.....	67
Reference:.....	69

# Chapter three

## CONTENTS

<b>3. INTRODUCTION TO EXPERIMENTAL TECHNIQUES OF SYNTHESIS AND CHARACTERIZATION</b> .....	<b>72</b>
3.1. Introduction.....	72
3.2. Bulk preparation using ceramic route .....	73
3.2.1. Introduction .....	73
3.2.2. Preparation of mixture of raw materials (starting chemicals) .....	75
3.2.3. Ceramic powder synthesis - dry and binder added homogenization.....	76
3.2.4. Green body formation.....	77
3.2.5. Pre-sintering - Heat treatments of drying and binder burnout.....	79
3.2.6. Final sintering.....	82
3.3. Film preparation using spray pyrolysis technique (SPT).....	85
3.3.1. Introduction.....	85
3.3.2. Experimental setup .....	87
3.3.4. Preparative parameters of spray deposition technique .....	98
3.3.5. General scheme of optimization of spray parameters.....	102
3.4. Characterization techniques .....	103
3.4.1. Density measurements .....	103
3.4.2. Thickness and surface roughness measurements .....	106
3.4.3. Thermal analysis.....	107
3.4.4. X-ray Diffraction.....	110
3.4.5. Scanning electron microscopy and Energy dispersive x-ray spectroscopy.....	113
3.4.6. Atomic Force Microscopy (AFM).....	116
3.4.7. Electrical characterizations.....	119
References:.....	129

# Contents

# Chapter four

## CONTENTS

<b>4. SYNTHESIS AND CHARACTERIZATION OF GADOLINIUM DOPED CERIA IN BULK FORM USING SOLID STATE REACTION METHOD</b> .....	<b>134</b>
Keywords: Gd doped Ceria, Solid state reaction method, Effect of preparative parameters of ceramic route, Effect of doping % of Gd in ceria.....	134
4.1. Introduction.....	135
4.2. Experimental.....	136
4.2.1. Synthesis of GDC samples.....	136
4.2.1.1. Introduction.....	136
4.2.1.2. Characterizations of starting (raw) powders by XRD.....	136
4.2.1.3. Synthesis of Ce <sub>1-x</sub> Gd <sub>x</sub> O <sub>2-δ/2</sub> (x = 0.1, 0.2 and 0.3) powders.....	138
4.2.1.4. Green body (pellet) formation - using dry pressing.....	140
4.2.1.5. Pre-sintering - drying and binder burnout step.....	141
4.2.1.6. Final sintering and Sample Identifications.....	141
4.2.2. Characterizations.....	142
4.3. Results and discussions.....	144
4.3.1. Introduction.....	144
4.3.2. Section - A: Properties of Ce <sub>1-x</sub> Gd <sub>x</sub> O <sub>2-δ</sub> sintered at different temperatures.....	145
4.3.2.1. Structural characterizations.....	145
4.3.2.2. Morphological characterizations.....	151
4.3.2.3. Density measurements.....	154
4.3.2.4. Electrical characterizations.....	157
4.3.2.5. Outcomes of studies carried out in Section A.....	164
4.3.3. Section - B: Precise optimization of processing parameters and Gd doping.....	165
4.3.3.1. Structural and elemental characterization.....	165
4.3.3.2. Morphological characterizations and relative density measurements.....	169
4.3.3.3. Electrical characterizations.....	173
4.4. Conclusions.....	181
References.....	182

# Chapter five

## CONTENTS

### 5. SYNTHESIS AND CHARACTERIZATION OF 10%GD DOPED CERIA (GDC10) THIN FILMS USING SPRAY PYROLYSIS TECHNIQUE..... 186

**Keywords:** CeO<sub>2</sub> and GDC10 thin films, Spray pyrolysis technique, XRD, EDAX, SEM, APM, effect of thickness on electrical properties..... 186

5.1. Introduction.....	187
5.2. Experimental.....	188
5.2.1. Introduction.....	188
5.2.2. CeO <sub>2</sub> (ceria) thin films.....	190
5.2.2.1. Synthesis of ceria thin films.....	190
5.2.2.2. Characterizations and optimizations.....	190
5.2.3. GDC10 thin films.....	190
5.2.3.1. Synthesis of GDC10 thin films.....	190
5.2.3.2. Characterizations and optimizations.....	191
5.3. Results and discussions.....	192
5.3.1. Introduction.....	192
5.3.2. TG-DTA of cerium nitrate $Ce(NO_3)_3 \cdot 6H_2O$ .....	192
5.3.3. Synthesis and characterizations of CeO <sub>2</sub> thin films on glass substrate.....	194
5.3.3.1. Effect of precursor solution concentrations.....	194
5.3.3.2. Effect of annealing on crystalline nature of ceria thin films.....	197
5.3.4. Synthesis and characterizations of GDC10 (Ce <sub>0.9</sub> Gd <sub>0.1</sub> O <sub>2-δ</sub> ) thin films.....	198
5.3.4.1. Optimization of substrate temperature.....	199
5.3.4.2. Optimization of precursor solution concentration.....	206
5.4. Conclusions.....	215
References.....	216

# Contents

# Chapter six

## CONTENTS

### 6. SYNTHESIS AND CHARACTERIZATION OF 10%GD DOPED CERIA (GDC10) THIN FILMS ON CERAMIC SUBSTRATES..... 220

**Keywords:** GDC, Thin film, NiO-GDC, Spray pyrolysis, Impedance spectroscopy..... 220

6.1. Introduction.....	221
6.2. Experimental.....	222
6.2.1. Synthesis of GDC and NiO-GDC ceramics substrates.....	222
6.2.2. Synthesis of GDC/GDC and GDC/NiO-GDC structures.....	223
6.2.3. Characterizations.....	224
6.3. Results.....	225
6.3.1. Micro-structural and electrical properties of GDC/GDC structures.....	225
6.3.2. Micro-structural properties of NiO-GDC substrates at different stages of its processing and electrical properties of NiO-GDC* substrate.....	232
6.3.3. Micro-structural and electrical properties of GDC deposited on NiO-GDC* substrate.....	238
6.4. Discussions.....	243
6.4.1. Atomic force microscopy of GDC films deposited on ceramic substrates.....	243
6.4.2. Formation of nano-crystalline GDC thin films.....	246
6.4.3. Effect of substrates on film thickness.....	246
6.4.4. Electrical characterizations.....	248
6.5. Conclusions.....	252
References.....	253

# Contents

Chap 8. Summary and Conclusions

## Chapter eight

CONTENTS

8. SUMMARY AND CONCLUSIONS.....	284
Major achievements of the research.....	291
FUTURE SCOPE.....	292

I N D E X

Chap 7. GDC in bulk and thin film form as solid electrolyte

## Chapter seven

CONTENTS

7. Gd DOPED CERIA IN BULK AND THIN FILM FORM AS SOLID ELECTROLYTE FOR IT-SOLID OXIDE FUEL CELLS.....	256
7.1. Introduction.....	257
7.1.1. A general consideration of thin films.....	257
7.1.2. Importance of thin films in solid oxide fuel cells.....	260
7.2. Discussions.....	261
7.2.1. Structural comparison.....	261
7.2.2. Comparison of surface and fractured morphologies.....	263
7.2.3. Comparative elemental analysis.....	266
7.2.4. Comparison of electrical performance of optimized GDC samples.....	267
7.2.4.1. Comparison of dc conductivity measurement of bulk GDC and GDC/glass substrate.....	268
7.2.4.2. Comparison of ac conductivity measurements of bulk GDC and GDC/ceramic substrate.....	271
7.2.5. Open circuit voltage (OCV) measurements.....	272
7.2.5.1. Fundamentals of fuel cell performance.....	276
7.2.5.3. Experimental for OCV measurements.....	277
7.2.5.4. OCV measurements in different fuel cell conditions.....	277
7.2.5.4. Comparison of OCV data with reported values.....	279
7.3. Conclusions.....	281
References.....	281

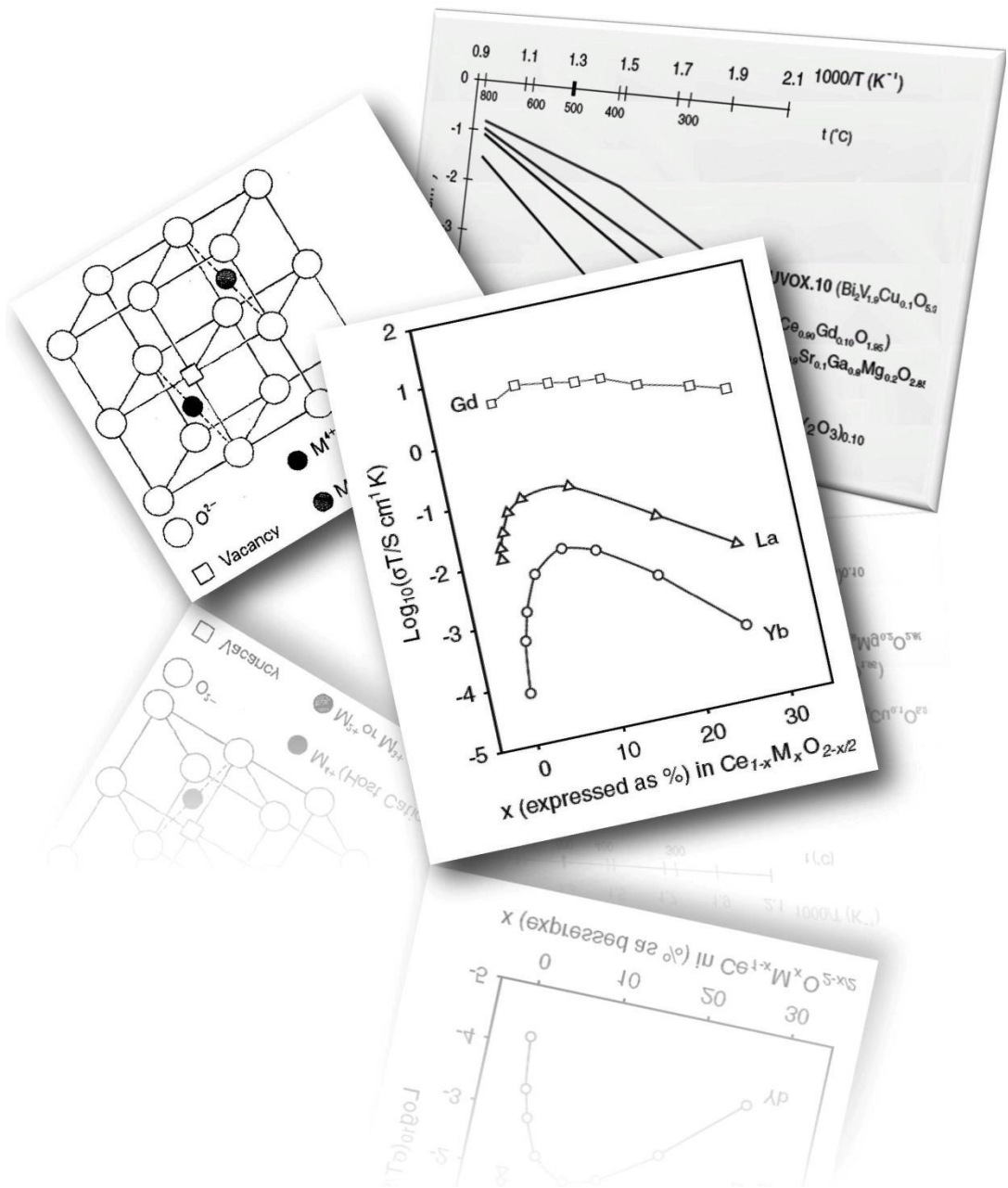
I N D E X





# Chapter one:

## Introduction







# Chapter one

## CONTENTS

1. INTRODUCTION.....	2
1.1. Solid state ionic conductors (solid electrolytes).....	3
1.2. Oxide ion conductors (OICs) .....	4
1.3. Applications of Oxide Ion Conductors:.....	7
1.4. Obstacles in commercialization of OIC devices (particularly for SOFCs) and the resolutions.....	9
1.5. Relevant literature survey .....	11
1.5.1. 8% Ytria stabilized zirconia (YSZ).....	12
1.5.2. Sc-stabilized-Zirconia, $Sc_xZr_{1-x}O_{2-x/2}$ (ScSZr),.....	13
1.5.3. $La_{0.8}Sr_{0.2}Ga_{0.8}Mg_{0.2}O_3$ , (LSGM) .....	13
1.5.4. $Ba_2In_2O_5$ .....	14
1.5.5. Stabilized $\delta$ - $Bi_2O_3$ .....	15
1.5.6. Doped ceria.....	15
1.6. Importance of pure and doped ceria.....	16
1.6.1. Gd doped ceria (GDC).....	18
1.6.2. Shortfalls in the use of GDC as solid electrolytes and the resolutions over it... ..	19
1.6.3. Synthesis of GDC by the cost effective ceramic route (solid state reaction).....	21
1.6.4. GDC thin film as solid electrolyte for IT- or LT-SOFCs.....	22
1.7. Scope of research work.....	26
References:.....	29

## **1. INTRODUCTION**



### 1.1. Solid state ionic conductors (solid electrolytes)

Solid electrolytes are a class of materials exhibiting high ionic conductivity, like liquid electrolytes, although they are in the solid state. Unlike liquid electrolytes, solid electrolytes usually have a rigid framework structure and there is at least one mobile ionic species. Such materials have been known for several decades. For example, Nernst (1899) demonstrated that the electrical conduction through  $\text{ZrO}_2\text{-Y}_2\text{O}_3$  at elevated temperatures was mainly due to mobile oxygen ions.

Before the discovery of solid ion conducting materials, it was generally believed that a solid material with a rigid crystal structure cannot obviously conduct much electrical current due to ionic movements. The discovery of unexpectedly large electrical conductivity in AgI (1934) [1] and in doped zirconia (1943) [2] completely changed the scenario. Desire for understanding of the basic phenomenon behind these solid state materials (ionic conductors), created enormous interest in scientific community and brought up the new field of *Solid State Ionics*. These materials were termed as “*solid electrolytes*”, to account its physical property (*solid*) and its ability of electrical conduction through the motion of ions (*electrolytes*). Solid electrolytes are characterized by high ionic conductivity and negligible electronic conduction. The ionic conduction in solid electrolytes is primarily determined by the presence of lattice defects (this aspect is made clear in *chapter 2*). The concentration of these lattice defects and its mobility plays the decisive role in eventual amount of ionic conduction in solid electrolytes. Thus, ionic conduction in solid electrolytes may be occurring due to motion of anions or cations which are referred as *anionic conductors* or *cationic conductors*, respectively. However, there is a category of solid electrolyte which exhibits ionic conduction due to simultaneous motion of both the ionic species.

Among all the solid ion conductors, most extensively studied ionic conductors are oxygen ion conductors (OICs - anionic), because of its wide range of applications. However, the ionic conductivities of the OICs are, in general, orders of magnitude lower than that of the cationic conductors (also termed as *super-ionic conductors*). The activation energies of OICs are also higher. For example, the super-ionic conductor,  $\text{RbAg}_4\text{I}_5$ , exhibits a room temperature conductivity of 0.12S/cm with activation energy of  $\sim 0.1\text{eV}$  while for a typical oxygen ion conductor ( $\text{ZrO}_2 - 9\text{mole\% Y}_2\text{O}_3$ ), the same value of conductivity is achieved only at  $1000^\circ\text{C}$  with activation energy of around  $1.0\text{eV}$ . Due to their high electrolyte polarization the



oxygen ion conductors are unsuitable for room temperature applications and can only be used above 500–600°C depending on the particular material. Among the anionic conductors, OIC is the focus of this thesis.

Solid electrolytes (mostly OICs) presently find wide applications, few of them are,

- i. Energy storage by new types of high-performance batteries,
- ii. Efficient energy conversion by fuel cells,
- iii. Generation of hydrogen fuel by electrolysis,
- iv. Chemical sensors,
- v. Solar cells,
- vi. Electro-chromic windows or displays, etc.

These applications will have tremendous impact on many aspects of our life, environment, and economy. More recently, and particularly in the past two decades, the pace of research has been rapidly driven by the requirements for new clean energy sources, sensors, and high energy density batteries [3].

## 1.2. Oxide ion conductors (OICs)

A very interesting subgroup of anionic conductor materials is the oxides that exhibit oxygen ion conductivity. There has been a continued drive for their development because of the promise of important technological devices [4].

Oxides with high ionic conductivity have open structure, such as fluorite or pyrochlore. The ideal fluorite structure is shown in figure 1. This structure is relatively open and it shows large tolerance for high levels of atomic disorder, which may be introduced either by doping, reduction or oxidation. The binary oxides,  $\text{ThO}_2$ ,  $\text{CeO}_2$ ,  $\text{PrO}_2$ ,  $\text{UO}_2$ , and  $\text{PuO}_2$ , possess this structure in the pure state while  $\text{ZrO}_2$  and  $\text{HfO}_2$  are stabilized to the fluorite structure by doping with divalent or trivalent oxides. The addition of such dopants to these fluorite oxides gives rise to the creation of oxygen vacancies (lattice defects), which are responsible for the ionic conduction in these oxides.



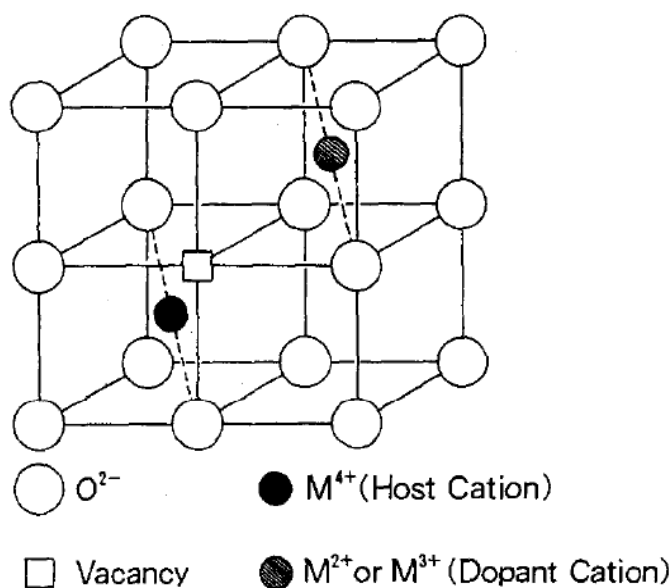


Figure 1. A half unit cell of the fluorite structure showing the position of dopant cation-oxygen vacancy associate, [5].

Most of the oxygen ion conductors crystallize in the cubic fluorite structure, which include oxides like zirconia, thoria, ceria and bismuth trioxide. Some mixed oxides with perovskite structure also exhibit oxygen ion conduction. Pure thoria and ceria have fluorite structure which is stable from room temperature to their melting points, however only polymorphs of zirconia and bismuth oxide are stable in different temperature ranges. For zirconia, the fluorite phase is stabilized only when it is doped with di- or tri-valent metal oxides like  $CaO$ ,  $MgO$ ,  $Y_2O_3$ ,  $Sc_2O_3$  and a large number of rare earths, while for  $Bi_2O_3$ , the fluorite phase exists only at higher temperatures ( $>730^\circ C$ ) and it is difficult to stabilize this phase at room temperature. The ionic conductivity of these oxides particularly of  $ZrO_2$ ,  $ThO_2$  and  $CeO_2$  is greatly enhanced when doped with lower valent metal oxides and is believed to be due to the creation of excess oxygen vacancies. However, addition of aliovalent oxides to  $Bi_2O_3$  in an attempt to stabilize the fluorite phase at room temperature was resulted in a lowering of conductivity.

Current flow in these oxygen ion conductors occurs by the motion of oxide ions through the crystal lattice. The oxygen ions move from one crystal lattice site to another crystal lattice site by thermally-activated hopping, with a superimposed drift in the direction of the electric field. Thus ionic conductivity is highly temperature



dependent; however at high temperatures can approach values close to 0.1 S/cm (fig. 2) [6]. From figure 2 it can be seen that ceria based electrolytes shows, stable phase (unlike BICUVOX.10) with comparatively higher conductivity throughout the temperature range than the other OICs.

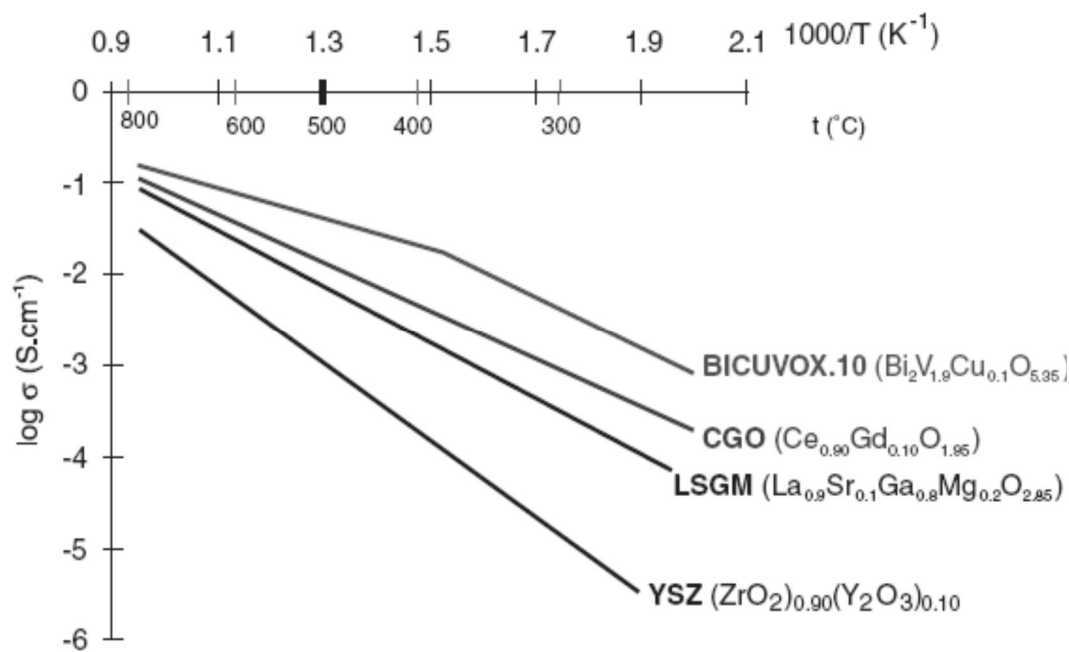


Figure 2. The ionic conductivity of some of popular OICs as a function of  $1000/T$  [6].

Figure 3 shows the isothermal conductivity of some ceria solid solutions at temperatures close to 200°C, which clearly indicate that the conductivity drops with relatively modest additions of the rare earth ion, when the percentage of vacancy concentration is small [7]. The maximum in conductivity is caused by the interaction of the substitution of rare earth ions and oxygen vacancies. In preparation of good OICs it is strongly advised that while introducing vacancies by doping, the crystal lattice should be kept as undisturbed as possible. This explains why some of the best oxygen ion conductors are materials such as zirconia-Scandia,  $\text{Zr}_{1-x}\text{Sc}_x\text{O}_{2-\delta}$ , and gadolinia doped ceria  $\text{Ce}_{1-x}\text{Gd}_x\text{O}_{2-\delta}$  (GDC), where the host and dopant ion are very close in size [5]. Zirconia-Scandia is often ruled out on the ground of its cost, but the next best material, YSZ, is a standard material for use in high temperature solid oxide fuel cells (HT-SOFCs) and GDC is a strong candidate for use in lower temperature SOFCs operating at temperatures as low as 550°C.



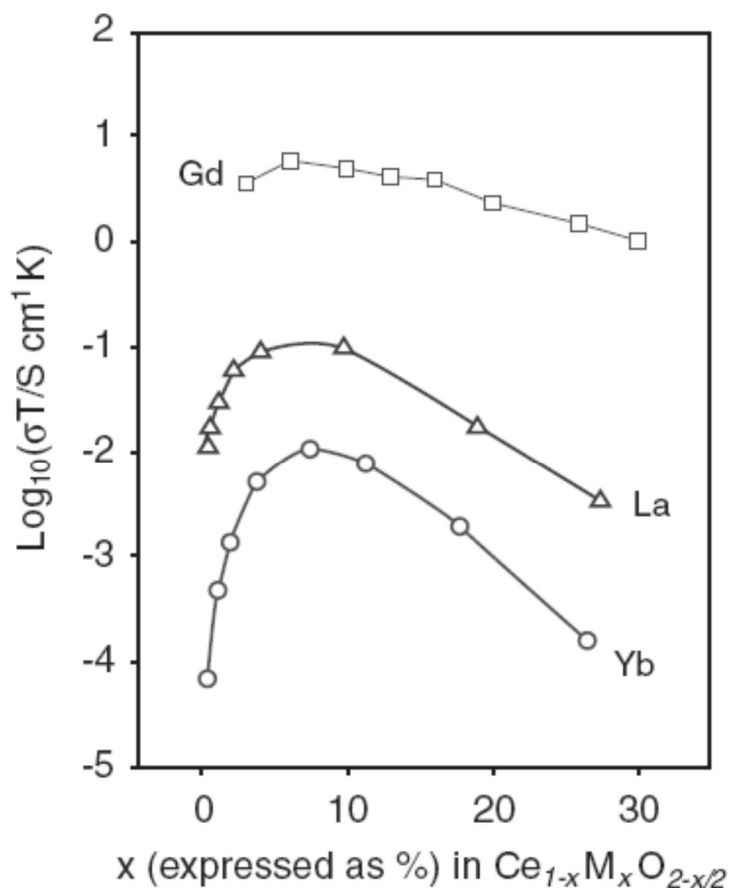


Figure 3. The isothermal conductivity of some ceria solid solutions at temperatures close to 200°C [7].

### 1.3. Applications of Oxide Ion Conductors:

Most important applications of the oxygen ion conductors are based on galvanic cells which uses one of OIC material as electrolyte together with suitable electrodes on either side. Measurement of the open circuit voltage using a reference electrode on one side of the cell enables one to determine the oxygen activity on other side.

#### 1. Oxygen pump

The most interesting applications of oxygen ion conductors is in control of oxygen content [8, 9] in a flowing inert gas (electrochemical oxygen pump) which requires application of an external voltage across the wall of a solid electrolyte tube



through which the gas is allowed to flow. The technique is extensively used in solid electrolyte research and has been tried in removal of oxygen from liquid metals [10].

## 2. Oxygen Sensor

This is important technological applications of oxide electrolytes. For oxygen sensors the principle is similar to that of thermodynamic measurements. Such sensors are extensively used to measure oxygen content in molten metals; gaseous atmospheres like furnace flue gas or car exhaust and thereby help in the control of fuel-air ratio at an optimum level. Stabilized zirconia is usually used as the electrolyte and air as the reference electrode. They can be fabricated with several designs [11].

## 3. Fuel Cell

High temperature fuel cell (SOFC) is an extremely efficient energy conversion device. It uses gaseous fuels which are burnt e.g. inside a tubular electrolyte (for tubular cell configuration), normally made of stabilized zirconia. The air is supplied from outside through the tube wall. The voltage across the wall is ~ 1 volt at 1000°C. However, most of the recent developments are based on thin film modular concept using porous support tube on which the electrolyte and electrode are deposited one after the other by thin film technology [12]. The thickness of the individual layers varies between 30-100µm and the length of the unit cell is 1 cm. Zirconia stabilized with  $Y_2O_3$  or  $Y_2O_3$  and  $Yb_2O_3$ , is usually used as the electrolyte. The fuel electrode can be either nickel-zirconia cermet or pure metals like Ni, Co, etc. There are several possible materials for air electrode (cathode). Electrodes are electronically conducting single oxides or mixed oxides with perovskite structure. The disadvantages in most of them are thermal expansion mismatch and low conductivity and hence lead to reduced reliability of overall device.

## 4. Others

Other applications of OICs which are of recent origin include electrolysis of steam at high temperature to generate hydrogen and as electro-catalyzers for various





chemical reactions in the gaseous phase like decomposition of nitric oxide [13, 14], synthesis of methane [15] and oxidation of ammonia to nitric oxide [16]. Working principle of these cells is similar to that of electrochemical oxygen pump described earlier.

#### **1.4. Obstacles in commercialization of OIC devices (particularly for SOFCs) and the resolutions**

The rigid structure of solid electrolytes has some advantages as well as disadvantages. On one hand, solid electrolytes have number of applications due to their rigid structure and liquid electrolyte like ion conductivity while on the other hand its commercialization is not possible due to its high operating temperature (~1000°C). The formulations of materials having the property of solid electrolytes with lower operating temperature are believed to play the key role in commercialization of SOFCs. However, the worldwide attempts in that direction are going on.

The reduction of operating temperature will solve number of problems related to reliability, efficiency and commercial manufacturing of the SOFCs. Lowering the operating temperature of SOFCs promises the following immediate advantages:

##### *1. Use of metallic interconnects:*

Lower operating temperature of SOFCs will allow the device designer to use the metallic interconnectors instead of interconnectors made from state-of-art techniques especially for high temperature conditions. This will definitely reduce the production cost of unit device. Lower operating temperature also offers low aging effects of device components e.g. interconnectors etc., leading to higher reliability.

##### *2. Easier sealing of system:*

As the operating temperature is reduced, the quantity of materials required for sealing would be less. Moreover comparatively inferior quality of sealing



material would be sufficient for sealing. This leads to further reduction in cost of device fabrication.

3. *Smaller thermal mismatch:*

Thermal mismatch of the device components is one of the major challenges in front of the available commercial SOFCs. This mismatch between the components leads to degradation in the performance of the cell with time span. But for lower operating temperature SOFCs this problem would be less or may disappear and lead to greater reliability in its operation.

4. *Less insulation:*

Less insulation material is needed to fabricate the complete system leading to lowering the cost of overall production of devices.

5. *Rapid startup with less energy consumption:*

Lower operating temperature of SOFCs will need less energy to attain the operating temperature, enabling the enhancement in conversion efficiency of devices. Also the operating temperature will be attained in comparatively shorter time leading to quick and better performance.

To use a solid electrolyte material for an application in OIC devices e.g. SOFC, it must have ionic conductivity of the order of 0.1 S/cm at its operating temperature. The commercial version of OIC devices e.g. SOFC, uses Yttria Stabilized Zirconia (YSZ) as solid electrolyte. The YSZ electrolyte shows required ionic conductivity (i.e. 0.1 S/cm) at 1000°C. In order to reduce the operating temperature, two approaches are widely applied [17-19], which are as follows:

- A. *By decreasing the thickness of traditional YSZ electrolyte* which leads to decrease in resistance of dense electrolyte membranes and thereby reduce the operating temperature, or



- B. Use of *an alternate material* which shows higher ionic conductivity at comparatively lower temperatures.

Although YSZ is considered to be the most reliable electrolyte for SOFC so far, many studies have been done on other materials seeking an alternative for YSZ, since; YSZ shows the limiting magnitude of electrical conductivity at high operating temperature such as 1000°C. When the operating temperature of SOFC is too high (e.g. ~1000°C), many interface reactions such as electrode/solid-electrolyte, electrode/inter-connector and inter-connector/solid electrolyte would decrease the efficiency and the stability of the cell. The serious efforts were put forward by various research groups to achieve the overall goal of commercialization of SOFCs by developing alternative materials with reduced operating temperatures. The literatures were surveyed systematically and the most important research works is described in next section.

### 1.5. Relevant literature survey

There are several series of materials on to which the research had been carried out with the intention of its use as solid electrolytes in OPDs such as gas sensors, Solid Oxide Fuel Cells (SOFCs), etc. Most of the work is concerned with the materials such as doped zirconia,  $\text{La}_{0.8}\text{Sr}_{0.2}\text{Ga}_{0.8}\text{Mg}_{0.2}\text{O}_3$  (LSGM), doped ceria, etc. Among them, Yttria-stabilized zirconia (YSZ) with the cubic-fluorite structure has been the most extensively investigated and used practically.

The electrical conductivity of fluorite-related oxides is shown in figure 4, according to Steele [20]. It can be seen from the figure that  $\text{Bi}_2\text{O}_3$ , and Yttria-stabilized  $\text{Bi}_2\text{O}_3$  are most electrically conductive. However, these oxides are not structurally stable and easily reduced under reductive atmospheres and hence they are not suitable as electrolytes for SOFCs. As seen in figure 4, electrical conductivity of gadolinia-doped ceria (GDC) is about one order of magnitude higher than that of YSZ and it is about  $0.1\text{Scm}^{-1}$  at 1073K, and hence ceria-based electrolytes have collected much attention as alternative to YSZ. It is noted, however, that ceria-based oxides are also reduced to give electronic conduction under reductive atmospheres.

The dopant cation size and its effect on the host crystal lattice structure are the major factors determining the ionic conductivity of solid electrolytes. Zirconia



generally have lattice structures, which are either too small or too large to accommodate a wide range of rare earth dopants, while the host lattice of ceria is more compatible with a wider range of these trivalent cations. The magnitude of electrical conductivity and the stability under reductive atmospheres for ceria-based oxides are greatly dependent on the kind and quantity of doping elements.

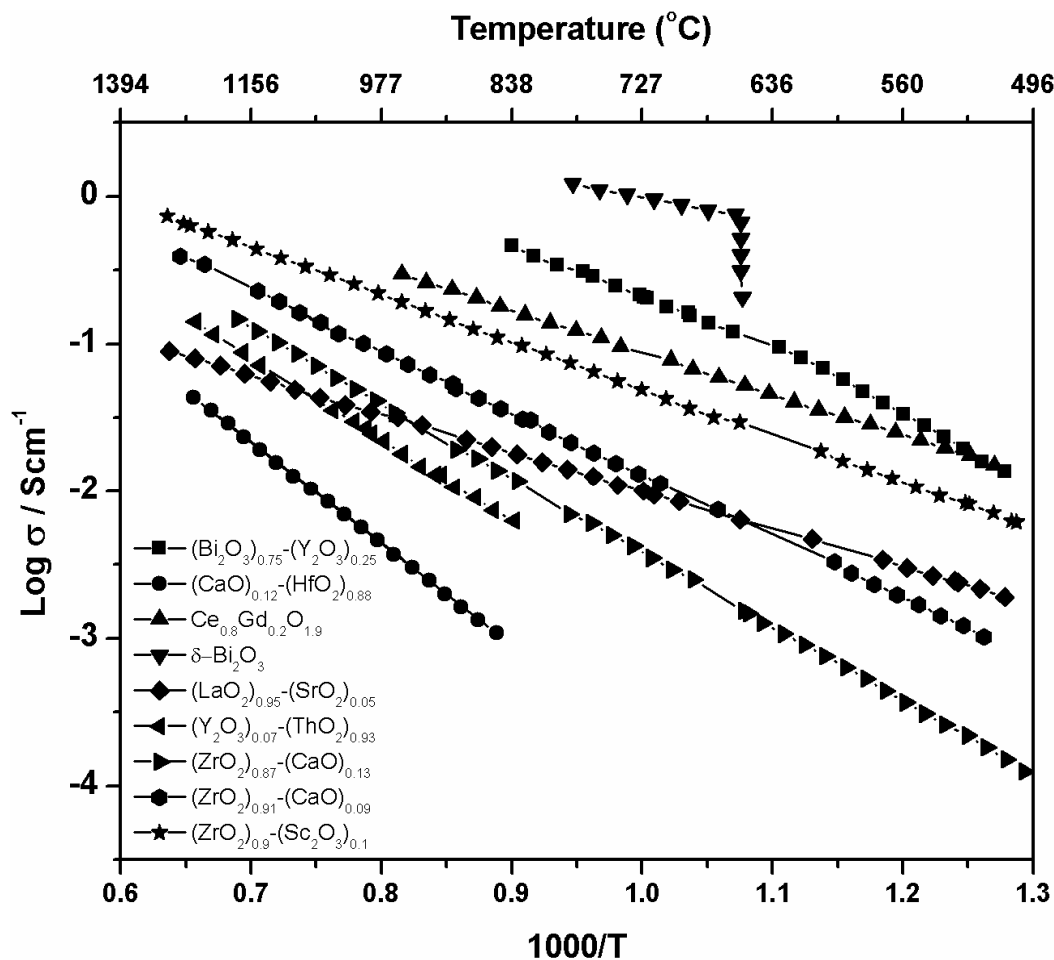


Figure 4 Electrical conductivity of fluorite oxides, [20].

### 1.5.1. 8% Yttria stabilized zirconia (YSZ)

Even 8% Yttria stabilized zirconia (YSZ) has so far been the choice for solid electrolyte, its ideal operating temperature of 800–1000°C poses a large number of engineering and materials problems. However, its chemical and mechanical stability over a wide range of oxygen partial pressures and temperatures has motivated the research to increase its conductivity. One challenge so far has been to reduce the



operating temperature while keeping the high ionic conductivity of YSZ (i.e. 0.1 S/cm). It is well known fact that the ionic conductivity varies with the preparation route and sintering conditions of the electrolyte due to the resultant different characteristics in the microstructure. A number of groups are investigating the connection between the microstructure and the ionic conductivity of YSZ electrolytes through varying the sintering conditions of nano-sized YSZ powders [21-23]. Further research is going on the synthesis of nano-crystallized YSZ by spray pyrolysis and the effect of spray parameters on morphology and sintering behavior [24] in order to lower the sintering temperature of YSZ.

### 1.5.2. Sc-stabilized-Zirconia, $Sc_xZr_{1-x}O_{2-x/2}$ (ScSZr),

Sc-stabilized-Zirconia,  $Sc_xZr_{1-x}O_{2-x/2}$  (ScSZr), with an ideal doping level of  $x = 0.08-0.11$ , is often seen as a potential replacement for YSZ, as it possesses the highest ionic conductivity of all the zirconates and stability in a wide range of partial pressure of oxygen, matching that of YSZ. Higher ionic conductivity means that it can be used at lower temperatures than YSZ with an increase in performance [25] and is thus seen as an attractive replacement for YSZ. Due to these benefits, it has been studied by a number of groups [26-28] and compatibility studies found that ScSZr can be used with the LSCF cathode. The problem with ScSZr is the difficulty in synthesis of the electrolyte. Powders often lack compositional uniformity and have to be synthesized at high temperatures for long times to get sufficient gas tightness. The electrolyte can, therefore, have different oxide ion conductivity depending on the preparation method [29]. The materials challenge at present is, therefore, to reduce the sintering temperature and time, with achieving consistent ionic conductivity necessary for large scale commercial production.

### 1.5.3. $La_{0.8}Sr_{0.2}Ga_{0.8}Mg_{0.2}O_3$ , (LSGM)

A perovskite oxide,  $La_{0.8}Sr_{0.2}Ga_{0.8}Mg_{0.2}O_3$  (LSGM), [30, 31] has oxide ion conductivity higher than that of YSZ at intermediate temperatures, 550–800°C, of 0.1S/cm at 800°C. It has good chemical stability and negligible electronic conductivity over a large range of oxygen partial pressures [32]. Some studies, however, indicated that LSGM is not stable in reducing atmospheres, in hydrogen



there is a significant depletion of B-site ions, particularly volatilization of  $\text{Ga}_2\text{O}$  occurs [33] in these conditions. Formation of phases such as  $\text{La}(\text{OH})_3$  and  $\text{LaSrGaO}_4$  were also observed in humidified hydrogen at  $1000^\circ\text{C}$  [34], whereas in CO and  $\text{CO}_2$  formation of alkaline earth carbonates occurs. At intermediate temperatures ( $600\text{--}800^\circ\text{C}$ ), however, volatilization of  $\text{Ga}_2\text{O}$  is not a problem, and this material has been studied for application in the IT-SOFC. Other disadvantages with LSGM are the undesired segregation of impurities during synthesis such as  $\text{LaSrGa}_3\text{O}_7$  and  $\text{LaSrGaO}_4$  [35]. Previous studies also reported an adverse reaction with NiO [36], hence causing a degradation of the Ni/LSGM anode with the formation of  $\text{LaNiO}_3$ . It was suggested that a buffer layer between the electrolyte and the anode would be needed or a careful selection of electrode material is necessary. Even having wider purely ionic conductivity domain, the LSGM is kept out-of-the-way on the basis of expensive raw materials (e.g. gallium) required for their preparation [37].

#### 1.5.4. $\text{Ba}_2\text{In}_2\text{O}_5$

Systems based on the  $\text{Ba}_2\text{In}_2\text{O}_5$ , structure have been studied since Goodenough et al. [38] have demonstrated fast ion conduction in  $\text{Ba}_2\text{In}_2\text{O}_5$  above  $925^\circ\text{C}$ , which was attributed to an order–disorder transition. It was found that at  $1040^\circ\text{C}$ ,  $\text{Ba}_2\text{In}_2\text{O}_5$  transforms into a disordered cubic structure with pure oxide ion conductivity. Many groups have since tried to reduce the temperature of onset of oxide ion conductivity by attempting to stabilize the disordered cubic form with cation substitution for Ba or In. Systems of the general formula  $\text{Ba}_2(\text{In}, \text{M})_2\text{O}_5$  ( $\text{M} = \text{Ga}, \text{Al}, \text{Sc}, \text{Y}, \text{Yb}, \text{W}, \text{Cu}, \text{Ce}, \text{Zr}, \text{Si}, \text{Ti}, \text{Sn}, \text{Ta}, \text{Nb}$ ) and  $(\text{Ba}, \text{M})_2\text{In}_2\text{O}_5$  ( $\text{M} = \text{Sr}, \text{La}, \text{Pb}$ ) were investigated. The most promising candidate was found to be  $(\text{Ba}_{1-y}\text{La}_y)_2\text{In}_2\text{O}_{5+y}$ . Compatibility studies [39] with potential cathode materials found that the ideal cathode for this electrolyte was  $(\text{La}_{0.6}\text{Sr}_{0.4})(\text{Mn}_{1-x}\text{Fe}_x)\text{O}_{32d}$  as  $(\text{La}_{0.7}\text{Sr}_{0.3})\text{CoO}_{32d}$  formed a small amount of the insulating phase  $\text{SrIn}_2\text{O}_4$  on sintering. Ni was found to be a compatible anode for this electrolyte. The oxide ion conductivity of this system is strongly affected by the crystal symmetry, oxygen content and unit cell free volume. The region of oxide ion conductivity is wider than for GDC; however it is still not suitable for use with pure hydrogen fuel as electronic conductivity would appear in the system, reducing the power density [40].



### 1.5.5. Stabilized $\delta$ - $\text{Bi}_2\text{O}_3$

At room temperature  $\text{Bi}_2\text{O}_3$  is predominantly an electronic conductor. However, high-temperature  $\delta$ - $\text{Bi}_2\text{O}_3$  phase with fluorite-related structure has the highest known oxide-ion conductivity  $\sigma_0 \approx 2.3 \text{ S/cm}$  at  $800^\circ\text{C}$ . On the other hand, this phase is only stable in the narrow temperature interval i.e. between  $730^\circ\text{C}$  and its melting point at  $804^\circ\text{C}$ . Takahashi et al. [41] demonstrated that the  $\delta$ -phase can be stabilized to lower temperatures by cation substitution for Bi; the stability range can be extended to room temperature by incorporation of 22–27 mol%  $\text{WO}_3$ , 25–43 mol%  $\text{Y}_2\text{O}_3$ , or 35–50 mol%  $\text{Gd}_2\text{O}_3$ . However, substitution of another cation for Bi lowers the conductivity, and the highest oxide-ion conductivity occurs at the lowest concentration of the substituent required to stabilize the  $\delta$ -phase to room temperature, which is found for  $\text{Bi}_{0.8}\text{Er}_{0.2}\text{O}_{1.5}$  [42]. However, these stabilized phases have been shown to age at  $600^\circ\text{C}$  due to transformation to a vacancy-ordered rhombohedra phase having significantly lower oxide-ion conductivity [43]. Fung et al. [44] have reported that this serious shortcoming can be overcome by the addition of less than 5% of  $\text{ZrO}_2$  or  $\text{ThO}_2$ . Similar small additions of  $\text{CeO}_2$  have also been shown to suppress aging of  $\text{Bi}_{0.75}\text{Y}_{0.25}\text{O}_{1.5}$  [45]. However,  $\text{Bi}_2\text{O}_3$ -based electrolytes are expected to be reduced in the atmosphere at the anode of a SOFC. The thin layer of Sm-based ceria on the anode side of the electrolyte can be expected to cease this problem. But the relatively large thermal-expansion coefficient of about  $15 \times 10^{-6} \text{ K}^{-1}$  of  $\text{Bi}_{0.75}\text{Y}_{0.25}\text{O}_{1.5}$  [46] prohibits while doing so.

### 1.5.6. Doped ceria

Pure ceria has a fluorite-type structure over wide range of temperature and oxygen partial pressure ( $x = 0-0.3$  in  $\text{CeO}_{2-x}$ ). The electronic defect concentration and conductivity increases with the increasing degree of non-stoichiometry (increasing temperature and decreasing oxygen partial pressure). Doping of ceria with a number of oxides such as  $\text{CaO}$ ,  $\text{Sm}_2\text{O}_3$ ,  $\text{Gd}_2\text{O}_3$ ,  $\text{Yb}_2\text{O}_3$ ,  $\text{Y}_2\text{O}_3$ ,  $\text{La}_2\text{O}_3$ , increases the concentration of oxygen-ion vacancies and the material exhibits high ionic conductivity. The stability regime is significantly higher for doped-ceria in comparison with pure ceria. Gadolinia doped ceria (GDC) was an exciting discovery



due to its high ionic conductivity at relatively low temperatures that makes it an ideal candidate for intermediate temperature solid oxide fuel cells, operating at 550–650°C [47-52]. It is now known that the ionic conductivities of ceria rare earth oxide systems depend on the ionic radii of the added cation, and the most promising systems so far seem to be Gd and Sm doped ceria. At present, a number of groups are working to reduce the thickness of the GDC electrolyte [21] in order to increase the ionic conductivity at these temperatures.

As the solid electrolyte is most important component in any fuel cell device, considerable effort has been directed towards the identification of novel materials for oxide ion conduction as discussed above. Rigorous operating regimes mean that few materials have the appropriate set of electrical, chemical and mechanical properties to produce a successful material that can compete with the established electrolytes [53]. A. J. McVovy [54] in conclusion of his review on ‘Thin SOFC electrolytes and their interfaces—A near-term research strategy’ suggested that, “...the recent trends of SOFC operation at lower temperatures in order to reduce the constraints on materials selection and obtain less demanding operating conditions is possible by improvements in materials preparation and cell fabrication procedures, together with a more intimate control of interface profiles and structures, rather than adoption of innovative alternative materials” [55].

### 1.6. Importance of pure and doped ceria

Pure ceria (cerium oxide) is an important metal oxide having a fluorite-type structure over wide range of temperature and oxygen partial pressure. It is used in many catalyst formulations as an oxygen storage component [56]. At low oxygen partial pressure, both doped and pure ceria are mixed ionic and electronic conductors and hence are also considered to be as promising SOFC anode materials. Marina et al. [57] presented the detailed work of preparation and performance of SOFC with GDC as anode. The mixed-conductive state of ceria and doped ceria, are oxygen permeable under oxygen partial pressure differences at elevated temperatures, with no need for additional electronic power or mechanical gas pumping [58].

In the past several years, CeO<sub>2</sub> based materials have been intensely investigated as catalysts, structural and electronic promoters of heterogeneous





catalytic reactions [59] and oxide ion conducting solid electrolytes in electrochemical cells [60]. The solid electrolyte is a key component of solid-state electrochemical devices, which are increasingly important for applications in energy conversion, chemical processing, sensing and combustion control applications [61, 62]. The high ionic conductivity coupled with the low activation energy for ionic conduction makes doped ceria an attractive material for use at temperatures below 800°C, which would allow greater flexibility in the design of electrode and interconnectors in electrochemical cells [63]. Doped ceria is also an important material for applications in controlling the air-to-fuel ratio in automobile exhaust [64]. Bera et al. [65] reported a new, extremely efficient room temperature H<sub>2</sub>-O<sub>2</sub> recombination catalyst, using Pt-substituted ceria, Ce<sub>1-x</sub>Pt<sub>x</sub>O<sub>2-d</sub> prepared by the combustion of aqueous solution containing calculated amounts of (NH<sub>4</sub>)<sub>2</sub>Ce(NO<sub>3</sub>)<sub>6</sub>, H<sub>2</sub>PtCl<sub>6</sub> and oxalyldihydrazide. The activity of catalyst is much more than that reported for Pt/SiO<sub>2</sub> or Pt/Al<sub>2</sub>O<sub>3</sub>. This catalyst has already been successfully employed for H<sub>2</sub> + O<sub>2</sub> reaction in a sealed lead acid battery to prolong its life and efficiency [66]. Liu et al. [67] used sintered Ce<sub>0.8</sub>M<sub>0.2</sub>O<sub>2-δ</sub> (M=La, Y, Gd, Sm) powder prepared by sol-gel method to synthesize ammonia at atmospheric pressure.

Property	Value (unit)
Density	7.22 gm/cm <sup>3</sup>
Melting point	Ca. 2750 K
Specific heat	Ca. 460 J/kg <sup>-1</sup> K
Thermal conductivity	Ca. 12 W/m K
Refractive index	Ca. 2.1 visible Ca. 2.2 infrared
Relative dielectric constant (0.5-50 MHz)	11
Young's modulus	Ca. 165 x 10 <sup>9</sup> N/m <sup>2</sup>
Poisson's ratio	Ca. 0.3
Hardness	5-6

Table 1. Some physical properties of pure stoichiometric CeO<sub>2</sub> [68]

Considering importance of doped and pure ceria, Mogens Mogensen et al. [68] put his efforts to collect the available data (Table 1) on its physical, chemical,



electrochemical and mechanical properties, predominantly in the temperature range from 200 to 1000°C. Mogens Mogensen et al. also pointed out several areas where further research is needed in order to make a better basis for the evaluation of the real potential and limits for the practical application of ceria in solid oxide fuel cells and other solid state electrochemical devices.

Ionic conductivity in doped ceria is closely related to oxygen-vacancy formation and migration properties. Andersson et al. [69] presented a quantum-mechanical study of the influence of different trivalent impurities on these properties. Their results reveal the relation between vacancy properties at the atomic level and the macroscopic ionic conductivity. Andersson et al also cleared that the basic principle for the choice of a dopant, is the ability of the dopant to minimize the internal strain of the lattice. Calculated relaxation patterns showed that upon doping with trivalent ions, the Ce-O inter-atomic distances decrease which could be smaller for an increasing atomic number of the lanthanide elements [70]. However, the investigation carried out by G. Bryan Balazs et al. [71] did not found firm correlation between these two variables i.e. between conductivity and ionic radius, although the conductivity generally increased with increasing ionic radius of the dopant cation. Balazs et al. [71] in his article reported the ionic conductivities of cerium oxide doped with oxides of the entire rare earth series (except Pm) using ac impedance. All of these samples showed an increase in the conductivity over un-doped ceria, with Gd, Sm and Y doped ceria exhibiting the highest values. At present, ceria based electrolytes appear to be the most promising amongst high ionic conductivity electrolytes.

### 1.6.1. Gd doped ceria (GDC)

Ceria-based electrolytes have relatively large unit cells compared to systems based on zirconia and, as a consequence, ceria-based systems have larger channels through which oxygen ions pass during conduction. Bevan and Summerville [72] demonstrated, using lattice parameter data, that the introduction of the  $Gd^{+3}$  ions into the  $CeO_2$  lattice minimizes unit cell expansion or contraction. The work performed by Bevan and Summerville was further analyzed by Kilner [73]. Kilner assumed that the  $Ce^{+4}$  and  $Gd^{+3}$  ions have a similar size in the defect-fluorite structure and correlated to confirm the fact that  $CeO_2-Gd_2O_3$  system is one of the highest ionically conducting,



ceria-based binary systems [74]. It was thought that the substitution of larger dopants into ceria crystal lattices blocks the path of the migrating oxygen ions more effectively, thus increasing the ion-migration enthalpy [75].

Though incorporation of Gd into ceria has shown increased ionic conduction [76], with the hope of further enhanced conductivities researcher experimented with co-doping of ceria. F.Y. Wang et al. [77] reported that  $Gd^{3+}$  and  $Sm^{3+}$  co-doped ceria based electrolytes prepared by Citric-Nitrate Combustion process (CNP) for intermediate temperature solid oxide fuel cells (IT-SOFCs) showed much higher ionic conductivities at 773–973 K compared to the singly doped ceria. And hence Wang et al stated that these co-doped ceria are more ideal electrolyte materials of ITSOFCs. However, controversial results on co-doping effect were also reported. For example, Herle et al. [78] found that co-doped ceria showed significant higher ionic conductivity (by 10–30%) than the best singly doped materials (similar to Wang et al), whereas, Yoshida et al. [79, 80] found that a doubly doped ceria with  $La^{3+}$  and  $Y^{3+}$  did not show any combined effects on ionic conductivity.

### ***1.6.2. Shortfalls in the use of GDC as solid electrolytes and the resolutions over it***

Even having an excellent ionic conduction behavior, GDC has a relatively narrow region of oxide ion conductivity as an electronic component [81] is introduced on reduction, producing a short circuit in the cell. When the electrolyte is subjected to partial pressure of oxygen typically associated with the anode side of a fuel cell, its electronic contribution to the overall conductivity increases. This increase in electronic conduction, due to the reduction of  $Ce^{4+}$  to a  $Ce^{3+}$  state, shorts out the electrolyte resulting in failure of the electrolyte material [82]. Under these condition the doped ceria is partially reduced and its lattice parameter increases leading to the generation of stress in the electrolyte. Atkinson [83] calculated these stresses for a range of different parameters which includes doping level (Gd), temperature, oxygen activity, etc. and indicated that the maximum ‘safe’ operating temperature for Gd doped Ceria at an anode is about 750°C.

To deal with this negative aspect Marquesa and Navarra [84] proposed to use double layer electrolyte configuration to avoid cell efficiency losses. They have reported the performance of such double layer electrolyte cells consisting of one gadolinia doped ceria (GCO) supporting layer covered by one Ytria stabilized



zirconia (YSZ) electron blocking layer might be located either on the cell cathode or anode side.

To observe the effects take place on microstructure of reduced electrolytes, Badwal et al. [85] investigated the impedance behavior and microstructure of the GDC20 exposed to mild fuel environments (H–N mixtures) at 1000°C. A substantial expansion of the lattice as a consequence of the reduction of  $\text{Ce}^{4+}$  to  $\text{Ce}^{3+}$  was observed, which in turn led to the development of micro-cracks and loss of continuity at the grain boundary region with an increase in both, the grain boundary and the lattice resistivity. The large increase in the grain boundary resistivity in reduced specimens was attributed to the observed micro-cracking and possibly the formation of new phase regions with extremely poor oxygen-ion conductivity along grain boundaries during the reduction. In another attempt to understand the effect of reduction on doped ceria based electrolytes N. Maffei and A.K. Kuriakose [86] made thermo-gravimetric analysis of the electrolytes (co-doped with gadolinium and praseodymium) in hydrogen and observed that a chemical reduction of the material begins at about 700°C. The weight loss recorded in TGA was accompanied by  $\text{H}_2\text{O}$  evolution in the same temperature range confirming the chemical reduction of the doped ceria electrolyte. Hence, the authors concluded that a fuel cell incorporating the doubly doped ceria electrolyte may be safely operated at around 700°C for long periods of time. However, at operating temperatures approaching 800°C, the fuel cell incorporating doubly doped ceria would be unstable. It is interesting to note here that the co-doped ceria still narrow down the oxygen ion conducting regime by putting the constraint on upper side to be 700°C ('safe' operating temperature), while it was 750°C for singly doped ceria.

To address the significant problem with ceria based materials of poor stability at low partial pressure of oxygen, a number of approaches have been taken (other than mentioned above), such as finding the ideal doping level and ion to balance stability with adequate oxide ion conductivity, decreasing the operating temperature and improving materials processing etc. In an effort to minimize the GDCs' instability at lower oxygen partial pressures, other ceria based materials of the general formula  $\text{Ce}_{1-x}\text{M}_x\text{O}_{2-\delta}$ , where  $\text{M} = \text{Gd}, \text{Sm}, \text{Ca}, \text{Mg}$  have been studied [49, 52].  $\text{Gd}_{0.1}\text{Ce}_{0.9}\text{O}_{1.9}$  (GDC10) was the preferred choice for the electrolyte, with a compromise between higher stability to reduction and good oxide ion conductivity at 600°C as higher Gd



concentration materials are more readily reduced, though the oxide ion conductivity is increased. Doshi et al. have shown that  $\text{Ce}_{0.8}\text{Gd}_{0.2}\text{O}_{1.9}$  (GDC20) is purely an ionic conductor in fuel environments only below  $450^\circ\text{C}$  [87]. Decreasing the temperature of operation for GDC to  $600^\circ\text{C}$  appears to minimize the reduction of the electrolyte; however, lower temperatures result in the greater loss of power density due to the decrease in the ionic conductivity.

### 1.6.3. Synthesis of GDC by the cost effective ceramic route (solid state reaction)

Various ceramic powder synthesis and processing methods have been used to prepare doped ceria with desired properties, including hydrothermal synthesis [88], homogeneous precipitation [89], sol–gel process [90], glycine–nitrate process [91], etc. Huang et al. [90] while investigating the structural, thermal expansion and ionic conductivity of solid electrolytes found that the uniform small sized particle allows the sintering of the samples into highly dense ceramic pellets at reduced temperature. Solid-state reaction, a simple and cost-effective method, is often adopted to prepare electrode materials [92, 93] and bulk electrolyte samples [94, 95].

Y.J. Leng et al. [51] introduced solid-state reaction technique for in situ fabrication of  $\text{Ce}_{0.8}\text{Gd}_{0.2}\text{O}_{1.90}$  electrolyte from ceria and gadolinia. With this method, expensive GDC powder is not required; instead much cheaper ceria and gadolinia powders are used. Leng et al. fabricated dense electrolyte made of  $\text{Ce}_{0.8}\text{Gd}_{0.2}\text{O}_{1.90}$  (GDC20) powder and supported by Ni-GDC cermet anode. With LSCF-GDC composite cathode an excellent cell performance with the maximum power density of 578, 358, and  $167\text{mW}/\text{cm}^2$  at  $600^\circ\text{C}$ ,  $550^\circ\text{C}$  and  $500^\circ\text{C}$ , respectively was achieved.

In regard of doping variation of Gd, Zha et al. [96] synthesized electrolytes of  $\text{Ce}_{1-x}\text{Gd}_x\text{O}_{2-x}$  (GDC) and  $\text{Ce}_{1-x}\text{Sm}_x\text{O}_{2-x}$  (SDC) ( $x = 0-0.25$ ) using an oxalate co-precipitation process, and found the maximum electrical conductivity at a dopant concentration of  $x = 0.15$ , for both the cases. In a similar study, Kudo and Obayashi [97] found the peak conductivities for Gd doped ceria were at 20 mol%  $\text{Gd}_2\text{O}_3$  dopant concentration. The difference between them may be due to the investigated concentration ranges. In Zha et al.'s work, the dopant concentrations were intensively studied from  $x = 0-0.25$  with interval of 0.05, while in the later work the range was from  $x = 0-0.5$  with an interval of 0.10. However, according to Zha et al. even if the



peak conductivities were obtained at 15mol% for Gd- and Sm-doped ceria, it does not mean that they are the best ones among GDC and SDC electrolytes for practical SOFCs. Other electrochemical and mechanical properties, such as ionic transference number, thermal expansion constant and compatibility with other fuel cell components, should also be taken into account in the selection of appropriate electrolyte materials. In a more recent paper, Steele [49] summarized other authors work and indicated that the total conductivity peaks around 25 mol%  $Gd_2O_3$  concentration.

The sintering of solid state reaction method plays the key role in preparation of the final product with desired characteristics. H. Inaba [98] studied the sintering behavior of ceria and gadolinia-doped ceria powders by measuring density and grain size as a function of sintering time. Densification rate and grain growth rate of ceria with a fine particle size were larger than those with a large particle size. However, grain growth rate of gadolinia-doped ceria was observed to much smaller than that of pure ceria, but densification rate was considerably larger. They suggested that the rate-determining step of densification is the rate of diffusion of oxygen, which is large in gadolinia-doped ceria compared to pure ceria.

Further if the starting powders for solid state reaction exhibits some impurities it would propagate throughout the synthesis procedure. While addressing this aspect, Zhang et al. [99] studied three groups of  $Ce_{1-x}Gd_xO_{2-\delta}$  ( $0.05 \leq x \leq 0.3$ ) ceramics, with  $SiO_2$  contents of 30, 200 and 3000ppm, and demonstrated the effects of both gadolinia and silica contents on the ionic conductivities. It was found that, with increasing  $SiO_2$  content, the composition of maximum total conductivity shifted to high 'x' values. Meanwhile, the values of the maximum total conductivity were reduced significantly with increasing  $SiO_2$  content. To a large extent, the blocking behavior of grain boundaries is mainly attributed to the presence of thin siliceous films.

#### **1.6.4. GDC thin film as solid electrolyte for IT- or LT-SOFCs**

To enhance the long-term performance and stability and to widen the material selection, it is desirable to lower the operating temperature of SOFCs from the  $1000^\circ C$  to an intermediate/low-temperature range of  $500-800^\circ C$ . At operating temperature below  $700^\circ C$ , low-cost ferrite stainless steel could be used as the



components of fuel cell systems such as interconnects, gas manifolds and heat exchangers leading to reduced costs of total system. Lower operating temperature also implies fewer degradation problems, less thermal mismatch between cell components. However, significant barriers to intermediate/ low-temperature SOFCs are the increase of electrolyte resistance and high electrode over-potentials.

There are two prime approaches to overcome these problems: the first is to decrease the electrolyte thickness [100, 101] and the second is to use electrolyte materials with high ionic conductivity at low temperature such as doped LaGaO<sub>3</sub> [102] and doped ceria [103]. In addition, reduction of the electrode polarization resistance [104] also would be helpful in reducing the operating temperature. The reduction in thickness of dense electrolytes consequence in minimized internal ohmic loss [105] leading to higher conductivity at lower temperature.

To lower the operating temperature, extensive research has been conducted to look for new fluorite-type materials with conductivity values larger than those of zirconia-based electrolytes. It is clear from the viewpoint of structure that the simplest way to enlarge the bottleneck, through which oxygen ions can migrate, is to occupy the cation sites in host lattice with polarizable cations. As the polarizability of an ion increases with its radius, big cations must be preferred. However, to maintain the stability of the fluorite structure, the ratio between the cation and the anion radii must remain close to 0.70. On the basis of an oxide ion radius of 0.138 nm, the optimum cation size is close to 0.1 nm. Such a large radius is typically of the order of that of 4f elements. Since in lanthanide series contraction of ionic radius occur with the atomic number; only elements located at the beginning of the lanthanide series can ideally fit the size requirement [106, 107]. Keeping this theory in mind people are researching on the cerium-based solid solution to obtain highest conductive system and found that Gd doped ceria (GDC) gives maximum conductivity compared to other dopants.

Thin film technology could enable Gd doped ceria electrolytes to be operated at further reduced temperature, thereby eliminating the negative aspect of reducing behavior at or above 700°C and in low oxygen activity circumstances. In such case, according to Xia and Liu [108], partial internal shorting arising from the electronic conduction of GDC becomes insignificant. Also the previous researches [105, 109] indicated that although Ce<sup>4+</sup> can be reduced to Ce<sup>3+</sup>, this reduction occurs only in reducing atmospheres and especially at higher temperatures (>700°C). Similarly, no



evidence for electronic conductivity was seen in the investigation carried out by Balazs and Glass [71], except when the sample was exposed to a reducing atmosphere, or was intentionally biased with a large voltage across the sample ( $>1V$ ).

To reduce the electrolyte thickness, various techniques such as tape casting, slurry coating, electrochemical vapor deposition, physical vapor deposition, vacuum plasma spray and colloidal coating have been used in its fabrication. In addition, considerable effort has been made on the development of low-temperature SOFCs based on thin film electrolyte of doped ceria. e.g., Doshi et al. [78] reported a max power density of  $140\text{mW}/\text{cm}^2$  at  $500^\circ\text{C}$  for a  $\text{H}_2/\text{air}$  fuel cell with a  $30\text{-}\mu\text{m}$  thin film GDC. Anode-supported cell was prepared by a multi-layer tape casting technique.

According to Atkinson [74], thin film technology not only helps to reduce the operating temperature of cell but also minimize the risk of fracture in ceria based electrolytes. Under the low oxygen activity conditions at the SOFC anode, the ceria is partially reduced and its lattice parameter increases leading to the generation of stress in the electrolyte. These stresses have been calculated by Atkinson for a range of different parameters which shows that maximum tensile stresses are related to the non-stoichiometry of the electrolyte and suggested that the self supporting planar electrolytes should be allowed to relax by bending in order to minimize the risk of fracture and that supported electrolytes should be made as thin as possible.

There are numerous examples in the literatures which emphasizes use of thin films to lower the operating temperature ( $T_{OP}$ ). Few to mention, the demonstrations of reduction of operating temperature reported in literature are summarized in table 2.

Ref.	Preparation tech.	Material	Application
[105]	Aerosol-assisted metal-organic CVD technique	Gadolinia-doped ceria (GDC), on anode (NiO + YSZ) substrates	Intermediate temperature Solid oxide fuel cells (IT-SOFCs)
[107]	Wet ceramic processes	GDC as interlayer at cathode	SOFCs

Table 2. Demonstrations of reduction of operating temperature reported in literature.





[110]	Spin-coating technique	GDC20–CoFe <sub>2</sub> O <sub>4</sub>	Oxygen permeable devices
[111]	Wet-chemical process	Anode-supported GDC electrolyte	IT-SOFCs
[112]	Spin-coating technique	Anode-supported Ce <sub>0.9</sub> Gd <sub>0.1</sub> O <sub>1.95</sub> thin electrolyte	Single-chamber (SC-) SOFCs for mobile and portable power generation systems [113, 114]
[115]	Spray pyrolysis technique	YSZ and GDC solid electrolyte	SC-SOFCs

Table 2. (Continued...)

Operating micro-solid oxide fuel cells ( $\mu$ -SOFCs) with gadolinia doped ceria (GDC) thin films as electrolytes is advantageous due to: (a) the high ionic conductivity at intermediate operating temperatures compared to state-of-the-art Ytria-stabilized zirconia (YSZ) [55, 116, 117]; (b) the possibility to combine low-cost ceramic thin film coating methods, such as spray pyrolysis, with traditional silicon micromachining technologies; and (c) The reduction of the ohmic losses through the cell resulting in higher power outputs [118].

Due to these reasons, it is interesting to investigate the electrical properties of ceria-based thin films also for  $\mu$ -SOFC applications. Other advantages of fuel cells with thin electrolytes are reduced materials cost and improved fuel cell characteristics [55, 119, 120]. Ceria-based thin films also have attracted great interest as gas sensors operating at low temperatures [121].

Previous investigations [122-129] have shown the strong possibilities for the fabrication of thin electrolyte films using chemical spray deposition techniques, as this technique has the potential to prepare the dense & 2-10 $\mu$ m thick films, which are necessary for a solid electrolyte to be operated at lower temperature.

To gain the advantages of chemical spray pyrolysis technique, D. Perednis, and L.J. Gauckler [130] applied it to deposit thin, dense electrolyte films on porous anode substrates with two different atomizers, namely electrostatic and air blast type, for generation of aerosol. They found that most of the time it is more difficult to deposit gas-tight and smoother films by electrostatic atomizers compared to those



deposited using an air blast atomizer. It was also observed that a sub-micron thin electrolyte film deposited using the spray pyrolysis could close pores with size of up to  $3\mu\text{m}$ . The cells containing sprayed, ultra-thin electrolytes were operated at  $770^\circ\text{C}$  and a power output of  $550\text{mW}/\text{cm}^2$  was achieved.

Rupp et al. [131] investigated the relation between electrical property and microstructure of nano-crystalline  $\text{CeO}_2$  and GDC thin films and compared to data of bulk materials.  $\text{CeO}_2$  and  $\text{Ce}_{0.8}\text{Gd}_{0.2}\text{O}_{1.9-x}$  thin films were fabricated by spray pyrolysis and pulsed laser deposition, and the influence of the ambient average grain size on the total DC conductivity was investigated. Dense and crack-free  $\text{CeO}_2$  and  $\text{Ce}_{0.8}\text{Gd}_{0.2}\text{O}_{1.9-x}$  thin films were produced that withstand annealing up to temperatures of  $1100^\circ\text{C}$ . The dopant concentration and annealing temperature affected highly the grain growth kinetics of ceria-based thin films. Rupp et al. in an another study, investigated the chemical homogeneity of as-deposited and annealed  $\text{Ce}_{0.8}\text{Gd}_{0.2}\text{O}_{1.9-x}$  thin films which were prepared using spray pyrolysis [132]. After the topmost layer was removed by  $\text{Ar}^+$  sputtering, the thin films showed a surprisingly homogeneous dopant concentration of 0.6 at% gadolinia in ceria, independent of the film depth. However, spray-pyrolysis-related residues of the precursors (i.e., chlorine from the precursor salt, carbon from the pyrolysis solvents, and water) was found at unexpected depths in the film and even after annealing at temperatures as high as  $1000^\circ\text{C}$ . It was understood by authors that in the case of traces of water, organic solvents and chlorine, do not alter the electrical properties of the thin films considerably [133-135], because the conductivity of the film is mainly determined by the dopant level, the strain in the grains, and the amount of grain boundaries (grain size).

## 1.7. Scope of research work

Solid Oxide Fuel Cell (SOFC) is well known forthcoming high efficient power generation devices (operating temperature ( $T_{\text{OP}}$ ) =  $1000^\circ\text{C}$ ), since it converts gaseous fuel electrochemically into electricity with a very efficient (>60%) and eco-friendly manner. In recent years, to overcome commercialization related problems of SOFCs, such as its cost of fabrication, reliability, durability etc., researchers gradually has been shifted towards the development of intermediate and low temperature (IT and LT) SOFCs (operated below  $700^\circ\text{C}$ ). IT or LT-SOFCs has inherent potential of



reduction in the cost of the cell fabrication materials by allowing use of standard quality sealant, interconnects, etc. instead of high quality materials for the same. In addition to reduction in cost of fabrication it also offers better reliability, portability and operational life. These advantages over HT-SOFCs ( $T_{OP} > 800^{\circ}\text{C}$ ) would certainly make IT and LT-SOFC, a most appropriate prospective power generation device for commercial realization.

Both the strategies which are supposed to be stressed to overcome the bottleneck of operating temperatures of SOFCs are employed in this particular research. (i) Use of alternate solid electrolyte having high ionic conductivity at reduced temperature was preferred over the conventional solid electrolyte; thereby  $T_{OP}$  would be kept below  $700^{\circ}\text{C}$ . (ii) The thickness of electrolyte decreased to such an extent (using thin films preparation technique) that it would offer less ohmic losses for ionic conduction but should not allow fuel cross over. The thin film with relative density of the order of 90% with 10-20 $\mu\text{m}$  thickness would suffice the purpose. Further the reduction of  $T_{OP}$  increases the electrode potentials across the electrode/electrolyte interface and thus in addition to above mentioned strategies the reduction of electrode-electrolyte interfacial resistance was also followed. The search of alternate material for solid electrolytes has resulted into exciting discovery of 10% gadolinia doped ceria (GDC). Its high ionic conductivity at relatively low temperatures makes it an ideal candidate for intermediate temperature solid oxide fuel cells, operating at  $550\text{--}650^{\circ}\text{C}$ . In order to increase the ionic conductivity at further lower temperatures, the thickness of the GDC electrolyte would be reduced (10-20 $\mu\text{m}$ ). Reduction in  $T_{OP}$  in addition to improved ionic conductivity would be helpful to avoid the well known transition of GDC from ionic to electronic conductor (by  $\text{Ce}^{4+} \rightarrow \text{Ce}^{3+}$ ) in fuel cell environment. To employ the thin film electrolyte in SOFCs, it has to be supported by some kind of substrate and if the substrate itself could act as an electrode for SOFC, it would be an added advantage.

In the proposed research, it was decided to synthesize the GDC and to demonstrate its use in IT-SOFCs. Initially, it was planned to synthesize the bulk GDC and study its different properties. For this, solid state reaction method was preferred due to its cost effective nature and ease of preparation procedure. The commercially available initial precursor materials were used to synthesize the GDC bulk. The process parameters of solid state reaction method were varied along with doping percentage of gadolinia in ceria to demonstrate its effect on structural, morphological



and electrical properties of the prepared samples. This study was expected to provide intimate knowledge of processing parameters of solid state reaction method and its effect on the final product. It was also decided to vary Gd content in ceria to recognize the optimum level of doping for better solid-electrolyte properties. Attempts were made to synthesize samples with best results in electrical performance with an intention to use it in IT-SOFCs.

Thin films of GDC for optimum concentration of Gd in ceria were prepared using Spray Pyrolysis Technique (SPT) due to its simplicity, cost effective nature and ease of preparation procedure. In this part of research, it was planned, initially, to prepare GDC films onto glass substrate to understand the film growth mechanism. A systematic variation in different preparative parameters of SPT was considered to prepare the electrolyte-quality films. Further these films were characterized at each step of optimization procedure by XRD, SEM, EDAX, AFM, and were analyzed for better understanding of SPT.

Moreover, to demonstrate the solid-electrolyte-grade qualities of GDC films, it was also planned to study its interfacial properties with one of the SOFC electrodes. For this purpose, initially, ceramic anode material (NiO-GDC) as ceramic substrates (flat and thin) was prepared using solid state reaction method. These ceramic substrates were characterized and analyzed for the desired composition, porosity, flatness and thinness. Further, the good-quality GDC films were prepared on to ceramic substrates by the SPT to form electrolyte\electrode structure. The characterization of formed structure (electrode/electrolyte) was carried out during each step of optimization of SPT; using various techniques, such as, XRD, SEM, EDAX, AFM, impedance spectroscopy, etc. These characterizations helped us to narrow down the range of preparative parameters of SPT and post heat treatments. These optimizations were resulted in GDC films with desired properties and a good quality interface with the anode substrate. The formed interface was characterized using impedance spectroscopy.

Finally, the samples were characterized for open circuit voltage (OCV) measurements to test its performance in typical fuel cell conditions.



**References:**

- [1] L.W. Strock, *J. Phys. Chem. B* 25 (1934) 441.
- [2] C.Wagner, *Naturwissenschaften*, 31(1943) 265.
- [3] S. J. Skinner and John A. Kilner, “Oxygen Ion conductor: Review Feature”, *Materials Today*, March 2003 30.
- [4] J. Kilner, S. Benson, J. Lane, D. Waller, *Chemistry and Industry* 22 (1997) 907.
- [5] J.A. Kilner, B.C.H. Steele, in: *Non-stoichiometric Oxides*, ed. O.T. Sorensen, *Academic Press, New York* (1981).
- [6] Vannier, R. N., *Proc. Europ. Mat. Res. Soc. Symp.* (2002)
- [7] J. A. Kilner, *Solid State Ionics* 129 (2000) 13
- [8] D. Yuan, F.A. Kroger, *J. Electrochem. Soc.* 116 (1969) 594.
- [9] Y.K. Agarwal, D.W. Short, R. Gruenke, R.A. Rapp, *ibid*, 121 (1974) 354.
- [10] K.E. Oberg, L.M. Friedman, W.M. Boorstein, R.A. Rapp, *Met. Trans.* 4 (1973) 75.
- [11] H. Okamoto, H. Obayashi, T. Kudo, *Solid State Ionics* 3/4 (1981) 453.
- [12] A.O. Isenberg, *Solid State Ionics* 3/4 (1981) 431.
- [13] T.M. Gur, R.A. Huggins, *J. Electrochem. Soc.* 126 (1979) 1067.
- [14] T.M. Gur, R.A. Huggins :in *Fast Ion Transport in Solids Proc. Int. Conf. Lake Geneva, P. Vashishta, J.N. Mundy and G.K. Shenoy ed., North Holland, Amsterdam*, (1979) 109.
- [15] T.M. Gur, R.A. Huggins, *Solid State Ionics* 5 (1981) 563.
- [16] C.T. Sigal, C.G. Vayenas, *ibid*, 5 (1981) 567.
- [17] S.C. Singhal, *Solid State Ionics*, 135 (2000) 305.
- [18] B.C.H. Steele, *Solid State Ionics*, 129 (2000) 95.
- [19] M. Mogensen, N.M. Sammes, G.A. Tompett, *Solid State Ionics* 129 (2000) 63.
- [20] B.C.H. Steele, In: *High Conductivity Solid Ionic Conductors*, Ed. T. Takahashi, *World Scientific, Singapore*, (1989).
- [21] T. Fukui, K. Murata, S. Ohara, H. Abe, M. Naito, K. Nogi, *J. Power Sources*, 125 (2004) 17.
- [22] X. J. Chen, K. A. Khor, S. H. Chan, L. G. Yu, *Mater. Sci. Eng.*, A-335 (2002) 246.
- [23] Q. Zhu, B. Fan, *Solid State Ionics*, 176 (2005) 889.



- [24] M. Gaudon, E. Djurado, N. H. Menzler, *Ceram. Int.*, 30 (2004) 2295.
- [25] D. Lee, I. Lee, Y. Jeon, R. Song, *Solid State Ionics*, 176 (2005) 1021.
- [26] T. I. Politova, J. T. S. Irvine, *Solid State Ionics*, 168 (2004) 153.
- [27] C. Haering, A. Roosen, H. Schichl, M. Schnoller, *Solid State Ionics*, 176 (2005) 261.
- [28] C. Varanasi, C. Juneja, C. Chen, B. Kumar, *J. Power Sources*, 147 (2005) 128.
- [29] Z. Lei, Q. Zhu, *Solid State Ionics*, 176 (2005) 2791.
- [30] H. M. T. Ishihara, Y. Takita, *J. Am. Chem. Soc.*, 116 (1994) 3801.
- [31] T. Ishihara, Y. Hiei, Y. Takita, *Solid State Ionics*, 79 (1995) 371.
- [32] O. Yamamoto, *Electrochim. Acta.*, 45 (2000) 2423.
- [33] K. Yamaji, T. Horita, M. Ishikawa, N. Sakai, H. Yokokawa, *Solid State Ionics*, 108 (1998) 415.
- [34] K. Yamaji, T. Horita, M. Ishikawa, N. Sakai, H. Yokokawa, *Solid State Ionics*, 121 (1999) 217.
- [35] A. Matraszek, L. Singheiser, D. Kobertz, K. Hilpert, M. Miller, O. Schulz, M. Martin, *Solid State Ionics*, 166 (2004) 343.
- [36] K. Huang, M. Feng, J. B. Goodenough, C. Milliken, *J. Electrochem. Soc.*, 144 (1997) 3620.
- [37] S.W. Tao, F.W. Poulsen, G.Y. Meng, O.T. Sorensen, *J. Mater. Chem.*, 10 (2000) 1829.
- [38] J. B. Goodenough, J. E. Ruiz-Diaz, Y. S. Zhen, *Solid State Ionics*, 44 (1990) 21.
- [39] K. Kakinuma, S. Machida, T. Arisaka, H. Yamamura, t. Atake, *Solid State Ionics*, 176 (2005) 2405.
- [40] K. Kakinuma, T. Arisaka, H. Yamamura, T. Atake, *Solid State Ionics*, 175 (2004) 139.
- [41] T. Takahashi, T. Esaka, H. Iwahara. *J. Appl. Electrochem.*, 5 (1975) 197.
- [42] M.J. Verkerk A.J. Burggraaf. *J. Electrochem. Soc.*, 128 (1981) 75.
- [43] E.D. Wachsman, G.R. Ball, N. Jiang, D.A. Stevenson. *Solid State Ionics*, 52 (1992) 213.
- [44] K. Fung, H.D. Back, A. Virkar. *Solid State Ionics*, 52 (1992) 199.
- [45] K. Huang, M. Feng, J.B. Goodenough. *Solid State Ionics*, 89 (1996) 17.
- [46] V.V. Kharton, E.V. Naumovich, A.A. Yaremchenko, F.M.B. Marques. *J. Solid State Electrochem.*, 5 (2001) 160.



- [47] S. Wang, T. Kato, S. Nagata, T. Kaneko, N. Iwashita, T. Honda, M. Dokiya, *Solid State Ionics*, 477 (2002) 152.
- [48] B. C. H. Steele, *Solid State Ionics*, 134 (2000) 3.
- [49] B. C. H. Steele, *Solid State Ionics*, 129 (2000) 95.
- [50] T. S. Zhang, J. Ma, L. B. Kong, P. Hing, J. A. Kilner, *Solid State Ionics*, 167 (2004) 191.
- [51] Y. J. Leng, S. H. Chan, S. P. Jiang, K. A. Khor, *Solid State Ionics*, 170 (2004) 9.
- [52] C. Hatchwell, N. M. Sammes, I. W. M. Brown, *Solid State Ionics*, 126 (1999) 201.
- [53] G. Corbel, S. Mestiri, P. Lacorre, *Solid State Sci.*, 7 (2005) 1216.
- [54] A.J. McEvoy, *Solid State Ionics*, 132 (2000) 159.
- [55] M. Mogensen, N.M. Sammes, G.A. Tompett, *Solid State Ionics*, 129 (2000) 63.
- [56] E. J. Romano, K. H. Schulz, *App. Surf. Sci.*, 246 (2005) 262.
- [57] O. A. Marina, C. Bagger, S. Primdahl, M. Mogensen, *Solid State Ionics*, 123 (1999) 199.
- [58] Z. Shao, W. Yang, Y. Cong, H. Dong, J. Tong, G. Xiong, *J. Membr. Sci.*, 172 (2000) 177.
- [59] A. Trovarelli, *Catal. Rev.-Sci. Eng.*, 38 (1996) 439.
- [60] H. Inaba, H. Tagawa, *Solid State Ionics*, 83 (1996) 1.
- [61] T. Takahashi, A. Kozawa (Eds.), *Application of Solid Electrolytes*, Jec Press, Ohio, 1980.
- [62] W. Giipel, T.A. Jones, M. Kieitz, I. Lundstrijm, T. Seiyama (Eds.), *Chemical, Biochemical Sensors*, Vol. 2, 3, Vch, Weinheim, 1991/1992.
- [63] Y. Maki, M. Matsuda, T. Kudo, *U.S. Patent No.* 3 607 424 (Sept. 21, 1971).
- [64] E.M. Logothetis, *National Symposium on Ceramics on: The Service of Men*, Washington Dc (1976, June 7).
- [65] P. Bera, M. S. Hegde, K. C. Patil, *Current Science*, 80 (25 June 2001) 12.
- [66] B. Hariprakash, P. Bera, S.K. Martha, S.A. Gaffoor, M.S. Hegde, A.K. Shukla, *Electrochem. Solid-State Lett.*, 4 (2001) A23.
- [67] R.-Q. Liu, Ya-Hong Xie, Ji-De Wang, Zhi-Jie Li, Ben-Hui Wang, *Solid State Ionics*, 177 (2006) 73.



- [68] M. Mogensena , N. M. Sammes, G. A. Tompsett, *Solid State Ionics*, 129 (2000) 63.
- [69] D. Andersson, S. I. Simak, N. V. Skorodumova, I. A. Abrikosov, B. Johansson, *Appl. Phys. Sci.*, [Www.Pnas.Org Cgi Doi 10.1073 Pnas.0509537103](http://www.pnas.org/cgi/doi/10.1073/pnas.0509537103)
- [70] S. Yamazaki, T. Matsui, T. Ohashi, Y. Arita, *Solid State Ionics* 136–137 (2000) 913.
- [71] G. Bryan Balazs, Robert S. Glass, *Solid State Ionics*, 76 (1995) 155.
- [72] D.J.M. Bevan, E. Summerville, In: K.A. Gschneider, L. Eyring (Eds.), *Handbook On The Physics, Chemistry of Rare-Earths*, North Holland, Amsterdam, Vol. 4, 1979.
- [73] J.A. Kilner, *Solid State Ionics*, 8 (1983) 201.
- [74] S.P.S. Badwal, F.T. Ciacchi, *Ionics*, 6 (2000) 1.
- [75] R.J. Stafford, S.J. Rothman, J.L. Routbort, *Solid State Ionics*, 37 (1989) 67.
- [76] T.S. Zhang, J. Ma, S.H. Chan, P. Hing, J.A. Kilner, *Solid State Sciences*, 6 (2004) 565.
- [77] F.Y. Wang, S. Chen, S. Cheng, *Electrochemistry Communications*, 6 (2004) 743.
- [78] J.V. Herle, D. Seneviratne, A.J. Mcevoy, *J. Eur. Ceram. Soc.*, 19 (1999) 837.
- [79] H. Yoshida, T. Inagaki, K. Miura, M. Inaba, Z. Ogumi, *Solid State Ionics*, 160 (2003) 109.
- [80] H. Yoshida, H. Deguchi, K. Miura, M. Horiuchi, *Solid State Ionics*, 140 (2001) 191.
- [81] N. M. Sammes, Z. Cai, *Solid State Ionics*, 100 (1997) 39.
- [82] J. Petterson, *Alfred University Doctoral Thesis, Alfred Ny*, (2003).
- [83] A. Atkinson, *Solid State Ionics*, 95 (1997) 249.
- [84] F.M.B. Marquesa, L.M. Navarroat, *Solid State Ionics*, 100 (1997) 29.
- [85] S.P.S. Badwal, F.T. Ciacchi, J. Drennan, *Solid State Ionics*, 121 (1999) 253.
- [86] N. Maffei, A.K. Kuriakose, *Solid State Ionics*, 107 (1998) 67.
- [87] R. Doshi, V.L. Richards, J.D. Carter, X. Wangand M. Krumpelt, *J. Electrochem. Soc.*, 146 (1999) 1273.
- [88] M. Hirano, E. Kato, *Commun. Am. Ceram. Soc.*, 79 (1996) 777.
- [89] S.W. Zha, Q.X. Fu, Y. Lang, C.R. Xia, G.Y. Meng, *Mater. Lett.*, 47 (2001) 351.





- [90] W. Huang, P. Shuk, M. Greenblatt, *Solid State Ionics*, 100 (1997) 23.
- [91] K.A. Gschneidner Jr., L. Eying (Eds.), *Handbook on The Physics, Chemistry of Rare Earths, Non-Metallic Compounds*, North- Holland Pub. Co., Amsterdam, 3 (1979) 525.
- [92] L. Qiu, T. Ichikawa, A. Hirano, N. Imanishi, Y. Takeda, *Solid State Ionics*, 158 (2003) 55.
- [93] K. Wang, R.S. Ticky, J.B. Goodenough, *J. Am. Ceram. Soc.*, 81 (1998) 2565.
- [94] T.S. Zhang, L.B. Kong, Z.Q. Zeng, H.T. Huang, P. Hing, Z.T. Xia, J.A. Kilner, *J. Solid State Electrochem.*, 7 (2003) 348.
- [95] Y.J. Leng, S.H. Chan, S.P. Jiang, K.A. Khor, *Solid State Ionics*, 170 (2004) 9.
- [96] S. Zha, C. Xia, G. Meng, *Journal of Power Sources*, 115 (2003) 44.
- [97] T. Kudo, H. Obayashi, *J. Electrochem. Soc.*, 123 (1976) 415.
- [98] H. Inaba, T. Nakajim, H. Tagaw, *Solid State Ionics*, 106 (1998) 263.
- [99] T.S. Zhang, J. Ma, S.H. Chan, P. Hing, J.A. Kilner, *Solid State Sciences*, 6 (2004) 565.
- [100] S. De Souza, S.J. Visco, L.C. De Jonghe, *Solid State Ionics*, 98 (1997) 57.
- [101] J.W. Kim, A.V. Virkar, K.Z. Fung, K. Mehta, S.C. Singhal, *J. Electrochem. Soc.*, 146 (1999) 69.
- [102] J.W. Yan, Z.G. Lu, Y. Jiang, Y.L. Dong, C.Y. Yu, W.Z. Li, *J. Electrochem. Soc.*, 149 (2002) A1132.
- [103] C. Xia, M. Liu, *J. Am. Ceram. Soc.*, 84 (2001) 1903.
- [104] S.P. Jiang, Y.J. Leng, S.H. Chan, K.A. Khor, *Electrochem. Solid-State Lett.*, 6 (2003) A67.
- [105] H.Z. Song, H.B. Wang, S.W. Zha, D.K. Peng, G.Y. Meng, *Solid State Ionics*, 156 (2003) 249.
- [106] J. C. Boivin, B. Mairesse, *Chem. Mater.*, 10 (1998) 2870.
- [107] T. L. Nguyen, K. Kobayashi, T. Honda, Y. Limura, K. Kato, A. Neghisi, K. Nozaki, F. Tappero, K. Sasaki, H. Shiraham, K. Ota, M. Dokiya, T. Kato, *Solid State Ionics*, 174 (2004) 163.
- [108] C. Xia, M. Liu, *Solid State Ionics*, 152 (2002) 423.
- [109] T.H. Etsell, S.N. Flengas, *Chem. Rev.*, 70 (1970) 339
- [110] I. Kagomiy, T. Lijim, H. Takamur, *Journal of Membrane Science*, 286 (2006) 180.
- [111] S. D.Kim, S. H. Hyuna, J. Moona, J.H. Kima, R.H. Song, *Journal of Power*



- Sources, 139 (2005) 67.
- [112] A. Tomita, D. Hirabayashi, T. Hibino, Z. M. Nagao, M. Sano, *Electrochem. Solid-State Lett.*, 8 (2005) A63.
- [113] T. Hibino, A. Hashimoto, T. Inoue, J. Tokuno, S. Yoshida,, M. Sano, *Science*, 288 (2000) 2031.
- [114] T. Hibino, A. Hashimoto, T. Inoue, J. Tokuno, S. Yoshida, M. Sano, *J. Electrochem. Soc.*, 148 (2001) A544.
- [115] P. Bohac, L. Gauckler, *Solid State Ionics*, 119 (1999) 317.
- [116] C. Kleinlogel, L.J. Gauckler, *Solid State Ionics*, 135 (2000) 567.
- [117] M. Gödickemeier, K. Sasaki, L.J. Gauckler, *Journal of Electrochemical Society*, 144 (1997) 1635.
- [118] D. Perednis, L.J. Gauckler, *Solid State Ionics*, 166 (2004) 229.
- [119] S.A. Barnett, *Energy*, 15 (1990) 1.
- [120] I. Taniguchi, R.C. Van Landschoot, J. Schoonman, *Solid State Ionics*, 160 (2003) 271.
- [121] P.T. Moseley, *Sens. Actu. B.-Chemical*, 6 (1992) 149.
- [122] T. Setoguchi, M. Sawano, K. Eguchi, H. Arai, *Solid State Ionics*, 37 (1990) 502.
- [123] E.M. Kelder, O.C.J. Nijs, J. Schoonman, *Solid State Ionics*, 68 (1994) 5.
- [124] A.A. Van Zomeren, E.M. Kelder, J.C.M. Marijnissen, J. Schoonman, *J. Aerosol. Sci.*, 25 (1994) 1229.
- [125] C.H. Chen, A.A.J. Buysman, E.M. Kelder, J. Schoonman, *Solid State Ionics*, 80 (1995) 1.
- [126] K.L. Choy, In: W.E. Lee (Ed.), *British Ceramic Proceedings, Ceramic Films, Coatings, The Institute of Materials*, 54 (1995) 65.
- [127] K.L. Choy, W. Bai, B.C.H. Steele, In: A.J. Mcevoy, K. Nisancioglu (Eds.), *Materials, Processes, 10<sup>th</sup> SOFC Workshop, Les Diablerets, Int. Energy Agency*, (1997) 233.
- [128] N.H.J. Stelzer, C.H. Chen, L.N. Van Rij, J. Schoonman, In: A.J. Mcevoy, K. Nisancioglu (Eds.), *Materials, Processes, 10<sup>th</sup> SOFC Workshop, Les Diablerets, Int. Energy Agency*, (1997) 236.
- [129] K.L. Choy, W. Bai, In: A.J. Mcevoy, K. Nisancioglu (Eds.), *Materials, Processes, 10<sup>th</sup> SOFC Workshop, Les Diablerets, Int. Energy Agency*, (1997) 252.



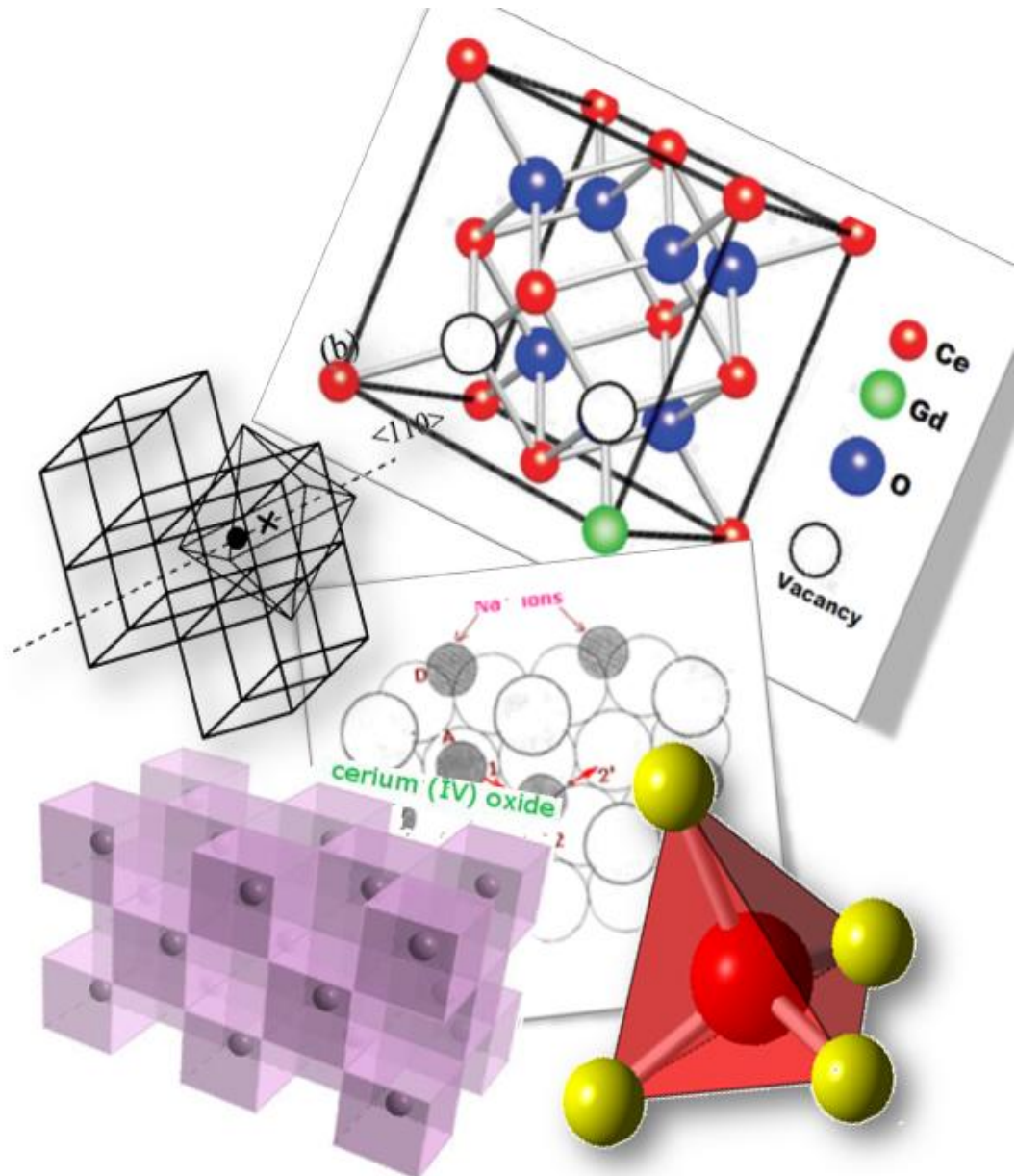
- [130] D. Perednis,, L.J. Gauckler, *In 8<sup>th</sup> International Symposium on Solid Oxide Fuel Cells , Paris: France; The Electrochemical Society; (2003) 970.*
- [131] Jennifer L.M. Rupp, Ludwig J. Gauckler, *Solid State Ionics*, 177 (2006) 2513.
- [132] Jennifer L. M. Rupp, Tanja Drobek, Antonella Rossi, Ludwig J. Gauckler, *Chem. Mater.* 19 (2007) 1134.
- [133] Kim S., Merkle R., Maier J., *Solid State Ionics* 161 (2003) 113.
- [134] J. L. M. Rupp, L. J. Gauckler, *Solid State Ionics* 177 (2006) 2513.
- [135] J. L. M. Rupp, A. Infortuna, L. J. Gauckler, *J. Am. Ceram Soc.* 90 (2007) 1792.





# Chapter two:

*Ionic conduction mechanism and electrical behavior of pure and doped ceria*





# Chapter two

## CONTENTS

2. IONIC CONDUCTION MECHANISM AND ELECTRICAL BEHAVIOR OF PURE AND DOPED CERIA.....	38
2.1. Introduction .....	39
2.2. Ion conduction mechanisms in solid electrolytes .....	40
2.2.1. Conduction mechanisms .....	40
2.2.2. Mobile ion concentrations – doping effects.....	42
2.2.3. Ion trapping effects.....	43
2.2.4. Potential energy profile.....	44
2.2.5. The activation energy for conduction .....	45
2.2.6. Hopping rates.....	46
2.2.7. The ac conductivity span: local motions and long range conduction.....	47
2.2.8. An example of solid electrolyte: Oxide ion conductors.....	48
2.3. Crystal structure and electrical behavior of pure and doped ceria ....	49
2.3.1. About cerium (Ce) element [5].....	49
2.3.2. Crystal structure of ceria.....	51
2.3.2.1. Fluorite structure of $CeO_2$ .....	51
2.3.2.2. Stoichiometry of fluorite structured $CeO_2$ .....	53
2.3.2.3. Holes in fluorite structured $CeO_2$ .....	53
2.3.3. Defect structure of ceria.....	55
2.3.3.1. General format of Kröger-Vink notation.....	56
2.3.3.2. Intrinsic defects (or disorders) in ceria.....	57
2.3.3.3. Extrinsic defects (disorder) in ceria.....	59
2.3.3.4. Defect concentrations in pure and doped ceria.....	61
2.3.4. Ionic conductivity in ceria and doped ceria.....	63
2.3.5. Electrical behavior of pure and doped ceria .....	66
2.3.5.1. Influence of doping.....	66
2.3.5.2. The temperature dependence.....	67
Reference:.....	69

## **2. IONIC CONDUCTION MECHANISM AND ELECTRICAL BEHAVIOR OF PURE AND DOPED CERIA**





## 2.1. Introduction

Even the high ionic conductivity in crystalline solids is a relatively rare phenomenon; it is widely recognized due to its numerous applications in modern life style. Most ionic solids are electrical insulators unless they exhibit electronic conductivity. They begin to show significant levels of ionic conductivity only at high temperatures, as the melting point is approached. Materials in the family of crystalline *solid electrolytes* (also called *superionic conductors*, *fast ion conductors* or *optimized ionic conductors*), however, exhibit high conductivity in one of their ionic sublattices - the *mobile ion sublattice* - at temperatures well below melting. For the sake-of-comparison, conductivities of different type of materials are presented in table 1.

	Material	Conductivity (S/cm)
Ionic Conductors	Ionic crystals	$<10^{-14}$
	Solid electrolytes	$10^{-10}$ – $10^{-5}$
	Strong (liquid) electrolytes	$10^{-10}$ – $10^3$
Electronic conductors	Metals	$10^5$ – $10^9$
	Semiconductors	$10^{-1}$ – $10^6$
	Insulators	$< 10^{-12}$

Table 1. Comparison of conductivities of different type of materials.

The first half of this chapter is focused on the general consideration for ion conduction mechanisms in solid electrolytes. A basic model of ion transport is presented which contains the essential features necessary to describe conduction in solid electrolytes. The model is based on the isolated hopping of the mobile ions; in addition, brief mention is made on the influence of ion interactions between both the mobile ions and the immobile ions of the solid lattice (ion hopping) and between different mobile ions. It is likely that in solid electrolytes, such ion interactions and cooperative ion movements are important and must be taken into account if a quantitative description of ionic conductivity is to be attempted. The second half of this chapter deals with structure of the ceria based solid electrolytes and their electrical behavior.



## 2.2. Ion conduction mechanisms in solid electrolytes

### 2.2.1. Conduction mechanisms

Ionic conductivity occurs by means of ions hopping from a lattice site to the other lattice site in vicinity through a crystal structure. Therefore, it is necessary to have partial occupancy of energetically equivalent or near-equivalent sites (defects) in a crystal structure for a successful hop. There are two broad classes of *conduction mechanism*, namely *vacancy* and *interstitial migration mechanisms*. In vacancy migration, a number of sites that would be occupied in the ideal structure are in fact empty due to either a thermally generated *Schottky defect* (a cation and anion vacancy pair) formation or the presence of charged impurities. An ion adjacent to a vacancy may be able to hop into it leaving its own site vacant. This process is regarded as vacancy migration, although, it is the ions that hop. An example of vacancy migration in NaCl is shown schematically in figure 1a.

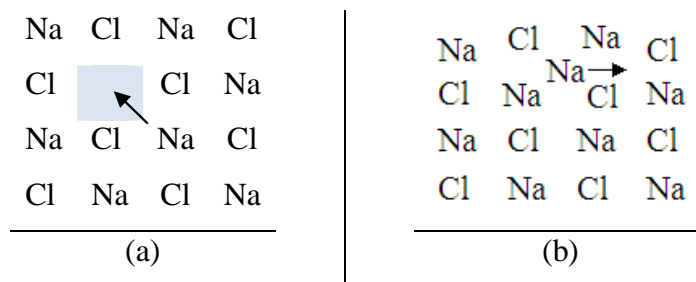


Figure 1. . (a) Vacancy and (b) interstitial migration mechanisms.

Interstitial sites are defined as those that would usually be empty in an ideal structure. Occasionally in real structures, ions may be displaced from their lattice sites into interstitial sites (*Frenkel defect* formation). Once this happens, the ions in interstitial sites can often hop into adjacent interstitial sites. These hops may be one stage in a long range conduction process. A schematic example is shown in figure 1b, a small number of  $\text{Na}^+$  ions are displaced into the tetrahedral interstitial sites and can subsequently hop into adjacent tetrahedral sites. It should be noted that while a small number of Frenkel defects may form in NaCl, conduction is primarily by means of vacancies whereas in some other structures, e.g. AgCl, Frenkel defects predominates.

The above two mechanisms may be regarded as isolated ion hops. Sometimes, especially in solid electrolytes, cooperative ion migration occurs. An example is



shown in figure 2 for the so-called *interstitialcy* or *knock-on* mechanism. A  $\text{Na}^+$  ion, A, in an interstitial site (of Na- $\beta$ -alumina) cannot move unless it persuades one of the three surrounding  $\text{Na}^+$  ions, B, C or D, to move first. Ion A is shown moving in direction 1 and, at the same time, ion C hops out of its lattice site in either of the directions, 2 or 2'.

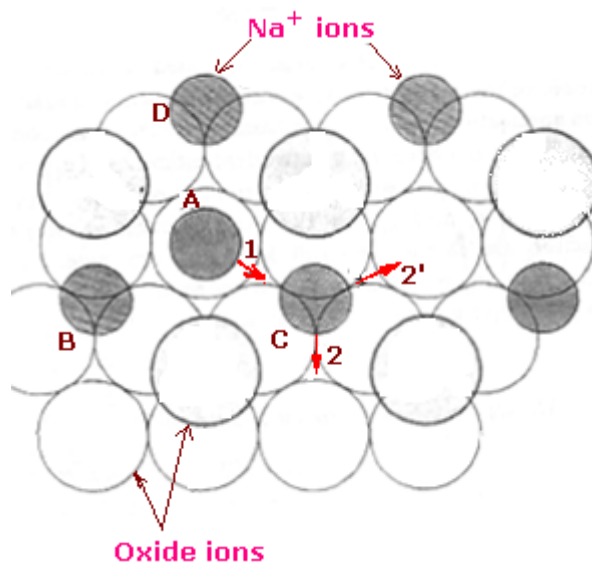


Figure 2. Interstitialcy migration mechanisms in  $\beta$ -alumina.

In crystalline electrolytes, *conduction pathways* for the mobile ions permeate the 'immobile ion sub-lattice' in one, two or three dimensions, depending on the structure of the material. Thus, in Na- $\beta$ -alumina, figure 2,  $\text{Na}^+$  ions can migrate only in to the sites containing the mobile ions which are not fully occupied and are connected, via open windows or *bottlenecks*, to adjacent sites. In crystalline electrolytes, the sites for the mobile ions are defined by the structure of the immobile sub-lattice. Therefore ionic conduction occurs by means of a series of definite hops between adjacent sites in the conduction pathways. For most of the time, the 'mobile' ions are located in a particular site, where they undergo thermal vibrations within the site. Just occasionally, they escape from their site and hop quickly into an adjacent site where they may then reside for a considerable time before either moving on or hopping back into their original site. This notion of occasional ion hops, apparently at random, forms the basis of *random walk theory* which is widely used to provide a semi-quantitative analysis or description of ionic conductivity [1]. In most solid electrolytes, without thermal activation it is very difficult to have a true liquid-like



motion of ions.

A simple and important expression for treating ionic conductivity,  $\sigma_{ir}$  is as the product of the concentration,  $c_i$ , of mobile species (interstitial ions or vacancies), their charge,  $q$  and their mobility,  $\mu_i$ :

$$\sigma_i = c_i q \mu_i, \quad (2.1)$$

This same equation is also used for the general electronic behavior of metals, semiconductors and insulators. However, the quantitative application of eq. 2.1 is not suitable for ionic conductors, since the great difficulty in obtaining independent estimates of  $c_i$  and  $\mu_i$ . *Hall effect* measurements can be used with electronic conductors to provide a means of separating  $c_i$  and  $\mu_i$  but the Hall voltages associated with ionic conduction are at the nano-volt level and are generally too small.

### 2.2.2. Mobile ion concentrations – doping effects

The parameter  $c_i$  in eq. 2.1 is capable of variation by many orders of magnitude in ionic solids. In good solid electrolytes such as Na- $\beta$ -alumina and RbAg<sub>4</sub>I<sub>5</sub>, all of the Na<sup>+</sup>/Ag<sup>+</sup> ions are potentially mobile and hence  $c_i$  is optimized. At the other extreme, in pure, stoichiometric salts such as NaCl, ionic conduction depends on the presence of crystal defects, whether vacancies or interstitials and the concentration of these is vanishingly small at room temperature. An important practical way of increasing the value of  $c_i$  is by means of doping with *alliovalent* (or *heterovalent*) ions. This involves partial replacement of ions of one type by ions of different formal charge. In order to retain charge balance, either interstitial ions or vacancies must be generated at the same time. If the interstitials or vacancies are able to migrate, an increase in conductivity can result.

For alliovalent doping of cations, there are four fundamental ionic mechanisms for achieving charge balance. These four ionic mechanisms are shown in figure 3, together with an example of each. Doping with a higher valent cation necessitates the creation of either cation vacancies (1) or anion interstitials (2), whereas doping with lower valent cations leads to the creation of either interstitial cations (3) or anion vacancies (4). In the examples and formulae shown, the number



of vacancies or interstitials increases with doping concentration,  $x$ . Usually in a particular material, there is a practical limit as to how many vacancies/interstitials can be introduced while still retaining a homogeneous solid solution phase. In many cases, this limit is small,  $\ll 1\%$  but in others it may be large, 10-20%, giving rise to massive defect concentrations.

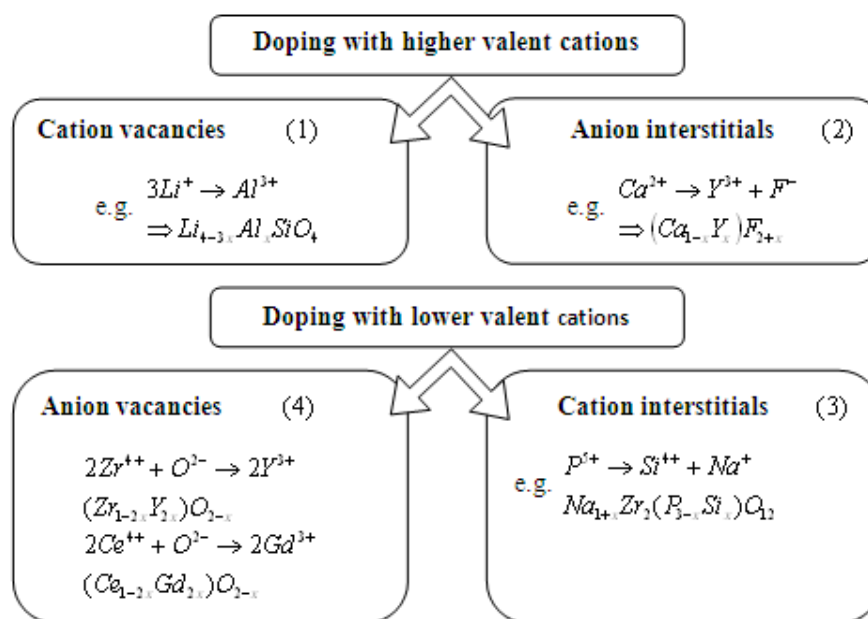


Figure 3. Solid solution formation by doping with aliovalent ions.

Rarely, it is possible to vary the composition to such an extent that it is possible either to fill completely a set of interstitial sites or to empty completely a particular set of lattice sites. When this happens, random walk theory predicts that at the half-stage, when the concentrations of filled and empty sites are equal, the ionic conductivity should pass through a maximum because the product of the concentration of mobile species,  $c_i$ , and sites to which they may migrate  $(1 - c_i)$  is at a maximum.

### 2.2.3. Ion trapping effects

It is also been seen that the aliovalent dopants may 'trap' or form complexes with the associated vacancies or interstitials. For an example, consider the case of the oxide ion conducting, Ca-stabilized zirconia system given by the general formula



$(Zr_{1-x}Ca_x)O_{2-x}$ . The replacement mechanism is



When we consider the defect charges on the species involved, using the *Kroger-Vink notation* (explained later) in which the superscripts  $\bullet$ ,  $'$  and  $\times$  refer to positive, negative and neutral species, the above equation may be rewritten;



The substitution of Ca onto a Zr site leaves a residual charge of '2-' on that site, whereas the oxygen vacancy,  $V_O$ , that is created carries an effective double positive charge. Since the aliovalent impurity and the anion vacancy carry opposite effective charges, they are likely to attract each other strongly, forming dipoles, quadrupoles or larger clusters. In order for the vacancy to move it must first break free from the cluster and this adds an additional barrier to the activation energy for conduction. The occurrence of such ion trapping is undesirable. In practice, in materials that contain potential traps such as charged aliovalent impurities/dopants, the conductivity values of a particular sample may actually decrease with time as the mobile ions gradually become trapped. Such *ageing effects* greatly limit the usefulness of a solid electrolyte in any device that needs to have a long working-life.

#### 2.2.4. Potential energy profile

The conduction pathway for a mobile ion can be considered as a series of potential wells and barriers. An example of a schematic energy profile is shown for NaCl (figure 4). In NaCl, a large energy barrier,  $\Delta H_m$  must be overcome for vacancy migration to occur. However, there is an interstitial site (Frenkel defect) in the conduction pathway which may be regarded as a transition state but it has such a shallow potential well that  $Na^+$  ions do not reside in it for significant times.



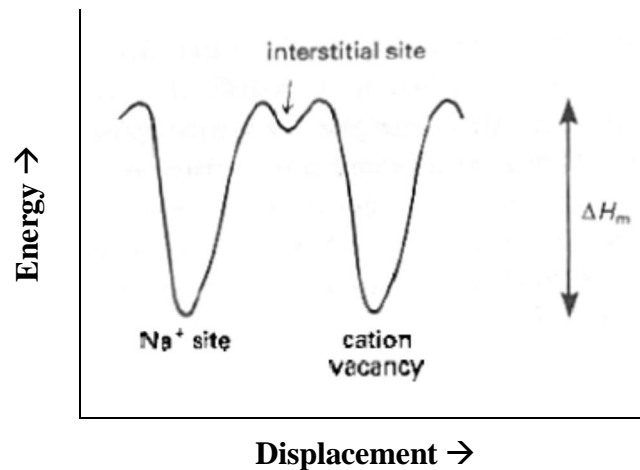


Figure 4. Potential energy profile for ion migration in NaCl.

### 2.2.5. The activation energy for conduction

The activation energy for conduction,  $\Delta H_m$ , is the major factor controlling the ionic mobility,  $\mu$ . The Arrhenius expression for conductivity is either

$$\sigma = \sigma_0 \exp(-\Delta H_m / RT) , \quad (2.4)$$

or

$$\sigma T = \sigma_0(T) \exp(-\Delta H_m / RT) \quad (2.5)$$

The  $\sigma_0$  or  $\sigma_0(T)$  are the pre-factor contains many terms, including the number of mobile ions. Of the two equations, eq. 2.5 is derived from random walk theory and has some theoretical justification; eq. 2.4 is not based on any theory but is simpler to use since data are plotted as  $\log \sigma$  vs.  $T^{-1}$  instead of as  $\log \sigma T$  vs.  $T^{-1}$ , based on eq. 2.5). Both forms of the conductivity Arrhenius equation are widely used; within errors the value of  $\Delta H_m$  that is obtained is approximately the same using either equation in many cases.

The activation energy represents the ease of ion hopping, as already indicated above and shown in figure 4. It is related directly to the crystal structure and in particular, to the openness of the conduction pathways. Most ionic solids have



densely packed crystal structures with narrow bottlenecks and without well-defined conduction pathways. Consequently, the activation energies for ion hopping are large, usually 1eV ( $\sim 96 \text{ kJ mole}^{-1}$ ) or greater and conductivity values are low. In solid electrolytes, by contrast, open conduction pathways exist and activation energies may be much lower than, as low as 0.03eV in AgI, 0.15eV in  $\beta$ -alumina and  $\sim 0.90\text{eV}$  in Yttria-stabilized zirconia. In solid electrolytes, thermally activated ion hopping processes occur and there is an inverse correlation between the magnitude of the activation energy and the frequency of successful ion hops (ion hopping rates).

### 2.2.6. Hopping rates

All solid state ionic conduction proceeds by means of hopping between well-defined lattice sites. Ions spend most of their time on specific sites where their only movement is that of small oscillations at lattice vibrational frequencies ( $10^{12}$ - $10^{13}$ Hz). Occasionally, ions can hop into adjacent sites. The ions hop quickly, on a timescale approaching but somewhat longer than that of a single lattice vibration. This is because the hop distance, typically 1-2 Å, is an order of magnitude greater than the atomic displacement during a lattice vibration.

In order to describe ionic conduction, two times are considered. One is the actual time,  $t_j$ , taken to jump between sites; this is of the order of  $10^{-11}$  to  $10^{-12}$  s and is largely independent of the material. The other time is the site residence time,  $t_r$ , which is the time (on average) between successful hops. The site residence times can vary enormously, from nanoseconds in the good solid electrolytes to geological times in the ionic insulators. Ion hopping rates,  $\omega_p$ , are defined as the inverse of the site residence times, i.e.

$$\omega_p = t_r^{-1} \quad (2.5)$$

Hopping rates are traditionally obtained from mechanical relaxation techniques such as internal friction or ultrasonic attenuation measurements (Almond and West, 1988). In these, the sample is squeezed or stressed at a certain frequency and ions may hop so as to relieve the stress. When the conditions are such that the frequency of the applied stress coincides with the ion hopping rate, a maximum in the





absorption (attenuation) occurs. Since hopping rates vary with temperature (in a manner dependent on the activation energy for hopping or conduction), the method usually used to determine  $\omega_p$ , involves a scan of temperature at fixed frequency. This gives an estimate of the temperature at which the ion hopping rate equals the applied frequency, figure 5. If the measurements are repeated over a range of set frequencies, the activation energy of ion hopping rates may be obtained. The ion hopping rate is an apparently simple parameter with a clear physical significance. It is the number of hops per second that an ion makes, on average.

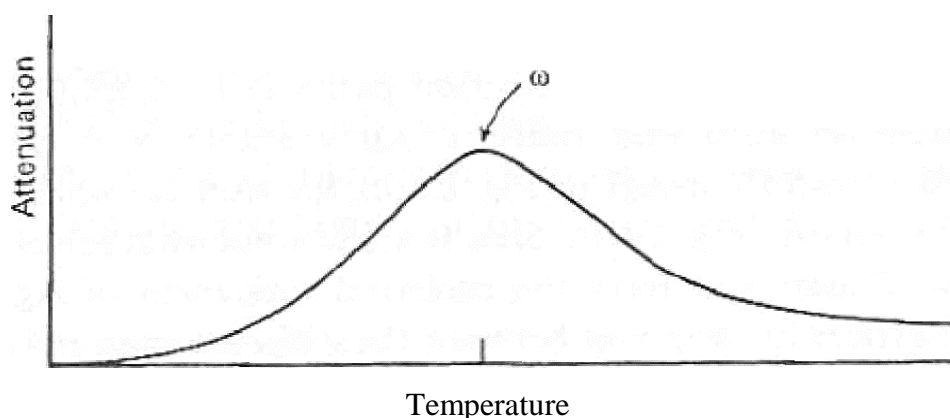


Figure 5. Temperature dependence of ultrasonic attenuation at fixed frequency  $\omega$  for an ionic conductor.

### **2.2.7. The ac conductivity span: local motions and long range conduction**

The above summarized ionic conduction mechanism in crystals is one of rapid hops between adjacent sites, separated by long residence times in which the ions are confined to oscillations within particular sites. The residence times depend on (amongst other things) the activation energy for hopping. Activation energy is a complex parameter that includes not only a physical barrier but also a longer range electrostatic barrier between the mobile ions. This arises whenever an ion hops out of a regular lattice site. Hopping generates local departures from electro-neutrality, which may also be viewed as the creation of dipoles. Such departures from local electro-neutrality act as a drag on further ion hops. Local electro-neutrality can be restored, by means of redistribution in the positions of the surrounding ions. After this process is complete, the ion under consideration is able to move again.



This effect is suggestive of a similar phenomenon in liquid electrolytes known as the *Debye-Falkenhagen effect*, where an ion has an associated *ion atmosphere* [2, 3]. For long range conduction to occur, the ion must drag along its ion atmosphere. One main difference from ionic conduction in crystalline solids is that both anions and cations are able to move in liquids. Therefore, both are likely to be involved in reorganization of the ion atmosphere. However in ionic solids, only one type of ion is involved, both in conduction and in the reorganization of its surrounding ion atmosphere. In materials with a high carrier concentration, mobile ions are certainly quite close together. Consequently, ions cannot hop in isolation but are influenced by the distribution of mobile ions in their vicinity. This contrasts with the behavior of dilute defect systems with low carrier concentrations. In these, the mobile ions are well separated from each other and their conduction can largely be treated in terms of isolated hops.

#### 2.2.8. An example of solid electrolyte: Oxide ion conductors

Oxides having fluorite-related structures are well-studied materials due to their importance in commercial applications. The materials based on  $ZrO_2$ ,  $ThO_2$ ,  $CeO_2$  and  $Bi_2O_3$  falls under this category [4]. Alivalent dopant in oxides like  $ZrO_2$ ,  $ThO_2$  and  $CeO_2$  leads high oxide ion conductivity due to creation of oxide vacancies. The dopants are usually alkaline earth or trivalent rare earth oxides.  $CeO_2$  and  $ThO_2$  have the cubic fluorite structure (well-known for its openness) and because of that it can be doped with large amounts of dopants to give extensive ranges of cubic solid solutions. However,  $ZrO_2$  is cubic only above  $\sim 2400^\circ C$ , and requires  $\sim 8\%$  of yttrium to stabilize the cubic form at room temperature.

$Bi_2O_3$  is different since, with its cation: anion stoichiometry of 2:3, it already has a large number of anion vacancies in the cubic  $\delta$ -form which is stable above  $730^\circ C$ . This accounts for its exceptional conductivity at these temperatures. Dopants are added to  $Bi_2O_3$  with the purpose of reducing the temperature of the 'α' (monoclinic)  $\rightarrow$  'δ' transition and stabilizing the cubic form to lower temperatures. A key factor in the possible applications of oxide ion conductors as an electrolyte is that their  $\sigma_{O^{2-}}$  transport number should be as low as possible. While the stabilized zirconia have an oxide ion transport number of unity in a wide range of atmospheres and oxygen partial pressures, the  $Bi_2O_3$ -based materials are easily reduced at low



oxygen partial pressures. This leads to the generation of electrons  $2O^{2-} \leftrightarrow O_2 + 4e$  and hence to a significant electronic transport number. Thus, although  $Bi_2O_3$ -based materials are the best oxide ion conductors, they cannot be used as the solid electrolyte, e.g. in fuel cell or sensor applications. Similar, but less marked, effects occur with ceria-based materials, due to the tendency of  $Ce^{4+}$  ions to become reduced to  $Ce^{3+}$ .

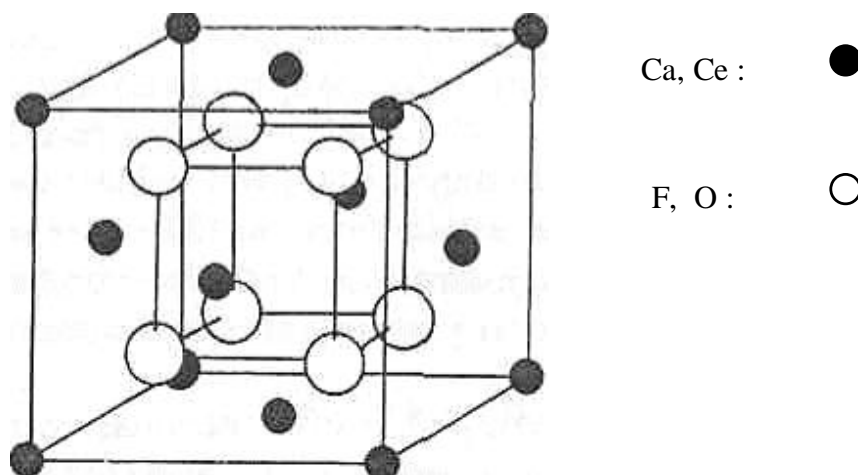


Figure 6. The fluorite structure of  $CaF_2$  or  $CeO_2$ .

The activation energies for oxide ion conduction in the various zirconia, thoria and ceria based materials are usually at least 0.8eV. A significant fraction of this is due to the association of oxide vacancies and aliovalent dopants (ion trapping effects). Calculations have shown that the association enthalpy can be reduced and hence the conductivity optimized, when the ionic radius of the aliovalent substituting ion matches that of the host ion. A good example of this effect is seen in Gd-doped ceria in which  $Gd^{3+}$  is the optimum size to substitute for  $Ce^{4+}$ .

## 2.3. Crystal structure and electrical behavior of pure and doped ceria

### 2.3.1. About cerium (Ce) element [5]

Cerium name is derived from the newly discovered and named asteroid called *Ceres* in 1801, only 2 years before the discovery of element. The element was discovered in 1803. It is the most abundant of the metals of the so-called rare earths.



Table 2 gives physical properties of cerium.

Atomic weight	140.115 (IV)
Atomic number	58
Melting point	798°C
Boiling point	3424°C
Specific gravity	6.770 (at 25°C)
Valence	3 or 4

Table 2. Properties of cerium metal.

Cerium is especially interesting because of its variable electronic structure. The energy of the inner 4f level is nearly the same as that of the outer or valence electrons, and only small amounts of energy are required to change the relative occupancy of these electronic levels. This gives rise to dual valence states. For example, a volume change of about 10% occurs when cerium is subjected to high pressures or low temperatures. It appears that the valence changes from about 3 to 4 when it is cooled or compressed.

Cerium is an iron-gray lustrous metal. It is malleable, and oxidizes very readily at room temperature, especially in moist air. Except for europium, cerium is the most reactive of the “rare-earth” metals. The pure metal is likely to ignite if scratched with a knife. Ceric (IV) salts are orange red or yellowish while cerous (III) salts are usually white. Cerium is a component of misch metal, which is extensively used in the manufacture of pyrophoric alloys for cigarette lighters, etc.

While cerium is not radioactive, the impure commercial grade may contain traces of thorium, which is radioactive. The oxide is an important constituent of incandescent gas mantles and it is emerging as a hydrocarbon catalyst in “self-cleaning” ovens. In this application it can be incorporated into oven walls to prevent the collection of cooking residues.



### 2.3.2. Crystal structure of ceria

#### 2.3.2.1. Fluorite structure of CeO<sub>2</sub>

Cerium (Ce) element has two stable valence states; Ce<sup>4+</sup> and Ce<sup>3+</sup>, and it is the unique rare-earth for which dioxide is the normal stable phase contrary to the others for which Ln<sub>2</sub>O<sub>3</sub> (lanthanide series) is the normal stoichiometry. Ceria is most popular oxide as it finds number of applications in catalysis, chemicals, glass and ceramics, phosphors and metallurgy. These applications are due to its

- i) Potential redox chemistry involving its Ce(III) and Ce(IV) states,
- ii) High affinity for oxygen and
- iii) Electronic structure related absorption/excitation energy bands.

The crystal structure of CeO<sub>2</sub> is of fluorite type (space group – Fm3m, figure 7). In general, the ionic compounds of the form RX<sub>2</sub> (typical example is CaF<sub>2</sub>), in which the ratio of the ionic radii ‘r’ satisfy the inequality,

$$\frac{r(X^-)}{r(R^{2+})} \leq \frac{\sqrt{3}+1}{2} \text{ or } \frac{r(X^-)}{r(R^{2+})} \leq 1.36, \quad (2.6)$$

can form the fluorite structure. For example, consider the inequality for ‘Ce’ and ‘O’ elements for the formation of fluorite structure (table 3) i.e.

$$\frac{r(O)}{r(Ce)} \leq 1.36. \quad (2.7)$$

Thus in accordance with above inequality there is ~91% (22 of 24) formation chances of fluorite structure in case of Ce and O elements with different combinations of valance states and co-ordination numbers.



Ionic species ↓	→		O <sup>2+</sup>		
	CN* ↓	r (Å)	2	6	8
Ce <sup>3+</sup>	6	1.01	1.19	<b>1.38</b>	<b>1.40</b>
	8	1.14	1.05	1.21	1.23
	10	1.23	0.85	0.98	1.00
	12	1.34	0.63	0.73	0.74
Ce <sup>4+</sup>	6	0.87	0.73	0.84	0.86
	8	0.97	0.75	0.87	0.88
	10	1.07	0.70	0.81	0.82
	12	1.14	0.61	0.71	0.72

\* CN is the coordination number; the number of nearest neighbors of the given atom.

Table 3. The possible combinations of Ce and O to form the fluorite crystal structure.

The crystal structure of CeO<sub>2</sub> ( $\equiv$  CaF<sub>2</sub>) can be viewed as a face-centered cubic array of cerium (green) ions with the oxygen (red) ions residing in the *tetrahedral holes* formed by Ce<sup>4+</sup> ions (figure 7a). One can also view this structure as a simple cubic array of oxygen with a cerium in the center of alternate cubes. In figure 7b, cubes formed by array of oxygen ions with cerium ions at alternate body center position of cube is illustrated. Considered that way, there are obviously diagonal planes of cubes containing no cations and these voids are called *octahedral holes*. These octahedral planes will obviously be planes allowing defects to jump or hop through the lattices, accounting for fluorite's good oxide ion conduction properties.

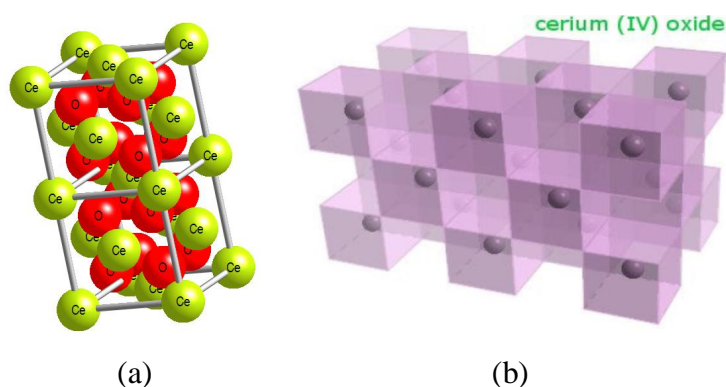


Figure 7. The crystal structure of CeO<sub>2</sub>; (a) two unit cells (b) alternate view.



### 2.3.2.2. Stoichiometry of fluorite structured $CeO_2$

Consider the stoichiometry of single unit cell of  $CeO_2$ . It can be seen that each of the corner cerium ions is  $1/8$  inside the cell; since there are eight corners these add up to one ion inside the cell. There are six faces to a single cell, each with a cerium ion one-half inside the cell. Therefore a single cell contains four cerium ions. A single cell also contains eight oxygen ions, each one located entirely within the unit cell. Since there are four cerium ions and eight oxygen ions inside the cell, the 1: 2 stoichiometry is maintained.

### 2.3.2.3. Holes in fluorite structured $CeO_2$

Regardless of whether hexagonal layers are stacked in an AB or ABC fashion, there exist two types of spaces or holes between the layers. One type of space is called an octahedral hole, and is formed between three atoms in one layer and three atoms in the layer immediately above or underneath. Although it takes six spheres to form an octahedron, the name is taken from the fact that the resulting shape has eight sides (triangle planes), figure 8.

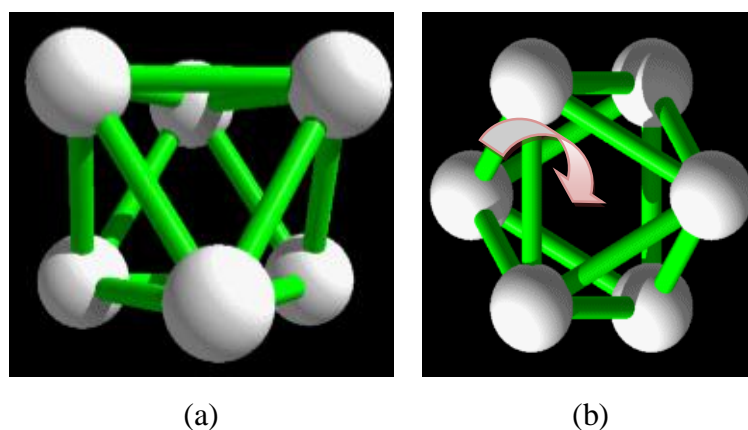


Figure 8. Octahedral hole formed between three atoms in one layer and three atoms in the layer immediately above or underneath; (a) Front view and (b) Top view.

Second type of space which exists between stacked hexagonal layers is called a tetrahedral hole. Tetrahedral holes are formed between three atoms in one layer and



a single atom immediately above or underneath, figure 9.

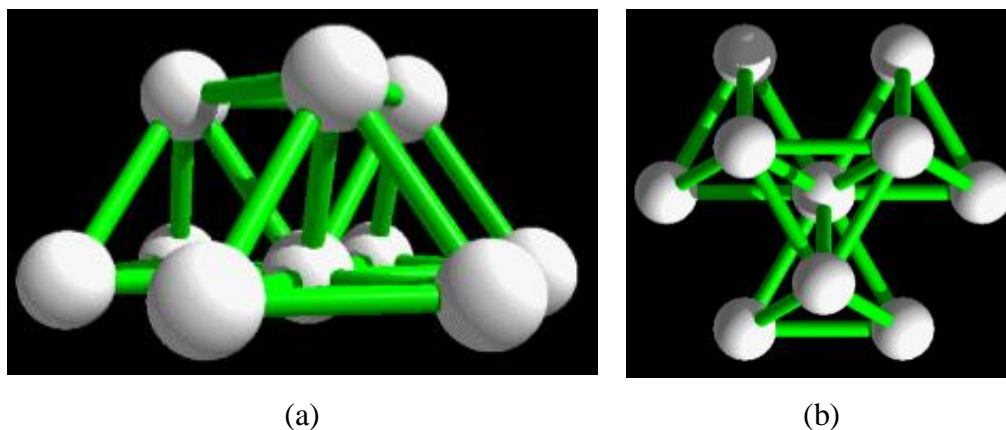


Figure 9. Tetrahedral hole formed between three atoms in one layer and a single atom immediately above or underneath; (a) Front view and (b) Top view.

In the fluorite structured  $\text{CeO}_2$ , the oxide ions reside within the tetrahedral holes formed by the face-centered cubic array of cerium ions, and the octahedral holes are vacant. Figure 10 illustrates incorporation of oxide ion in the hole. Figure 11 illustrates stack of ceria with oxygen ion residing in tetrahedral holes and the vacant octahedral holes.

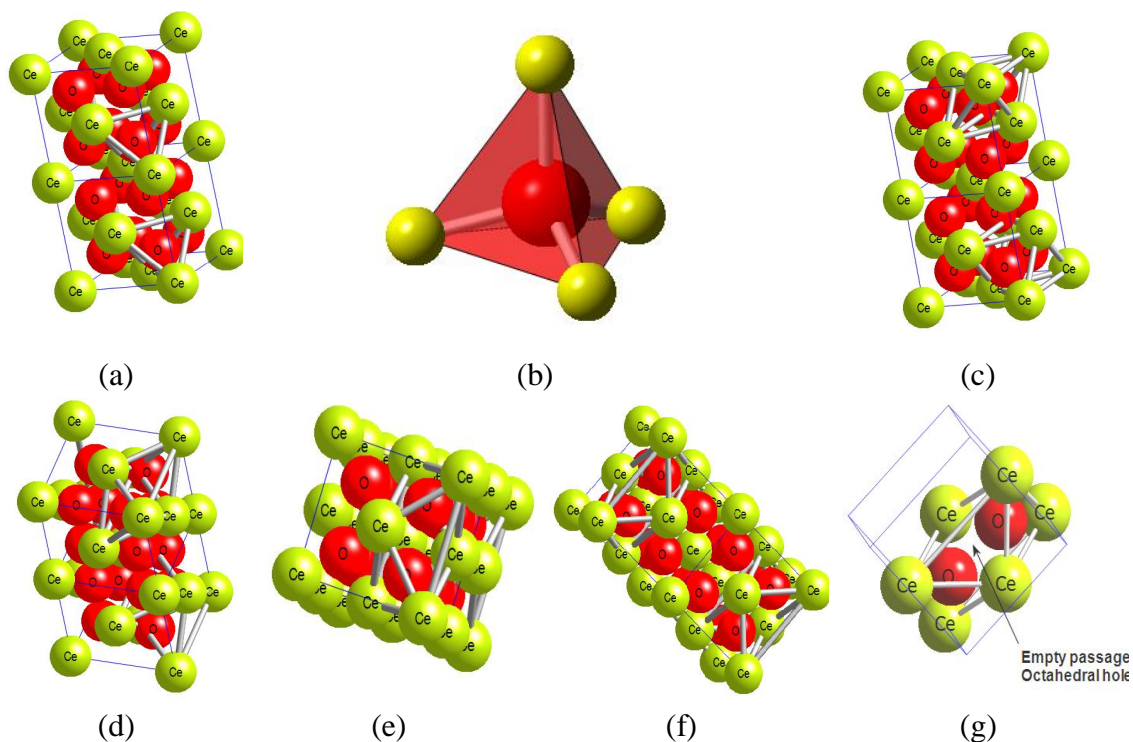


Figure 10. Illustration of (a-b) tetrahedral and (c-g) octahedral holes in  $\text{CeO}_2$ .





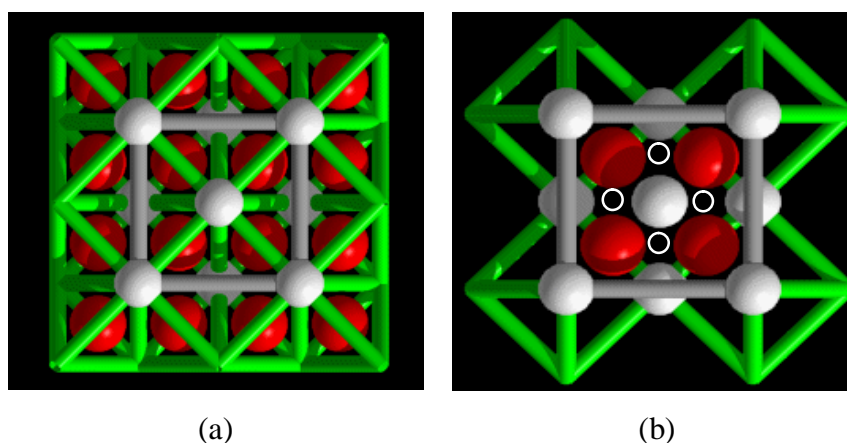


Figure 11. Illustration of (a) filled tetrahedral hole by oxide ion and (b) vacant octahedral hole (shown by hollow circles) in fluorite  $\text{CeO}_2$  structure

*Why oxide ion in fluorite structure resides in tetrahedral holes rather than octahedral holes?*

It is obviously, due to its stoichiometry. There are two oxygen atoms for every one cerium atom. Since an array of  $N$  atoms results in the formation of  $N$  octahedral holes, there would simply not be enough spaces for all oxygen atoms (stoichiometry of Ce: O is 1: 2). Suppose, the position of ions are reversed, with the oxygen ions forming the face-centered cubic array, there would be enough cerium ions to fill only  $1/4$  of the tetrahedral holes or  $1/2$  of the octahedral holes; this would be very inefficient. Theoretically, the descriptions of the fluorite structure given above are inaccurate in the sense that because the oxygen ions are in fact larger than the cerium ions, they therefore do not "fit inside" the tetrahedral holes. As can be seen in figure 11b, the cerium ions form a sort of "expanded" face-centered cubic structure and do not physically touch each other.

However materials such as  $\text{Li}_2\text{O}$ , form an anti-fluorite structure i.e. the positions of the anions and cations are reversed. The  $\text{O}$  anions are in the f.c.c. positions and the  $\text{Li}$  cations form a simple cubic array.

### 2.3.3. Defect structure of ceria

Defects in a crystal structure are nothing but the deviations from the perfect



periodic lattice. Though there are many ways in which crystal imperfections are observable, such as dislocations, surfaces and pores, all of these are essentially collections of zero dimensional point defects. Point defects consist of vacant lattice sites, atoms in non-regular lattice positions (interstitials) and occurrence of impurity atoms instead of host position. Many properties (e.g. conductivity, luminescence and diffusion) are influenced by the existence of these defects, which is particularly true for inorganic solids. Furthermore, it is not possible to produce a single crystal free of defects. Finally, as temperature increases, defects become even more significant.

In general, there are two types of defects called intrinsic and extrinsic defects. Former type of defects formed in a crystal is due to thermal disorder while extrinsic defects are created by impurities incorporated in hosts during its synthesis, introduction of alliovalent dopants or by the oxidation-reduction process. The creation and annihilation of defects in crystal lattices are in general described using so called “Kröger-Vink” notations. Kröger-Vink notation is set of conventions used to describe electrical charge and lattice position for point defects in crystals. It was proposed by F.A. Kröger and H.J. Vink [6].

### 2.3.3.1. General format of Kröger-Vink notation



‘*M*’ corresponds to the species. These would include:

- Atom – e. g. Si, Ni, O, Cl, Ce, etc.
- Vacancies – V
- Electrons – e
- Holes – h

‘*S*’ indicates the lattice site that the species occupies. For instance, Ni might occupy a Cu site. In this case, M would be replaced by Ni and S would be replaced by Cu. The site may also be a lattice interstice. In this case the symbol ‘*i*’ is used.

‘*C*’ corresponds to the electric charge of the species relative to the site that it occupies. To continue the previous example, Ni often has the same valency as Cu, so the relative charge is zero. To indicate null charge, ‘*x*’ is used (also nothing is written). A single ‘*•*’ indicates a single positive charge, while two would represent



two positive charges. Finally, ' signifies a single negative charge, so two, would indicate a double negative charge.

For examples:

$Al_{Al}^{\times}$	: An aluminum ion sitting on an aluminum lattice site, with neutral charge.
$Ni_{Cu}^{\times}$	: A nickel ion sitting on a copper lattice site, with neutral charge.
$V_{Cl}^{\bullet}$	: A chlorine vacancy, with single positive charge.
$Ca_i^{\bullet\bullet}$	: A calcium interstitial ion, with double positive charge.
$e'$	: An electron. A site isn't normally specified.

### 2.3.3.2. *Intrinsic defects (or disorders) in ceria*

This type of disorders in lattices requires thermal activation, rather than the addition of impurities or solutes. Hence, it is named as intrinsic (i.e. inherent) disorder. As temperature is raised, contributions to the free energy due to the entropy term (degree of disorder) increases the number of atoms that are displaced from regular lattice positions. Since, increase in entropy leads to increase in the magnitude of lattice vibrations and configurational term. However, the concentration of defects is able to remain finite. Since, an increase in thermal energy also gives rise to an increase in entropy, thus reducing the free energy, which in turn limits the defect formation in lattices.

The two most common types of crystalline intrinsic defects in ionic materials are Frenkel and Schottky defects. Frenkel disorder results when an atom is displaced from its regular site to an interstitial site, thus forming a defect pair (figure 12a). Several compounds including  $CeO_2$ , readily exhibit Frenkel disorder. For example,  $UO_2$ ,  $CaF_2$ , etc. all demonstrate the Frenkel anion type of disorder (i.e. anion interstitials and anion vacancies) while  $AgCl$ ,  $AgBr$  and  $Fe_3O_4$  all exhibit cation Frenkel disorder.

The other type of intrinsic disorder is Schottky disorder. Schottky disorder is the simultaneous occurrence of cation and anion vacancies in thermal equilibrium (figure 12b). In this case, vacancy defects must be formed in a number which maintains the electro-neutrality of the lattice.



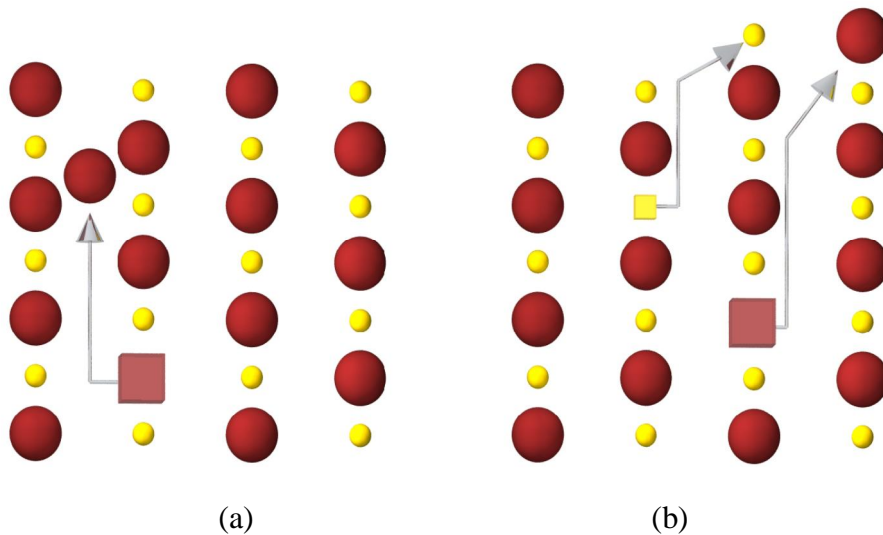
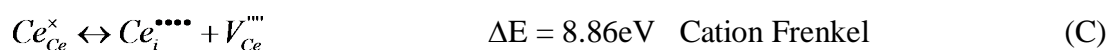
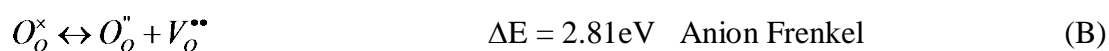
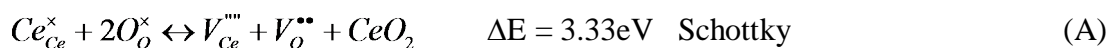


Figure 12. (a) Frenkel disorder and (b) Schottky disorder in an ionic crystal, where the square denotes a vacancy left by an ion which has displaced from its original site.

In general terms, Frenkel disorder is more likely when the anion and cation differ significantly in size and when the lattice polarization is pronounced. When the anions and cations are of similar size (as is the case of NaCl) Schottky disorder is favored. In close packed materials, there is little lattice space to accommodate an interstitial ion. It follows that Frenkel disorder is not favored in these materials. Conversely, in open structures such as of  $\text{CeO}_2$  (fluorite structure), Frenkel disorder is more easily accommodated.

The sources of intrinsic disorder in stoichiometric  $\text{CeO}_2$  due to thermal excitation are represented as follows (using Kröger-Vink notation),



which are the (A) Schottky, (B) Anion Frenkel, and (C) Cation Frenkel defect mechanisms, respectively. The energies for the individual defects, as well as the reaction enthalpies are listed in table 4.



$V_o^{\bullet\bullet}$	$V_{Ce}^{\bullet\bullet\bullet}$	$O_i^{\bullet}$	$Ce_i^{\bullet\bullet\bullet\bullet}$	Schottky energy per defect	Anion Frenkel energy per defect	Cation Frenkel energy per defect
16.06	83.52	-10.43	-65.80	3.33	2.81	8.86

Table 4: Disorder reaction energies (in eV).

From the table 4 it can be seen that the possibility of cation Frenkel defects forming is extremely low. The Schottky defect energy is higher than the anion Frenkel energy, which implies that  $[V_{Ce}^{\bullet\bullet\bullet}] \ll [O_i^{\bullet}]$ . Hence, the most likely form of intrinsic disorder is anion Frenkel. In the agreement of the above, Faber et al. [7] examined the electron density distribution using XRD and concluded that the amount of interstitial Ce ( $[I_{Ce}^{\bullet\bullet\bullet}]$ ) is less than 0.1% of the total defect concentration in  $CeO_{2-x}$ . However, the anion Frenkel energy is still quite high, thus such disorder will be flooded by the effect of non-stoichiometry in  $CeO_2$  (i.e. by doping).

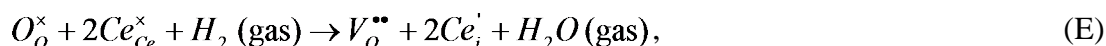
### 2.3.3.3. Extrinsic defects (disorder) in ceria

Intrinsic disorder is differentiated from extrinsic disorder on the basis of its reaction with ambience. Intrinsic disorder includes only thermally activated defect processes which occur within an otherwise perfect lattice where there is no reaction with the environment. Essentially, extrinsic disorder includes reaction with gaseous species from the environment that are constituents of the lattice and reaction with species from the environment that are not local to the lattice. Therefore, extrinsic disorder includes defects resulting from oxidation or reduction of lattices and/or the presence of dopants, impurities, etc. in a lattice.

To explain the former process in case of ceria, the reduction of ceria is possible at elevated temperatures with either in oxygen deficient environment or hydrogen rich environments. The oxidation-reduction (redox) processes of ceria are responsible for the creation of extrinsic defects which certainly produces non-stoichiometry in lattices. The process of ceria reduction in oxygen deficient environment, using Kroger Vink notation, may be written as,



while in the case of  $H_2$  environment it may be written as,



To understand the stoichiometry and non-stoichiometry in lattices, consider its historical development. Initially the stoichiometry was defined as the constant and fixed ratio of elemental constituents of a chemical compound. The concept of stoichiometry was proposed by Dalton's atomic hypothesis [8], and the Law of Definite Proportions, which was a product of the hypothesis. This law states that the constituent elements of any compound exist in distinct proportions. This law was the topic of debate between Proust, a supporter of the law, and his fellow Frenchman Berthollet, who suggested that the composition of solid compounds is by no means constant. Berthollet lost that debate, but was justified many years later in a paper by Kurnakov, where it was found that the constituents of various intermetallics varied in composition [9]. Schottky and Wagner also suggested that all inorganic solids are inherently non-stoichiometric [10].

The non-stoichiometry of metal oxides can be subdivided into two categories with respect to exact stoichiometry: *metal deficient* or *oxygen deficient*. Non-stoichiometry is a direct result of point defects and the extent of non-stoichiometry is measured by the net concentration of these defects [11]. Just as the reactions for Frenkel and Schottky disorder were electronically neutral, the reactions for non-stoichiometry must also be neutral through the formation of complimentary point defects (as presented in reactions (D) and (E)). In metal deficient oxides, if metal vacancies are formed, they are complimented by electronic defects on either remaining metal sites (increasing the valence state), on the oxygen site (lowering the charge) or by a delocalized charge. If the metal sub-lattice remains intact, the non-stoichiometry is aided by oxygen interstitial defects compensated by the electronic defects mentioned above. It follows that for the oxygen deficient system, metal interstitials or oxygen vacancies will be the predominant structural defects.

A possibly more clear example of extrinsic disorder, but still technologically important, is the presence of impurity defects which are non-resident to the compound. For example, doping a material (thus generating defects) can have pronounced effects on a variety of properties.

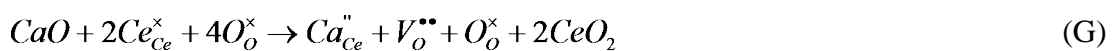
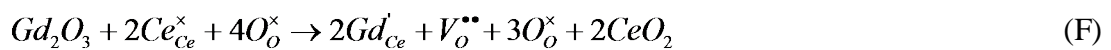


For example,

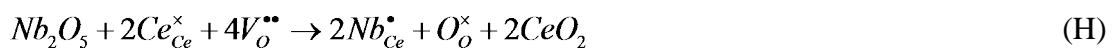
- Doping Si with group V atoms Sb, As, P or group III atoms In, Al or B creates charge carriers for n- and p- type semiconductors respectively.
- In addition, the solution of CaCl<sub>2</sub> lowers the density of KCl with the production of K vacancies.
- The cubic fluorite structure of ZrO<sub>2</sub> can be stabilized with a variety of oxides such as Y<sub>2</sub>O<sub>3</sub> or CaO.
- The cubic fluorite structure of CeO<sub>2</sub> shows drastic increase in ionic conductivity after doping the host by Gd<sub>2</sub>O<sub>3</sub> or Sm<sub>2</sub>O<sub>3</sub>.

The later examples of ZrO<sub>2</sub> and CeO<sub>2</sub> are particularly important in electrochemical applications due to its enhanced ionic conduction by the generation of anion vacancies.

Excess oxide (anion) vacancies can be introduced in CeO<sub>2</sub> by doping with oxides of metals with lower valencies (3 or 2), e.g. dissolution of Gd<sub>2</sub>O<sub>3</sub>, CaO in CeO<sub>2</sub>, which may be represented as follows,



Already existing oxide vacancies may be removed by doping with oxides of higher valency than 4, e.g. dissolution of Nb<sub>2</sub>O<sub>5</sub> in CeO<sub>2</sub>, which may be represented as follows,



#### 2.3.3.4. Defect concentrations in pure and doped ceria

Pure ceria exhibits a dramatic drop in the concentrations of oxide vacancies and oxide interstitial ions with increase in temperature. However, these concentrations



remain virtually constant in Gd/Sm doped ceria. Interstitial oxygen ions in ceria-containing compounds are likely to form during sample processing. When oxygen-deficient material is oxidized to  $\text{CeO}_2$  or  $(\text{Ce, Gd})\text{O}_2$ , absorbed oxygen ions may at first enter the roomier octahedral sites, rather than fill the spatially tight tetrahedral sites. If annealing temperature is not high enough they may not be able to overcome a potential barrier to get into the regular tetrahedral sites, and remain in the octahedral sites. However, only when the sample is treated at sufficiently high temperature thermally activated interstitial ions may enter to regular tetrahedral sites and recombine with vacancies.

Because of the slightly larger ionic radius of gadolinium/samarium ions, mixing of  $\text{Gd}_2\text{O}_3/\text{Sm}_2\text{O}_3$  with ceria will increase the lattice constant and produce the atomic-level relaxation at the smaller tetrahedral sites, making them easier to reach for the interstitial oxygen ions than in pure ceria. This may explain the enhanced stability of oxygen defects against thermal aging in doped ceria. However, the easier access to octahedral sites (since it is inherently roomier) and tetrahedral sites (achieved by doping) for oxide ion facilitates enhanced ionic conductivity in doped ceria by employing both the possible mechanisms, namely, vacancy and interstitial hopping mechanism (figure 13). At the same time, the interstitial oxygen ions are the "active" ions that provide necessary mobility of oxide ions, which is a crucial condition for ceria to function as an oxide ion conductor.

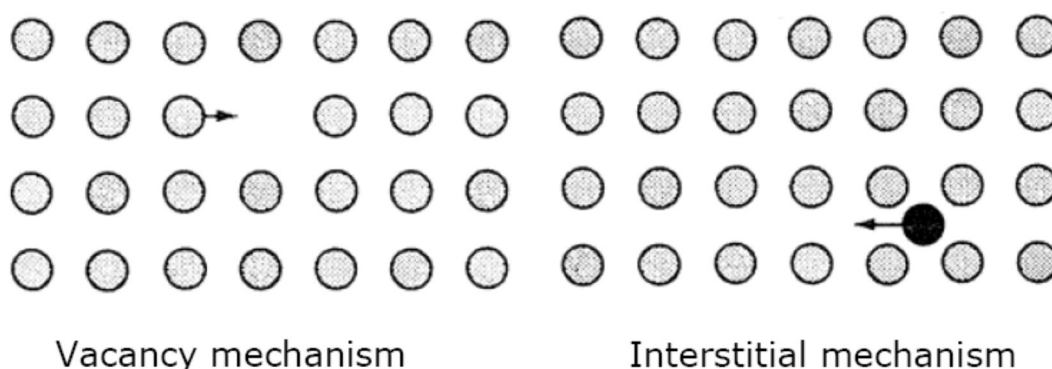


Figure 13. Schematic of showing two possible mechanisms for the movement of ions through a lattice.





### 2.3.4. Ionic conductivity in ceria and doped ceria

Because of their role as the electrolyte in solid oxide fuel cells (SOFCs), yttrium doped zirconia (YSZ) and Gd doped ceria (GDC) are technologically important oxygen ion conductors. The dopants in these materials serve to introduce anion defects that perhaps increase the ionic conductivity. As discussed in earlier section ceria possesses cubic fluorite structure from room temperature to its melting point while in case of zirconia it is only possible at high temperatures. This distinct property of ceria is advantageous to design SOFCs which can operate at comparatively less temperatures.

Doping of ceria is usually performed by substituting lower valence cations into the lattice, with the additional effect of introducing oxygen vacancies, however overall charge neutrality in lattice is maintained. These oxygen vacancies supply the equivalent sites allowing the oxygen ions to migrate (by hopping mechanism) and are the requirement for high ionic conductivity. A further remarkable feature of the fluorite structured ceria is that it is able to sustain a high degree of substitution and consequent non-stoichiometry, making these structures very highly disordered materials. Doping of the fluorite structured oxide for improvement in oxide ion conductivity is usually achieved by substitution of the host cation with a rare earths. Examples of such materials are doped zirconia, doped ceria etc. with the general formula  $Re_{1-x}A_xO_{2-\delta}$ , where 'A' is cations and 'Re' is the rare earth dopants.

The ionic motion in fluorite-based systems is the well-established vacancy based hopping mechanism, where one vacancy shifts position with a neighboring oxygen ion in a normal lattice position (figure 14). The easiest jump is along the edge of the cube formed by eight oxygen ions/vacancies.

In general, the ideal solid electrolyte, particularly oxide ion conductor, possess the following properties,

- A large number of the ions of one species should be mobile. This requires a large number of empty sites, either vacancies or accessible interstitial sites.
  - *Empty sites are needed for ions to move through the lattices.*



- The empty and occupied sites should have similar potential energies with a low activation energy barrier for jumping between neighboring sites.
  - *High activation energy decreases carrier mobility, very stable sites (deep potential energy wells) lead to carrier localization*
- The structure should have solid framework, preferably three dimensional, permeated by open channels.
  - *The migrating ion lattice should be "molten", so that a solid framework of the other ions is needed in order to prevent the entire material from melting.*
- The framework ions (usually anions) should be highly polarizable,
  - *Such ions can deform to stabilize transition state geometries of the migrating ion through covalent interactions.*

Optimization of oxygen transport in fluorite related systems, therefore, could be concentrated on simple considerations of dopants ionic size and charge. To avoid lattice distortion and strong defect association, host cation and dopants should have similar sizes and minimum charge difference. Dopants concentrations also should have an ideal level, since as high concentrations of defects increases defect interaction and reduction in ionic conductivity could cause [12, 13].

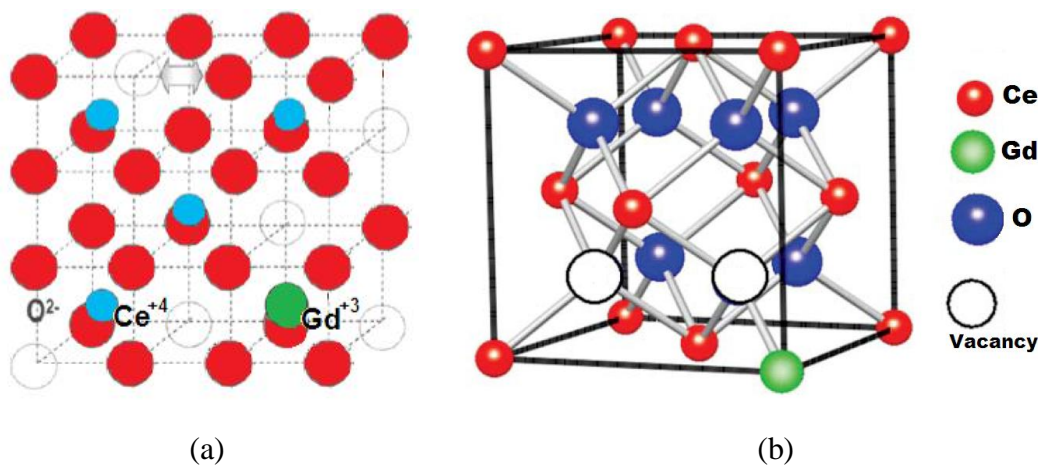


Figure 14. (a) Schematic view of the vacancy motion mechanism in the fluorite structure. Ions as filled circles, oxygen vacancies as empty circles. (b) Positions of various species in a disordered unit cell of Gd doped ceria.



In a perfect fluorite structure, all the tetrahedral sites are filled by oxygen ions, and all the octahedral sites are empty, figure 15a. Disordered fluorite structure of ceria, attained by doping of ceria by di- or tri valent rare earth oxides and/or by thermal activation of ceria, possesses oxygen defects in structure. Some oxygen ions (filled circle in figure 15b) occupy the interstitial octahedral sites, leaving vacancies in the tetrahedral sites (not shown in figure 15b). The interstitial oxygen ions are displaced from the centers of the interstitial octahedral sites in the  $\langle 110 \rangle$  directions. In general case, the concentration of oxide vacancies created in disordered ceria may exceed than that of interstitial oxide ions by doping of host, resulting in oxygen non-stoichiometry. Anions move primarily in  $\langle 100 \rangle$  directions by the vacancy mechanism, although more rarely  $\langle 110 \rangle$  jumps (interstitial) also occur. At intermediate temperatures interstitials were observed to make non-collinear interstitialcy jumps, but at higher temperatures the motion of interstitials makes little contribution to mass transport. The vacancies are very mobile and interstitials have little or no chance to move before being annihilated by a drifting vacancy [14].

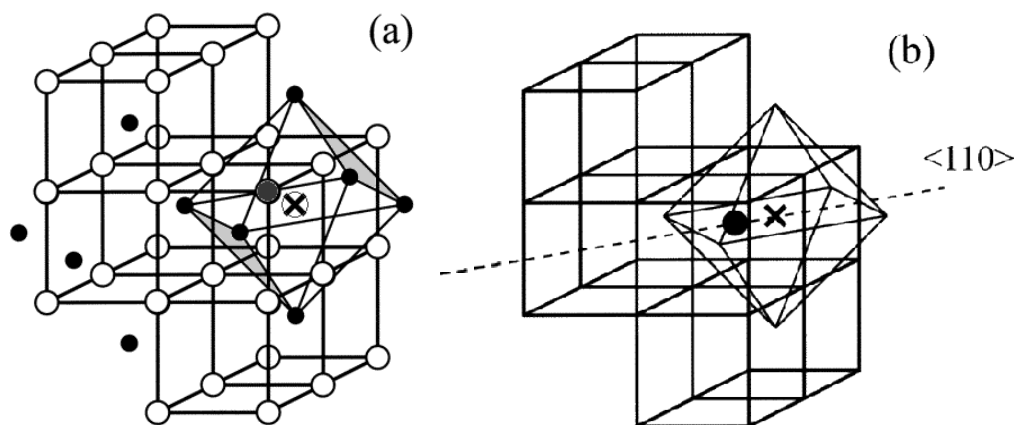


Figure 15. Schematic of ceria lattice showing (a) perfect fluorite structure of ceria ('X' is showing empty octahedral site) and (b) disordered fluorite structure of ceria with direction of motion of oxide defects through octahedral interstitial sites.

The rare earth doped ceria, which possesses the stable fluorite crystal structure for wide temperature range (RT–2300°C), are particularly well studied and an example of the isothermal conductivity maximum for a number of substituted ceria materials is shown in figure 16 [15]. As seen from figure 16, gadolinium doped ceria showed the higher conductivity at ~10% doping.



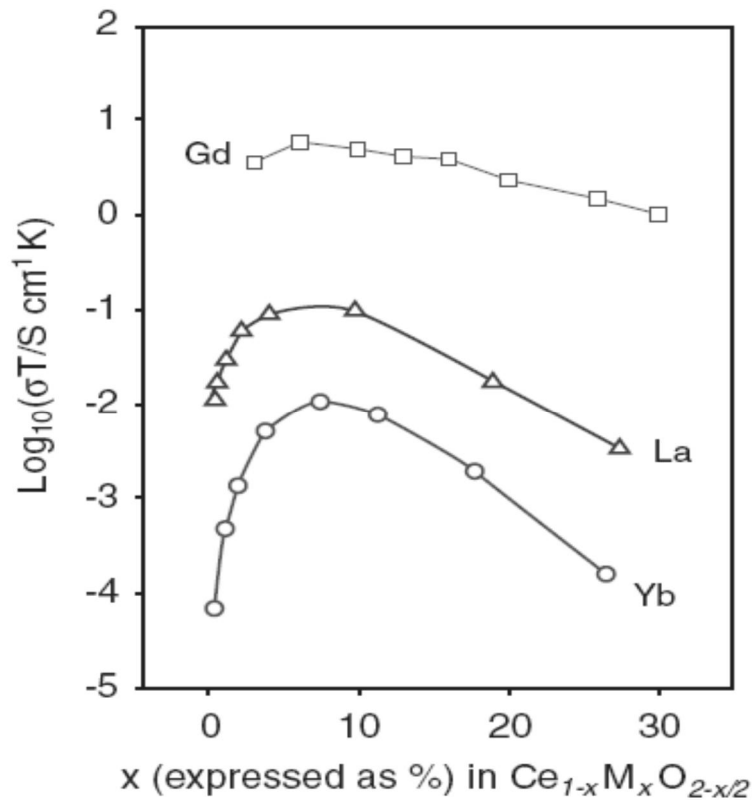


Figure 16. The isothermal conductivity of some ceria solid solutions at temperatures close to 200°C [15].

### 2.3.5. Electrical behavior of pure and doped ceria

#### 2.3.5.1. Influence of doping

Ceria can be classified as mixed conductor showing both electronic and ionic conduction. Its electrical properties are strongly dependent upon temperature, oxygen partial pressure and presence of impurities/dopants. At high temperatures and low oxygen partial pressures, ceria behaves as an n-type semiconductor and electrons liberated following the reduction are the primary charge carriers.



However, transition from n-type to p-type conduction is observed at lower



temperatures and higher oxygen partial pressures near stoichiometric composition, where electronic conductivity arises from holes introduced by impurities ( $IO$ ).



Ionic conductivity observed in ceria is due to the mobility of oxide ion vacancy by hopping mechanism. It is always much lower than the electronic conductivity in pure reduced ceria. However, the situation gets reversed in case of ceria doped with oxides of two or three-valent metals due to the introduction of oxide ion vacancy in host. The electronic conductivity in air may be very low and the doped ceria under these conditions are excellent solid electrolytes. The most important parameter which influences the ionic conductivity in fluorites is the cation match of dopants atom and host atom with the critical radius,  $r_c$ . The ratio of dopant cation to host cation must be closer to unity. Hence the earlier experimental as well as theoretical study showed that the ionic conductivity increases with increasing ionic radius of dopant in ceria, from Yb to Sm, but decreased at  $d_{\text{dopant}} > 0.109$  nm and the peak ionic conductivity is observed for doping of Gd (0.108nm) and Sm (0.109nm) in ceria.

### 2.3.5.2. The temperature dependence

Since, in general, ionic conductivity,  $\sigma_i$  is defined same as electrical conductivity (eq. 2.1). The temperature dependence variation of ionic conductivity is given by eq. 2.5, taking logs of both sides gives,

$$\log(\sigma T) = \log(\sigma_0(T)) - \Delta H_m / RT \quad (2.7)$$

Plotting  $\ln \sigma T$  vs.  $1/T$  should produce a straight line with a slope of  $-E_a$ .



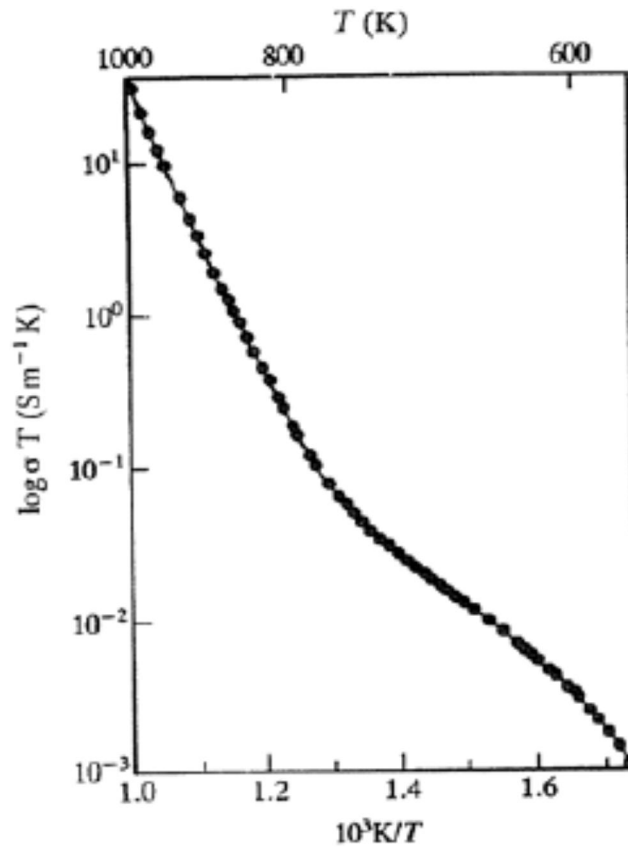


Figure 17. Typical plot of  $\ln \sigma T$  vs.  $1000/T$  for solid electrolyte.

The actual temperature dependence of the electrical conductivity in general can be shown as the three regions according to Kilner and Walters [16]. In region I, which appeared at high temperatures (not shown in figure 16), the electrical conduction is determined by the intrinsic defects (Schottky or Frenkel) in the crystal. In region II, electrical conduction is controlled by the population of charge-carrying defects determined by an aliovalent dopant or impurity. In region III, usually at low temperatures, the population of charge carrying defects is determined by the thermodynamic equilibrium between the free defects and the associated pairs. Since doped cerium oxides (fluorite structured) have a large number of oxygen vacancies, they only show the regions II and III.

In figure 17, differences in slopes are evident, which can be seen even in very pure crystals. At low temperatures extrinsic vacancies are most important. The concentrations of intrinsic vacancies are so small at low temperature that they may be ignored. The number of vacancies will be essentially constant;  $m$  (slope) in the extrinsic region thus will only depend on the mobility of mobile species due to



extrinsic defects, with the temperature dependence.

At high temperatures the concentration of intrinsic defects has increased so that it is similar or greater than the concentration of extrinsic defects. Thus in this region, for a system with Schottky defects and with Frenkel defects a plot of  $\ln \sigma T$  vs.  $1/T$  gives a larger value for the activation energy ( $E$ ), because it depends on both the activation energy for the cation jump ( $\Delta H_m$ ) and the enthalpy of formation of a *Schottky* and *Frankel defect*, given as

$$E_s = Ea + 1/2 \Delta H_s \quad \text{for a system with Frenkel defects}$$

$$E_F = Ea + 1/2 \Delta H_F \quad \text{for a system with Schottky defects}$$

respectively.

Additionally, according to Zhang et al [17], for a polycrystalline oxygen-ion electrolyte, the activation energy for total ionic conduction should come from three sources, that is, the enthalpy of migration of oxygen ions ( $\Delta H_m$ ), the association enthalpy of complex defects ( $\Delta H_a$ ), and the activation energy for the grain boundary conduction ( $E_{gb}$ ). However, in a low temperature range ( $\leq 500^\circ\text{C}$ ); these three sources simultaneously limit the total ionic conductivity. Further with increasing temperature, the grain boundary effect and the association enthalpy of complex defects (e.g.  $Gd'_{ce} - V_o''$ ) gradually disappears. As a result, only the enthalpy of migration of oxygen ions ( $\Delta H_m$ ) plays a major role in limiting the total ionic conductivity and thus the activation energy at high temperatures e.g.  $500\text{--}700^\circ\text{C}$  could be further smaller than that of at  $250\text{--}500^\circ\text{C}$ .

### Reference:

- [1] J. B. Goodenough, H. Y. P. Hong, J. A. Kafalas, *Mat. Res. Bull.*, 11 (1976) 203.
- [2] P. Debye, H. Falkenhagen, *Phys. Z.*, 29 (1928) 121.
- [3] P. Debye, E. Hiickel, *Phys. Z.*, 24 (1923) 185.
- [4] Steele, B. C. H. in *High Conductivity Solid Ionic Conductors*, ed. T. Takahashi, World Scientific, Singapore, (1989) 402.



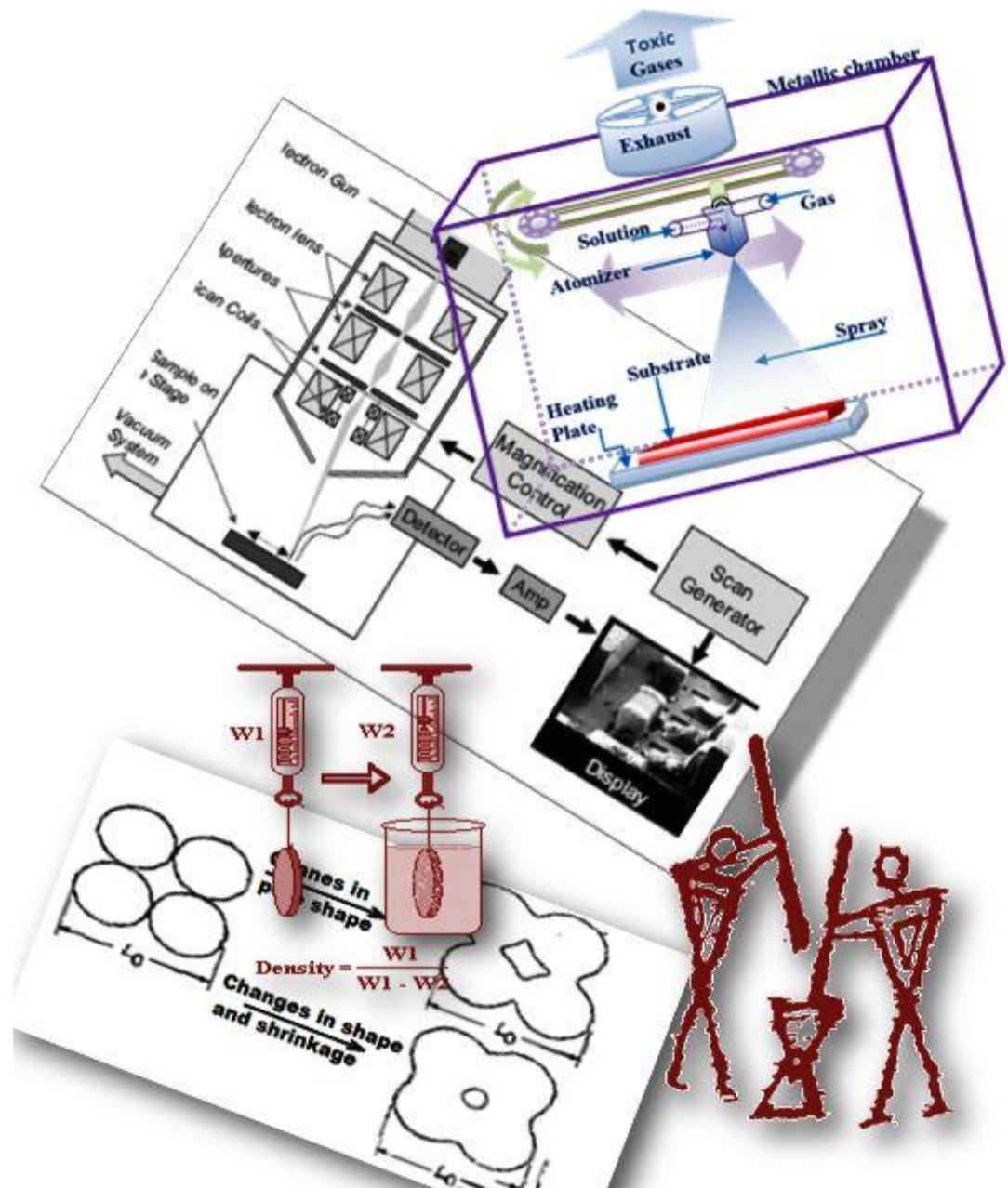
- [5] CRC *Handbook of Chemistry and Physics* for 21st century Copyright CRC Press LLC 2002.
- [6] F.A. Kröger, *Chemistry of Imperfect Crystals, North-Holland, Amsterdam, (1964) 194.*
- [7] J. Faber, C. Geoffroy, A. Roux, *App. Phys. A: Mater. Sci. Process.* 49 (1989) 225.
- [8] K. E. Sickafus, R. J. Hanrahan Jr., K. J. McClellan, J. N. Mitchell, C. J. Wetteland, D. P. Butt, P. III. Chodak, K. B. Ramsey, T. H. Blair, K. Chidester, Hj. Matzke, K. Yasuda, R. A. Verral, N. Yu, *Am. Ceram. Soc. Bull.*, 78 (1999) 1.
- [9] M. Leslie. *Program cascade, description of data sets for use in crystal defect calculations. Technical report, SERC Daresbury Laboratory Report DL/SCI/TM31T, 1982.*
- [10] H. Kleykamp, *J. Nucl. Mater.*, 131 (1985) 221.
- [11] J. van Geel, Hj. Matzke, J. Magill, *BNES*, 36 (1997) 305.
- [12] J.A. Kilner and B.C.H. Steele, in: *Nonstoichiometric Oxides, Academic Press Inc., NY 1981, pp. 233-269.*
- [13] J. Moscinski, P. W. M. Jacobs, *Proceedings of the Royal Society of London. Series A, Mathematical and Physical Sciences*, 398 (1985) 173.
- [14] E.C. Subbarao and H.S. Maiti, *Solid State Ionics* 11 (1984) 317.
- [15] J. A. Kilner, *Solid State Ionics* 129 (2000) 13.
- [16] J.A. Kilner, C.D. Walters, *Solid State Ionics* 6 (1982) 253.
- [17] Zhang T.S., Ma J., Cheng H., Chan S.H., *Mater. Res. Bull.* 41 (2006) 563.





# Chapter three:

*Introduction to experimental techniques  
of synthesis and characterization*





# Chapter three

## CONTENTS

3. INTRODUCTION TO EXPERIMENTAL TECHNIQUES OF SYNTHESIS AND CHARACTERIZATION.....	72
3.1. Introduction .....	72
3.2. Bulk preparation using ceramic route.....	73
3.2.1. <i>Introduction</i> .....	73
3.2.2. <i>Preparation of mixture of raw materials (starting chemicals)</i> .....	75
3.2.3. <i>Ceramic powder synthesis – dry and binder added homogenization.</i> .....	76
3.2.4. <i>Green body formation.</i> .....	77
3.2.5. <i>Pre-sintering – Heat treatments of drying and binder burnout</i> .....	79
3.2.6. <i>Final sintering.</i> .....	82
3.3. Film preparation using spray pyrolysis technique (SPT).....	85
3.3.1. <i>Introduction:</i> .....	85
3.3.2. <i>Experimental setup</i> .....	87
3.3.4. <i>Preparative parameters of spray deposition technique</i> .....	98
3.3.5. <i>General scheme of optimization of spray parameters</i> .....	102
3.4. Characterization techniques .....	103
3.4.1. <i>Density measurements</i> .....	103
3.4.2. <i>Thickness and surface roughness measurements</i> .....	106
3.4.3. <i>Thermal analysis</i> .....	107
3.4.4. <i>X-ray Diffraction</i> .....	110
3.4.5. <i>Scanning electron microscopy and Energy dispersive x-ray spectroscopy</i> .....	113
3.4.6. <i>Atomic Force Microscopy (AFM)</i> .....	116
3.4.7. <i>Electrical characterizations</i> .....	119
References:.....	129

### 3. INTRODUCTION TO EXPERIMENTAL TECHNIQUES OF SYNTHESIS AND CHARACTERIZATION



### **3.1. Introduction**

In current research, the synthesis of the Gd doped ceria in bulk and thin films were carried out using solid state ceramic route and spray pyrolysis technique, respectively. A brief introduction to experimental used for synthesis and characterization of materials are mentioned in this chapter. The first half of this chapter is committed for details of experimental of synthesis. Initially the broad classification of the various synthesis techniques is presented and later the details of well-suited techniques employed in current research are discussed. The choice of suitability of synthesis technique is judged from the literature survey of synthesis of materials of our interest. And also the synthesis techniques were scrutinized on the basis of its cost effectiveness, reproducibility and its possible extension to industrial level. The second half of this chapter includes the brief introductions of characterization techniques employed to characterize the prepared materials e.g. density measurements, XRD, SEM, EDAX, SEM, AFM, ac and dc conductivity measurements, etc.

### **3.2. Bulk preparation using ceramic route**

#### **3.2.1. Introduction**

Various synthesis and processing methods of ceramic routes have been used to prepare doped ceria with desired properties, including hydrothermal synthesis, homogeneous precipitation, sol-gel process, oxalate co-precipitation process, dry pressing process and glycine nitrate process (GNP) [1-4]. Ceramic form of solid materials is mostly used because of potentially low cost, ease in preparation and the prepared material shows great durability under adverse atmospheric conditions. In addition, it is possible to prepare wide range of various ceramic compositions. Therefore, in current research ceramic route for synthesis of GDC samples was adopted to figure out an exact optimum doping level.

To get the final product with desired properties using ceramic route, it is necessary to take into account the phase equilibrium of system, generally, this can be achieved by controlling the stoichiometry of mixture in preparation step and during



final sintering. The preparation procedure normally consists of five major steps (figure 1),

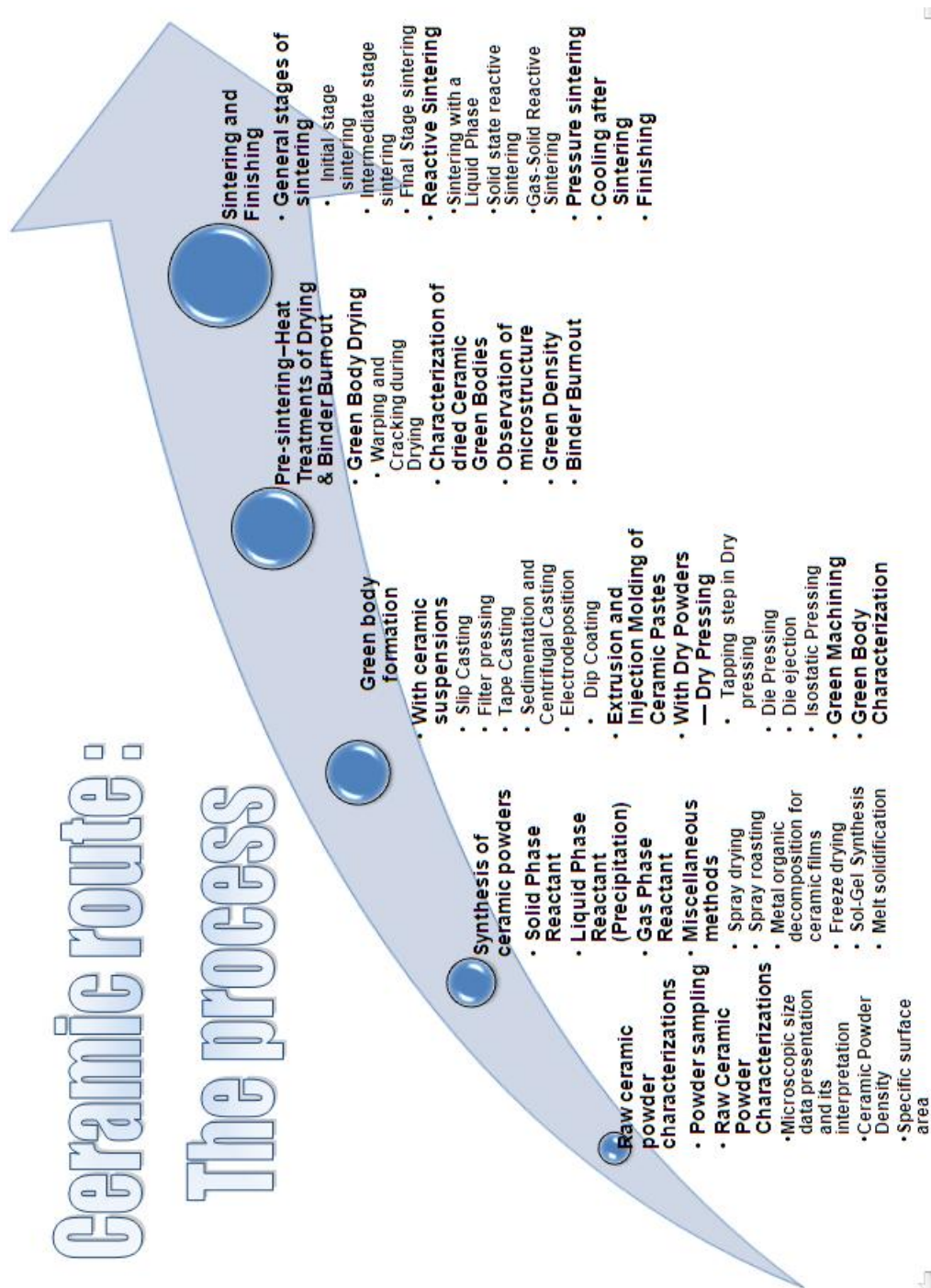


Figure 1. Various stages involved in ceramic route processing.

- i. Preparation of mixture of raw materials (starting chemicals)
  - To form an intimate mixture so as to maintain the appropriate proportions of metal ions in the final product.



- ii. Ceramic powder synthesis
  - Forming the desired ceramic compositions via physical or chemical routes
  - Thorough crushing or grinding of ceramic powders for homogenization of constituent powders (dry homogenization) and binder added homogenization.
- iii. Green body formation
  - Pressing of the binder added homogenized powder in desired shape.
- iv. Pre-sintering
  - Heat treatments of drying and binder burnout
- v. Final sintering and finishing.

These steps are briefly discussed in subsequent sections.

### ***3.2.2. Preparation of mixture of raw materials (starting chemicals)***

The raw materials must be verified for its chemical purity and particle characterization to avoid the formation of undesired chemical phase in the final products.

To form an intimate mixture so as to maintain the appropriate proportions of metal ions in the final product, weighing of the constituent starting chemicals with a sufficient accuracy is desirable. Any error in this step could lead to undesirable and/or irreversible phase formation in the final product. In practice, this step of weighing of the starting chemicals must be done with a micro-balance having high precision. Care must be taken while taking the weights of the constituent starting chemicals, handling it up to assembly of mixing and during mixing of these weighed powders in mixing assembly. After thorough mixing of the constituent starting chemicals it can be handled freely, as now the mixture have become a homogenized mixture and can be regarded as a single assemblage of powders.



### 3.2.3. Ceramic powder synthesis – dry and binder added homogenization.

The raw materials (starting chemicals) that are of either natural in origin or a natural mineral after thermal decomposition, requires crushing and grinding to obtain a desirable particle size distribution and homogenization of constituents, for most ceramic processing (figure 2).



Figure 2. Ancient ceramic powder synthesis technique.

To make the best use of the potential properties of ceramics, new ceramic powders with high chemical purity, uniform distribution of constituent starting chemicals and fine particle size are necessary. Table 1 gives an overview of the various methods for powder synthesis. These methods are generally broken into four categories:

- Solid phase reactant
- Gas phase reactant.
- Liquid phase reactant
- Miscellaneous synthesis methods





Solid phase reaction	Liquid phase reactant	Gas phase reaction	Miscellaneous methods
<ul style="list-style-type: none"> <li>• <i>Solid state reactants</i></li> <li>• Thermal decompositions of a solids</li> <li>• Oxidation or reduction of a solids</li> </ul>	<ul style="list-style-type: none"> <li>• Precipitation</li> <li>• Solution heating or cooling.</li> <li>• Evaporative salting-out</li> <li>• Chemical reaction with insoluble product</li> <li>• Hydrothermal synthesis</li> <li>• Forced insolubility</li> <li>• Dissolution re-precipitation</li> </ul>	<ul style="list-style-type: none"> <li>• Evaporative condensation</li> <li>• Gas phase reaction with solid product</li> <li>• Thermal decompositions</li> <li>• Oxidation or reduction reaction</li> <li>• Combination reaction with a solid product</li> </ul>	<ul style="list-style-type: none"> <li>• Solvent removal</li> <li>• Spray drying</li> <li>• Freeze drying</li> <li>• Spray roasting</li> <li>• Sol-gel synthesis</li> <li>• Molt solidification</li> </ul>

Table 1. Ceramic powder synthesis methods.

Among all the above mentioned powder synthesis methods, we employed the method which involves solid phase reactants. The brief information of the other categories is appended as *appendix I-A*.

### 3.2.4. Green body formation.

#### 3.2.4.1. Green body preparation

A green body can be made from a ceramic suspension, a ceramic paste or from a dry ceramic powder. It is molded into a shape with forces applied to either the individual particles, as in drag and gravitational forces, or to the mass of particles as, in ramming a dry powder onto a die or extruding a paste. After drying, the ceramic green body contains (1) the ceramic components; (2) a polymeric binder system



including dispersant, binder, and plasticizer, and (3) residual solvent used to make the initial ceramic suspension or paste.

The mechanical properties of ceramic powders are important in designing the equipment necessary to process the ceramic suspensions, pastes, and dry powders into ceramic green bodies. Each of the different raw materials for green body formation is used with different methods of ceramic green body formation. For example, (1) ceramic suspensions are used with slip casting, drain casting, tape casting, dip coating, filter pressing, and electro-deposition; (2) ceramic pastes are used with extrusion and injection molding; and (3) dry ceramic powders are used in die pressing, dry bag isostatic pressing, and wet bag isostatic pressing.

The uniformity in green body formation is essential for its uniform sintering. Any differences in the packing density of the ceramic powder will cause different shrinkage during sintering, which leads to warping or cracking of the shape during sintering. Depending on the initial state of the ceramic material, which can be either, a dry powder, a suspension or a paste, there are different methods of shape manufacture (*appendix I-B*).

Particular attention must be paid to the uniformity of powder packing, binder distribution, and solvent distribution because these play an important role in the next phases of processing i.e. drying, binder burnout and sintering. Inhomogeneities in these properties will lead to deforming and cracking of the ceramic piece during further processing. In current research we emphasize the use of dry pressing due to its simplicity and low cost nature. However, the brief information for other methods can be found in *appendix I-B*. Further there are two types of dry pressing, isostatic and die pressing. In the present work we have employed die pressing.

In die pressing, the dry ceramic powder is allowed to flow into a hardened steel mold. Then the materials are pressed by a die. This pressing action can be either uniaxial or biaxial, depending on the type of press. After a short period of time under pressure, the pressing action is decreased and the pressure is used to eject the green body from the press. Large production runs are almost always made with die pressing and not isostatic pressing. Important steps involved in dry pressing are explained in the *appendix I-B*.



#### 3.2.4.2. *Green Machining*

Many green pieces made by slip casting, uniaxial die pressing, or isostatic pressing are used as "rough stock." That means they are further shaped by machining techniques before subsequent processing. In the green state, ceramics are easily cut with cutting tools and ground with grinding. Green machining is much easier than machining after sintering. After sintering, the ceramic is very hard and difficult to machine.

#### 3.2.4.3. *Green Body Characterization*

The characterization of the ceramic green body after its fabrication is an important step if problems arise either during fabrication or during subsequent processing steps. These problems are typically warping and cracking of the green body. At this point in the processing, the green body is either still wet, if prepared from suspensions or pastes, or it contains binder, if prepared by dry pressing. At this stage green body characterization is concerned with the uniformity of packing density, particle size distribution, bulk chemistry, binder distribution, and anisotropic particle orientation. Non-uniformity of these green body properties leads to warping and cracking during drying, binder burnout and sintering.

#### 3.2.5. *Pre-sintering – Heat treatments of drying and binder burnout*

Green body consists of a mass of ceramic powder held together by either a liquid in the pores (if green body formation used ceramic suspension) or a polymer-binder (if green body formation uses spray dried or simply dry powder). The strength of the green body is determined either by the liquid in the pores or the polymer distributed at the particle-particle contacts. Drying the solvent out of the green body and thermal decomposition of the polymer (also surfactants and plasticizers) requires heat to be transferred into the green body to the location of either a chemical reaction or phase transformation. The necessary heat of evaporation for solvent drying and the heat of reaction (either exothermic or endothermic) for polymer thermal decomposition (also called binder burnout) must be supplied for the evaporation or reaction to continue. Once the heat of reaction is provided, the reaction can proceed.



Both evaporation and thermal decomposition of liquid or polymer in the pores give off huge volumes of gas for each gram of material reacted. This gas diffuses through the porous network of the green body. These mass transfer steps can also limit the rate of either evaporation or thermal decomposition of binders.

Different types of stress act on the green body during these processes. One such is the stress induced by thermal gradients in the green body. Another is the stress due to a gas pressure gradient in the green body, caused by the flow of gas from the inside of the green body to its surface. The later type of stress can also be due to a liquid pressure gradient in the green body caused by the flow of liquid from the inside of the green body to its surface. These stresses are additive and act to warp or crack the green body. When the green body's surface is in tension, it is most vulnerable to cracking because, like all ceramics, a green body is weakest in tension.

### 3.2.5.1. Green body drying

Simultaneous heat and mass transfer in both the boundary layer surrounding the green body and the pores inside the green body are responsible for the drying. To remove the solvent/binder used to suspend/bind the ceramic powder for green body formation, the green body is heated or placed in an atmosphere where the solvent evaporates/reacts. The weight loss during drying is schematically shown in figure 3.

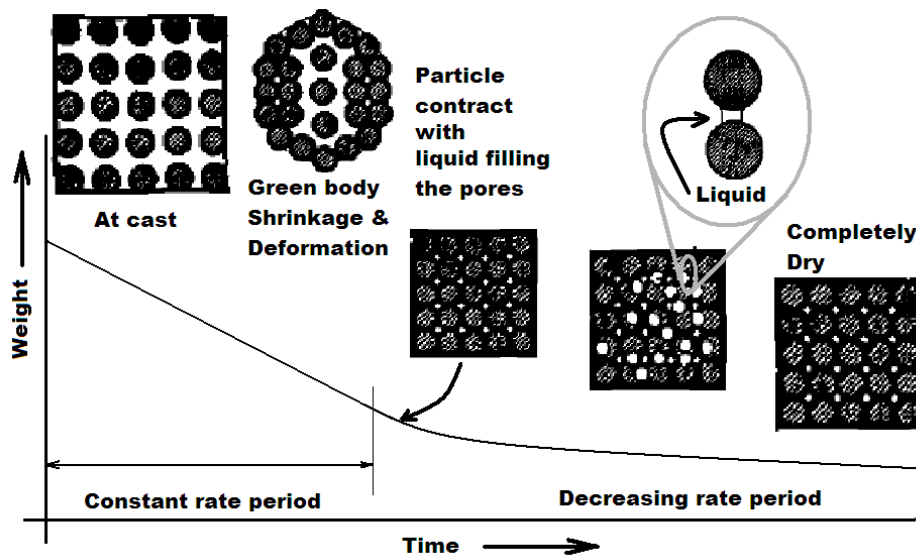


Figure 3. Schematic of drying of a ceramic green body; showing the weight loss and shrinkage of green body with time.



This figure shows a constant rate period where the surface of the green body is always wet by the flow of liquid to the surface. At some point, the particle network becomes rigid and no more shrinkage can take place. With particulate ceramics, this rigidity threshold takes place at high volume fraction where the particles come into contact.

#### *3.2.5.2. Warping and cracking during green body drying*

When the green body is wet by the solvent it has a compressive capillary force which holds it together. During drying this capillary force disappears. With a polymeric binder present, the compressive capillary force is replaced by the cohesive force of the binder, which is usually smaller than the original compressive capillary force of the solvent. In its weakened state during drying, the green body is susceptible to stress that may warp and crack it. Such stress is due to either (1) the capillary pressure gradient, (2) the pressure gradient of the escaping solvent, or (3) the differential thermal expansion of the ceramic because of temperature gradients within the green body. Each of these forms of stress can be manipulated by the rate at which the green body is dried (or cooled down). If the stress is non-uniform it will warp the green body. The surface of the green body is the most susceptible to stress.

#### *3.2.5.3. Binder Burnout*

The polymers (binder) are used to keep the particles in contact with each other, even after removing from the molds (die). This ceramic green body must be heat treated before the sintering, to decompose the binder. Since binders decomposes in an uncontrolled manner at sintering temperatures giving off huge volumes of gas at high pressure which may cause the green body to crack. In general, binder burnout is performed at temperatures between 300 and 700°C, much below the temperatures used for sintering. During binder burnout, the polymer undergoes a controlled thermal decomposition reaction that can take several forms. In general, thermal decomposition of polymers forms both volatile and solid residues as products of the reaction. The solid residues react further at higher temperatures to give subsequent volatile products and other solid residues. A small amount of polymer can produce an enormous volume of gas, which must be removed from the porous green body. The flow of this gas in



the porous network of the ceramic green body can create a pressure build-up which puts stress on the green body.

To remove the polymeric binder, the green body is heated often in an oxidizing atmosphere. During this process, the polymer degrades along many possible degradation pathways. Deep within the green body, the oxygen partial pressure is frequently small because it often cannot diffuse fast enough to keep up with the reactions taking place. For this reason, even under an oxidizing atmosphere, the center of the green body often undergoes degradation reactions with reducing conditions operating.

#### *3.2.5.4. Characterization of dried ceramic green bodies*

Ceramic green bodies are typically characterized in detail after drying, since no precaution is required to assure further weight loss in the green body. Green body characterization is typically done by observing the microstructure of a fracture surface with a scanning electron microscope, measuring the green body strength and determining its average density. In some cases the pore size distribution is also measured.

### **3.2.6. Final sintering.**

#### *3.2.6.1. Introduction*

After binder burnout green body consists of porous assembly of ceramic particles. At this stage the ceramic green body is at its most fragile state and must be handled with care or, better yet, simply not handled at all. Hence it is highly preferred that the binder burnout and the next step, sintering, are performed either (1) in the same furnace but at different temperatures (and sometimes in different atmospheres) or (2) in the same furnace (tunnel oven) although in different sections.

Sintering is a process whereby the porosity is removed from the ceramic green body, giving a fully dense ceramic piece. The flow of material to fill the pores can take place by different methods from diffusion to viscous flow. Each of these processes is speeded up by increasing the temperature. As the ceramic green body sinters



it decreases in volume. Non-uniform shrinkage causes stress to build up, resulting in warping and cracking.

### 3.2.6.2. Sintering

Sintering takes place in three primary stages: an initial stage, an intermediate stage, and a final stage. The distinction between initial and intermediate stage sintering is somewhat unclear. Figure 4 shows the sintered density obtained after 4 hr at each temperature for two particle sized distribution of  $\text{Al}_2\text{O}_3$  powders. In figure 4, the finer powder sinters to a higher density at a lower temperature because it has a higher specific surface area.

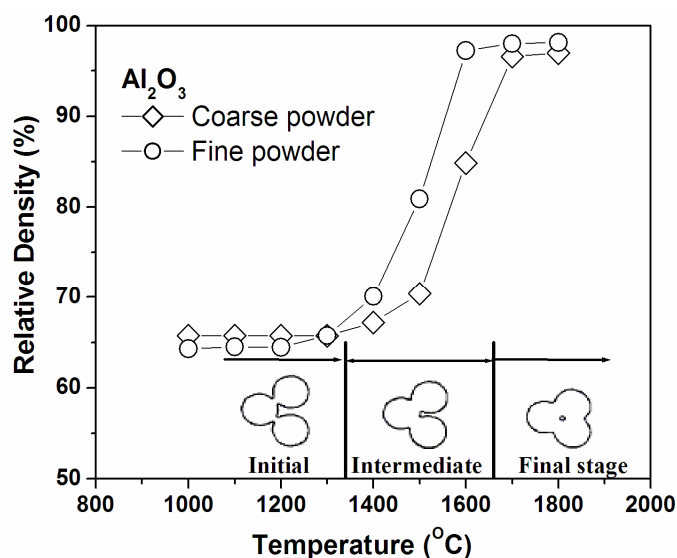


Figure 4. Densification of two alumina powders ( $d = 1.3$  and  $0.8\mu\text{m}$ ) showing the initial, intermediate and final stages of sintering. Sintering was carried out at a constant heating rate of  $7.3^\circ\text{C}/\text{min}$  [5].

The driving force for sintering is the reduction of the surface energy of a powder compact by the replacement of solid-air interface with lower energy solid-solid interfaces. This driving force for sintering is small and should not be wasted on mechanisms (such as surface diffusion and evaporation-condensation) that do not lead to densification. From figure 4, the various stages of sintering can be described as flow-chart shown in figure 5,



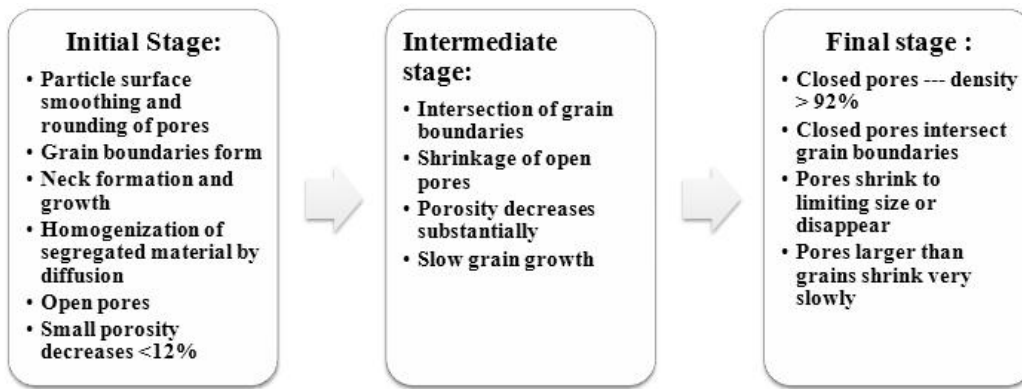


Figure 5. Various sintering stages.

These stages are the typical progression of events that take place during sintering. However, sometimes the density does not increase though the pores change shape. This is called coarsening. The difference between sintering and coarsening is schematically shown in figure 6.

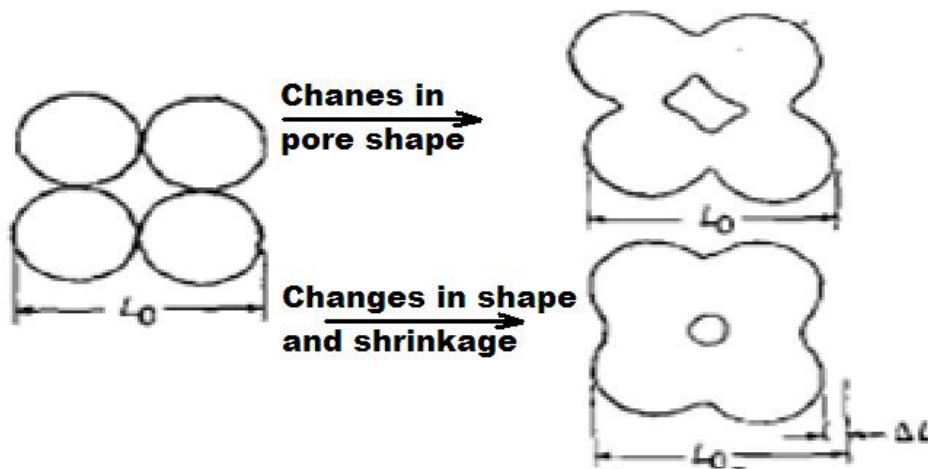


Figure 6. The difference between coarsening and sintering (shrinkage).

If the inter-particle separation distance remains the same, coarsening takes place. If the inter-particle separation distance decreases, sintering takes place. Only sintering leads to an increase in density, which is referred to as densification.





### 3.3. Film preparation using spray pyrolysis technique (SPT)

#### 3.3.1. Introduction:

There are several methods for thin oxide film depositions, which can be divided into two groups based on the nature of the deposition process. The physical methods include physical vapor deposition (PVD), laser ablation, molecular beam epitaxy, and sputtering, while the chemical methods comprise gas phase deposition methods and solution techniques. The gas phase methods which utilizes the gas phase reactants for depositions are chemical vapor deposition (CVD) [6, 7] and atomic layer epitaxy (ALE) [8], while spray pyrolysis [9], sol-gel [10], spin- [11] and dip-coating [12] methods employ precursor solutions and hence fall in the liquid phase reactant methods. Various deposition techniques are summarized in the figure 7.

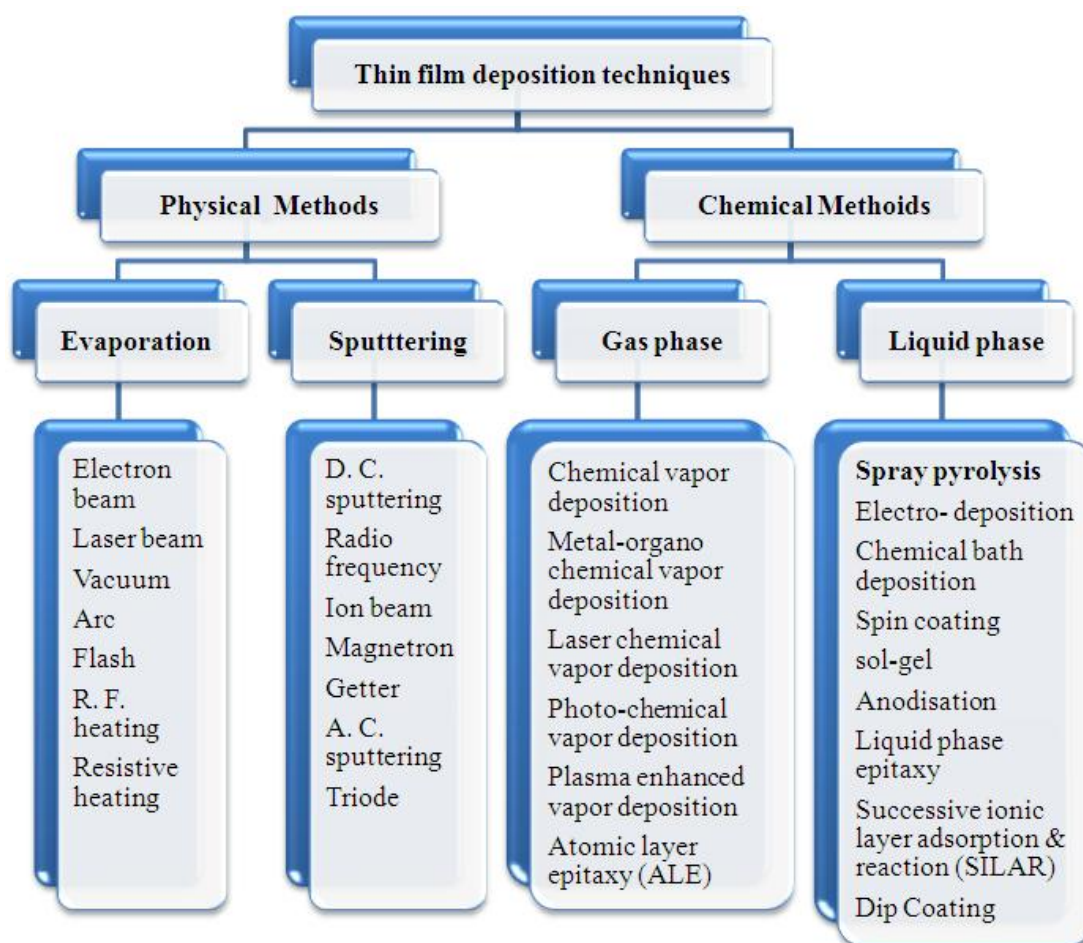


Figure 7. Various types of thin film deposition techniques.



The choice of the particular method depends on the several factors like, (a) material to be deposited, (b) nature of the substrate (c) required film thickness, (d) structure of the film and (e) application of the films. The physical methods are employed to deposit many binary and ternary compounds and different alloys. However the techniques mentioned under the category of physical methods are overwhelmed with certain drawbacks and difficulties. A careful and precise control of the source temperature is required for obtaining good stoichiometric films and particular composition of the alloy films. Chemical methods are relatively cheaper and easier in comparison with physical methods. Amongst chemical methods, the spray pyrolysis technique (SPT) is the most popular deposition method to prepare a wide variety of dense as well as porous oxide films, ceramic coatings, and powders. Even multi-layered films can be easily prepared using this versatile technique. These films (including the films prepared from powders) were used in various devices such as solar cells, sensors, and solid oxide fuel cells, etc. The properties of deposited thin films highly depend on the preparation conditions. The substrate surface temperature is the most critical parameter as it influences film roughness, cracking, crystallinity, etc. Processes involved in spray pyrolysis technique, such as atomization of the precursor solution, aerosol transport, and decomposition of the precursor plays the decisive role. Unlike many other film deposition techniques, spray pyrolysis represents a very simple and relatively cost-effective method.

The influence of various preparative parameters of SPT, on film formation process has been reviewed by C. M. Lampkin [13]. Thereafter due to good productivity of this technique on a large scale and simplicity of the apparatus, it offered most attractive way for the formation of thin films of metal oxides [14-25], metallic spinel type oxides [26-29], binary chalcogenides [30-35], ternary chalcogenides [36, 37], superconducting oxides [38-41] etc. Apart from its simplicity, spray pyrolysis technique has number of advantages, such as:

- Unlike closed vapor deposition method, spray pyrolysis neither requires high quality targets and/or substrates nor does it require vacuum at any stage, which is a great advantage, if the technique is to be scaled up for industrial applications.



- Spray pyrolysis technique can produce films even on less robust material because it operates at moderate temperature (100-550°C) and at ambient pressures.
- By changing composition of the spray solution during the spray process, it can be used to make layered films and the films having composition gradients throughout the thickness.
- It offers an extremely easy way to dope films with any element in any proportion by merely adding it in some form to the spray solution.
- The deposition rate and the thickness of the films can be easily controlled over a wide range by changing the spray parameters, thus eliminating the major drawbacks of chemical methods such as sol-gel which produce films of limited thickness.
- Unlike high power methods such as radio frequency magnetron sputtering (RFMS), it do not cause local over-heating that can be harmful for materials to be deposited. There are virtually no restrictions on substrate material, dimension or its surface profile.

### **3.3.2. Experimental setup**

#### **3.3.2.1. Introduction**

Films prepared by the spray pyrolysis technique have been used in various devices e.g. solar cells, sensors, anti-reflection coatings, thermal coatings, as electrolytes in solid oxide fuel cells, and many others. The technique involves spraying a solution of precursors (metal salt) onto a heated substrate. Droplets sprayed impacts on the substrate surface, spread into a disk shaped structure, and undergo thermal decomposition. The shape and size of the disk depends on the momentum and volume of the droplet, as well as the substrate temperature. Consequently, the film is usually composed of overlapping disks of metal salt being converted to oxide on the heated substrate. Every sprayed droplet reaching the surface of the hot substrate undergoes pyrolytic (endothermic) decomposition and forms a single crystalline or cluster of crystallites (polycrystalline) as a product. The other volatile by-products and solvents escape in the vapor phase. The substrates provide thermal energy for the



thermal decomposition and subsequent recombination of the constituent species, followed by sintering and crystallization of the clusters of crystallites and thereby resulting in coherent film.

The main process parameters of the spray deposition are the deposition (i.e. substrate) temperature, the solution flow rate, the composition and concentration of precursor compound, the solvent properties and the droplet size distribution. Also the nature of the substrate surface can influence the film nucleation and growth. The substrate temperature is usually held at 150-550°C. A typical solution flow rate is 5-20 ml/minute. Various precursors (halides, acetates, nitrates and organo-metallic compounds) and solvents, e.g., water, butanol, butyl acetate and butyl carbitol, have been used in literature.

### 3.3.2.2. The setup:

Figure 8, shows the schematic diagram of the experimental setup of spray pyrolysis technique.

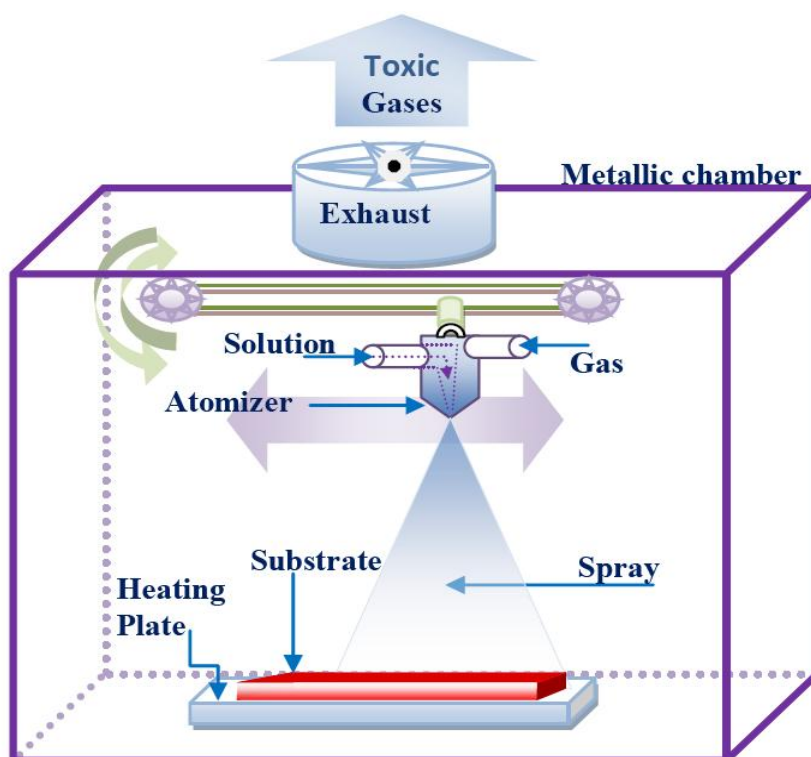


Figure 8. Schematic of experimental setup of spray pyrolysis technique.



It mainly consists of (a) Air tight metallic chamber with an assembly of exhaust, (b) Atomizer – spray nozzle with rotor (c) Substrate heater with temperature controller, (d) Solution quantity controller and (e) Extra accessories as per the requirement of the atomizer system.

*a. Airtight metallic chamber with an assembly of exhaust:*

For deposition of metal oxide films, the metal salts solution is sprayed on to heated substrates. Volatile gases as byproduct from the sprayed mist caused during the pyrolytic decomposition may have toxic gases. Hence, it is necessary to fix the spraying assembly in an airtight metallic chamber. Inner surface of the chamber is generally painted with liquid epoxy in order to avoid the corrosion of the chamber. An outlet of the chamber is fitted to an exhaust to remove the gasses evolved during spray deposition.

*b. Atomizers – Spray nozzles attached to rotor (for lateral motion)*

The spray pattern, distribution of droplets and spray rate depends on geometry of atomizer. Atomizers are an assembly in which the liquid phase reactants are transformed into fine droplets (mist) of the solution which can be formed with different techniques which includes air blast [42], ultrasonic [43] and electrostatic atomizing techniques [44].

Numerous reports were published on the mechanism of liquid atomization. Rizkalla and Lefebvre examined the influence of liquid properties on air blast atomizer spray characteristics [45]. Similarly, in literature there are discussions on results concerning the application of the air blast atomizer [35], theory of ultrasonic atomization [46], study of the electrostatic atomization of liquids [47], etc. Compared with other atomization techniques, the electrostatic spray deposition technique has been used only recently for thin film deposition, whereas liquid atomization by means of an electric field and by air blast techniques has been investigated for many years and hence understood well.

Rotor is an attached assembly to the atomizer to increase the area of deposition. Using this rotor, the spraying nozzle moved in lateral direction in an oscillatory manner about its mean position. This oscillatory motion of nozzle enables



large area deposition. In some cases the one dimensional lateral motion is extended to two dimensional motions to further increase the area of deposition. The rotor arrangement also serves the purpose of distributing the cooling effect which obviously generates at the spot where the solution is just sprayed. This distribution of cooling area enables to increase the thickness of the films, which was not possible with stationary nozzles. Due to this distribution of the cooling region, higher spray rate is possible and which consequently results into higher deposition rates. The stationary nozzle produces the cooling effect at the same spot causing distraction of substrate temperature (expected to be constant throughout the deposition process) and thereby restrict longer duration of depositions and hence the thickness of the film.

*c. Substrate heater with temperature controlling arrangement*

In spray pyrolysis deposition the pyrolytic action of sprayed solution takes place due to the heated substrates. The substrate temperature must be kept constant throughout the deposition process. For this reason, the heating plate for the heating of substrates is connected with a temperature controlling unit. This temperature controlling unit senses the temperature of heating plate using a thermo-couple (preferably Alumel-Chromel thermocouple) which remains in contact with surface of the heating plate. Thermocouple gives signal (proportional to its temperature) to the controller circuitry and according to set point controller controls the power supply to the heater. At the temperature of interest (i.e. at set point), the controller switches off the power supply of heater with the help of electric-relay circuit. Due to break in the current to heating-coil, the heating coil stops heating as there is no current to drive heating. Spraying of cool solution mist on the substrates kept on heating plate leads to cooling of heating plate. When the temperature of heating plate decreases from the set point due to cooling, the controller starts the power supply to heater again. This cycle is allowed to repeat until the end of deposition.

Since the energy required for pyrolysis of the sprayed solution is acquired from the substrate surface, the substrate surface must be kept at the temperature of interest and not that of the heating plate surface. Hence the offset temperature must be added to the temperature of our interest to account the temperature gradient produced due to thermal conductivity of the substrate. Thus the offset temperature of for different substrate may differ as per its thermal conductivity.



*d. Solution quantity meter*

This arrangement is intended to quantify the amount of solution sprayed during deposition. Basically, it consists of the calibrated glass cylinder in which the solution is filled in. This cylinder also enables us to determine the rate of solution sprayed during the deposition for a particular period.

*e. Extra accessories as per the requirement of the atomizer system*

▪ *For air-blast atomizer – Gas regulator valve with flow meter:*

In air-blast type of atomizer the spray is generated with the help of supersonic air. It is observed that with increases in gas pressure to atomize the solution, size of droplets goes on decreasing. Hence for the optimized droplet distribution, the gas pressure for the atomization of solution must be regulated during deposition. Thus, for gas pressure controlling the carrier gas is passed through the gas regulator. To quantify the gas pressure, the gas flow meter is also introduced into the gas tubing. Since the droplet size distribution plays a critical role in morphological properties of deposited material, this arrangement requires special attention. However, it is also observed that with increase in gas pressure spray rate also increase up to certain critical limit and after that it drops suddenly.

▪ *Ultrasonic atomizer – electronic circuitry:*

In ultrasonic atomizer the titanium nozzle has to vibrate at ultrasonic frequency. This requirement needs an electronic circuitry which can generate the desired frequencies. The frequency generated is then transported to nozzle by the mechanical means. The ultrasonic vibration of nozzle produces small drops of the solution filled in, which then allowed to fall on substrate for the deposition.

▪ *Electrostatic atomizer – High dc voltage power supply*

In the electrostatic atomizer a high voltage is usually applied to a metal capillary tube through which a precursor solution is fed. The electric field induces the



surface charge that causes an outward electrostatic pressure on the solution. The precursor solution can be atomized in different ways, depending on the applied voltage. Hence the stable and high voltage supply with an arrangement of variation of voltage is required along with metal capillary. However, in this arrangement the spraying nozzle (metal capillary) is pointing vertically up is preferred as it allows the spray of droplets with a distribution above a particular size. For this purpose more complex substrate heating arrangement is required.

### 3.3.3. Film formation mechanism in spray pyrolysis

Very few models about the mechanism of spray deposition and film formation have been reported. There are number of processes occur either sequentially or simultaneously during film formation by spray pyrolysis. Generally, the model includes precursor solution atomization, droplet transport and evaporation, spreading on the substrate, drying and decomposition of the precursor salt. Thin film deposition using spray pyrolysis can be divided into three main steps: atomization of the precursor solution, transport of the resultant aerosol and decomposition of the precursor on the substrate.

#### 3.3.3.1. Atomization

The first step in spray pyrolysis is generation of spray with the help of atomizers. In atomizers the filled precursor solution is transformed into fine droplets and forced or directed towards the substrates. Air blast, ultrasonic and electrostatic atomizers are normally used in spray pyrolysis techniques which have their own parameter to control the droplet distribution. E.g. in air-blast atomizer, the gas flow rate determines the droplet distribution for the spray. Similarly, in ultrasonic and electrostatic atomizer, the ultrasonic frequency and applied potential, respectively controls the droplet distribution. The morphological properties of the films directly depend upon these droplet distributions. If the droplet distribution is narrow the films are observed to have uniform grain sizes.

In general, every atomizing technique requires at least two components, namely solution – to be dispersed into droplets and driving force – to disperse the





solution. Formation of droplets from atomization may be accomplished in three stage process (figure 9).

- *Stage I:*

The driving force produces a disturbance in the liquid, which then propagate through liquid in the form of wave.

- *Stage II:*

This disturbance creates wave in the falling liquid, which consequently lead to formation of fragments or ligaments from liquid.

- *Stage III:*

Later these fragments or ligaments disintegrate into larger droplets. Further these larger droplets undergo breakup and generate smaller droplets, which may not have uniform sizes and hence forming droplet distribution. However, these smaller droplets may also undergo coalescence during collision in further flight towards the substrate.

The three stage process results in droplet distribution with atomizing medium. In air-blast type atomizer the atomizing medium is air. The resultant droplet distribution of solution with air is referred as “Aerosol”. This aerosol is then transported to substrate where the deposition of the metal salt in thin film form occurs.

#### *3.3.3.2. Aerosol transport:*

In this step the Aerosol produced in the first stage is transported to the deposition site. In this step, the aerosol undergoes vaporization of the solvent, formation of precipitate and pyrolysis of the precipitate in sequence. The energy required for transport of aerosol is gained from the driving force of atomizing medium. The energy required for phase transition from aerosol to precipitate is



supplied from the temperature gradient produced by the heated substrate in the deposition chamber (see figure 10a).

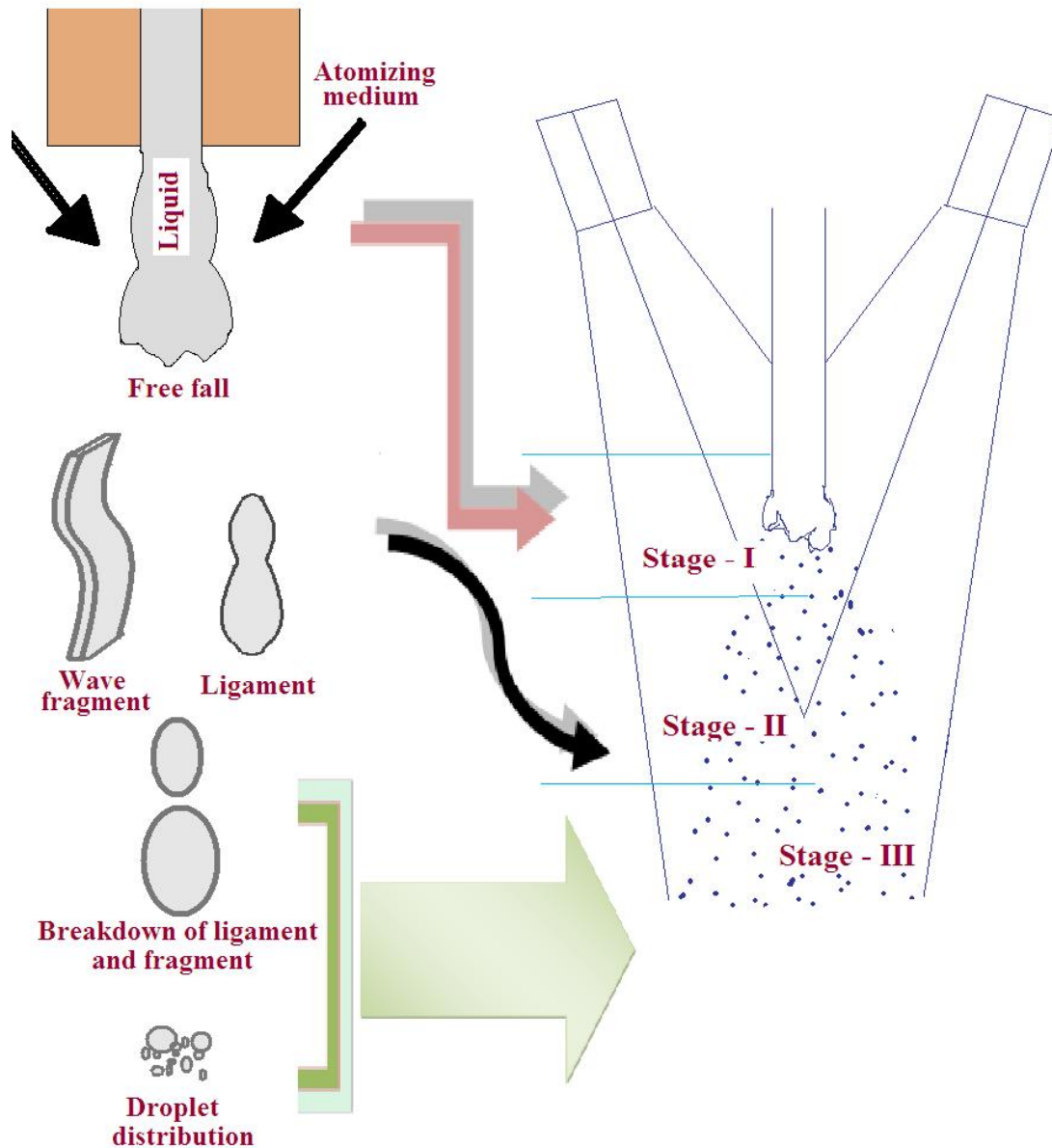


Figure 9. Atomization stages.

During the transport of aerosol towards the heated substrate, initially aerosol gets warmed and undergoes vaporization of solvent and leads to a size reduction (shrinkage) of the droplet and to the development of a concentration gradient within the droplet. As the droplet moves to heated substrate, continuous vaporization of solvent takes place and consequently leads to formation of precipitate. The



precipitation of the precursor in droplet occurred as the concentration exceeds the solubility limit. When the precipitate reaches closer to the substrate, the sudden increase in air temperature leads to pyrolytic decomposition of the precipitate and forms the solid particles. The mechanism of aerosol transition as function of temperature gradient is shown in figure 10.

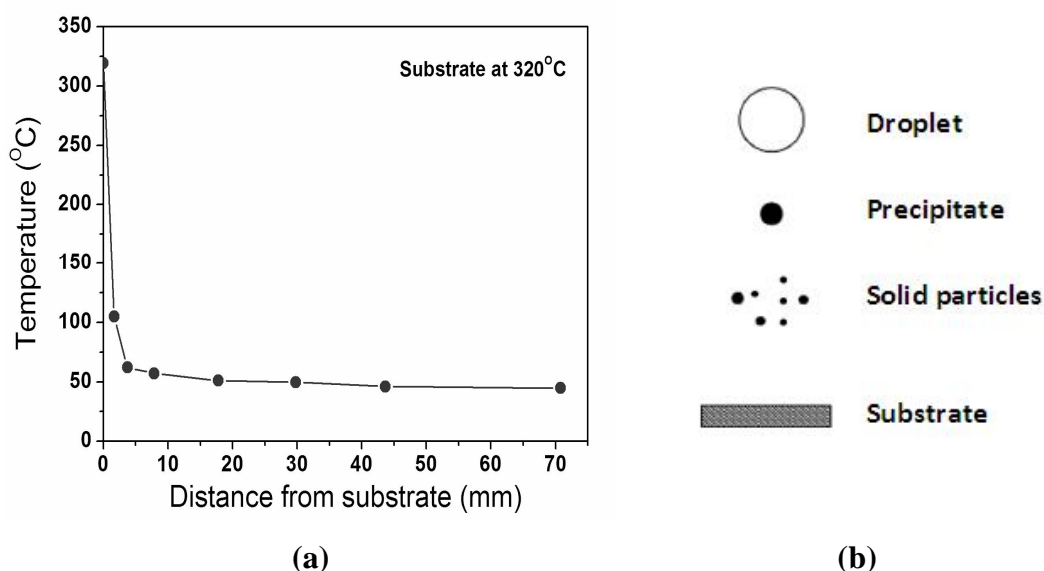


Figure 10. (a) Temperature gradient as function of distance from substrate. (b) Transition of aerosol as function of temperature gradient produced by heated substrate, during aerosol transport.

This aerosol transport is mainly responsible for the structural and morphological properties of spray deposited films. The complete pyrolysis of sprayed precursor solution in this step provides surety of phase formation. The sufficient temperature gradient is thus necessary for complete pyrolysis of the spray. If the temperature is not optimized the evaporation of solvent may be in premature or exceedingly matured state, which may result in un-desired results in deposited films. Deposition of premature solid particles results in the spitting effect, while that of the exceedingly mature particles hovered over the substrate and may fly away from the deposition site (substrate). In both the situation the deposited material may have undesirable properties.



### 3.3.3.3. Decomposition of precursor on substrate, nucleation and growth of films

When the precipitate reaches the substrate, the precipitate undergoes decomposition and then nucleation and growth of thin films on the substrate take place. Many processes occur simultaneously when a droplet hits the surface of the substrate, namely, evaporation of residual solvent, spreading of the droplet and salt decomposition. These processes are strongly depending on the type of salt and substrate temperature used for spray deposition.

If the droplet reaches the substrate which is at low temperature (not sufficient for decomposition) (process A in figure 11) the droplet splashes onto the substrate and then decomposes. At slightly higher temperatures (process B in figure 11) the solvent evaporates completely during the flight of the droplet and dry precipitate hits the substrate, where decomposition occurs. At even higher temperatures (process C in figure 11) the solvent get evaporated before the droplet reaches the substrate. Then the solid precipitate melts and vaporizes without decomposition on the substrate. At the still higher temperatures (process D in figure 11) the precursor vaporizes before it reaches the substrate, and consequently the solid particles are formed after the chemical reaction in the vapor phase.

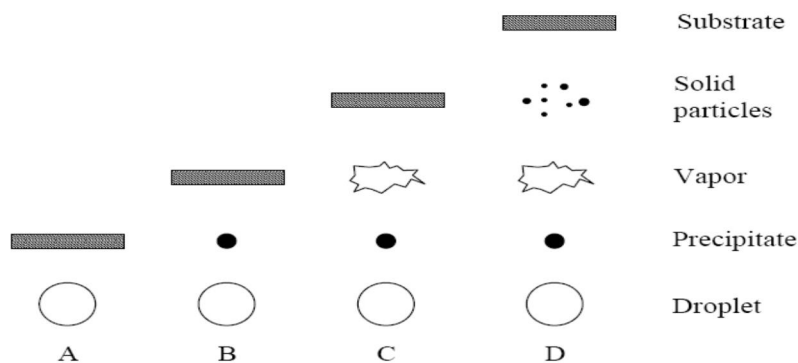


Figure 11. Decomposition of precursor solution.

After decomposition of the precursor on the substrate (process B in figure 11) the subsequent nucleation and grain growth results in the formation of film. There are number of models proposed for the nucleation and growth mechanism. Here the mechanism discussed by Perdnis [48] is described in brief.



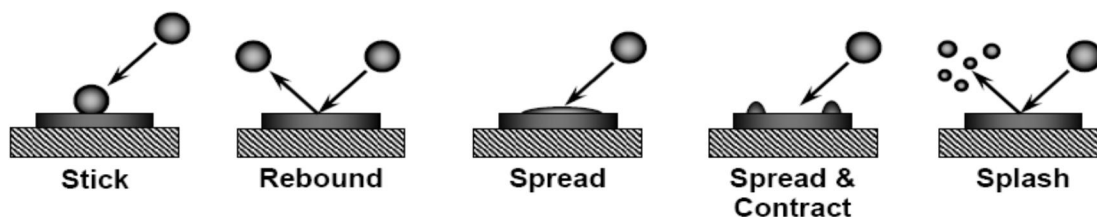


Figure 12. Five possible droplet impacts on heated substrate.

Five possible droplet impacts are shown in figure 12. A droplet hitting the surface may stick, rebound, spread or splash on the surface. The spreading of impacted droplets can lead to the formation of a dense film. The sequence after the droplet has hit the surface depends on its size, viscosity and velocity. If droplets are too small they will rebound due to the retarding thermophoretic forces which are strongest close to the substrate, where the temperature gradient is largest. If they are too viscous or dry, they will stick and if they are too fast, they will splash. If the droplets spread but the velocity is too high, rings are formed. Consequently, only the spreading of droplets with not too high a velocity will lead to the formation of a dense film.

After droplet impact, the physical and chemical properties of a precursor solution play an important role. In this stage, the spreading of the impacted droplet, the evaporation of residual solvent and precursor decomposition take place simultaneously. Fast spreading of droplets leads to the formation of smooth films. The substrate should provide enough heat and temperature for solvent evaporation and salt decomposition. If this is not the case, cracks will develop due to liquid film contraction upon drying. The contraction of a spread droplet on the surface leads to a build-up of stress in the still liquid but viscous film, and when the stress exceeds the local tensile strength, the film fractures. When the impacting droplet contains just sufficient amount of solvent, it spreads over the substrate surface and forms a disk shaped splat. With increasing temperature, the impacting droplets contain less solvent. These nearly dry droplets will stick on the substrate without spreading, and consequently more particles will occur on the film. Finally, at too high deposition temperatures, the solvent of the droplets evaporates before the droplet reaches to the substrate, and, as result, powder will be obtained. From these observations it is recommended to avoid complete solvent evaporation in the droplet during



transportation (since it leads either powder formation or rough films) and enhance the spreading of impacted droplets on the substrate.

Chen et al. [49] while describing the model for thin film deposition using spray pyrolysis considered that it is necessary to have the wet droplets to reach the substrate surface for dense film formation. In contrast to the model for dense film deposition, slow spreading of droplets on the substrate and a salt concentration gradient within the obtained splat are necessary to obtain porous films. The substrate surface temperature, the surface tension of the solution, and the boiling point of the solvent were found to be the most important parameters for the deposition of porous films. Chen et al also suggested that the type of precursor salt have an influence on porous film formation.

#### ***3.3.4. Preparative parameters of spray deposition technique***

The choice of a salt is the most important decision to be made before parameter optimization for SPT. The type of salt directly influences three spray parameters:

- Substrate temperature
  - Should be sufficiently high to decompose the salt,
- Salt concentration
  - Limits the maximal concentration in the solution and
- Type of solvent
  - Restricts the choice of salts due to their insolubility in some solvents.

Therefore, the optimal spray parameters usually differ considerably for each type of salt.

##### ***3.3.4.1. Type of salt***

The extremely large choice of precursors is one of the advantages of the spray pyrolysis technique. The main requirements for the precursor salt are:



- A salt must be soluble in an alcoholic or aqueous (water) solvent and
- It must decompose into an oxide at the deposition temperature.

Few examples of precursor salts are metal chlorides, metal nitrates and metal-organic salts, etc.

*a. Chlorides*

Chlorides have the following advantages: high solubility in ethanol and low price. However, they are extremely chemically aggressive and cause corrosion of the experimental setup. Also, part of the chlorine ions can remain in the deposited film, causing changes in the material properties. The chlorine impurities also hinder the crystallization of the initially amorphous thin film.

*b. Nitrates*

The main drawback of the chloride precursor was its corrosive action. Nitrates appear to be possible substitutes for the chlorides. The solubility of metal nitrate in ethanol and water is adequate. The decomposition temperatures of the nitrates are much less than that of the chlorides. At the same time, all volatile bi-products of the metal nitrates are in gases form and complete decomposition occurs without any impurity phases in the deposited films.

*c. Metal-organic salts*

The metal-organic salts are another type of salt which can be used as precursor solution. However, the higher cost of metal-organic salts is their main drawback. On the other hand, metal-organic salts have higher solubility in organic solvents.

*3.3.4.2. Substrate (-surface) temperature*

The substrate temperature is the most important spray parameter. At temperatures below optimum value, the droplets deposited remain rich in solvent. Therefore, a thin, wet layer is present on top of the film during deposition. Too fast



drying of this layer results in stresses and subsequent cracking. At high temperatures (> optimal value) the deposited spray droplets are almost dry before reaching the substrate. Therefore, discrete particles are formed on the surface due to slow spreading. This increases the surface roughness. If the substrate temperature is still higher the droplet impacting the substrate experiences repulsive thermophoretic force and leads to fly off of the dried droplet and results in either no deposition at all or powdery deposition with zero adhesion with the substrate.

At the optimal value of substrate temperature only, the solvent in the droplet evaporates completely at the surface of the substrate and the deposit material lands on substrate. Consequently, the landed particle undergoes the nucleation and growth, which leads to formation of thin film.

The determination of substrate temperature is one of the crucial terms in spray pyrolysis technique. Generally, the substrate temperature is kept at the decomposition temperature of salt used, which can be determined from Thermo gravimetric analysis plots. These plots also provide information about the temperature of phase formation which is useful for determining that the further heat treatment is necessary or not. However, substrate to nozzle distance, solution flow rate, solution concentration, etc. adds some correction factor in setting of the substrate temperature. For less substrate to nozzle distance than the optimum the length of flight of aerosol is insufficient to undergo the pyrolytic decomposition and may lead to spitting of the solvent on the substrate. On the other hand if the distance is too far the aerosol transported evaporates before reaching to the substrate and hence leads to powdery deposition. For higher solution flow rate, sizes of droplet is found to be larger which then affect the rate of evaporation during aerosol transport and leads to splat formation on the substrate. However, if the solutions flow rate is too small the droplets evaporate before reaching the substrate and leads to powdery deposition. Solution concentration affects the rate of precipitation during the aerosol transport.

#### 3.3.4.3. Solution flow rate

Generally the precursor solution flow rate has a minor effect on the film morphology. It may not exceed a certain value, at which film cracking can occur. The maximum value again depends on the type of atomizer, deposition temperature, nozzle to substrate distance, etc.





For example, for air-blast type of atomizer solution flow rate may range from 30 ml/h to 120 ml/h, while in case of electrostatic atomizer it could be as less as 1ml/h to 8ml/h.

#### *3.3.4.4. Nozzle to substrate distance*

Each nozzle has a spraying angle (solid cone). Therefore, the nozzle to substrate distance determines the area coated and the deposition rate. The smaller distance of the atomizer to the substrate, the higher the deposition rate and the smaller the coated area. However, every experimental spray pyrolysis setup has an upper and lower limit for the distance to the substrate determined mainly by the type of atomizer and the substrate size.

For example,

In the electrostatic deposition setup, where a precursor solution is atomized using high voltage, the lower distance limit is determined by the substrate size. The upper limit is influenced mainly by the maximum voltage which is determined by the characteristics of the high voltage power supply unit.

However in the air-blast deposition setup, where the precursor solution is atomized using an air stream, the minimal nozzle to substrate distance is limited by the cooling effect of the air flow. At small distances pronounced cooling of the substrate occurs and also requires more heat from the heating plate, because the droplet mass flow density increases with decreasing distance. Consequently, at a critical distance of spray nozzle to substrate surface it will be impossible to reach the optimal deposition temperature. The upper limit is determined by the distance at which the spray pattern collapses. Generally, the maximum distance depends on spray nozzle parameters such as the geometry of atomizer and air pressure.

#### *3.3.4.5. Solvent*

By changing the solvent, physical properties of the solution such as boiling point, solubility of salts, spreading behavior of droplets on the substrate can be controlled. Therefore, the type of solvent influences not only the maximum salt concentration, but also the deposition temperature, the optimal solution flow rate, and as a consequence the deposition rate. Chen et al. reported that it is necessary to use a



solvent with a high boiling point in order to deposit a dense film [50]. Since it is obvious that with precursor solution having higher boiling point requires higher (substrate) temperature to get evaporates at the surface of the substrate.

#### 3.3.4.6. Deposition time

It is generally observed that the film thickness increases with increase in deposition time up to critical thickness and then it suddenly drop down. The critical limit for the deposition of a material depends upon the sticking coefficient of the substrate and deposit. When the critical thickness is achieved the further growth of film is not possible and if forced to do so the further impacting of the droplets may remove the deposited material from the substrate. This process consequently results in sudden drop down of thickness of the film.

It is also noticeable that with increase in deposition time the morphology of the films gets modified. E.g. in electrostatic deposition setup, film's surface morphology changes from grains incorporated in films to fractal surfaces, while in case of air-blast deposition setup no remarkable changes in the surface morphology of the films were observed [48].

#### 3.3.4.7. Additives

It has been shown that the morphology of a film can be tailored using additives in the precursor solution [51, 52]. Perednis [48] reported effect of additive polyethylene glycol (PEG) to modify the properties of the precursor solutions for yttrium-stabilized zirconia (YSZ) thin film deposition. After addition of PEG, YSZ thin films showed lower surface roughness implying that the polymer improves the spreading behavior of the droplets on the substrate which demonstrate a significant role of additives on the microstructure of the films.

#### 3.3.5. General scheme of optimization of spray parameters

From above discussion it is clear that for the optimization of spray parameter one cannot vary all the parameter simultaneously. Even keeping one parameter constant varying the other is still tough task for the optimization of spray parameters.



Since these spray parameters are inter-related, one can set the default parameter for particular setup and vary few spray parameters.

Here the general scheme for the optimization of preparative parameter for air-blast spray pyrolysis technique is given. Initially fix the default spray parameter such as atomizing unit (nozzle), nozzle to substrate distance, etc. As the substrate temperature is an important spray parameter it should be initially determined from the TGA plots of the precursor salt of interest. At this substrate temperature, concentration of solution is then optimized by trial and error method. These experiments give the optimized substrate temperature and solution concentration.

If the expected system is some other phase doped into host material, the optimization of substrate temperature and concentration of solution is to be repeated again to see the effect on the doped phase. However in this step the variation in the parameter must be in the vicinity of the earlier optimized parameter for the host material. This further optimization is necessary since the dopant phase act as additive to host precursor solution. As discussed in earlier section of ‘additives’, the additive affect more than three spray parameters by changing the physical properties of precursor solution.

If the TGA-DTA plots showed any phase formation temperature which is at higher than that of the decomposition temperature of the precursor salt used, the post heat treatment at that of higher temperature is necessary to form the phase. If the depositions were taken at temperature lower than that of the decomposition temperature there is strong possibility of entrapped solvent. If such films are heat treated at further higher temperature, the film may turn in to cracked films after heating which were appearing dense and smooth at the stage of as deposited.

### **3.4. Characterization techniques**

#### **3.4.1. Density measurements**

The density measurement is carried out in this study to determine the extent of porosity in prepared samples. The study is mandatory in characterization of bulk samples prepared by solid state reaction, since the porosity is one which obviously occurs in solid state synthesized samples counting toward its disadvantage. The extent of porosity can be evaluated in its reverse term i.e. by determining the relative



density. The relative density of the prepared samples is the ratio of measured density to its theoretical density. The theoretical density is calculated using the formula given as, (for  $A_{1-x}B_xO_{2-x/2}$  cubic system)

$$d_{th} = \frac{4}{N_A a^3} \left[ (1-x)M_A + x \cdot M_B + \left( 2 - \frac{1}{2} \cdot x \right) M_O \right] \quad (3.4)$$

Where, ' $d_{th}$ ' is the theoretical density,

' $x$ ' the (in our case gadolinium) B content,

' $a$ ' the lattice constant at room temperature of  $A_{1-x}B_xO_{2-x/2}$  system,

$N_A$  the Avogadro number, and

$M_{A, B, O}$  refers to respective atomic weights.

But, when density of porous materials is to be determined then the simple relation i.e. mass/volume could not give the exact result. There are few other methods which can be used to determine the density of porous materials and one of them is using Archimedes principle. In this study Archimedes principle is implemented to determine density of samples as it is simple and easy to perform with simple calculations. In this method the sample whose density to be determined is immersed in a fluid with known density (e.g. Water, density = 1gm/cc). The weight of sample when immersed in fluid (water) and in air is determined (figure 13). The measured weight then kept in following formula to estimate the density of sample,

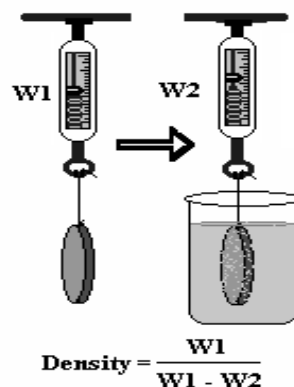


Figure 13. Schematic presentation of Archimedes principle to determine the density of samples.



$$\text{Density of sample } (\rho_s) = \frac{\text{Weight in air } (W_1)}{\text{Weight in air } (W_1) - \text{Weight when immersed in fluid } (W_2)}$$

Or symbolically it can be written as,

$$\rho_s = \frac{W_1}{W_1 - W_2} \quad (3.5)$$

- **The derivation of relation,**  $\rho_s = W_1 / (W_1 - W_2)$

The Archimedes principle states that body immersed in a fluid is buoyed up by a force equal to the weight of the displaced fluid. This principle applies to both floating and submerged bodies and to all fluids. This method is well suited for porous samples even.

Density is defined as the ratio of mass to the volume,

$$\rho = \frac{W/g}{V} \quad (3.5a)$$

Where, 'g' is gravitational constant,  $9.8 \text{ m/s}^2$ ,

'W' the weight of sample and

'V' the volume of sample

Let us consider  $W_1$  and  $V_1$  are the weight in air and volume of the sample whose density to be calculated. When specimen is immersed in the fluid its weight reduces to by an amount  $\Delta W = W_1 - W_2$  (say). Where,  $W_2$  is weight of specimen in fluid. Now, according to Archimedes principle, buoying force exerted due to fluid on specimen causes reduction in weight of specimen by  $\Delta W$ . Consider  $\rho_f$  is density of fluid,  $\Delta W$  the weight of displaced fluid and  $V_2$  is volume of displaced fluid, then

$$\rho_s = \frac{W_1/g}{V_1} \text{ and} \quad (3.5b)$$

$$\rho_f = \frac{\Delta W/g}{V_2} \quad (3.5c)$$



where  $\rho_s$  is density of sample.

Since, volume of sample in air is equal to volume of fluid displaced,  $V_1 = V_2$  therefore,

$$\frac{W_1/g}{\rho_s} = \frac{\Delta W/g}{\rho_f} \quad (3.5d)$$

canceling out the 'g' from both sides we get,

$$\frac{W_1}{\rho_s} = \frac{\Delta W}{\rho_f} \quad (3.5e)$$

$$\rho_s = (W_1/\Delta W) \cdot \rho_f \quad (3.5f)$$

$$\rho_s = (W_1/(W_1 - W_2)) \cdot \rho_f \quad (3.5g)$$

For water as fluid,  $\rho_f =$  density of water = 1 gm/cc, then relation becomes,

$$\rho_s = W_1/(W_1 - W_2) \quad (3.5h)$$

where, ' $\rho_s$ ' is the density of sample in gm/cc, ' $W_1$ ' the weight of sample in air (in gm) and ' $W_2$ ' the weight of sample in water (in gm).

### 3.4.2. Thickness and surface roughness measurements

Film thickness is an important parameter in the study of the film properties. Amongst different methods for measuring the film thickness, we employed AMBIOS make XP-1 surface profiler. This method also reveals surface roughness of films in addition to the thickness of films. To determine the thickness of the film, it is mandatory to prepare a step between the substrate and films.

Surface profiler consists of a stylus attached to an electric sensor. This stylus is allowed to move over a surface of which the roughness and thickness is to be



determined. While moving the stylus over a surface its vertical position, which is already been calibrated, sends the signal to sensor corresponding to its relative ups and downs (figure 14). This data is then further manipulated by in-built software to real world units i.e. in nm or microns. Exactly the same principle can be employed to determine the thickness of the films, provided that a step must be kept between film and substrate. When the stylus moves across this step it counts for comparatively large jump. This movement is repeated number time to obtain the consistent values, which were then averaged to determine the thickness of the film.

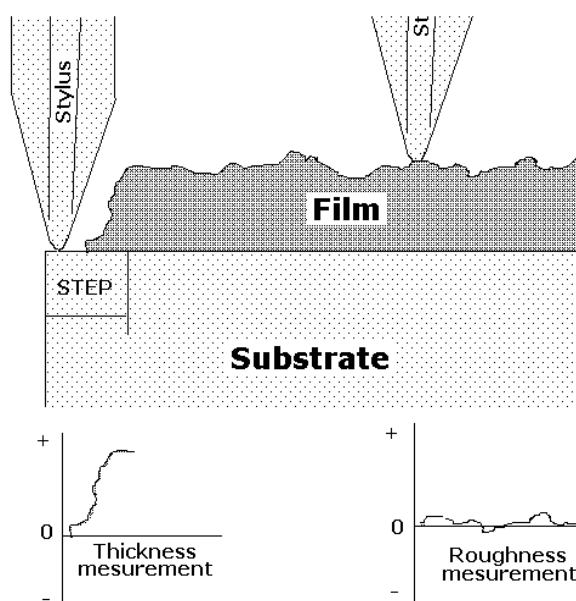


Figure 14. Determination of thickness and surface roughness using surface profiler.

### 3.4.3. Thermal analysis

Thermal analysis is carried out to determine physical or chemical changes in a system under investigation, as a function of temperature (in different gases also – figure 15). Two common complimentary techniques in this category are differential scanning calorimetry (DSC) and thermo-gravimetric analysis (TGA). These methods are typically used to determine the material properties of organic polymers as the sample is heated or cooled in a controlled manner or held isothermally for a specified time. Differential thermal analysis (DTA) is a method similar to DSC, but performed at higher temperatures for metals, minerals, ceramics, and glasses [53].



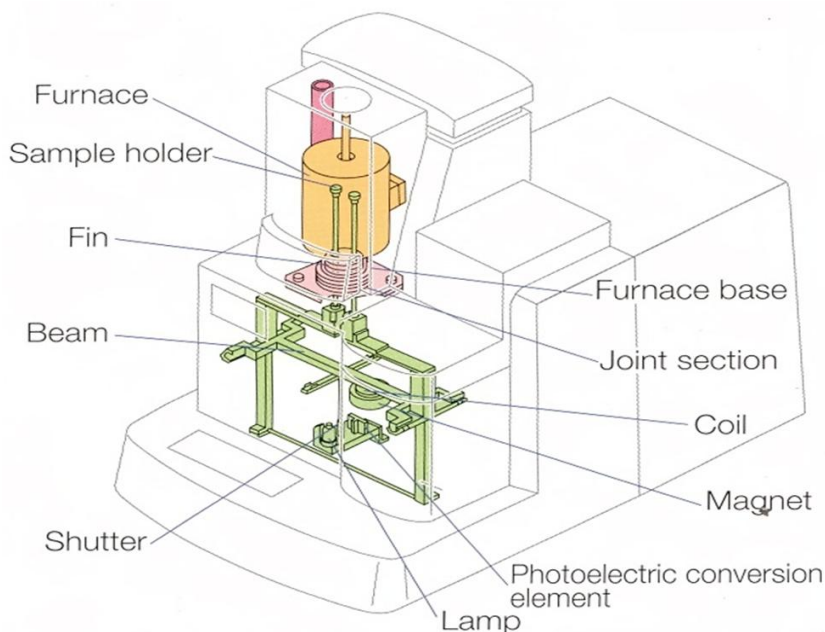


Figure 15. Schematic illustration of TG-DTA experimental assembly.

#### 3.4.3.1. Differential scanning calorimetry (DSC) –

Differential scanning calorimetry measures heat flow to or from a sample as a function of temperature and time. A small portion of a sample is placed in an aluminum pan and heated and/or cooled in a controlled manner. A reference material (usually an empty aluminum pan) simultaneously undergoes the same programmed time/temperature routine. Calorimetric measurements are made during the heating/cooling cycle.

Two methods can be used for the calorimetric measurements.

- i. Differences in temperature between the sample and reference material can be measured as the same amount of heat energy (calories) is added to both or
- ii. Differences in the amount of heat energy added to both are measured as the temperature for both the sample and reference are kept constant.

In both cases, the heat flow and temperature of the sample are monitored in comparison to the reference material. The analysis is usually performed in an inert gas atmosphere, such as nitrogen. The amount of energy absorbed (endotherm) or evolved (exotherm) as the sample undergoes physical or chemical changes (e.g. melting, crystallization, curing) is measured in calories as a function of the temperature change. Any material reactions involving changes in heat capacity (e.g. glass transition) can also be detected.





The thermal cycle for DSC typically can range from less than 50°C to 300°C or greater. The principles for differential thermal analysis (DTA) are similar to DSC, but the temperature range for DTA can reach temperatures greater than 1500°C.

#### *3.4.3.2. Differential thermal analysis (DTA) –*

DTA involves heating or cooling a test sample and an inert reference under identical conditions, while recording any temperature difference between the sample and reference. This differential temperature is then plotted against time, or against temperature. Changes in the sample which lead to the absorption or evolution of heat can be detected relative to the inert reference. Differential temperatures can also arise between two inert samples when their response to the applied heat treatment is not identical. DTA can therefore be used to study thermal properties and phase changes. A DTA may be defined formally as a technique for recording the difference in temperature between a substance and a reference material against either time or temperature as the two specimens are subjected to identical temperature regimes in an environment heated or cooled at a controlled rate.

#### *3.4.3.3. Thermo-gravimetric analysis (TGA)*

TGA continuously measures the weight of a sample as a function of temperature and time. The sample is placed in a small pan connected to a microbalance and heated in a controlled manner and/or held isothermally for a specified time. The atmosphere around the sample may consist of an inert gas, such as nitrogen, or a reactive gas, such as air or oxygen. The heating program may start in an inert atmosphere and then be switched to air at a certain point to complete the analysis. Weight changes observed at specific temperatures correlate to evaporation of sample components, decomposition, oxidation/reduction reactions, or other reactions or changes. Fourier transform infrared spectroscopy (FTIR) or mass spectroscopy (MS) may be used in conjunction with TGA to analyze and identify the evolved gases from constituents evaporated from the sample at specific temperatures.



#### 3.4.3.4. Applications of thermal analysis

DSC is ideal for studying reversible reactions of thermoplastics such as melting-crystallization points and glass transition temperature. It is also used in the study of purity, heat capacities, and the effects of additives. Similarly, DTA analysis is used for determining the temperatures for melting and solid state phase transformations in metals, minerals, and ceramics. However, as TGA instrument measures the temperature and weight of the sample, thermally activated events can be recorded. These events are expressed as weight loss or weight change for a given time or temperature (i.e. it may also be expressed as a rate of weight loss). The onset temperature for the weight loss is also recorded. These data is correlated and information about properties like thermal stability, moisture or solvent content, additive or filler content, oxidation or decomposition temperatures and its rate etc. can be deduced.

Thermal events such as melting, glass transition, and other changes in TGA are not detected because there is no change in sample mass associated with these events. Identification of the constituents driven off as evolved gases may be obtained when the TGA is used in conjunction with FTIR or mass spectroscopy. The main applications of TGA include the measurement of thermal stability, ageing characteristics, decomposition, reactivity and the structures of compounds. It has obvious uses in the determination of the moisture content of powders, water of hydration and of carbon monoxide and carbon dioxide evolution from carbonates etc. Decomposition reactions can be studied in a variety of imposed environments to yield information on the reduction of metal ores. In organic chemistry the technique has been widely used to study the degradation of polymers and to investigate the pyrolysis of coals. TG can also be used to record isothermal and isobaric weight changes.

#### 3.4.4. X-ray Diffraction

##### 3.4.4.1. X-Ray Diffraction Theory

An electron in an alternating electromagnetic field will oscillate with the same frequency as the field. When an X-ray beam hits an atom, the electrons around the atom start to oscillate with the same frequency as the incoming beam. In almost all



directions we will have destructive interference, that is, the combining waves are out of phase and there is no resultant energy leaving the solid sample. However the atoms in a crystal are arranged in a regular pattern, and in a very few directions we will have constructive interference. The waves will be in phase and there will be well defined X-ray beams leaving the sample at various directions. Hence, a diffracted beam may be described as a beam composed of a large number of scattered rays mutually reinforcing one another.

Let us consider an X-ray beam incident on a pair of parallel planes P1 and P2, separated by an inter-planar spacing  $d$  (figure 16). The two parallel incident rays  $I$  and  $2$  make an angle ' $\theta$ ' with these planes. A reflected beam of maximum intensity will result if the waves represented by  $I'$  and  $2'$  are in phase, the path difference between  $I$  to  $I'$  and  $2$  to  $2'$  must then be an integral number of wavelengths, ' $\lambda$ '. We can express this relationship mathematically in Bragg's law.

$$2d \sin \theta = n\lambda \quad (3.6a)$$

Diffraction occurs from planes set at angle ' $\theta$ ' with respect to the incident beam and generates a reflected beam at an angle ' $2\theta$ ' from the incident beam. Rewriting Bragg's law we get

$$\sin \theta = \lambda/2d, \text{ for } n = 1. \quad (3.6b)$$

Therefore the possible ' $2\theta$ ' values where we can have diffraction are determined by the unit cell dimensions. However, the intensities of the reflections are determined by the distribution of the electrons in the unit cell. The highest electron densities are found around atoms. Therefore, the intensities depend on what kind of atoms we have and where in the unit cell they are located. Planes going through areas with high electron density will reflect strongly, planes with low electron density will give weak intensities.

A typical diffraction spectrum consists of a plot of reflected intensities versus the detector angle ' $2\theta$ '. The ' $2\theta$ ' values for the peak depend on the wavelength of the anode material of the X-ray tube. It is therefore customary to reduce a peak position to the inter-planar spacing  $d$  that corresponds to the  $h, k, l$  planes that caused the



reflection. The values of the  $d$ -spacing depend only on the shape of the unit cell. We get the  $d$ -spacing as a function of ' $2\theta$ ' from Bragg's law.

$$d = (\lambda/2)\sin \theta. \quad (3.6c)$$

Each reflection is fully defined when we know the  $d$ -spacing, the intensity (area under the peak) and the indices  $h, k, l$ . If we know the  $d$ -spacing and the corresponding indices  $h, k, l$  we can calculate the dimension of the unit cell.

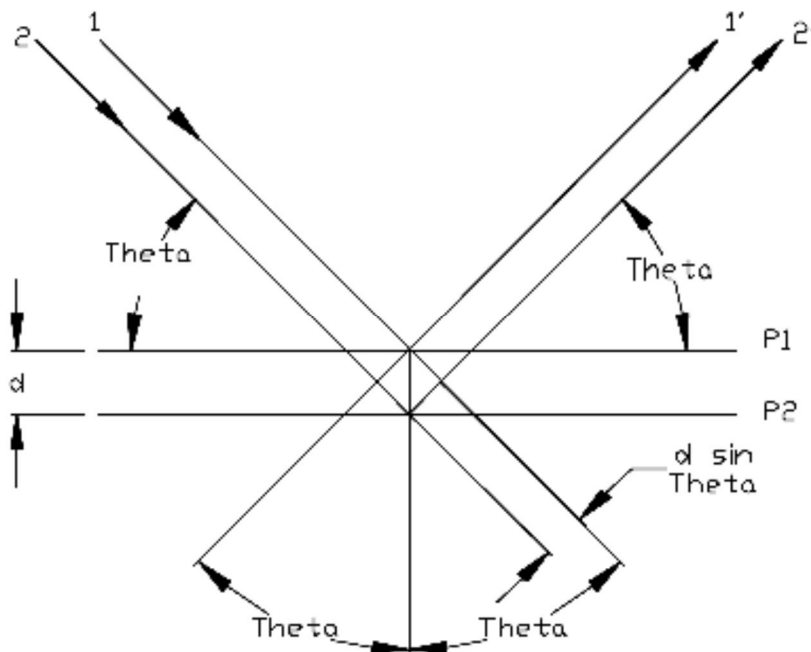


Figure 16. Ray diagram of X-ray diffraction at crystal planes.

#### 3.4.4.2. Standard Diffraction Pattern Database

International Center Diffraction Data (ICDD) or formerly known as (JCPDS) Joint Committee on Powder Diffraction Standards is the organization that maintains the database of inorganic and organic spectra. The database is available from the Diffraction equipment manufacturers or from ICDD. Currently the database is supplied either on magnetic or optical media. Two database versions are available are the PDF I and the PDF II. The PDF I database contains information on  $d$ -spacing,



chemical formula, relative intensity, quality information and routing digit. The PDF II database contains full information on a particular phase including cell parameters. The data base format consists of a set number and a sequence number. The set number is incremented every calendar year and the sequence number starts from 1 for every year. The yearly releases of the data base are available in September of each year.

#### *3.4.4.3. Applications of X-ray diffraction*

The most common use of powder (polycrystalline) diffraction is in chemical analysis. This can include phase identification (search/match), investigation of high/low temperature phases of solid solutions and determinations of unit cell parameters of new materials. Other than identification of solids, XRD can be used to determine polymer crystallinity, residual stress, texture analysis, etc.

#### *3.4.5. Scanning electron microscopy and Energy dispersive x-ray spectroscopy*

##### *3.4.5.1. Introduction*

Scanning electron microscopy (SEM) is a method for high-resolution imaging of surfaces. The SEM uses electrons for imaging, much as a light microscope uses visible light. The advantages of SEM over light microscopy include much higher magnification (>100,000X) and greater depth of field up to 100 times that of light microscopy. Qualitative and quantitative chemical analysis information is also obtained using an energy dispersive x-ray spectrometer (EDS) unit which is an attached assembly with SEM.

##### *3.4.5.2. Scanning electron microscopy (SEM)*

In SEM (figure 17), an electron gun generates a beam of electrons above the sample chamber. The electrons are produced by a thermal emission source, such as a heated tungsten filament, or by a field emission cathode. The energy of the incident electrons can be as low as 100eV or as high as 30KeV depending on the evaluation objectives. The electrons are focused into a small beam by a series of electromagnetic lenses in the SEM column. Scanning coils at the end of the column direct and position



the focused beam onto the sample surface. The electron beam is scanned in a raster pattern over the surface for imaging.

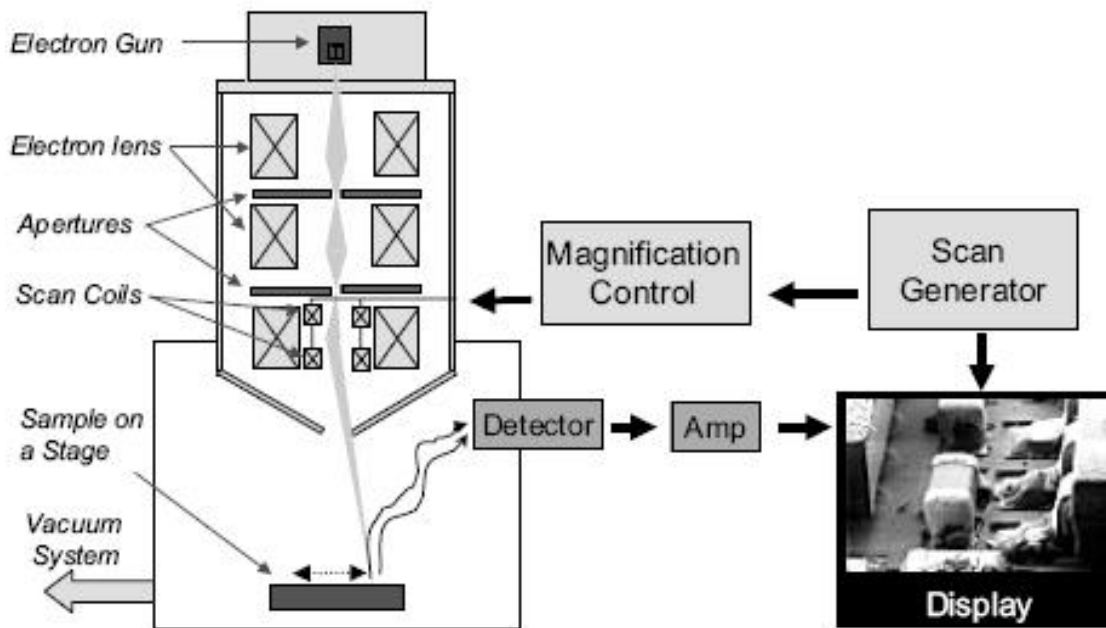


Figure 17. Schematic of scanning electron microscope.

The incident electrons cause electrons to be emitted from the sample due to elastic and/or inelastic scattering events within the sample's surface and near-surface material. Electrons that are ejected by an elastic collision of an incident electron, typically with a sample atom's nucleus, are referred to as backscattered electrons. The energy of backscattered electrons will be comparable to that of the incident electrons. Emitted lower-energy electrons resulting from inelastic scattering are called secondary electrons which formed by collisions with the nucleus where substantial energy loss occurs or by the ejection of loosely bound electrons from the sample atoms. The energy of secondary electrons is typically 50eV or less.

To create an SEM image, the incident electron beam is scanned in a raster pattern across the sample's surface and then emitted electrons are detected for each position in the scanned area by an electron detector. The intensity of the emitted electron signal is displayed as brightness on a cathode ray tube (CRT i.e. display screen).



The SEM column and sample chamber are at a moderate vacuum to allow the electrons to travel freely from the electron beam source to the sample and then to the detectors. High-resolution imaging is done with the chamber at higher vacuum, typically from  $10^{-5}$  to  $10^{-7}$  Torr. Imaging of nonconductive, volatile, and vacuum-sensitive samples can be performed at higher pressures.

#### *3.4.5.3. Energy Dispersive X-Ray Spectroscopy (EDS or EDX)*

EDS or EDX is a chemical microanalysis technique used in conjunction with scanning electron microscopy (SEM). The EDS technique detects x-rays emitted from the sample during bombardment by an electron beam to characterize the elemental composition of the analyzed volume. Features or phases as small as  $1\mu\text{m}$  or less can be analyzed.

Bombardment of electrons on the surface of sample leads to electrons to eject from atoms comprising the sample's surface. The resulting electron vacancies are filled by electrons from a higher state, and an x-ray is emitted to balance the energy difference between the two electrons' states. The x-ray energy is characteristic of the element from which it was emitted.

X-ray detector in EDS measures the relative abundance of emitted x-rays versus their energy. When an incident x-ray strikes the detector, it creates a charge pulse, which is then converted to a voltage pulse by a charge-sensitive preamplifier. The energy, as determined from the voltage measurement, for each incident x-ray is sent to a computer. The computer is then used to store the data for its analysis. The spectrum of x-ray energy versus counts is evaluated to determine the elemental composition of the sampled volume.

The sample x-ray energy values from the EDS spectrum are compared with known characteristic x-ray energy values to determine the presence of an element in the sample. Elements with atomic numbers ranging from that of beryllium to uranium can be detected.



### 3.4.6. Atomic Force Microscopy (AFM)

#### 3.4.6.1. Introduction

As name of this characterization technique suggests that it does microscopy of sample surface using interactions between atomic forces of probing tip and that of sample surface. In AFM, a small probe scans the sample to obtain information about the sample's surface. The information gathered from the probe's interaction with the surface can be as simple as physical topography or as diverse as measurements of the material's physical, magnetic, or chemical properties. These data are collected as the probe is scanned in a raster pattern across the sample. Thus, the AFM microscopic image shows the variation in the measured property, e.g., height or magnetic domains, over the area scanned.

The AFM probe is a small cantilever beam with a very sharp tip ( $< 100\text{\AA}$  in diameter) at one end. The probe is attached to a piezoelectric scanner tube, which scans the probe across a selected area of the sample surface. Inter-atomic forces between the probe tip and the sample surface cause the cantilever to deflect as the sample's surface topography (or other properties) changes. A laser light reflected from the back of the cantilever measures the deflection of the cantilever (figure 18). This information is fed back to a computer, which generates a map of topography and/or other properties of interest. Areas as large as about  $100\mu\text{m}^2$  to less than  $10\text{nm}^2$  can be scanned using AFM.

#### 3.4.6.2. Modes of AFM

AFM operated in 2 modes, namely contact mode and tapping mode. In contact mode AFM, the AFM-probe is scanned at a constant force between the probe and the sample surface to obtain a 3D topographical map, while in intermittent contact (i.e. tapping) mode AFM, the probe cantilever is oscillated at or near its resonant frequency.

- In contact mode AFM, when probe cantilever is deflected by topographical changes, the scanner adjusts the probe position to restore the original





cantilever deflection. Lateral resolution of  $< 1\text{nm}$  and height resolution of  $< 1\text{\AA}$  can be obtained in contact mode AFM.

- However, in tapping mode AFM, the oscillating probe tip is scanned at a height where it barely touches or “taps” the sample surface. The system monitors the probe position and vibrational amplitude to obtain topographical and other property information. Accurate topographical information can be obtained even for very fragile surfaces. Optimum resolution is about  $50\text{\AA}$  lateral and  $< 1\text{\AA}$  height. Images for phase detection mode, magnetic domains, and local electric fields are also obtained in this mode.

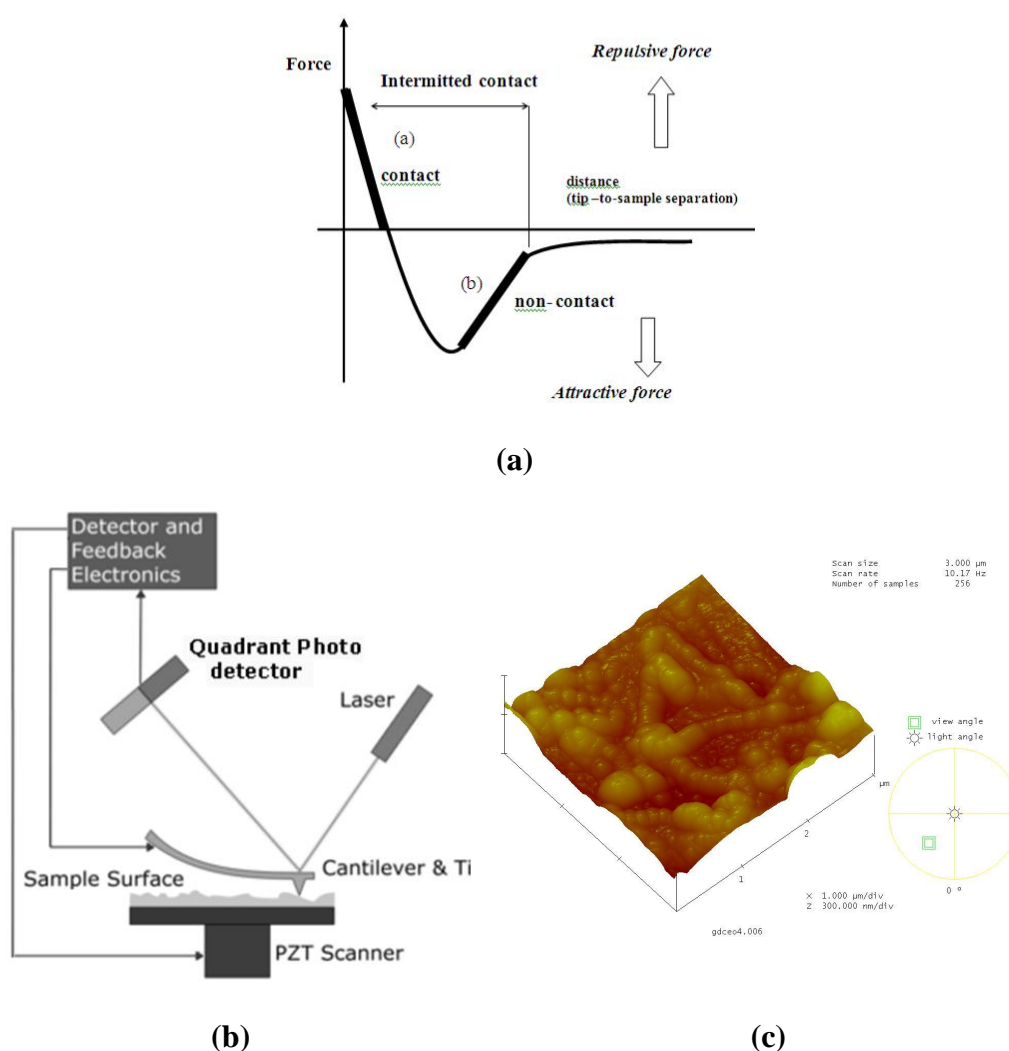


Figure 18. (a) Inter-atomic force versus the distance curve for the operation of the AFM. (b) Schematic diagram of atomic force microscope (AFM) and (c) Typical topography obtained by AFM for 10%Gd doped ceria thin films (this work).



### 3.4.6.3. Microscopy with AFM

Other than topographical microcopies, AFM can be used to study other microcopies such as

- *Lateral Force Microscopy*

This mode measures the lateral deflection of the probe cantilever as the tip is scanned across the sample in contact mode. Changes in lateral deflection represent relative frictional forces between the probe tip and the sample surface. This kind of microscopy is useful to determining the clear appearance of grain boundaries in the sample surface.

- *Phase Detection Microscopy*

With the system operating in tapping mode, the cantilever oscillation is damped by interaction with the sample surface. The phase lag between the drive signal and actual cantilever oscillation is monitored. Changes in the phase lag indicate variations in the surface properties, such as visco-elasticity or mechanical properties. A phase image, typically collected simultaneously with a topographical image, maps the local changes in material's physical or mechanical properties.

- *Magnetic Force Microscopy*

This mode maps local variations in the magnetic forces at the sample's surface. The probe tip is coated with a thin film of ferromagnetic material that will react to the magnetic domains on the sample surface. The magnetic forces between the tip and the sample are measured by monitoring cantilever deflection while the probe is scanned at a constant height above the surface. A map of the forces shows the sample's natural or applied magnetic domain structure.



#### *3.4.6.4. AFM image analysis*

Since the images are collected in digital format, a wide variety of image manipulations are available for AFM data. Quantitative topographical information, such as lateral spacing, step height, and surface roughness are readily obtained. Images can be presented as two-dimensional or three-dimensional representations in hard copy or as digital image files for electronic transfer and publication.

#### *3.4.7. Electrical characterizations*

##### *3.4.7.1. Introduction*

The polycrystalline material consists of grains and grain boundaries. The electrical characteristic of such materials strongly depend upon the micro-structural properties. The electrical characterization of ceramics developed by solid state reaction generally gives the idea of polycrystalline nature of the samples. Similarly this can be extended to thin films prepared using spray pyrolysis technique. The overall electrical conductivity is measured using dc conductivity measurement. Since, the grain boundaries act as a source of resistance, in early 60's Guiland [54] concluded that the resistance of the material mainly arises from grain boundaries and they act as a source of impurities and usually preferred site of inclusions. But now-a-days the sophisticated instrumentation is able to separate out the grain and grain boundary contributions from total electrical conductivity. The ac conductivity measurement through impedance spectroscopy enables us to separate out the contribution in conductivity from grains and grain boundaries.

##### *3.4.7.2. dc conductivity measurements*

In general, the electrical resistivity of oxides is extremely sensitive to its purity and perfection of the crystal. In all cases, the electrical resistivity is very high at low temperatures and decreases rapidly as the temperature is raised, usually in an exponential trend. This type of variation can be due either to ionic conduction or due to electronic semi-conduction. dc conductivity measurements enable us to determine the total conductivity of the samples under investigation originating from grain, grain



boundaries and electrode process. In contrast to ac conductivity measurements (impedance spectroscopy – explained in next section) it could not be able to separate out the contributions from above mentioned origins, however, it provides comparatively easier and quicker way to determine the electrical property of samples. Apart from its simplicity, it does not require state-of-art instruments. In dc measurements, the sample is biased by dc power supply and the variation in current ( $I$ ) is measured (for a fixed voltage ( $V$ )) as the temperature of sample under investigation is changed (figure 19).

The resistance ( $R = V/I$ ) of sample measured as function of temperature is used to calculate resistivity values. Resistivity, ' $\rho$ ' is calculated using simple relation given as,

$$\rho = R \cdot A / l \quad (3.7a)$$

Where, ' $R$ ' is resistance of sample,

' $A$ ' the cross sectional area through which the current passes through and ' $l$ ' the length of path current through the sample.

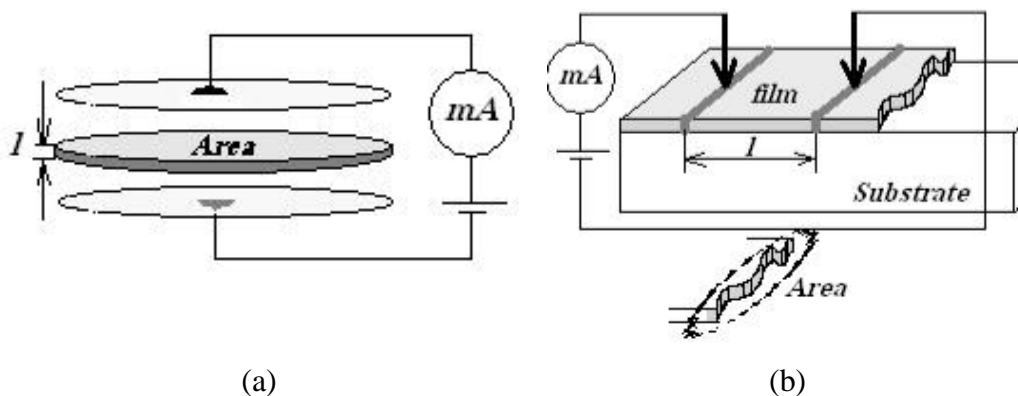


Figure 19. Schematic showing the parameters ' $R$ ', ' $A$ ' and ' $l$ ' used in calculation of ' $\rho$ ' in the case of (a) bulk and (b) thin film samples.

From obtained resistivity values one can determine conductivity by taking its reciprocal,



$$\sigma = 1/\rho \quad (3.7b)$$

The dc conductivity can be represented as Arrhenius relation and is given by,

$$\sigma = \sigma_0 \exp(-E_a / KT) \quad (3.8a)$$

Where, ' $E_a$ ' is the activation energy for conduction,

' $T$ ' the absolute temperature,

' $K$ ' the Boltzmann constant and

' $\sigma_0$ ' the pre-exponential factor.

This can be modified further to obtain activation energy for the conduction.

However, the category of oxides which shows ionic conduction presents rather different behavior from standard Arrhenius relation. These oxides follow the modified Arrhenius relation which governs the thermally activated conduction, where the conductivity is observed to be the function of temperature. To consider the temperature dependence conductivity, above standard Arrhenius relation is modified as,

$$\sigma = (\sigma_0 / T) \exp(-E_a / KT) \quad (3.8b)$$

for thermally activated conduction. This can be again modified to obtain the ' $E_a$ ' for the observed process in dc conductivity.

#### *3.4.7.3. ac conductivity measurements using impedance spectroscopy*

##### ▪ *Introduction*

Impedance spectroscopy is a powerful method to characterize the electrical properties of materials and interfaces [55]. In case of a polycrystalline electrolyte, the electrolyte resistance comprises bulk and grain boundary contributions, and the electrode resistances may be caused by bulk as well as interfacial effects. In a conventional, stationary two-electrode dc measurement, one only obtains the overall



sample resistance, i.e. the sum over all these individual processes. In a four-electrode arrangement, the use of different electrodes for current supply and voltage measurement can eliminate the influence of the electrodes. More detailed information on the electrical properties of a system is generally provided by a frequency dependent measurement of the ac resistance. In an impedance spectroscopy experiment, a small, alternating electrical signal is applied to the sample, and its response (the resulting current or voltage) is measured. By varying the frequency,  $\omega$ , over several orders of magnitude, one can in many cases distinguish individual resistive processes due to differences in their relaxation times. The time required for a polarized region to equilibrate after an electrical perturbation is characteristic for the specific electrochemical process. If the relaxation times (or frequencies) of two processes are sufficiently different they can be separately measured by impedance spectroscopy. The condition is often fulfilled in solid state electrochemistry, since the relevant characteristic relaxation times (e.g. for electrode processes as compared to transport across grain boundaries) typically differ by several orders of magnitude. Even if a separation is initially not possible, one can often shift the relaxation frequencies in a favorable way by varying the experimental conditions.

Since, impedance analysis of linear circuits is much easier than analysis of non-linear circuits. Therefore, ac impedance is normally measured with a small excitation signal, as it generates pseudo linear response in current signals. In a linear (or pseudo-linear) system, the current response to a sinusoidal potential will be a sinusoid at the same frequency but shifted in phase (figure 20).

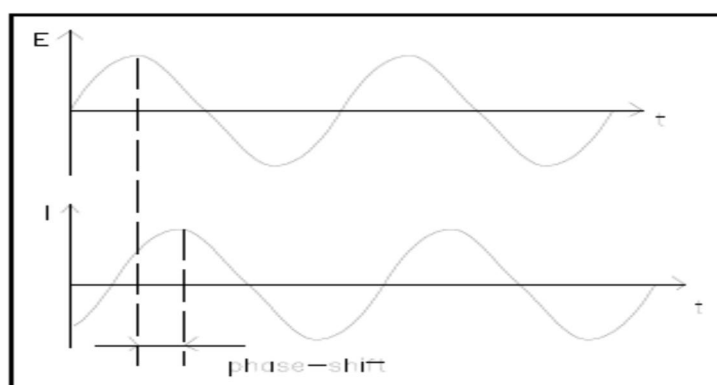


Figure 20. Sinusoidal current response in a linear system.



- Impedance as a complex number

The excitation signal, expressed as a function of time, has the form

$$E_t = E_o \sin(\omega t) \quad (3.9a)$$

where,  $E_t$  is the potential at time  $t$ ,

$E_o$  is the amplitude of the signal, and

$\omega$  is the radial frequency.

The relationship between radial frequency  $\omega$  (expressed in radians/second) and frequency  $f$  (expressed in hertz) is:

$$\omega = 2\pi f \quad (3.9b)$$

In a linear system, the response signal,  $I_t$ , is shifted in phase ( $\phi$ ) and has a different amplitude,  $I_o$ .

$$I_t = I_o \sin(\omega t + \phi) \quad (3.9c)$$

An expression analogous to Ohm's Law allows us to calculate the impedance of the system as

$$Z = \frac{E_t}{I_t} = \frac{E_o \sin(\omega t)}{I_o \sin(\omega t + \phi)} = Z_o \frac{\sin(\omega t)}{\sin(\omega t + \phi)} \quad (3.9d)$$

The impedance is therefore expressed in terms of a magnitude,  $Z_o$ , and a phase shift,  $\phi$ . With Euler's relationship,

$$\exp(j\phi) = \cos \phi + j \sin \phi \quad (3.9e)$$

It is possible to express the impedance as a complex function. The potential is described as,



$$E_t = E_o \exp(j\phi) \quad (3.9f)$$

and the current response as,

$$I_t = I_o \exp(j\phi) \quad (3.9g)$$

The impedance is then represented as a complex number,

$$Z = \frac{E}{I} = Z_o \exp(j\phi) = Z_o (\cos \phi + j \sin \phi) \quad (3.9h)$$

- *Experimental impedance data presentation*

To display experimental impedance data, different kinds of plots based on impedance  $Z$ , admittance  $Z^{-1}$ , modulus  $i\omega Z$  or complex capacitance  $(i\omega Z)^{-1}$  are used. Most common in solid state ionics are representations in the complex impedance plane (imaginary vs. real part of  $Z$ , often referred to as Cole-Cole plot) and Bode-plots ( $\log(Z_{\text{real}})$  or  $\log(Z_{\text{imag}})$  vs.  $\log(\omega)$ ).

- *Nyquist or Cole-Cole plot*

The expression for  $Z(\phi)$  is composed of a real and an imaginary part. If the real part is plotted on the X axis and the negative of imaginary part on the Y axis of a chart, we get a "Nyquist plot". Since in this plot the y-axis is negative and that each point on the Nyquist plot is the impedance at one frequency figure 21. On the Nyquist plot the impedance can be represented as a vector (arrow) of length  $|Z|$ . The angle between this vector and the x-axis is  $\phi (= \arg. Z)$ .





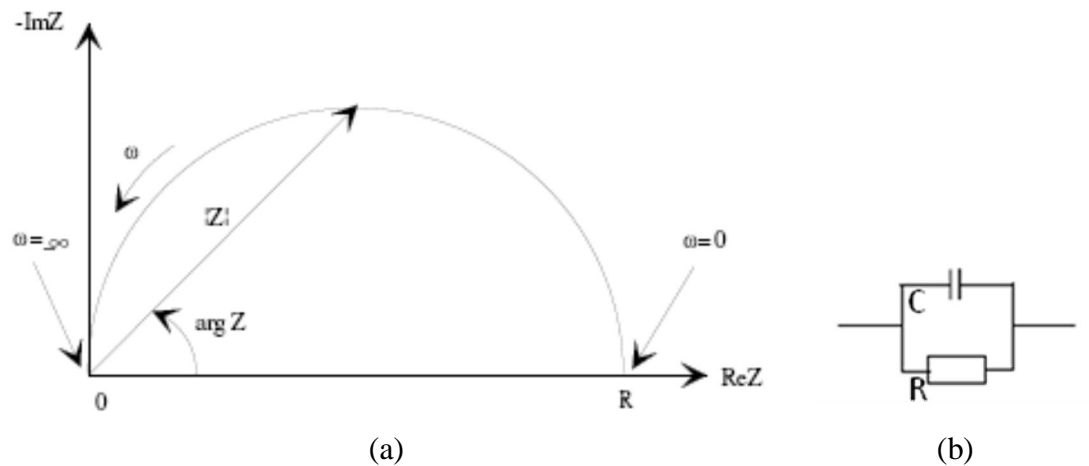


Figure 21. (a) The Nyquist plot in figure results from the electrical circuit (b).

### o Bode-plot

Another popular presentation method of impedance data is the Bode-plot. The impedance is plotted with log frequency on the x-axis and both the absolute values of the impedance ( $|Z|=Z_0$ ) and the phase-shift on the y-axis. The Bode plot for the electric circuit shown in figure 30b is shown in figure 22. Unlike the Nyquist plot, the Bode plot does show frequency information.

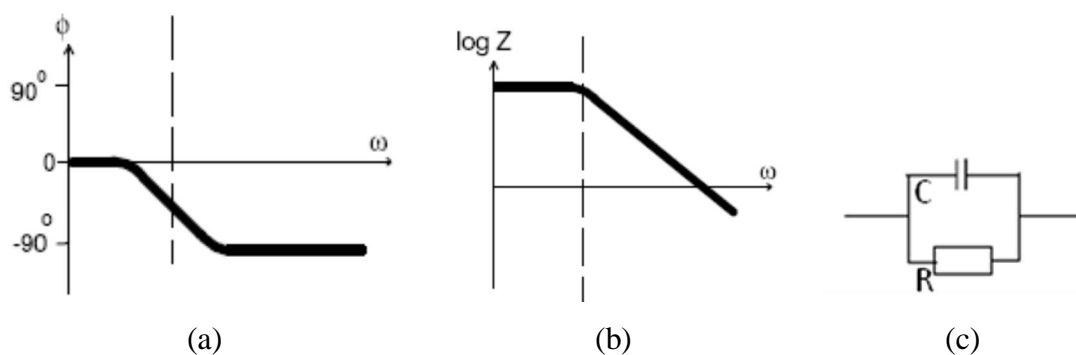


Figure 22. (a) and (b) are bode plots for the electric circuit shown in (c).

### o Interpretations of measured impedance spectra

The interpretation of measured impedance spectra may be simple to extremely difficult, depending on the complexity of the investigated system. The most popular



approach is based on constructing an electrical network representation, a so-called equivalent circuit. Such a network model, which may consist of resistors  $R$ , capacitors  $C$  and other elements, has to approximate the measured  $Z(\omega)$  well over the whole frequency range. The simplest case is a single RC-element, i.e. one resistor and one capacitor in parallel, with impedance

$$\bar{Z}_{ac} = \frac{R}{1 + i\omega RC} \quad (3.10)$$

In the complex impedance plane, such impedance yields a semicircle with diameter  $R$  (figure 23a). It is clear that in the limit  $\omega \rightarrow 0$  the influence of the capacitance has to vanish and the dc resistance  $R$  is obtained. At higher frequencies, the real part of the impedance  $Z_{\text{real}}$  decreases due to the dielectric “opening” of the capacitance (displacement current), whereas the imaginary part  $Z_{\text{imag}}$  (or the phase shift between the currents going through the resistor and the capacitor) increases. The frequency where these two currents are equal and the imaginary part of the impedance reaches its maximum is the relaxation frequency,  $\omega_R$ , of the RC element. It is given by

$$\omega_R = \frac{1}{RC} \quad (3.11)$$

Two serial RC elements lead to two well-separated semicircles in the complex impedance plane if their relaxation frequencies are sufficiently different (figure 23b). Hence, if a measurement yields one or several well-separated semicircles, the resistances and relaxation frequencies of the underlying processes can immediately be read from the Cole-Cole plot, and thus a capacitance can be calculated for each process. The magnitude of a capacitance is often already a strong indication of its physical origin. Typical orders of magnitude of some capacitances in solid state electrochemistry are given in table 2 [56-58].



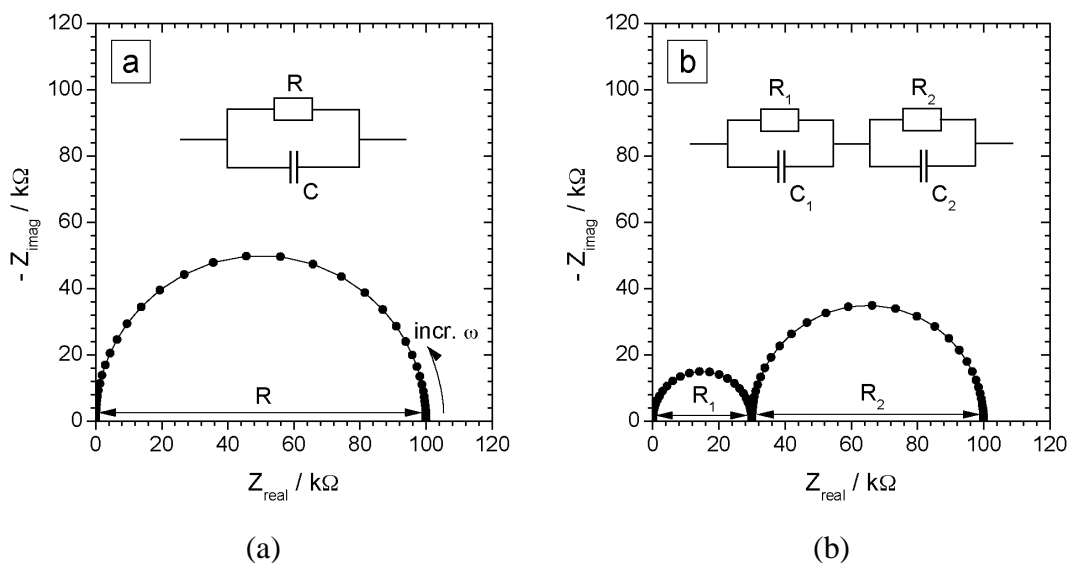


Figure 23. (a) Simulated impedance spectra of one RC-element and (b) two serial RC elements with substantially different relaxation times; parameters:  $R = 100\text{k}\Omega$ ,  $C = 1\mu\text{F}$ ;  $R_1 = 30\text{k}\Omega$ ,  $R_2 = 70\text{k}\Omega$ ,  $C_1 = 1\text{nF}$ ,  $C_2 = 10\mu\text{F}$ ; frequency range:  $10^{-3}$ - $10^6$  Hz.

Capacitance	Corresponding physical process	Typical value per area ( $\text{F}/\text{cm}^2$ )
$C_{\text{bulk}}$	Dielectric relaxation in bulk material	$\sim 10^{-12}$
$C_{\text{gb}}$	Grain boundary polarization in a polycrystalline material	$\sim 10^{-8}$
$C_{\text{dl}}$	Electrical double layer polarization at solid/solid interface	$\sim 10^{-5}$
$C_{\text{chem}}$	Oxygen stoichiometry polarization in the bulk of a mixed conducting thin film electrode	$\sim 10^{-2}$

Table 2. Typical orders of magnitude of some capacitances observed in solid state ionics (100 nm thick film)

In many situations, the required equivalent circuit representation and thus the interpretation of impedance spectra are more complicated. Some of the difficulties frequently encountered when interpreting impedance spectra shall briefly be mentioned in the following:

Obviously, difficulties emerge if two serial processes have similar relaxation frequencies. In such a case the two semicircles overlap, and the resulting impedance



behavior may appear as a single, distorted arc in the complex impedance plane [59]. The decision on whether or not such a distorted semicircle consists of two components is decided by the empirical fact that experimental semicircles are always “non-ideal” to some degree. Apparently, an RC element generally oversimplifies the real situation. A path frequently followed in order to deal with depressed semicircles is to replace the capacitor of an RC element by a so-called constant phase element Q, with impedance

$$\bar{Z}_Q = \frac{1}{Q(i\omega)^n} \quad (3.12)$$

A constant phase element may thus be regarded as a generalization of a capacitance, which takes account of the “non-ideality” of experimentally observed semicircles. The parameter n, a constant defined by above equation, is essentially a measure of the degree of “depression” of such an arc. For n = 1, the constant phase element is identical to a capacitance, corresponding to a perfect semicircle in the Cole-Cole plot. For n < 1, one obtains more or less depressed arcs. By introducing constant phase elements one can often achieve an accurate fitting also for non-ideal impedance arcs. From the fitting parameters Q and n, a capacitance C can then be calculated according to [59],

$$C = (R^{1-n}Q)^{1/n} \quad (3.13)$$

Reviewing the literature in the field of solid state ionics, one finds that equivalent circuits are frequently proposed ‘ad hoc’ and tested in terms of their apparent agreement with the measured spectra. Intuitively, a good correspondence between experimental data and fit curve may then be taken as a confirmation that the proposed circuit provides a good description of the system under investigation. Such a course of action, however, may be problematic since even an excellent fit, i.e. very close agreement of experimental data and fit curve over a wide frequency range, is in general insufficient proof for the correctness of a model. The reason is that equivalent circuits are often not unique. Well-known are the cases where two (or more) physically different equivalent circuits are ‘mathematically equivalent’ in terms of



their overall response, i.e. the same frequency dependence of the impedance  $Z(\omega) = Z_{real}(\omega) + iZ_{imag}(\omega)$  can be obtained with both circuits, however in general with different values for the individual circuit elements. An example is shown in figure 24.

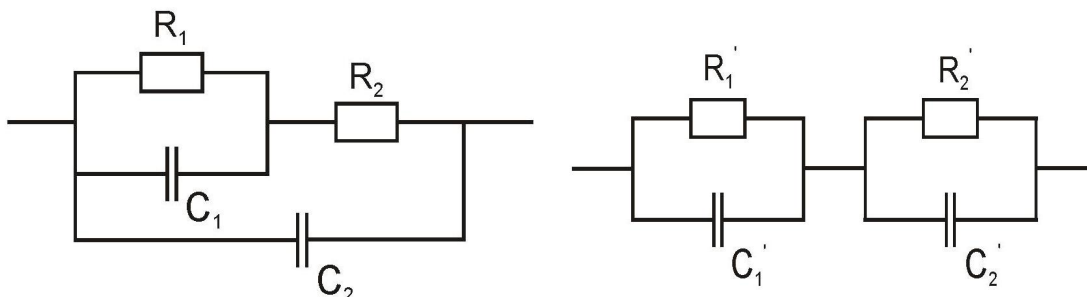


Figure 24. Example of two “mathematically equivalent” circuits

#### References:

- [1] L.D. Jadhav, S.H. Pawar, M.G. Chourashiya, *Bull. Mater. Sci.* 1 (2007) 30.
- [2] S. W. Zha, Q. X. Fu, Y. Lang, C. R. Xia, G. Y. Meng, *Mater. Lett.* 47 (2001) 351.
- [3] W Huang, P. Shuk, M. Greenblatt, *Solid State Ionics* 100 (1997) 23.
- [4] C. Xia, M. Liu, *Solid State Ionics* 152 (2002) 423.
- [5] Reed J. S., “*Principles of Ceramic Processing*”, p. 449, Wiley, New York, 1988.
- [6] W.A. Bryant, *J Mater. Sci.*, 12 (1977) 1285.
- [7] R.N. Ghoshtagore, *J Electrochem. Soc.*, 125 (1978)110.
- [8] T. Suntola, *Thin Solid Films* 216 (1992) 84.
- [9] R.R. Chamberlin, J.S. Skarman, *J Electrochem. Soc.* 113 (1966) 86.
- [10] C.J. Brinker, A.J. Hurd, G.C. Frye, K.J. Ward, C.S. Ashley, *J Non-Crystalline Solids* 121 (1990) 294.
- [11] C.C. Chen, M.M. Nasrallah, H.U. Anderson, *J Electrochem. Soc.* 140 (1993) 3555.
- [12] C.J. Brinker, G.C. Frye, A.J. Hurd, C.S. Ashley, *Thin Solid Films* 201 (1991) 97.
- [13] C. M. Lampkin, *Prog. Crystal Growth Charact.* 1 (1979) 395.
- [14] S.K. Pawar, S.H. Pawar, *Mat. Res. Bull.* 18 (1983) 211.



- [15] P. S. Patil, *Mater. Chem. Phys.* 59 (1999) 185.
- [16] M. Fujimoto, T. Urano, S. Murai, Y. Nishi, *Jpn. J. Appl. Phys.* 28 (1989) 2587.
- [17] Yagi, K. Kakizawa, K. Murakami, S. Kaneko, *J. Ceram. Soc. Jap.* 102 (1994) 296.
- [18] C. H. Lee, L. Y. Lin., *Appl. Surf. Sci.* 92 (1996) 163.
- [19] Aoki, G. Nogami, *J. Electrochem. Soc.* 143 (1996) 191.
- [20] D. Craigen, A. Mackintosh, J. Hickman, K. Colbow, *J. Electrochem. Soc.* 133 (1986) 1529.
- [21] P. S. Patil, E. A. Ennaoui, C. D. Lokhande, M. Muller, M. Giersig, K. Diesner, H. Tributsch, *Thin Solid Films* 310 (1997) 57.
- [22] P. Bohac, L. Gauckler. *Solid State Ionics* 119 (1999) 317.
- [23] R.K. Nimat, C.A. Betty, S.H. Pawar, *Appl. Surf. Sci.* 253 (2006) 2702.
- [24] R.K. Nimat, R.S. Joshi, S.H. Pawar. *Materials Sci., Engg. B.* 137 (2007) 93.
- [25] M.G. Chourashiya, S.H. Pawar, L.D. Jadhav, *Appl. Surf. Sci.* 254 (2008) 3431.
- [26] C. H. Chem., A. A. J. Buysman, E. M. Kelder, J. Schoonman, *Solid State Ionics* 80 (1995) 1.
- [27] B. Lefez, P. Nkeng, J. Lopitiaux, *Mater. Res. Bull.* 31 (1996) 1263.
- [28] R. N. Singh, J. F. Koenig, G. Poillerat, P. Chartier, *J. Electroanal. Chem.* 314 (1991) 214.
- [29] C. S. Huang, C. S. Tao, C. H. Lee, *J. Electrochem. Soc.* 144 (1997) 3556.
- [30] J. P. Mangalhara, R. Thangraj, O. P. Agnihotri, *Bull. Mater. Sci.* 10 (1988) 333.
- [31] J. De Merchant, M. Cocivera, *J. Electrochem. Soc.* 143 (1996) 4054.
- [32] V. V. Killedar, C. D. Lokhande, C. H. Bhosale, *Thin Solid Films* 289 (1996) 14.
- [33] G. Valyomana, S. Mathew, K. P. Vijaykumar, C. Purushottam, *Bull. Mater. Sci.* 16 (1993) 55.
- [34] K. Y. Rajpure, A. M. Patil, C. D. Lokhande, C. H. Bhosale, *Thin Solid Films* 331 (1997) 114.
- [35] S. Lopez, S. Granados, A. Ortiz, *Semiconductor Sci. Technol.* 11 (1996) 433.
- [36] Y. D. Tembhurkar, J. P. Hirde, *Bull. Mater. Sci.* 17 (1994) 465.
- [37] W. A. S. A. Ghafor, A. A. Awad, N. S. Othman, *Ind. J. Pure Appl. Phys.* 31 (1993) 123.



- [38] S. P. S. Arya, H. E. Hinterman, *Thin Solid Films* 193 (1990) 841.
- [39] S. Kumari, A. K. Singh, O. N. Srivastava, *Supercond. Sci. and Technol.* 9 (1996) 405.
- [40] S. H. Pawar, P. N. Pawaskar, *Mater. Res. Bull.* 30 (1995) 277.
- [41] Y. Moriwaki, T. Sugano, C. Gasser, A. Fukuoka, K. Nakanishi, S. Adachi, K. Tanabe, *Appl. Phys. Lett.* 69 (1996) 3423.
- [42] A.A. Rizkalla, A.H. Lefebvre, *J Eng. Power*, 97 (1975) 173.
- [43] R. Rajan, A.B. Pandit, *Ultrasonics*, 39 (2001) 235.
- [44] M. Cloupeau, B. Prunet-Foch, *J Electrostatics*, 25 (1990) 165.
- [45] C.M. Lampkin, *Progress in Crystal Growth and Characterization of Materials*, 1 (1979) 405.
- [46] R. Rajan, A.B. Pandit, *Ultrasonics*, 39 (2001) 235.
- [47] A.M. Ganan-Calvo, J. Davila, A. Barrero, *J Aerosol Sci.*, 28 (1997) 249.
- [48] D. Perednis, "Thin film deposition by spray pyrolysis and the application in solid oxide fuel cells", *Ph.D. Thesis, Swiss Federal Institute of Technology, Zurich*, 2003.
- [49] C.H. Chen, E.M. Kelder, J. Schoonman, *J Mater. Sci.* 31 (1996) 5437.
- [50] C.H. Chen, E.M. Kelder, P.J.J.M. van der Put, J. Schoonman, *J Mater. Chem.* 6 (1996) 765.
- [51] C.H. Chen, E.M. Kelder, J. Schoonman, *J Euro. Ceram. Soc.* 18 (1998) 1439.
- [52] S.G. Kim, K.H. Choi, J.H. Eun, H.J. Kim, C.S. Hwang, *Thin Solid Films* 377 (2000) 694.
- [53] M. I. Pope, M.J. Judd, 'Differential Thermal Analysis', London, Heyden, Academic Press (1977) 1-2.
- [54] C. Guillaud, M.C. R. Paulus, *Acad. Sc.* 242 (1956) 2525.
- [55] *Impedance Spectroscopy - Emphasizing Solid Materials and Systems*, edited by J. R. Macdonald (John Wiley & Sons, Inc., New York, USA, 1987).
- [56] Y. L. Yang, C. L. Chen, S. Y. Chen, C. W. Chu, A. J. Jacobson, *J. Electrochem. Soc.* 147, (2000) 4001.
- [57] F. S. Baumann, J. Fleig, M. Konuma, U. Starke, H.-U. Habermeier, J. Maier, *J. Electrochem. Soc.* 152 (2005) A 2074.
- [58] J. Fleig, *Habilitation Thesis*, Ulm, Germany, 2002.
- [59] R. A. De Souza, J. A. Kilner, *Solid State Ionics* 106 (1998) 175.

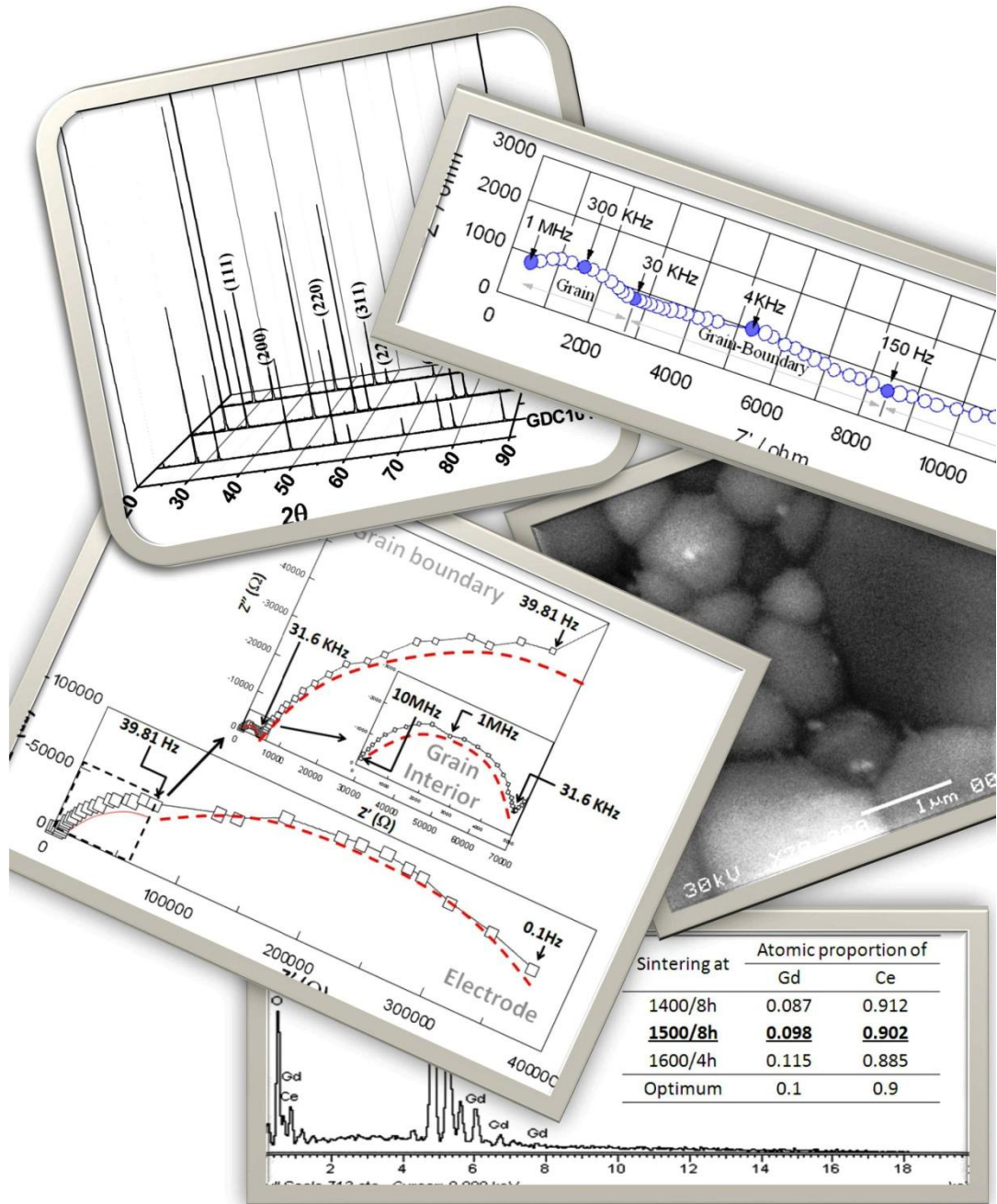






# Chapter four:

## *Synthesis and characterization of Gadolinium doped ceria in bulk form using solid state reaction method*





# Chapter four

## CONTENTS

4. SYNTHESIS AND CHARACTERIZATION OF GADOLINIUM DOPED CERIA IN BULK FORM USING SOLID STATE REACTION METHOD. ....	134
Keywords: Gd doped Ceria, Solid state reaction method, Effect of preparative parameters of ceramic route, Effect of doping % of Gd in ceria, .....	134
4.1. Introduction .....	135
4.2. Experimental.....	136
4.2.1. <i>Synthesis of GDC samples</i> .....	136
4.2.1.1. <i>Introduction</i> .....	136
4.2.1.2. <i>Characterizations of starting (raw) powders by XRD</i> .....	136
4.2.1.3. <i>Synthesis of <math>Ce_{1-x}Gd_xO_{2-x/2}</math> (<math>x = 0.1, 0.2</math> and <math>0.3</math>) powders</i> .....	138
4.2.1.4. <i>Green body (pellet) formation – using dry pressing</i> .....	140
4.2.1.5. <i>Pre-sintering – drying and binder burnout step</i> .....	141
4.2.1.6. <i>Final sintering and Sample Identifications</i> .....	141
4.2.2. <i>Characterizations</i> .....	142
4.3. Results and discussion .....	144
4.3.1. <i>Introduction</i> .....	144
4.3.2. <i>Section – A: Properties of <math>Ce_{1-x}Gd_xO_{2-\delta}</math> sintered at different temperatures</i> .....	145
4.3.2.1. <i>Structural characterizations:</i> .....	145
4.3.2.2. <i>Morphological characterizations:</i> .....	151
4.3.2.3. <i>Density measurements:</i> .....	154
4.3.2.4. <i>Electrical characterizations:</i> .....	157
4.3.2.5. <i>Outcomes of studies carried out in Section A</i> .....	164
4.3.3. <i>Section – B: Precise optimization of processing parameters and Gd doping</i> .....	165
4.3.3.1. <i>Structural and elemental characterization</i> .....	165
4.3.3.2. <i>Morphological characterizations and relative density measurements</i> .....	169
4.3.3.3. <i>Electrical characterizations</i> .....	173
4.4. Conclusions.....	181
References.....	182

#### 4. SYNTHESIS AND CHARACTERIZATION OF GADOLINIUM DOPED CERIA IN BULK FORM USING SOLID STATE REACTION METHOD.

##### Abstract:

The gadolinium-doped ceria (GDC) is considered as one of the most promising solid electrolytes for intermediate temperature solid oxide fuel cells (IT-SOFCs), due to its lower operating temperature. The ionic conductivity of ceria-based electrolytes is mostly depend upon types of dopants, its composition, microstructure, local structure, impurity and processing during its synthesis etc. Therefore, the structural, morphological and electrical properties of GDC prepared using solid state reaction method were studied as a function of doping concentration of 'Gd' and processing parameters of ceramic route. The lattice parameter, density, surface morphology and electrical conductivity of GDC samples were observed to vary with sintering temperatures. Further an increase in lattice parameter with concentration of Gd confirms the dissolution of  $Gd_2O_3$  in  $CeO_2$ . However, with increase in Gd doping the crystallite size and grain size was observed to decrease. All GDC samples sintered at 1773K showed uniform and smoother surfaces with conductivity  $\sim 0.1$  S/cm at 1073K and activation energies less than 0.9eV. From this study the optimum processing parameters and doping concentration of Gd in ceria to prepare GDC for better ionic conductivity and higher bulk density were extracted. The study clarified that the 10%Gd doping in ceria gives better ionic conductivity than that of other doping concentrations; however, the density of the samples sintered at 1773K gives relative density in the range of 85-93%<sup>†</sup>.

The conclusion drawn from above studies suggested that higher sintering temperature and sintering duration for 10%Gd doped ceria (GDC10) (best ionic conductor among other doping concentrations) is necessary to prepare enough dense samples to be used as solid electrolyte for IT-SOFC. Hence in further study GDC10 samples were sintered at 1673K, 1773K and 1873K in air for longer duration and their structural, elemental, morphological and electrical properties were recorded<sup>‡</sup>. The optimized process parameters were applied to other compositions in order to see any enhancement in the electrical performance. An additional step of binder burnout was added while synthesizing the different compositions of GDC. The 10%Gd doped ceria composition showed higher electrical properties over the other doping concentrations<sup>§</sup>.

**Keywords:** Gd doped Ceria, Solid state reaction method, Effect of preparative parameters of ceramic route, Effect of doping % of Gd in ceria.

<sup>†</sup> This work is published in *Bulletin of Material Science* and *Materials Chemistry and Physics*.

<sup>‡</sup> This work is published and presented at *ICEAR-2007* at IIT, Bombay.

<sup>§</sup> This work is submitted to *Journal of Material Science*.



#### 4.1. Introduction

Intermediate temperature solid oxide fuel cells (IT-SOFCs) have been of immense interest as they offer many advantages over high temperature SOFCs (HT-SOFCs), which include smaller thermal mismatch between its components, rapid startup with less energy consumption, etc. The doped ceria with high ionic conductivity at relatively low temperatures is considered to be a strong candidate as a solid electrolyte in SOFCs, in addition to its applications in oxygen sensors, oxygen separation pumps, etc. [1-6]. Ceria have been doped with variety of cations. However, the host lattices of ceria are more compatible with trivalent cations and the stable structure is obtained for the ratio between cations and anions radii close to 0.70 [7]. The ceria is, therefore, either doped with gadolinium or samarium [8], of which, gadolinium-doped ceria (GDC) is mostly recommended as promising solid electrolytes [9, 3-6].

From introductory discussion in previous chapter (Chapter 3) on and the literature survey on synthesis of Gd doped ceria in bulk form (Chapter 1), it was found that the Solid State Reaction (SSR) method is a cost effective and suitable preparation method for experimenting with different doping concentrations of Gd into ceria [10-15]. But, as ceramic route on one hand enables easy synthesis and exact doping in host compounds, in general, the samples prepared remain porous and inhomogeneous. However, the porosity and in-homogeneity of samples can be avoided using proper thermal treatments. The electrical properties of polycrystalline solid electrolytes is observed to depend not only on the chemical composition of the material but also to a large extent on various micro-structural parameters, e.g. porosity [16, 17], grain connectivity, grain boundary contents, etc. which can be delicately controlled by the thermal treatments during its processing [18].

The main aim of carrying out the synthesis and characterization of GDC ceramic samples using ceramic route were to optimize the concentration of Gd doping in ceria for better ionic conduction. In addition the process parameters of ceramic route such as binder amount, calcination temperature, sintering temperature, sintering duration, etc. were optimized to study the effect on relative densities, microstructural and electrical properties. Optimum Gd doped ceria was studied further in thin film form. The optimized process parameters of ceramic route acquired were further utilized to prepare the anodic ceramic substrates for film depositions.



## 4.2. Experimental

### 4.2.1. Synthesis of GDC samples

#### 4.2.1.1. Introduction

The general procedure to be followed for the synthesis of ceramic body includes 5 major steps.

- Raw ceramic powder characterizations,
- Synthesis of ceramic powders,
- Green body formation,
- Pre-sintering for binder burnout,
- Sintering and Finishing.

These steps also include sub steps which must be carefully invoked during the synthesis to obtain a well defined final product.

To prepare Gd doped ceria (GDC),  $\text{CeO}_2$  and  $\text{Gd}_2\text{O}_3$  were used as starting materials. These chemicals were characterized for their purity by XRD. After confirmation of purity of chemicals, it is taken for the further processing steps which include calculation of weights for preparation of mixture, dry homogenization of the mixture, binder added homogenization, pellet formation – dry pressing, pre-sintering – binder burnout and final-sintering. Each of these steps is discussed in detail.

#### 4.2.1.2. Characterizations of starting (raw) powders by XRD

The  $\text{CeO}_2$  and  $\text{Gd}_2\text{O}_3$  powders as starting materials were used to synthesize GDC. These chemicals were purchased from HIMEDIA INC. with purity and other specifications mentioned on the bottle as given in table 1:



Manufacturer	HIMEDIA Laboratories Pvt. Ltd.	
Molecular Formula	Cerium (IV) Oxide; CeO <sub>2</sub>	Gadolinium Oxide; Gd <sub>2</sub> O <sub>3</sub>
Molecular Weight	172.1	362.5
Minimum assay	99.95%	99.9%
Grade	A.R.	A.R.
Product No.	RM 1442	RM 1682
Quantity (wt. in gm)	100	5

Table 1. Specifications mentioned on the bottles of raw chemicals.

However, to crosscheck the phase purity of the starting chemicals, structural characterization of the chemicals was carried out. Figure 1 shows the XRD pattern of CeO<sub>2</sub> and Gd<sub>2</sub>O<sub>3</sub> powders. These XRD patterns were compared with their respective JCPDS-PDF (Joint Commission for Powder Diffraction Standard-Powder Diffraction Files) No. 81-0792 for CeO<sub>2</sub> and 76-0155 for Gd<sub>2</sub>O<sub>3</sub> and were indexed accordingly. It was found that starting chemicals purchased were pure in quality and however, if there were any impurities, their concentration would be below the detection limit of XRD [19]. Both the material possesses cubic lattice structure with lattice parameter 5.411 Å for CeO<sub>2</sub> (std. '*a*' = 5.412 Å) and 10.80 Å for Gd<sub>2</sub>O<sub>3</sub> (std. '*a*' = 10.79 Å). The crystallite size calculated by Scherer's formula for both was around 35–45nm.

The crystallite sizes of both the starting chemicals were nearly same. In ceramic processing, having the narrow particle size distribution is advantageous, as it facilitates uniform sintering of ceramic bodies.

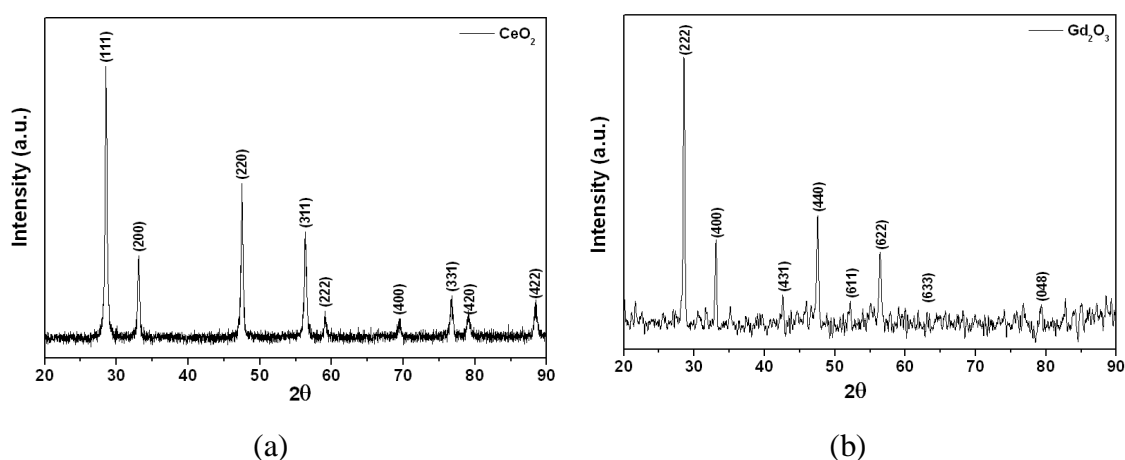


Figure 1. XRD pattern of commercially available powder of (a) CeO<sub>2</sub> and (b) Gd<sub>2</sub>O<sub>3</sub>.



### 4.2.1.3. Synthesis of $Ce_{1-x}Gd_xO_{2-x/2}$ ( $x = 0.1, 0.2$ and $0.3$ ) powders

GDC were synthesized for different doping concentration of Gd. Gd doping concentration was varied as 10, 20 and 30 mol% in  $CeO_2$  to synthesize  $Ce_{0.9}Gd_{0.1}O_{1.95}$  (GDC10),  $Ce_{0.8}Gd_{0.2}O_{1.90}$  (GDC20) and  $Ce_{0.7}Gd_{0.3}O_{1.85}$  (GDC30), respectively. The processing parameters were varied to study its effects on structural, morphological and electrical properties of the samples. The steps involved in the synthesis of GDC powder is discussed in following sections.

#### a. Calculation of weights for preparation of mixture

It is an important step as it decides the ratio of metal and oxides ions in the final product. Any error in this step will propagate throughout the process and results in un-expected results e.g. un-expected stoichiometric/non-stoichiometric phase formation in final product. Calculating the weights for preparation of mixture with desire stoichiometry/non-stoichiometry is far easier than that of taking the exact weight on micro-balance. Since, former depends on mathematical formulation, while later includes the accuracy of the micro-balance, its precision and also on the expertness of the instrument handler. Here the single pan microbalance (SICO POPULAR Balance Works, Waranasi; Model No. 8B4/100) with least count of 0.00001 gm was employed to take the weights.

The calculations of weights were done for GDC and are listed in table 2.

<b>For 20 gm of <math>Ce_{1-x}Gd_xO_{2-x/2}</math> (<math>x = 0.1, 0.2</math> and <math>0.3</math>)</b>			
	$x = 0.1$ (GDC10)	$x = 0.2$ (GDC20)	$x = 0.3$ (GDC30)
<b>CeO<sub>2</sub></b>	17.9050 gm	15.8320 gm	13.7814 gm
<b>Gd<sub>2</sub>O<sub>3</sub></b>	2.0950 gm	4.1680 gm	6.2196 gm

Table 2. Weights of starting chemicals to prepare 20 gm of  $Ce_{1-x}Gd_xO_{2-x/2}$  ( $x = 0.1, 0.2$  and  $0.3$ ).





*b. Dry homogenization of the mixture*

Solid phase reactant of  $\text{CeO}_2$  and  $\text{Gd}_2\text{O}_3$  in calculated amounts of weights were taken into agate mortar for homogenization. The thorough mixing is critically important as it directly leads to isotropic properties in the final product. There are different techniques for the mixing and size reduction of starting chemicals. The intense mixing by techniques such as dry ball milling, wet ball milling, planetary ball milling, etc. results in decrease in particle size along with thorough mixing. However, the reduction in particle size achieved is at most up to  $1\mu\text{m}$ , even after continuous 40hrs ball milling.

The homogenization was confirmed by observing the change in color of powder which turned into yellowish white after thorough mixing. As the color of starting chemicals i.e. Ceria ( $\text{CeO}_2$ ) was yellow while that of  $\text{Gd}_2\text{O}_3$  is white, with an increase in dopant amount (Gd) the mixed powder shows added whitish shade.

*c. Calcination step*

After proper mixing of the starting chemicals, the mixture were heat treated in furnace at moderate temperature ( $\sim 800^\circ\text{C}$ ) for 2-3hrs in air. This step is important as it initiate the solid state reaction in the constituent powders. After this treatment the mixed powder is again homogenized in agate-mortar.

*d. Binder added homogenization*

Poly-Vinyl Alcohol (PVA) as binder was added to the homogenized calcined powders. The proportion of binder to calcined powder was optimized for better results. The amount of PVA more than that of optimum level leads to wet samples which upon heat treatment lead to evolution of huge amount of gases due to vaporization of organic PVA. These gases evolved during pre-sintering and sintering escapes from the samples and exert stresses on surface and bulk of the samples. Moreover, the stresses developed leads to cracking and/or warping of sample. On the other hand, if amount of binder (PVA) is less than that of optimum level, green body formed may not have enough strength to bear the handling from green body formation



assembly to the sintering assembly. Hence, such samples require very careful handling. Very dry samples may not sinter well as the available flowing media (PVA in liquid form at elevated temperatures) is less and hence shows decreased possibility of reactants to come in contact.

By precise trials, it was found that the optimum level of addition of PVA in mixture is about 5-7 wt% of that of total powder mixture. This optimization was confirmed by green body density characterizations before and after pre-sintering i.e. binder burnout process.

#### 4.2.1.4. Green body (pellet) formation – using dry pressing

The binder added powders were pressed in circular disk shaped pellets. The dimensions of the pellets were 1.23 cm in diameter and 0.15–0.34cm in thickness. The hydraulic press machine was employed to prepare the pellets. The powders were pressed at about moderate pressure (10-12tons/inch<sup>2</sup>) by uniaxial die pressing technique. The samples pressed at lower pressures resulted in less dense pellets, while higher pressing pressures resulted in pellets that were very brittle and prone to peeling and cracking [20].

##### a. Tapping of die

However, before pressing the powders in pellet form, uniform tapping of the die (filled with powders) was carefully adapted. Since in dry pressing, tapping increases the packing density and eliminate any in-homogeneities in the packing. This is by far an important consideration in view of prospective properties like density and desired shape of final product etc. If the die (mold) is not filled homogeneously, the final pressed shape will be very different from that of the die.

##### b. Green machining

The prepared green bodies (pellet) then polished to remove its surface roughness and loosely bounded surface particles. Some pellets were also showed unwanted edge formation at the periphery of the samples, which were removed by a sharp cutter.



#### 4.2.1.5. Pre-sintering – drying and binder burnout step

During final optimizations studies, pre-sintering step was strictly followed as it improved the densification rate during final sintering step. All the green bodies formed were dried and binder burning was carried out at about 1000°C for 2h in air.

Pre-sintering step in the fabrication of ceramic samples plays a crucial role. In general, the organic polymers (in our case PVA) are used to strengthen the ceramic green body. But when the green body is dried binder must be burned out before sintering as they decompose in an uncontrolled manner at sintering temperatures and gives off huge volumes of gases at high pressure. These highly pressurized gases may cause the green body to crack during its escape to ambient.

Prior to pre-sintering, green body formed in III step was having a mass of ceramic powder held together by organic polymer – binder (PVA). The polymer distributed at the particle-particle contacts gave the strength to the green body. When necessary heat of evaporation for polymer drying and the heat of reaction, either exothermic or endothermic, for polymer thermal decomposition were supplied, the evaporation and thermal decomposition of PVA in green body starts. Both evaporation and thermal decomposition of polymer gives off huge volumes of gases. These gases diffuse through the porous network of the green body. Different types of stresses act on the green body during these processes which includes thermal gradients, gas pressure gradient, liquid pressure gradient (caused by the flow of liquid from the inside of the bulk to its surface), etc. These stresses are additive and act to warp or crack the green body. Hence it is very much important to control the heating rate of green body in furnace. Here, the heating rate of 3°C/min was kept for all the samples.

#### 4.2.1.6. Final sintering and Sample Identifications

Final sintering temperature was varied to see its effect on properties of prepared samples and to optimize the sintering temperature. The pre-sintered (dried) samples from previous step were finally sintered at temperatures ranging from 1473–1873K for different durations in air. The heating and cooling rate was kept at 3K/min and 1K/min, respectively for all the samples. The samples with different doping % of



Gd in ceria and sintered at various temperatures and durations are identified as shown in table 3.

Composition → Sintering Temperature (K) ↓	x = 0.1 (GDC10)	x = 0.2 (GDC20)	x = 0.3 (GDC30)	
1473 / 2hrs in air	GDC114	GDC214	GDC314	} Section A
1573 / 2hrs in air	GDC115	GDC215	GDC315	
1673 / 2hrs in air	GDC116	GDC216	GDC316	
1773 / 2hrs in air	GDC117	GDC217	GDC317	
1673 / 8hrs in air	GDC1016	-	-	} Section B
1773 / 8hrs in air	GDC1017	GDC2017	GDC3017	
1873 / 4hrs in air	GDC1018	-	-	

Table 3. Sample identifications.

#### 4.2.2. Characterizations

The phase formation of the sintered GDC samples was studied using PHILIPS X-ray diffractometer (PW-3710) with Cu-K<sub>α</sub> radiation source ( $\lambda = 1.54056 \text{ \AA}$ ). The lattice parameter and crystallite size were estimated from the resultant spectra. The lattice parameter ' $a$ ' was calculated using the relation (for cubic lattices),

$$a = d \cdot \sqrt{h^2 + k^2 + l^2}, \quad (4.1)$$

where, ' $a$ ' is the lattice parameter, ' $d$ ' the inter planner distance and ( $hkl$ ) are the miller indices of the plane. The crystallite sizes were determined by using line broadening (FWHM – Full Width at Half Maxima) of most intense peak of XRD pattern in Scherer's equation given as

$$D = (0.9\lambda) / (\beta \cos\theta) \quad (4.2)$$



where,  $\beta$  is the FWHM of peak,  $\theta$  the angle of reflection and  $\lambda$  the radiation wavelength. The constant in above equation was '0.9', as the particles in the samples were assumed to be spherical in shape.

The relative density of prepared samples were estimated using the relation

$$\% \text{ density} = \frac{d_m}{d_{th}} \times 100, \quad (4.3)$$

where,  $d_m$  is the density of samples measured using Archimedes principle and  $d_{th}$  the theoretical density given as,

$$d_{th} = \frac{4}{N_A a^3} \left[ (1-x)M_{Ce} + x \cdot M_{Gd} + \left(2 - \frac{1}{2} \cdot x\right) M_O \right], \quad (4.4)$$

where,  $x$  is gadolinium content ( $x = 0.1, 0.2$  and  $0.3$ ),  $a$  the lattice constant at room temperatures i.e. 'a' calculated from eq. (4.1),  $N_A$  the Avogadro number ( $6.023 \times 10^{23}$ ), and  $M$  refers to the respective atomic weights [21].

The surface morphology of the samples was revealed using scanning electron microscope (SEM, JEOL-JSM-6360). The average grain size was estimated from higher magnification SEM images. Calculation of average grain diameter or grain size is done using Cottrell's method [22]. This method gives the relation between the number of intercepts of the grain boundary per unit length ( $P$ ), and total number of intercept ( $n$ ) as,

$$P = \left( \frac{n}{2\pi \cdot r} \right) M,$$

where, ' $M$ ', is the magnification factor and ' $r$ ', is the radius of circle. Using ' $P$ ', grain diameter (' $L$ ') can be calculated as,

$$L = \frac{1}{P-1} \quad (4.5)$$

The dc conductivity measurements were done using two-probe technique. Activation energies ( $E_a$ ) were calculated by fitting the conductivity data to the Arrhenius relation for thermally activated conduction, which is given as



$$\sigma = (\sigma_0 / T) \exp(E_a / KT), \quad (4.6)$$

where,  $E_a$  is the activation energy for conduction,  $T$  the absolute temperature,  $K$  the Boltzmann constant and  $\sigma_0$  the pre-exponential factor.

For primary analysis, ac impedance spectra were measured in air with a HP-4284A Precision LCR Meter (20Hz–1MHz), while for final optimization more sophisticated ac impedance analyzer were used (SOLARTRON 1260 – IMPEDANCE ANALYZER; 1mHz–10MHz). The samples were heated in a controlled manner during the measurements. The thermocouple was placed close to the sample for precise temperature measurements. The magnitude of the ac signal imposed on the sample was limited to 2 mV peak-to-peak. The surfaces of the samples were painted with silver/platinum paste and heat treated up to 773K prior the measurements. The samples then sandwiched between two silver/platinum foils from which the contacts were taken out for the measurements. The readings for  $Z'/R$  and  $Z''/X$  as the function of frequencies were taken for various constant temperatures. The ac impedance spectra were then analyzed to determine ac conductivity due to grain interior and grain boundaries in addition to the determination of total conductivities. The conductivity values determined were further utilized to obtain activation energy for the respective processes.

### 4.3. Results and discussion

#### 4.3.1. Introduction

The potential application of the GDC material prepared is in IT-SOFCs as solid electrolytes, which in principle requires better ionic conduction, negligible electronic conduction at intermediate temperature with density as high as possible (must be greater than 90% of its theoretical density). Here, the electrical properties of the GDC were observed to depend largely on doping concentration of the Gd in ceria and also on its morphological properties such as porosity and uniformity of the samples. The characterization of GDC samples for structural, morphological and electrical properties were carried out using XRD, SEM, EDAX and ac and/or dc



conductivity measurements and were correlated with processing and compositional parameters.

Optimization of Gd doping in ceria and process parameters of ceramic route were carried out in two parts,

- A. Effect of variation in final sintering temperature and doping concentration of Gd on micro-structural and electrical properties of GDC
- B. Precise optimization of processing parameters and Gd doping

#### **4.3.2. Section – A: Properties of $Ce_{1-x}Gd_xO_{2-\delta}$ sintered at different temperatures**

##### *4.3.2.1. Structural characterizations:*

Figure 2 shows the XRD patterns of GDC10, GDC20 and GDC30 composition sintered at different temperatures. The XRD data obtained for GDC10, GDC20 and GDC30 samples were compared with the JCPDS file nos. 75-0161, 75-0162 and 75-0163, respectively. All the patterns confirm the formation of fluorite structured Gd doped ceria (GDC) solid solution. All the GDC samples showed the presence of (111), (200), (220), (311), (222), (400), (331), (420) and (422) diffraction peaks in the scanning range 20–90° of 2 $\theta$ .



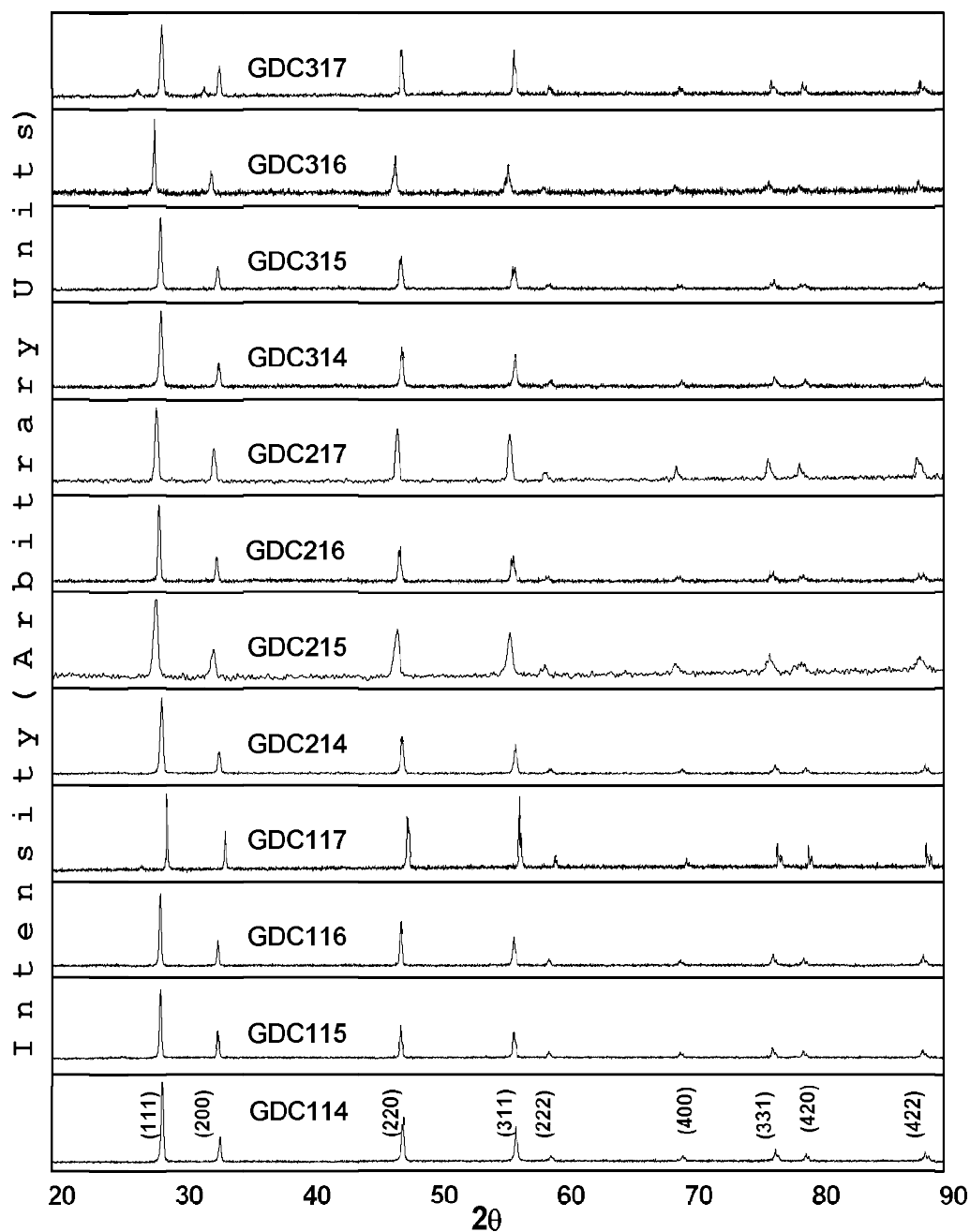


Figure 2. XRD patterns of GDC10, GDC20 and GDC30 compositions sintered at 1473K, 1573K, 1673K and 1773K for 2hrs in air.

Analysis of all the XRD patterns for its lattice parameter revealed that crystal structure of GDC was improved upon sintering and approaches to its standard values. The lattice parameter ' $a$ ' was calculated using the eq. (4.1) and its variation with sintering temperature for GDC10, GDC20 and GDC30 is shown in figure 3. It was





observed that the lattice parameter,  $a$ , for all dopant concentrations increases initially, reaches maximum and returns to the reported values [21]. This observation is consistent with variation of (111) peak position on  $2\theta$  scale, which can be clearly seen in figure 2. The maxima in figure 3, shifts to higher sintering temperature with an increase in Gd doping concentration. The deviation of lattice parameter from standard lattice parameter ( $\Delta a = |a_{calc} - a_{std}|$ ), is observed to increase with doping concentration. However,  $\Delta a$  was less than  $0.001 \text{ \AA}$  for GDC10, GDC20 and GDC30 samples sintered at 1773 K. As the sintering temperature provides the required energy to form the lattices, the sufficient lattice formation energy for GDC lattices is observed to be equal to 1773 K. The results observed are in agreement with earlier work reported by Muthukkumaran et al [23].

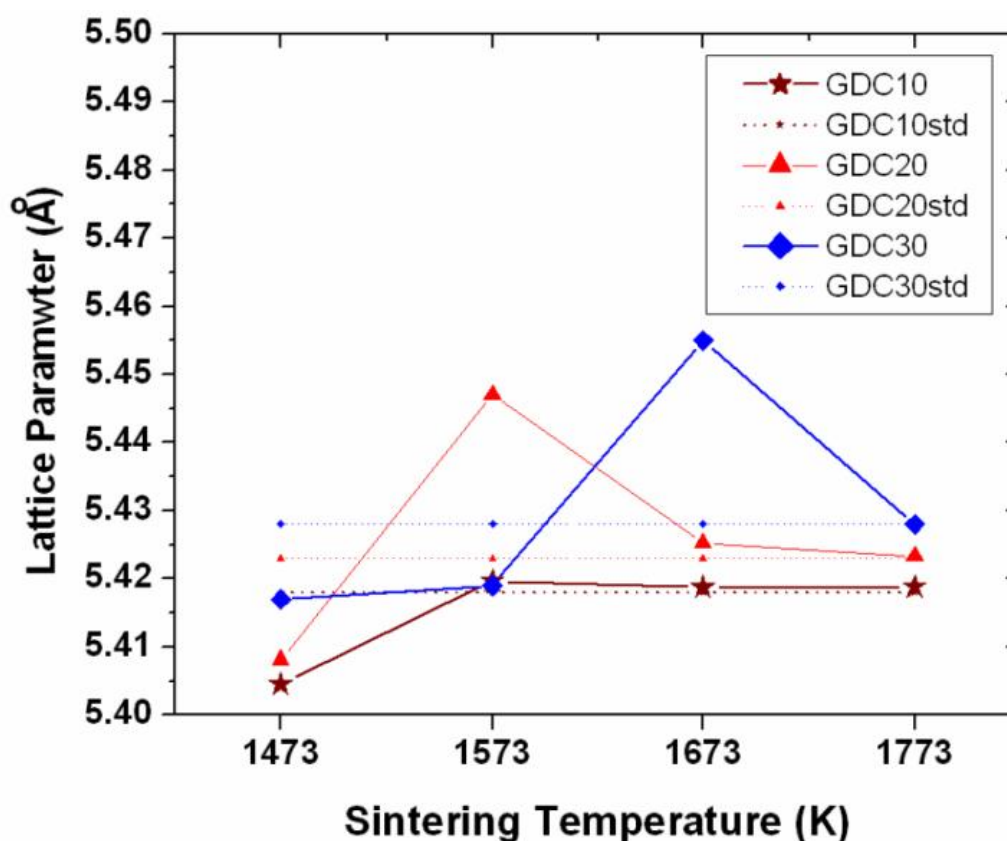


Figure 3. Variation of lattice parameter,  $a$ , of GDC10, GDC20 and GDC30 samples as function of sintering temperatures.



Pure ceria exhibits a dramatic drop in the concentrations of oxide vacancies and oxide interstitial ions with an increase in processing temperature. When  $Ce_{1-x}Gd_xO_{2-\delta}$  is processed at high temperature (i.e. for sintering temperature  $\geq 1473K$  but  $< 1773K$ ), oxygen ions (surface absorbed as well as offered by  $Gd_2O_3$  doping) may at first enter the roomier octahedral sites, rather than fill the spatially tight tetrahedral sites. If sintering temperature is sufficiently high (i.e. for sintering temperature  $\geq 1773K$ ) they may be able to overcome the potential barrier to get into the regular tetrahedral sites, and become a constituent of stable lattice. Hence, the lattice constant of  $Ce_{1-x}Gd_xO_{2-\delta}$  increases with sintering temperature, as the level of accommodation of oxygen ions in octahedral (interstitial) sites increases with sintering temperatures. The increase in lattice constant continues up to certain maximum value, i.e. highest accommodation level of oxygen ions in octahedral sites. When sintering is ended and sample is allowed to cool, the octahedral sites occupied during sintering starts to get vacant while some of them remain trapped in the lattices and leads to increased lattice parameter. However, when the sample is treated at sufficiently high temperature ( $\geq 1773K$ ) thermally activated interstitial ions may enter to regular tetrahedral sites and recombine with available vacancies in the lattices. Because of the slightly larger ionic radius of gadolinium ions, mixing of  $Gd_2O_3$  with ceria also increases the lattice constant and produces the atomic-level relaxation at the smaller tetrahedral sites, which enable easy penetration and depart of oxygen ions from the lattices. Hence, as observed here,  $\Delta a$  (deviation of lattice parameter from standard lattice parameter) at maxima for GDC solid solution increases as doping % of Gd increases. Also the point of  $\Delta a$  maxima shifts to higher sintering temperatures with an increase in doping % of Gd.

It is well established that, the large sized  $Gd^{3+}$  (radius 0.1nm) ions expand the host lattice of ceria (radius 0.096nm). Doping  $Gd_2O_3$  in  $CeO_2$  lattice induces uniform strain in the lattice as the material is elastically deformed. This effect causes the lattice plane spacing to change and the diffraction peaks to shift to new ' $2\theta$ ' position. Therefore, the lattice parameter ' $a$ ' of the doped ceria increases as the doping concentration of Gd increases. Further, an increase in lattice parameter with dopant concentration confirms the dissolution of  $Gd_2O_3$  in fluorite structure of  $CeO_2$ . This behavior of GDC follows the Vegard's law, which states that the lattice constant increases linearly with an increase in doping concentration [24]. The linear



dependence of lattice parameter,  $a$ , of GDC solid solution as function of doping % of Gd,  $x$ , for different sintering temperatures is depicted in figure 4. From figure 4, it can be clearly seen that the linear fit of GDC solid solutions sintered at 1773K is approaching standard one. This observation again confirms that the sufficient lattice formation energy for GDC lattice is equal to 1773K.

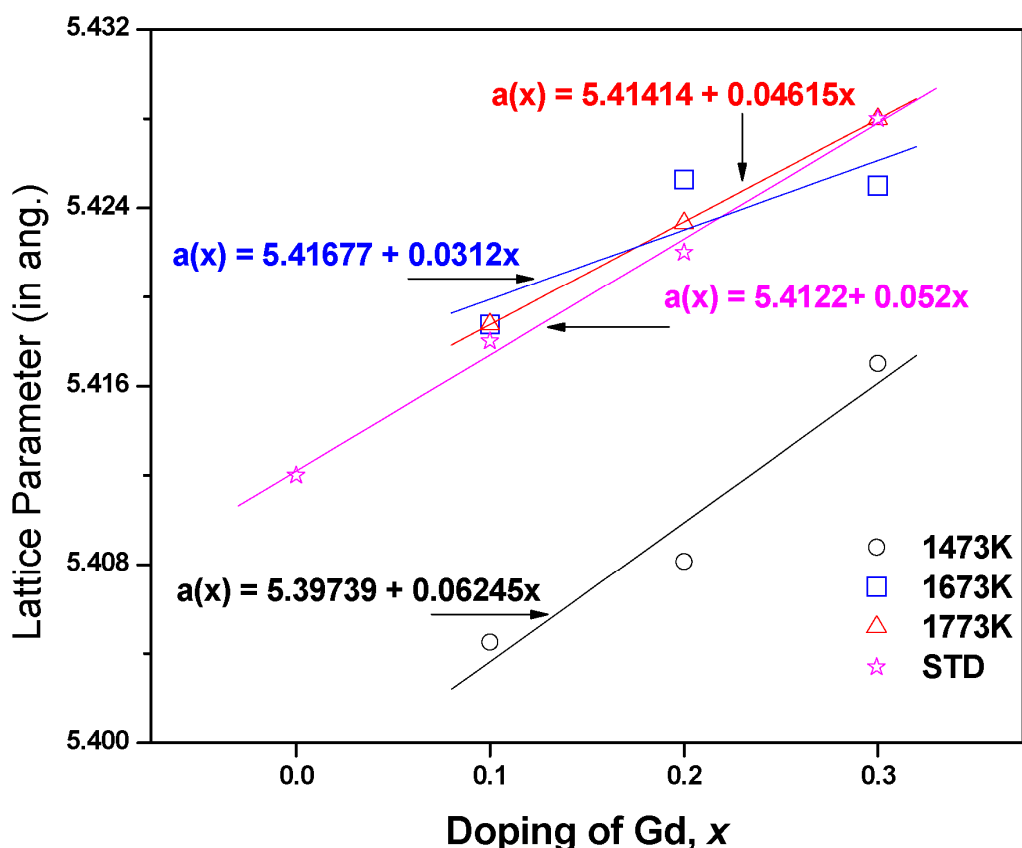


Figure 4. Linear dependence of lattice parameter,  $a$ , of GDC solid solution sintered at different sintering temperature with respect to doping percentage of Gd,  $x$ .

Figure 5 shows the variation of crystallite size calculated using eq. (4.2) for GDC solid solutions with sintering temperature. There is a common trend of increasing crystallite size with an increase in sintering temperatures. However, the rate of increase in crystallite size with sintering temperature is observed to decrease with an increase in doping % of Gd in ceria. The crystallite sizes of GDC10, GDC20 and GDC30 samples sintered at 1773K are 0.611 $\mu\text{m}$ , 0.503 $\mu\text{m}$  and 0.306 $\mu\text{m}$ , respectively.



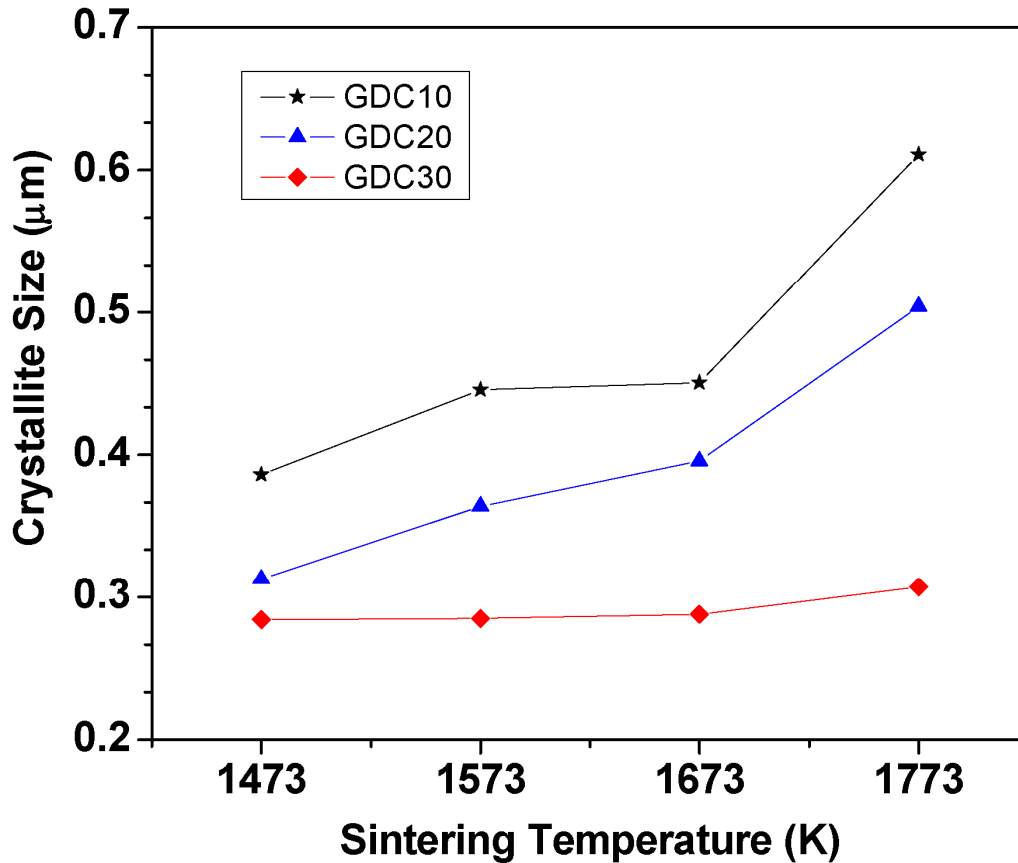


Figure 5. Variation of crystallite size of GDC solid solutions with respect to sintering temperatures.

Finally, when the XRD patterns of the GDC samples sintered at 1773K (figure 6), were observed carefully, it showed a diffraction peak due to  $\text{Ce}_2\text{O}_3$  at  $26.73^\circ$  (figure 6b), which reveals that reduction of  $\text{Ce}^{4+}$  to  $\text{Ce}^{3+}$  has occurred at this sintering temperature. This  $\text{Ce}_2\text{O}_3$  peak grows with an increase in dopant concentration. However, in addition to  $\text{Ce}_2\text{O}_3$  peak, a peak of comparable intensity was observed at  $31.91^\circ$  for GDC317 sample, which corresponds to  $\text{Gd}_2\text{O}_3$ . The emergence of  $\text{Gd}_2\text{O}_3$  peak may be attributed to the presence of un-dissolved  $\text{Gd}_2\text{O}_3$  phase in GDC317 sample.



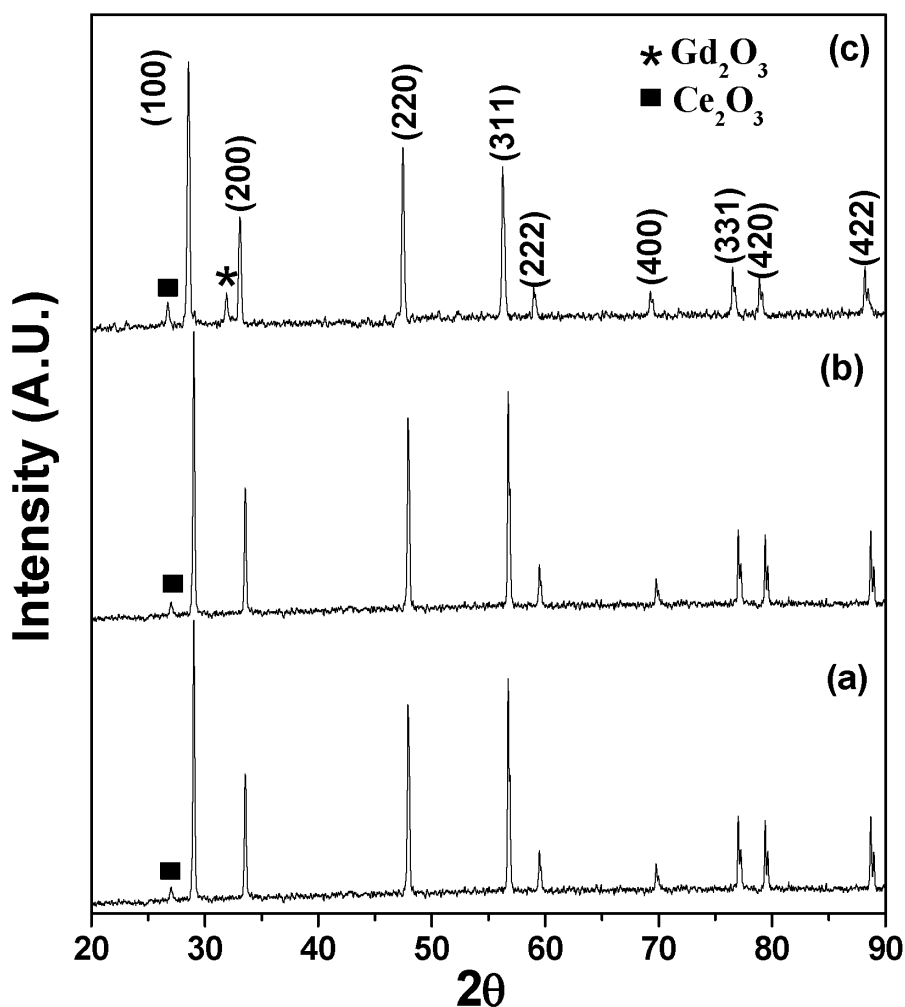


Figure 6. XRD patterns of (a) GDC117, (b) GDC217 and (c) GDC317 samples.

#### 4.3.2.2. Morphological characterizations:

The SEM images of samples showed in figure 7 clearly show the effect of sintering temperature on its surface morphology. In figure 7, sintering temperature increases from top to bottom while doping percentage of Gd increases from right to left. The amount of porosity as well as size of pores decreases as sintering temperature is increased. It can also be observed that the surface gets modified and become smoother with sintering temperature. All the three composition sintered at 1773K have comparatively uniform surface with almost no open porosity and cracks. However, with an increase in doping percentage of 'Gd' smoothness of sample surface was observed to decrease.





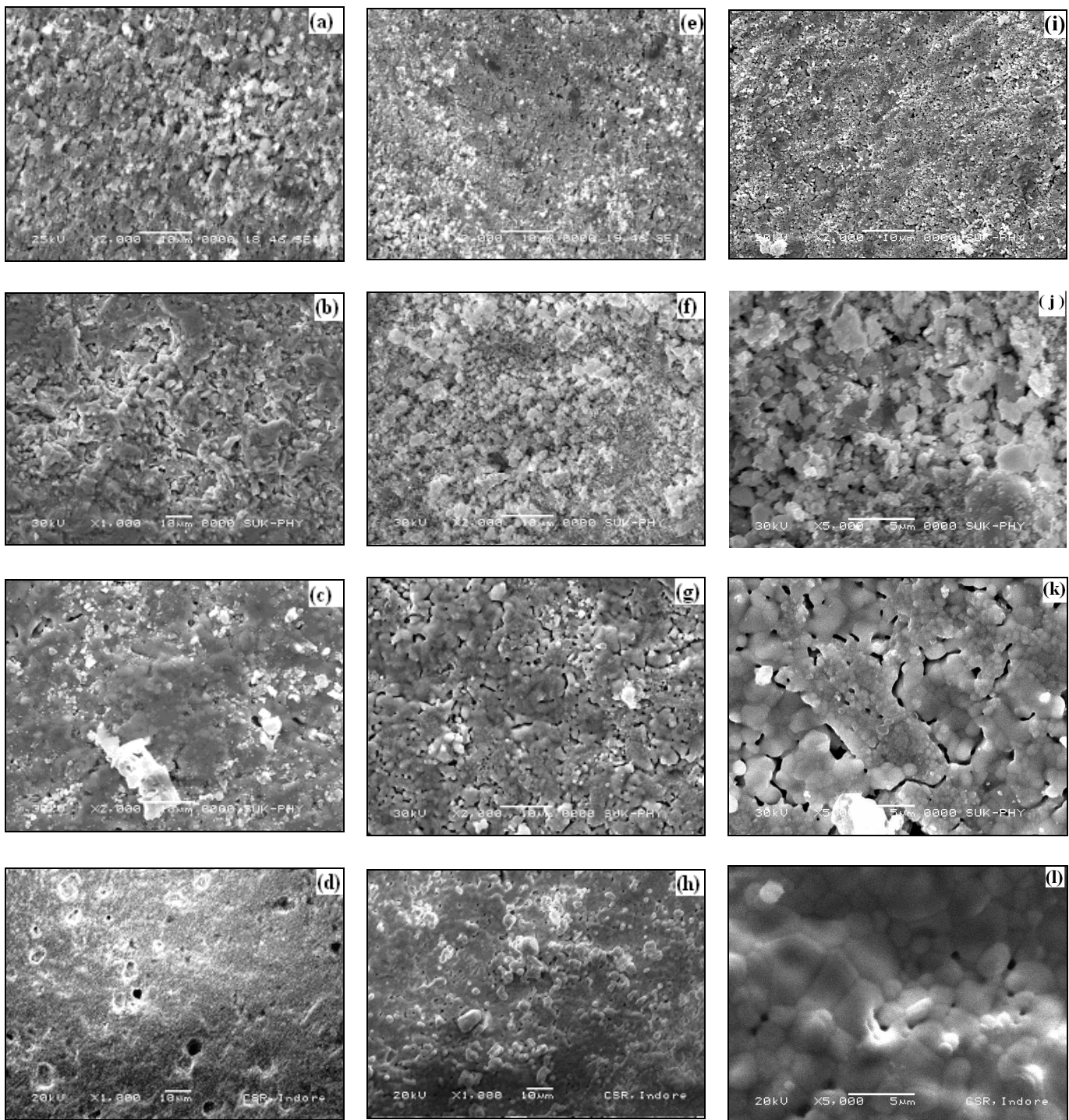


Figure 7. SEM of GDC10 (a–d), GDC20 (e–h) & GDC30 (i–l) samples sintered at 1473K, 1573K, 1673K & 1773K (top to bottom) respectively.



The SEM images at higher magnification were used to estimate grain size using Cottrell's method (eq. 4.5). A typical SEM image of GDC116 at high magnification (20,000 $\times$ ) is shown in figure 8.

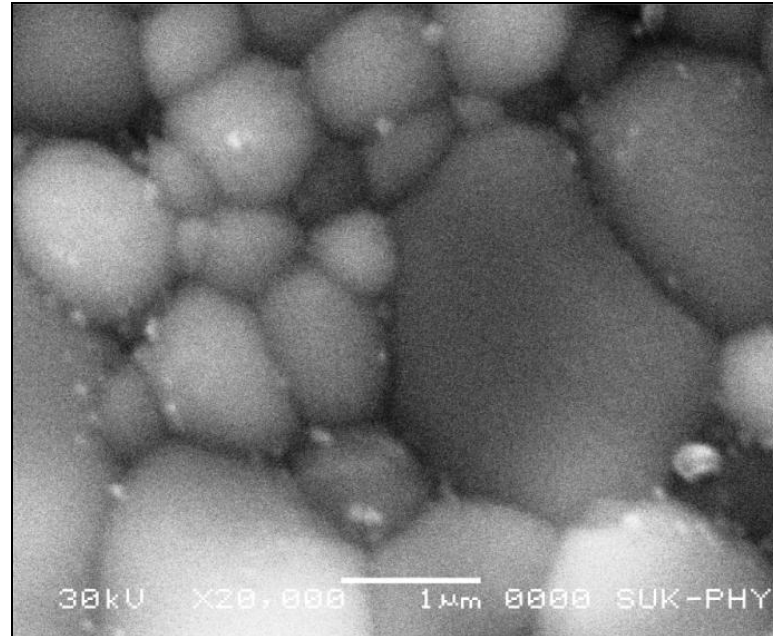


Figure 8. Typical SEM of GDC116 at high magnification (20,000 $\times$ ) used for grain size estimation using Cottrell's method.

The estimated grain sizes for samples are tabulated in table 4. The average grain size was observed to increase with an increase in sintering temperatures while decreases with an increase in doping concentration of Gd. The decrease in grain size with dopant concentration is in accordance with the fact that the addition of 'Gd' to ceria hampers the grain growth due to increased solute drag [25].

Sintering Temperature (K)	Grain size (in $\mu\text{m}$ )		
	GDC10	GDC20	GDC30
1473	0.75	0.50	0.40
1573	2.00	1.75	1.25
1673	2.50	2.25	1.80
1773	3.00	2.75	2.00

Table 4. The estimated average grain sizes from SEM images using Cottrell's method.



The similar behavior of inhibiting grain growth were reported for MgO-doped  $\text{Al}_2\text{O}_3$ ,  $\text{CaCl}_2$ -doped KCl,  $\text{ThO}_2$ -doped  $\text{Y}_2\text{O}_3$  [26], doped zirconia [27, 28] and Ytria-doped ceria [29]. The solute drag mechanism in general originates due to space charge effects. When a tri-valent dopant with an effective negative charge is present in the grain, overall electro-neutrality is maintained by creating an oxygen vacancy. The oxygen vacancies would concentrate and create effective positive charge in the surface/grain boundary due to surface/grain energy. Because of coulomb attraction of the space charge, the dopant segregates to the region adjacent to the surface/grain boundary. These excess dopant concentrated at the boundaries generates a sharp gradient between bulk and inter-grain interfaces. Thus, the dopant (solute) gradient gives a strong drag to the grain boundary mobility, resulting in an inhibition of grain growth. Direct experimental evidence for such a solute building-up in grain boundary has been obtained by various electronic optical techniques [27, 30, 31].

#### 4.3.2.3. Density measurements:

The densities of samples were determined using Archimedes principle. Figure 9 show the variation of relative density calculated using the eq. (4.3) as a function of sintering temperature. From figure 9 it is evident that the relative density is increased with an increase in sintering temperature. The relative densities for GDC10, GDC20 and GDC30 samples sintered at 1773K are 84%, 86% and 92% of theoretical density, respectively.

The relative density values were high for higher Gd doping % in ceria. The oxygen partial pressures in pores or defects are considered to be limited by the diffusion of oxygen in the bulk and therefore, the diffusion rate of oxygen in the bulk would be an important factor in densification. However, it is well known (also observed in this study) that with an increase in Gd doping % above 10mol%, reduction in overall diffusion of oxygen ions through the lattices (bulk oxide ionic conductivity,  $\sigma_{\text{Gr}}$ ) are observed. Hence after sintering there would be less oxygen in pores/defects of GDC20 and still lesser in GDC30 samples than that of GDC10 samples. Therefore, in a unit volume with an increase in Gd concentration the amount of oxygen diffused into the lattices would decrease leading to higher densities. Similar effects of oxygen partial pressure on the densities were observed in Mn–Zn ferrites by H. Inaba [32].





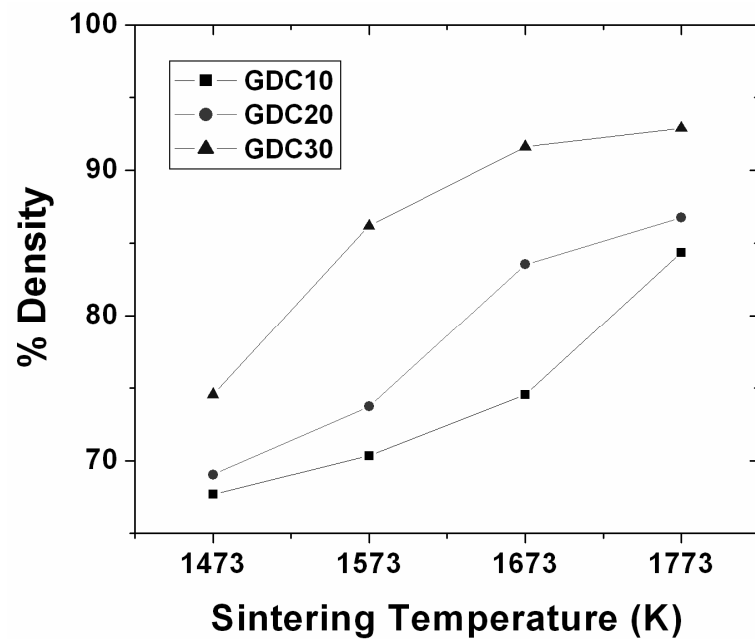


Figure 9. Variation of relative density with sintering temperature for GDC10, GDC20 and GDC30 samples.

Ikegami et al. [33] proposed a model where they states that grain growth and densification progresses simultaneously in a powdered compact by expressing the relation between the relative density  $\rho$  and average grain size  $d$  using the equation,

$$\log \left[ \frac{\rho(1-\rho_0)}{\rho_0(1-\rho)} \right] = K \log \left[ \frac{d}{d_0} \right] \quad (4.7)$$

where  $\rho_0$  is the initial particle size,  $d_0$  is the green density and  $K$  is a constant depending on the spread of the distribution of grain size and surface area of pore and grain. The relation between the relative density  $\rho$  and average grain size  $d$  according to eq. (4.7) is shown in figure 10. A linear dependence between relative density  $\rho$  and average grain size  $d$  holds for the samples. The proportional constant  $K$  can be regarded as a parameter showing the ratio of relative densification rate to grain growth rate. Thus, the GDC10 samples sintered at various temperatures has the least  $K$  and GDC30 samples had the largest  $K$ .



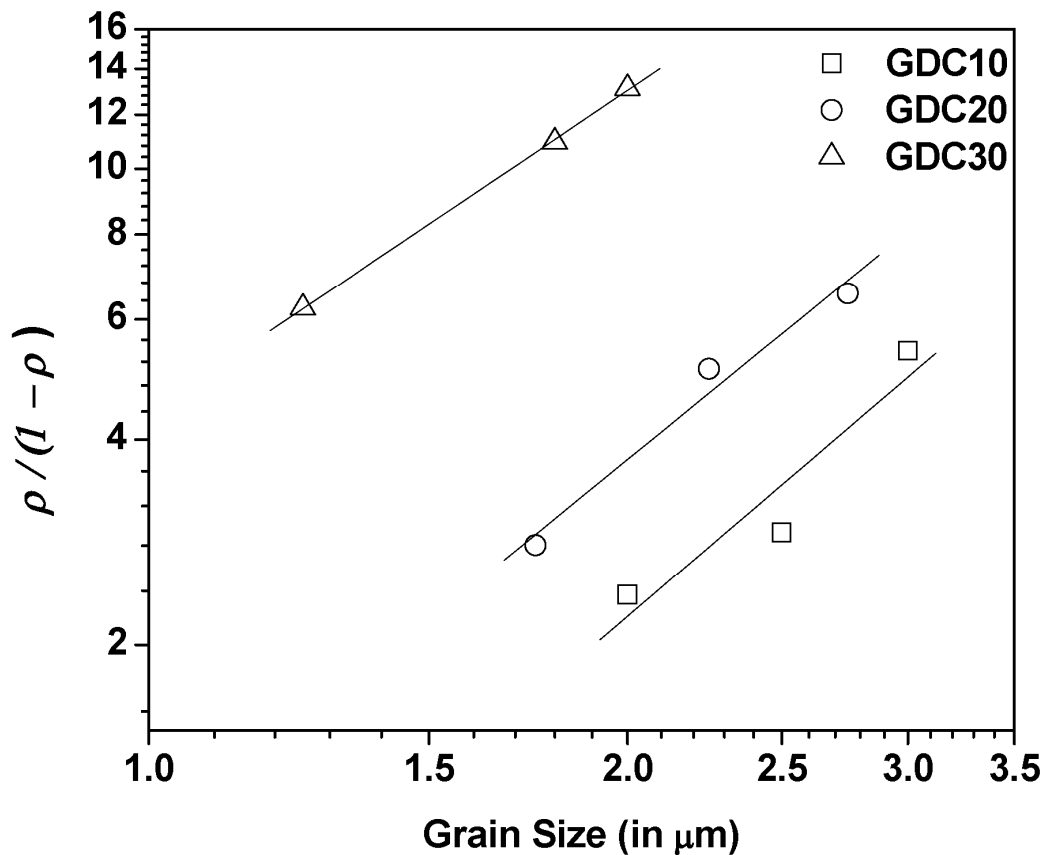


Figure 10. The relation between the relative density,  $\rho$  and average grain size,  $d$  according to eq. (4.7).

In the sample with a smaller grain size, diffusion near the surface/grain boundary during sintering may be faster and it would contribute to both densification and grain growth [34–36]. However, this was not true in our case, as from table 4, it is clear that the grain size of GDC10 samples are larger than that of GDC30 samples even the GDC30 samples showed largest  $K$ . Large  $K$  implies larger rate of densification or smaller rate of grain growth. However, in our case the large  $K$  for GDC30 is originated from the smaller rate of grain growth which is, as explained earlier, attributed to the solute drag effect. The difference of sintering behavior observed in our case and that of in ref [34–36] originates from the difference of the chemical composition of doped and pure systems, respectively, where the concentration of doping decides the mechanism of densification and grain growth.



#### 4.3.2.4. Electrical characterizations:

##### a. DC conductivity measurements

The dc conductivity measurements were carried out using two-probe method in air for the temperature range 298–1123K. The typical plots of  $\ln(\sigma T)$  vs.  $1000/T$  for GDC10, GDC20 and GDC30 are shown in figure 11 (sintered at 1773K). There are three regions with different slopes, similar to that of reported earlier by Kilner and Walters [37]. The changes in slopes were observed in the temperature range 568-583K and 918-933K, which may be attributed to initiation of ionic diffusion and to the slight change in conduction mechanism, respectively [8]. dc conductivity plots do not show any variation in the temperature ranges of change of slopes for different samples prepared either by employing different final sintering temperature or prepared with different dopant concentrations.

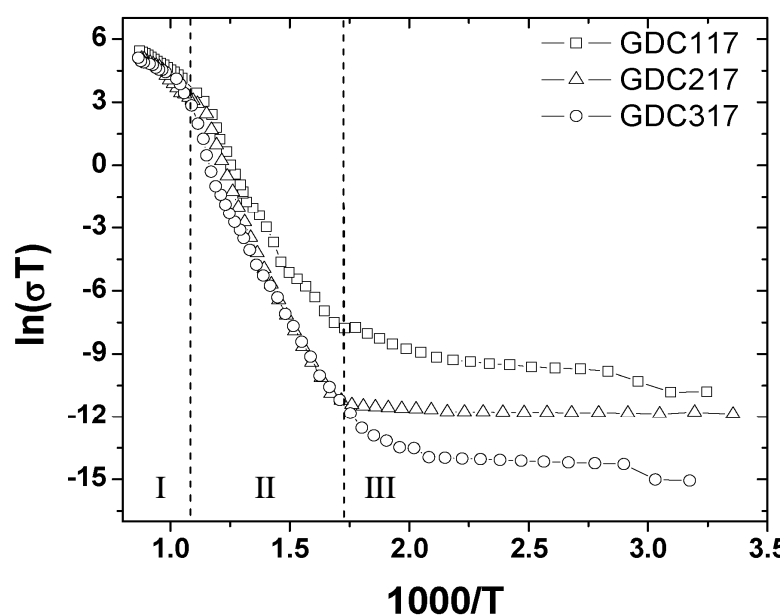


Figure 11. Variation of  $\ln(\sigma T)$  as function of  $1000/T$  for GDC samples sintered at 1773K.

According to Kilner and Walters [37], at high temperatures (i.e. greater than 918-933K; region I) electrical conduction is determined by the intrinsic defects (Schottky or Frenkel) in the crystal while in region II, electrical conduction is controlled by the population of charge-carrying defects determined by an aliovalent



dopant or impurity. In region III, usually at low temperatures, the population of charge carrying defects is determined by the thermodynamic equilibrium between the free defects and the associated pairs. In doped cerium oxides (fluorite structured) there would be a large number of oxygen vacancies and hence conduction due to the intrinsic defects (region I) is of insignificant amount. Thus the electrical conduction in region-I was nearly same as that of highest value achieved in region-II for all three compositions (figure 11).

Typical influence of sintering temperature on dc conductivity is illustrated in the figure 12 (for GDC30). The similar trends in plot were also observed for GDC10 and GDC20 samples sintered at different temperatures. For all dopant concentrations, the conductivity was observed to enhance with sintering temperature, which results in lowered activation energies. An increase in conductivity with sintering temperature is obviously due to improved grain growth.

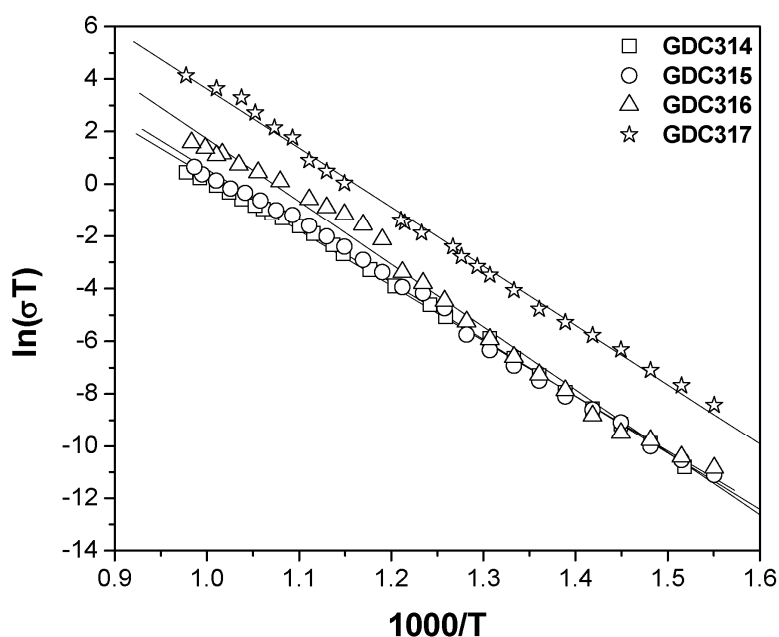


Figure 12. Typical effect of sintering temperatures on Arrhenius plot of dc conductivity of GDC30 samples.

The conductivity values at 1023K and activation energies calculated using eq. (4.6) are listed in table 5. It is evident from table 5 that for particular composition the activation energy for conduction goes on decreasing as sintering temperature is increased from 1473K to 1773K. An increase in conductivity with sintering



temperature is attributed to improved grain growth and intra-grain contacts. For optimized sintering temperature, the maximum dc conductivity was observed for GDC10 samples.

Sintering Temp. (K)	GDC10		GDC20		GDC30	
	Conductivity (S/cm)	$E_a$ (eV)	Conductivity (S/cm)	$E_a$ (eV)	Conductivity (S/cm)	$E_a$ (eV)
1473	$0.64 \times 10^{-3}$	1.25	$2.25 \times 10^{-3}$	1.37	$2.24 \times 10^{-3}$	1.27
1573	$0.94 \times 10^{-3}$	1.23	$1.00 \times 10^{-1}$	1.27	$4.28 \times 10^{-3}$	1.26
1673	$0.91 \times 10^{-1}$	1.04	$1.03 \times 10^{-1}$	1.14	$1.32 \times 10^{-2}$	1.22
1773	$1.20 \times 10^{-1}$	0.82	$1.05 \times 10^{-1}$	0.87	$1.10 \times 10^{-1}$	0.88

Table 5. Conductivity at 1023 K and activation energy ( $E_a$ ) of GDC samples.

For Gd doped ceria solid electrolytes, Zha et al [8] reported that the conductivity peaks at doping concentration of Gd,  $x = 0.15$ , (where,  $x$  is dopant concentration) while according to Yahiro et al [38] it peaks at  $x = 0.2$ . As we varied the dopant concentration with a large interval i.e. of  $\Delta x = 0.1$  and hence it may have masked the actual maxima, which might be at  $x = 0.15$ . However, above 990K the conductivity values are same ( $0.1 \text{ S-cm}^{-1}$  at 1023K), which almost equals the conductivity value of YSZ at 1273K [39].

In general (from table 5), it was observed that the activation energy increases with an increase in doping concentration of Gd in ceria. This observation could be attributed to the interactions of the substitutional cation with the charge-compensating oxygen vacancy it introduces. Since, from a combination of atomistic modeling [40, 41] and experimental studies [42], it was clear that the maximum in conductivity or a minimum in activation energy is caused by the interaction of the substitutional rare earth ion and the oxygen vacancy (point defects). Therefore, for higher dopant concentrations than the optimum (i.e.  $> 10\%$ ) results in distortion of crystal lattice, this increases the obstruction for electrical (ionic) conduction due to increasingly squeezed path for ion hopping. In addition the defect association, e.g.  $Gd_{Ce}^+ - V_o^{**}$  in our case, could increase with an increase in doping concentration and thereby dissociation of such pairs is restricted or postponed for higher operating temperature. Therefore,



for higher doping concentrations i.e. for GDC20 and GDC30 prepared with optimum sintering temperature showed higher activation energies of 0.87eV and 0.88eV respectively than that of for 10%Gd doping (0.82eV).

*b. Impedance measurements*

The impedance measurement is a well developed tool to separate out the bulk and grain boundary contributions to the total conductivity. The impedance spectrum is usually represented as negative of imaginary component of impedance ( $-Z''$ ) versus real component of impedance ( $Z'$ ), which is referred as Nyquist plot. The data points ( $Z'$ ,  $-Z''$ ) are measured for various frequencies. For typical polycrystalline materials data points on Nyquist plot approaches to the origin of plot as the frequencies of applied perturbation increases. Typically, the plot would be composed of three semicircles, each semicircle representing a distinct process whose time constant is sufficiently separated from the others over the range of measurement frequencies. The semicircles at higher and lower frequencies represent bulk and electrode processes, respectively, while that at intermediate frequencies represents grain boundary contribution. At higher temperatures, the time constants associated with the bulk and grain boundary impedances becomes much lower than those associated with the electrode interface. As a result, semicircles due to bulk and grain boundary disappear at higher temperatures, and only a semicircle due to electrode interfacial processes can be observed [43].

The typical Nyquist plot for GDC20 composition measured at 573K is shown in figure 13. It can be clearly seen that there exists three semicircles in the complex impedance plot corresponding to contribution from electrode, grain boundary and grain (i.e. grain interior) processes. However, with increase in measurement temperature, as mentioned earlier, the impedance contribution due to electrode processes increases and leads to enlargement of corresponding semi-circle in complex impedance spectra. Hence impedance spectra measured at higher temperature showed large semicircle due to electrode process and a tiny semi-circle corresponding to grain and grain boundary process at high frequency sides.



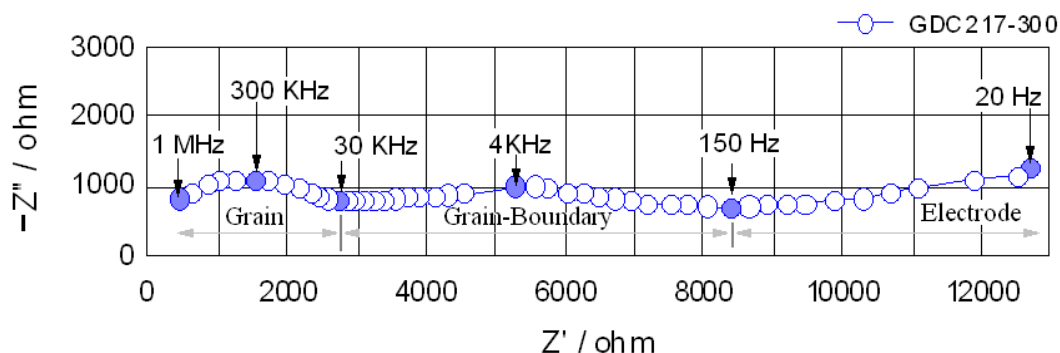


Figure 13. Typical complex impedance spectrum (Nyquist plot) for GDC217 sample measured at 573K.

At lower frequency side, if there exist a large capacitive (i.e. large  $-Z''$ ), it is believed that it is either due to ion blocking behavior of the sample at the electrode or it is due to electronic conduction in samples. As the ac impedance measurements were carried out in air and at temperature less than 1273 K (up to 873K), the possibility of electronic contribution, which in general occurs in GDC solid solution due to reduction of  $Ce^{4+}$  to  $Ce^{3+}$ , to the total conductivity is discarded. Hence it was understood that the spikes observed in impedance spectra at the lower frequency side is due to ion blocking behavior of electrodes and not due to electronic conduction in the samples.

It is well established fact that the microstructure e.g. density of grain boundaries, connectivity in grains, density of samples, etc. influence the ac impedance measurements. The typical effect of sintering temperature on ac impedance spectra for GDC20 samples measured at 573K is shown in figure 14. The maxima of capacitive values ( $-Z''$ ) of semicircle originating due to grain boundary decreases with an increase in sintering temperature. This confirms that with an increase in sintering temperature the density of grain boundaries decreases. Morphological characterization cleared that with an increase in sintering temperature, grain growth rate has improved (decreased grain boundary density). Thus it can be stated that the electrical contact between grains i.e. decreased grain boundary impedances (from impedance spectra) and compact grains (from SEM), improves with sintering temperatures.



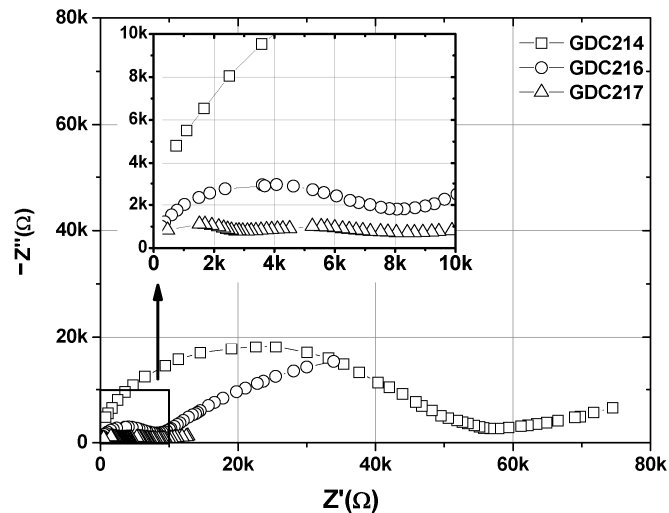


Figure 14. Typical effect of sintering temperature on ac impedance spectra measured at 573K for GDC20 samples.

An effect of doping concentration of Gd on impedance spectra of GDC solid solution is shown in figure 15. However, dependence of conductivity in GDC solid solution is not clear from the measured impedance plots (the frequency range was limited to 20Hz – 1MHz). And also the manual noting of data points puts large error bars in the measured readings. Hence no firm conclusions were drawn out of this part of measurements. However, by overall analysis of the total impedance, it was observed that total impedance of the GDC solid solution is more for higher concentration of ‘Gd’, indicating decrease in total ionic conductivity.

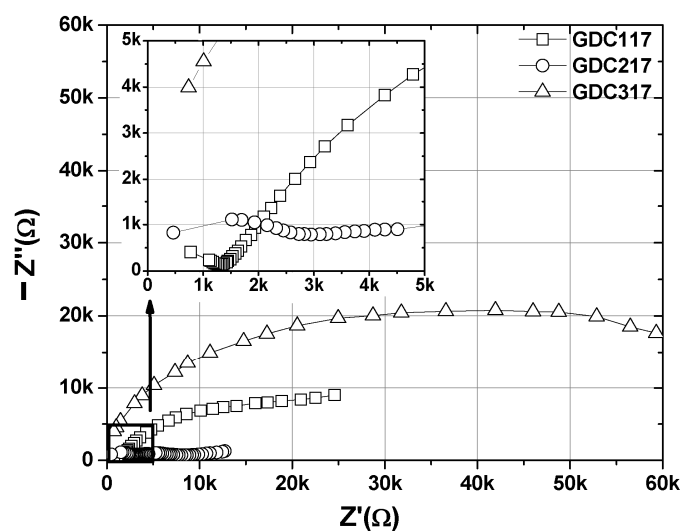


Figure 15. Typical effect of doping concentration of Gd on impedance spectra of GDC solid solution measured at 573K.





Figure 16 shows the typical effect of sintering on Arrhenius plots for ac conduction (calculated from the impedance data at 1 KHz at various measuring temperatures) for GDC20 samples. It can be seen from the plot that values of conductivity increases as sintering temperature is increased. Also the Arrhenius plots for ac conduction become steeper (increased slope) for increased sintering temperatures.

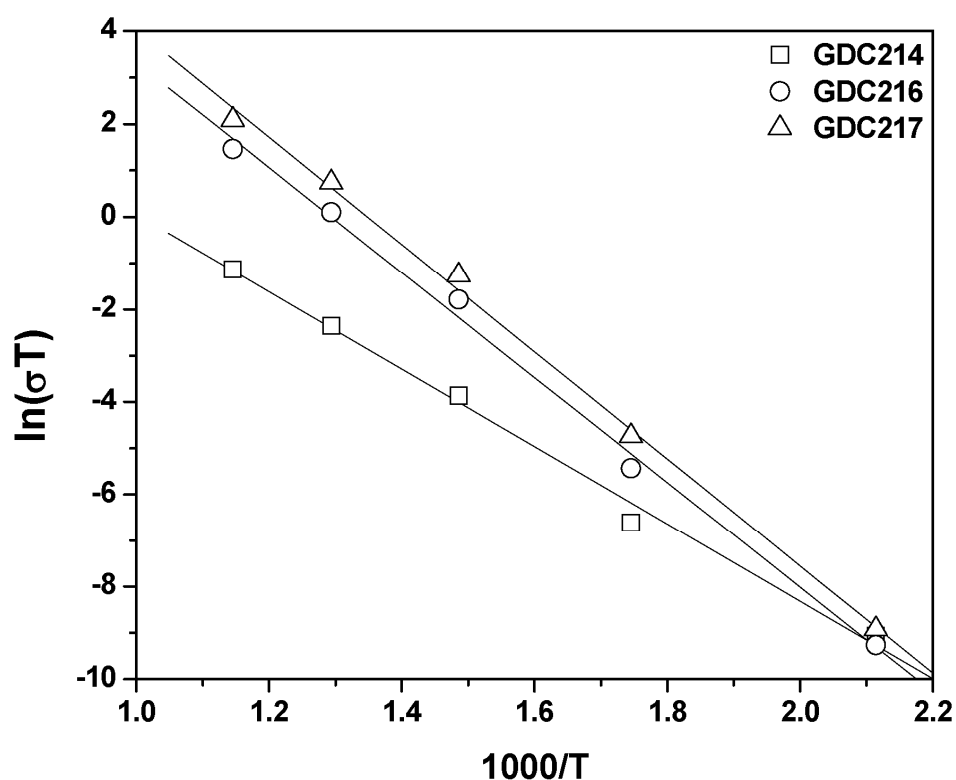


Figure 16. Typical effect of sintering temperatures on Arrhenius plots of ac conduction for GDC20 samples.

The ac conductance values were determined from the impedance data observed at 1 KHz frequency. With an increase in processing (sintering) temperature of samples the value of ac conductance were improved. The activation energy ( $E_a$ ) calculated using the eq. (4.6) is listed table 6. From these values of  $E_a$ , it is seen that although ionic conductivity (ac conductivity) in GDC10 samples are less than that of GDC20 samples, for every case of processing temperature, activation energy of ionic conductivity for GDC10 samples are least, which are in good agreement with reported



literature. This observation confirms that the GDC10 composition has better ionic conduction process than that of other compositions. However, the increasing trend of activation energy with sintering temperatures may be attributed to increased mean free path for ions within the grains (increased grain size).

Sintering temperature	Activation energy (eV)		
	GDC10	GDC20	GDC30
1473K	0.58	0.71	0.72
1573K	0.59	0.84	0.78
1673K	0.60	0.97	0.81
1773K	0.87	0.98	0.88

Table 6. The calculated activation energies for ac conductance.

#### 4.3.2.5. Outcomes of studies carried out in Section A

In this part of research, while synthesizing GDC solid solutions, processing parameters of ceramic route and doping concentration of Gd were varied and the effect on structural, morphological and electrical properties were studied.

The detailed analysis on micro-structural properties revealed that for a particular composition, as sintering temperature was increased, the densification and grain growth rate were observed to improve. However, with an increase in Gd doping concentrations the grain growth rate was observed to decrease while the densification rate was observed to increase. Detailed structural characterization of the samples sintered at 1773K showed the existence of a tiny  $\text{Ce}_2\text{O}_3$  peak for all three compositions studied. For 30% Gd doped ceria (sintered at 1773K), an extra peak due to  $\text{Gd}_2\text{O}_3$  phase was observed in addition to  $\text{Ce}_2\text{O}_3$  peak. Thus a provision to avoid the reduction during the sintering at high temperature should be practiced during the synthesis of GDC solid solution. Modification of conventional procedure of ceramic route is required. Also the maximum density achieved in this study was about 87-92% of theoretical value for the samples sintered at 1773K, which is not enough to use the samples as solid electrolyte.

The electrical characterizations of samples using dc and ac conductivity measurements showed that the electrical performance of the samples improves with



an increase in sintering temperature. The highest dc and ac conductance were observed for the samples sintered at 1773K. However, the activation energies ( $E_a$ ) for ac and dc conductivity were least for GDC10 composition for all the sintering temperatures employed in this study. Also there was a decreasing trend in  $E_a$  values of dc conductivity with an increase in sintering temperatures while it was reversed for ac conduction. Reverse trend of  $E_a$  for ac conduction was not cleared from measured impedance data and hence it was approximately attributed to an increase in mean free path of ions through grains due to enhancement in grain size with sintering temperature.

#### 4.3.3. Section – B: Precise optimization of processing parameters and Gd doping

According to Ma et al [44], Espositow et al [45] and from earlier studies i.e. section A [46] sintering temperatures and sintering duration plays the important role over the electrical properties of GDC solid solutions. However, high sintering temperature has been observed to induce the possibility of transition of valency in ceria based electrolytes. The concentration of Gd affects the electrical performance of the samples. Hence from the conclusions of earlier part of research final and precise optimization of processing parameters and Gd doping % were carried out. Initially the processing parameters such as addition of binder burnout step, variation in sintering temperature and duration were optimized for GDC10 and then applied for other compositions to optimize the doping concentration.

##### 4.3.3.1. Structural and elemental characterization

Figure 17 shows XRD patterns of GDC10 samples sintered at different temperatures, which were compared with JCPDS PDF no. 75-0161. All three samples showed the presence of (111), (200), (220), (311), (222), (400), (331), (420) and (422) reflection peaks in the scanning range 20–90° of  $2\theta$ . This confirms the ‘fcc’ structure of GDC10 sample. The GDC10 samples sintered at 1673 and 1773 are single phase and show no reflection peak due to reduction of ceria. However, a reflection peak due to  $\text{Ce}_2\text{O}_3$  emerges for GDC1018 at 26.73°. Obviously,  $\text{Ce}^{4+}$  has reduced to  $\text{Ce}^{3+}$ , which could be attributed to relatively higher sintering temperature than the optimum.



Thus, introduction of additional step of binder burn-out has shifted the reduction possibility by 100°C. The pre-sintering step allows the binder burnout prior to the final sintering and leads to a porous network of starting material's particles with excess amount of air in the pores. The presence of air in the sample pores during final sintering helps to avoid the reduction of ceria at 1773K (explained in next paragraph). However, even same porous network of starting material's particles with same amount of air in the pores could not avoid the reduction of ceria at 1873K, which may be attributed to thermally driven reduction of ceria.

The transition of Ce(IV) to Ce(III) as obtained in earlier investigation [46] for the samples sintered at 1773K/2h has not observed in the present work even for longer dwelling time (8h). This could be attributed to the additional step of binder-burnout introduced in the present work. It could be explained as follows: The PVA as binder (organic material) is commonly used during synthesis of green samples in ceramic route. When these green samples are introduced for thermal treatments, binder undergoes thermal decomposition and evolves voluminous product gases. When such green samples (having binder in its particle matrix) is allowed to sinter, the evolving gases have to find a way out of the sample. The evolving gases pressurize the surrounding particle matrix and flake out of the sample with keeping pore at its original place. However, these pores get filled during further heating process at higher temperatures. These evolving gases sometime block the contact of atmospheric air and particles at higher temperatures, where it could apparently establishes a very low oxygen partial pressure. If the pores (with low oxygen partial pressure) get blocked due to surface grain growth then the low oxygen partial pressure remains trapped in particle matrix. This apparent low oxygen partial pressure and high temperature greater than 1273K is a sufficient condition to provide the transition of Ce(IV) to Ce(III), a well known behavior of ceria. But the emergence of Ce<sub>2</sub>O<sub>3</sub> phase for GDC10 sample sintered at 1873K is solely attributed to the temperature in excess to optimum sintering temperature.

The lattice parameter '*a*' for GDC1016 was 5.4170Å, which increases to 5.4172Å for GDC1017 and further to 5.425Å for GDC1018. The crystallite sizes of the samples sintered at different temperature were calculated using the Scherrer's equation and was observed to increase with sintering temperature. It increases from 407nm for GDC1016 to 670nm for GDC1018. Similar increase in lattice parameter and crystallite size was reported by Morris et al. [47].



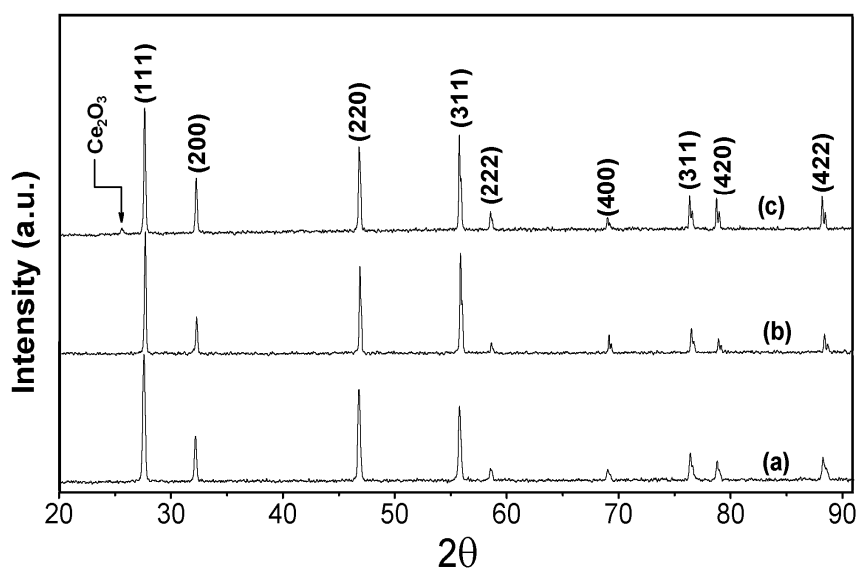


Figure 17. XRD patterns of (a) GDC1016, (b) GDC1017 and (c) GDC1018.

Energy dispersive analysis of X-ray (EDAX) was carried out to determine the exact atomic % in the sintered samples. The typical EDAX pattern of GDC10 sample sintered at 1873K is shown in figure 19. The atomic % of Gd and Ce were determined from the EDAX patterns of GDC10 samples as a function of sintering temperature and is shown in inset of figure 18. It signifies that Gd dissolution in ceria has increased with sintering temperature. However, it is to be noted that GDC10 samples sintered at 1773K/8h showed the Ce: Gd  $\approx$  0.9: 0.1, which was expected (optimum) dissolution of Gd into ceria.

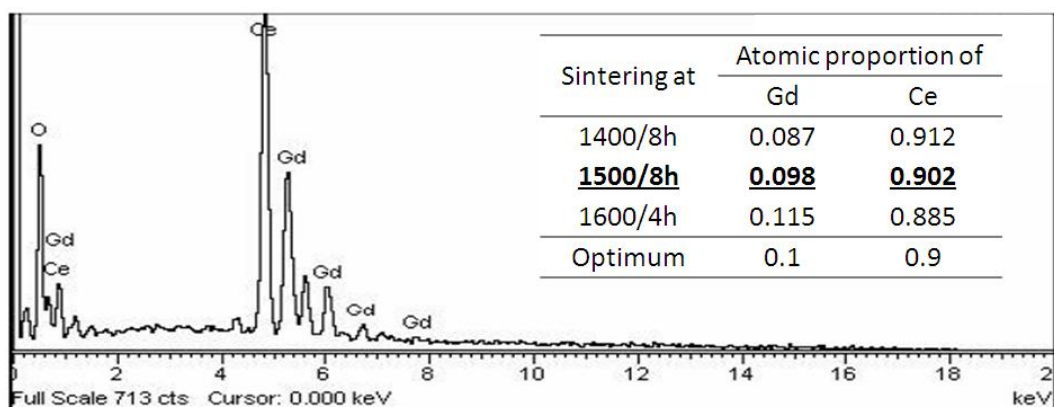


Figure 18. Typical EDAX pattern for GDC10 sample sintered at 1873K. Inset: Table showing atomic proportion of 'Ce' and 'Gd' in the sintered GDC10 sample.



In present work, GDC10 sample prepared with the binder burnout step at 1000°C and final sintering at 1773K/8h has shown fully dense GDC10 samples with expected phase pure composition. Hence sintering temperature at 1773K/8h was considered to be optimum and was applied to other compositions.

Figure 19 shows the XRD patterns of GDC1017, GDC2017 and GDC3017 samples prepared with optimized processing parameters. It confirms the formation of fluorite structured polycrystalline Gd doped ceria solid solutions. The XRD patterns of GDC1017, GDC2017 and GDC3017 matches well with respective JCPDS file nos. 75-0161, 75-0162 and 75-0163, respectively. There were no traces of  $\text{Ce}_2\text{O}_3$  phase detected. The crystallite size calculated using equation (4.2) for GDC1017, GDC2017 and GDC3017 are 0.980 $\mu\text{m}$ , 0.905 $\mu\text{m}$  and 0.470 $\mu\text{m}$ , respectively which clearly shows that with an increase in doping % of Gd, crystalline size drops slowly from GDC10 to GDC20 composition and falls rapidly for GDC30 composition.

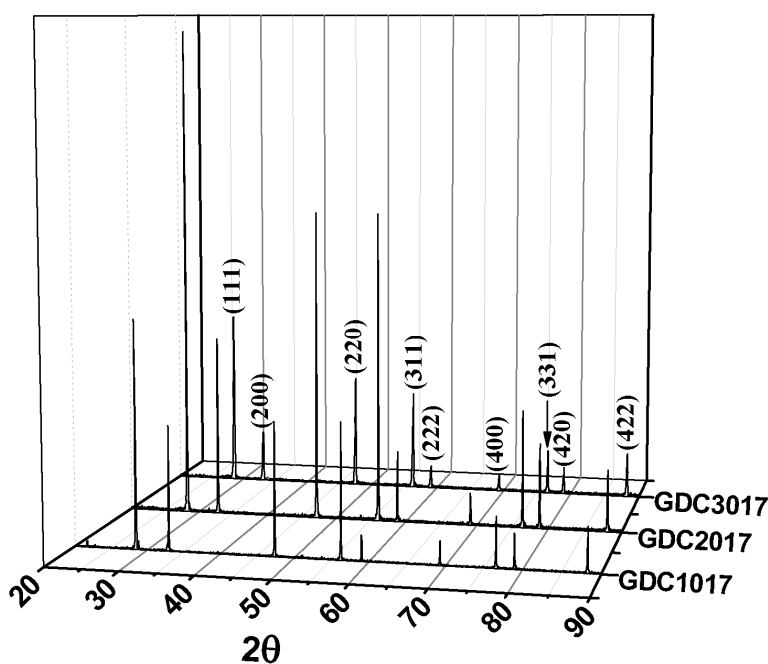


Figure 19. XRD patterns of GDC1017, GDC2017 and GDC3017 samples.

The lattice parameter for sintered GDC samples was observed to increase linearly with an increase in doping concentration of Gd in ceria. Figure 20 shows the dependence of  $a$ , unit cell parameter versus dopant concentration of  $\text{Gd}^{3+}$  ions,  $x$ , for



standard (from JCPDS) and prepared GDC samples. As the Gd concentration in composition increases, the lattice constant increases linearly as,  $a(x) = 5.414 + 0.047x$ , which indicates that these solid solutions obey Vegard's rule very well. The radii of  $\text{Ce}^{4+}$  and  $\text{Gd}^{3+}$  are 0.096 and 0.10nm, respectively [47] and hence when ceria is doped with larger sized  $\text{Gd}^{3+}$  ions with higher dopant concentration, the cubic ceria lattice expands. For standard values of lattice parameters (from JCPDS) for GDC, the linear relation is  $a(x) = 5.412 + 0.053x$ .

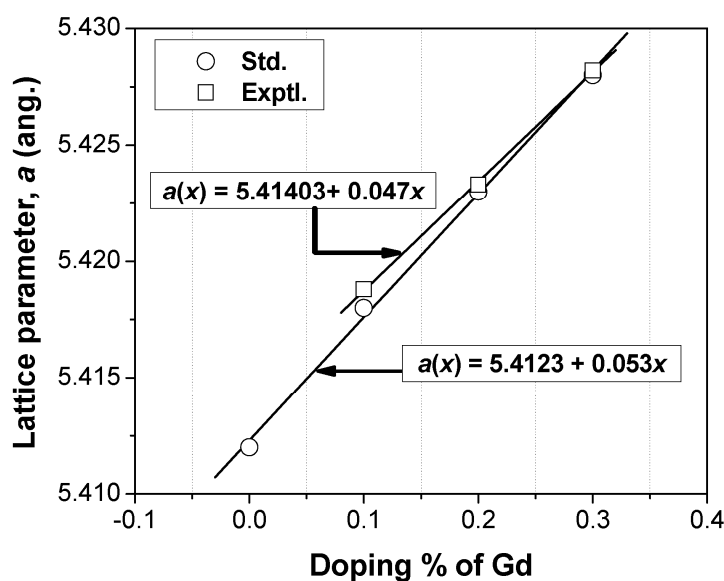
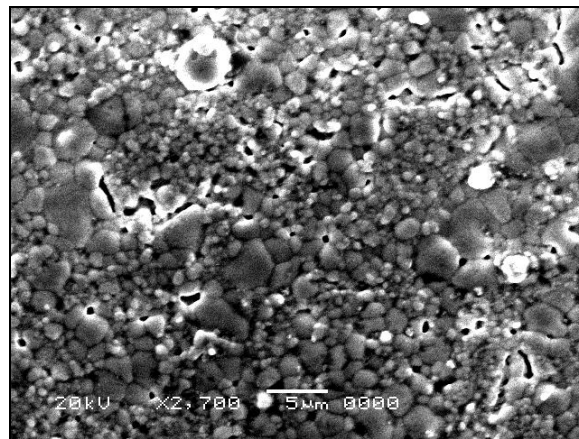


Figure 20. Variation of lattice parameter,  $a$ , with respect to doping % of Gd,  $x$ , in ceria solid solutions.

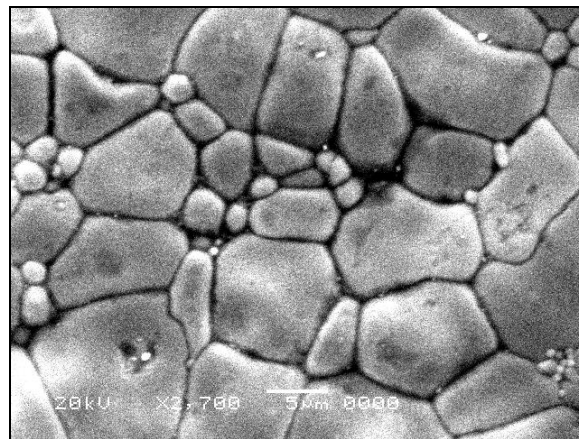
#### 4.3.3.2. Morphological characterizations and relative density measurements

The SEM images of GDC10 are shown in figure 21. As expected, the surface morphology is improved with sintering temperature. The grain size is observed to increase from  $2\mu\text{m}$  for sample sintered at 1673K (GDC1016) to  $5\mu\text{m}$  for GDC1017 sample and to  $11\mu\text{m}$  for GDC1018 sample, which implies that the grain growth rate in GDC1018 is much higher than that of other samples. GDC1016 sample have showed the porous surface which becomes denser for GDC1017 and GDC1018 samples. Further, more compact grains were observed for GDC1017 and GDC1018. The grain packing observed in SEM images was also reflected in the relative density measurements.

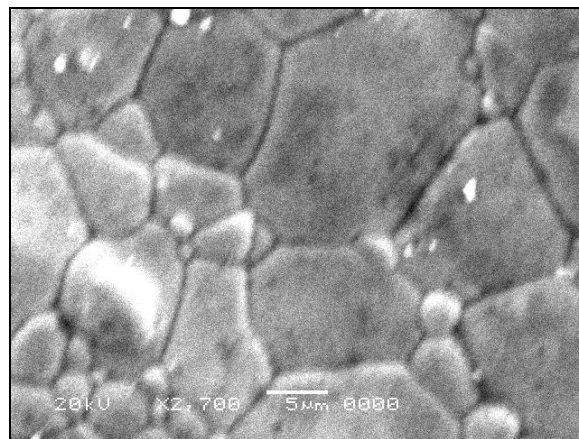




(a)



(b)



(c)

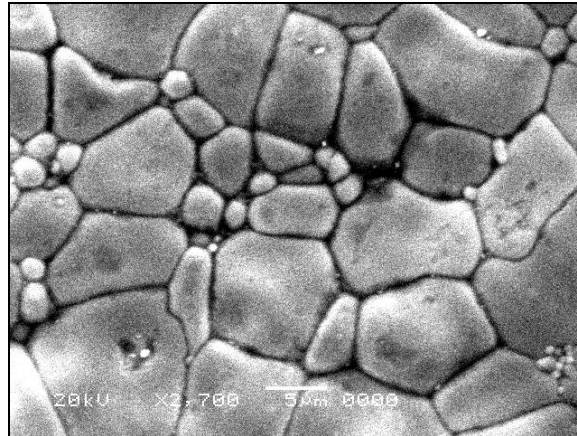
Figure 21. SEM of (a) GDC1016, (b) GDC1017 and (c) GDC1018.

The relative density for GDC1016 was 91% of theoretical value, which increased to 99% for samples sintered at 1773K for 8h (GDC1017). For further increase in sintering temperature i.e. sintering at 1873K for 4h (GDC1018), the relative density is lowered slightly to 98% of theoretical value. The decrease in the relative density observed for GDC1018 is obviously due to comparatively shorter

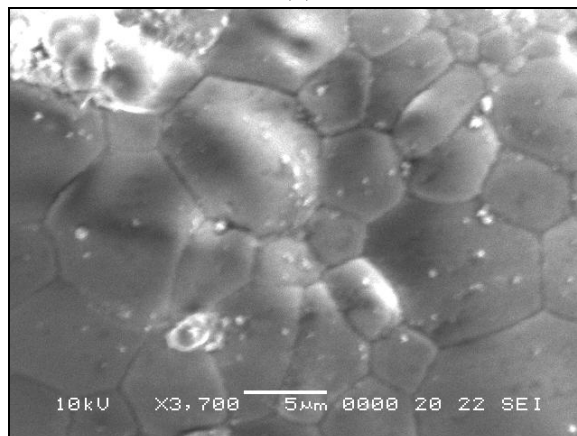




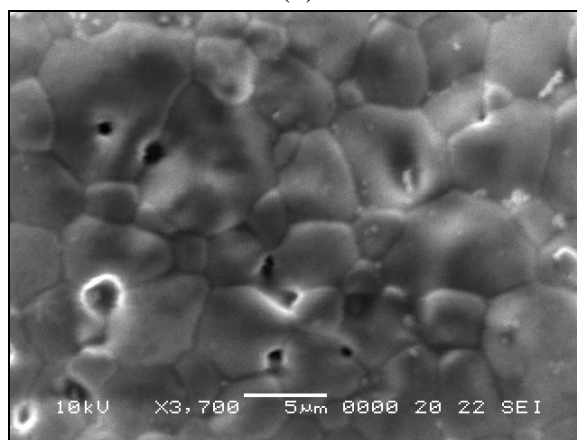
sintering duration employed i.e. 4h. Thus, this observation proves that in addition to sintering temperature, sintering duration certainly plays a supporting role in morphological and densification. Figure 22 shows SEM images of GDC1017, GDC2017 and GDC3017. SEM observation shows the compact and well connected grains with nearly uniform size for a particular composition.



(a)



(b)



(c)

Figure 22. SEM of (a) GDC1017, (b) GDC2017 and (c) GDC3017 samples.



The grain size determined using Cottrell's method and relative density is listed in table 7. The relative densities estimated were nearly same for all three compositions (greater than 98%). When these densities were compared with values from earlier studies (section A), there was much enhancement for the samples sintered at the same temperature. This enhancement in relative densities is entirely attributed to the pre-sintering step and increased sintering duration. Since, pre-sintering step burns binder from green body and dries it prior to the final sintering and hence allows large extent of shrinkage during final sintering, which further leads to higher density. This was not possible in case of sample preparation procedure without pre-sintering step, as followed in section A.

Sample ID	Average grain size ( $\mu\text{m}$ )	Relative density (%)
GDC1017	5.233	98.4
GDC2017	4.710	98.6
GDC3017	3.925	98.5

Table 7. Average grain size and relative densities for various GDC solid solutions.

From SEM images (figure 22) and table 7, it can be seen that the average grain size decreases with an increase in doping percentage of Gd in ceria, which is in agreement with earlier reported work [49]. This behavior is in accordance with the fact that addition of Gd to ceria makes the grain growth rates much slower and which is considered to be due to solute drag. Similar results were also published by H. Inaba et al [49] and in addition they observed that doped ceria becomes harder with an increase in Gd doping concentration.

It is interesting to note that as amount of Gd doping is increased, the grain growth is gradually postponed for a particular sintering temperature and duration. The SEM of GDC3017 sample (figure 22c) shows the sharp edged grains together with pores along the grain boundaries, at the same time the SEM of GDC2017 (figure 22b) shows the grains with comparably less sharp edges and almost no pores. In contrast to this, the SEM of GDC1015 (figure 22a) showed the globular shaped and relaxed grains with comparably narrow grain size distribution. The observed progress in grain growth or surface morphology as function of decrease in doping % of Gd exactly simulates the sequence in which the sintering mechanism progresses as function of



dwelling time. Thus correlating these, we can say that doping of Gd in ceria results in the delayed sintering mechanism, which in turn can be attributed to increase in solute drag for higher dopant concentrations. Accordingly, in general, it could be suggested that for the same sintering parameters, the compounds with different doping percentage could never attain the same grain morphology.

#### 4.3.3.3. Electrical characterizations

##### a. DC conductivity measurements

The dc conductivity measurement was done by two-probe method in the temperature range 300-1123K. The variations of  $\ln(\sigma T)$  with  $1000/T$  for GDC1016, GDC1017 and GDC1018 showed the similar behavior as that of earlier studied samples in section A. Hence it is also attributed to the same sources i.e. the change in slope at 573K is to initiation of ionic diffusion and that of at 923K may be due to slight change in mechanism of conduction.

The dc conductivity values at 973K for GDC1016, GDC1017 and GDC1018 is of the order of  $10^{-3}$  S/cm, which are lower than that of the samples prepared in earlier part of study (section A). This decrease in conductivity is attributed to the fact that with increase in thickness of sample, ohmic losses in the samples increases and hence it may lead to decrease in conductivity [50]. The thickness of pellets in earlier part of work was about 0.15–0.17cm, while that of samples studied in this section was 0.27–0.34cm (~2 times).

Figure 23 shows the variation of dc conductance for different measuring temperature. The conductivity values goes on increasing with measuring temperature for all three samples. However, comparably higher dc conductance was observed for GDC1017 sample for all the measuring temperatures while that of observed for GDC1016 remains constant. From activation energies ( $E_a$ ) for conductivity data, it is found that it decreases with an increase in sintering temperature. It was least for GDC1018 sample (0.7eV).



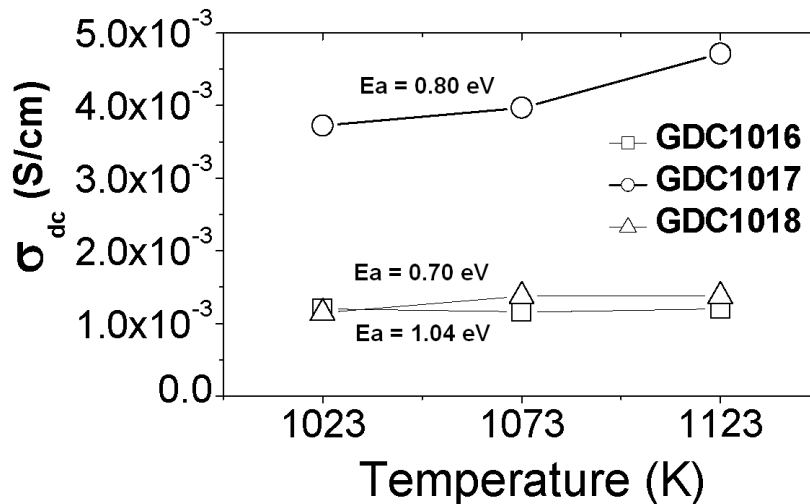


Figure 23. Variation of dc conductance with measuring temperature for GDC1016, GDC1017 and GDC1018 samples.

#### b. AC conductivity measurements

Figure 24 shows the impedance spectra of GDC1016, GDC1017 and GDC1018 samples measured at 573K. The impedance spectrum for all three samples showed the same trend consisting of a semi circle with tail at lower frequency. However, it should be noted the typical trend of three semicircles was missing in many cases due to the fact that the employed frequency range (20Hz-1MHz) was not wide as recommended (0.1Hz-15MHz) for characterization of solid ion conducting materials. Though these restrictions are there, the initial electrical characterization was done for frequency 20Hz – 1MHz to get an idea of ionic processes among the samples sintered at different temperatures.

In figure 24, semicircle due to grain boundary impedance for GDC1017 and GDC1018 is visible only in zoomed view (inset of figure 24). In all three plots semicircle originating from grain interior impedance is missing due to limit of frequency range. It is clear from figure that the sample sintered at higher temperature shows the lower span of semicircle on real axis. The decrease in diameter of semicircle for the sample sintered at higher temperature is consequence of reduced grain boundary contribution in the total impedance. This situation can be clearly recognized in its line plot which is shown in figure 24b, where arrows points to end of semi-circle due to grain boundary impedance responses. As observed in SEM images grains grow with



the sintering temperature and results into decreased density of grain boundaries, which is also confirmed from impedance data. However, it is noted here that SEM showed the surface morphology of the samples while impedance analysis confirms its bulk micro-structural as well as electrical properties without devastating the samples. The tails at lower frequency in impedance plots of GDC1017 and GDC1018 samples (not seen for GDC1016) is effect of electrode processes.

Ionic (ac) conductivity (for 1 KHz) estimated from ac measurements shows the improvement in its magnitude with sintering temperature. Ionic conductivity at 773K for GDC1016, GDC1017 and GDC1018 samples are  $0.21 \times 10^{-3}$  S/cm,  $0.43 \times 10^{-3}$  S/cm and  $0.53 \times 10^{-3}$  S/cm, respectively. However, the activation energy estimated from ac conductivity data showed a shallow fall in its value for GDC1017 (0.49eV) samples compared to GDC1018 (0.59eV) and GDC1016 (0.58eV) samples. This could be attributed to micro-structurally and electrically (for ion conduction) well developed grains, which was not true for GDC1016 sample. However, GDC1018 even showed well developed micro-structures (from SEM), the existence of undesirable phase in its XRD pattern may be attributing to its increased activation energy.

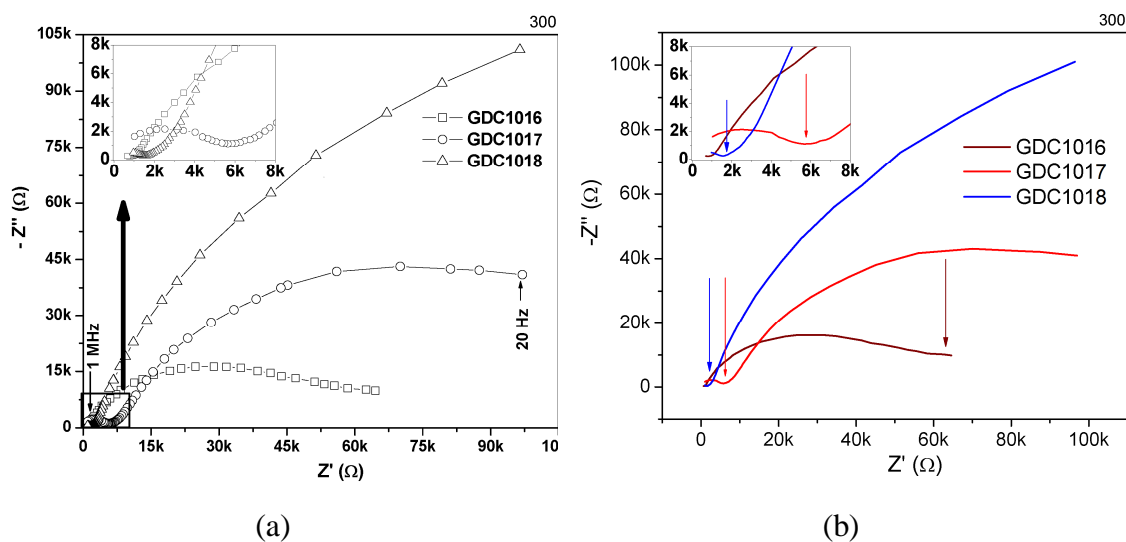


Figure 24. Complex impedance spectra of GDC1016, GDC1017 and GDC1018 samples at 573K.



c. Impedance analysis of  $Ce_{1-x}Gd_xO_{2-\delta}$ ; prepared with optimized processing parameters

For this part of study, highly sophisticated instrumentation for ac conductivity measurements were implemented for electrical characterization. The applied frequency range was varied from 0.1Hz to 10MHz, typically employed for the study of solid ionic materials. The typical complex impedance plot showing three semi-circles are illustrated in figure 25, however, they are merged and hence not showing their separate existence. Hence to avoid the complexity in analysis of the impedances, the electrode part is ignored. The semi-circles originating from electrode process, grain boundary process and grain interior process ends at 39.81Hz, 31.6 KHz and 10 MHz, respectively (figure 25). The notch observed at 1 MHz in grain interior impedance semicircle is due to switching of analyzer from 1MHz to a higher frequency value.

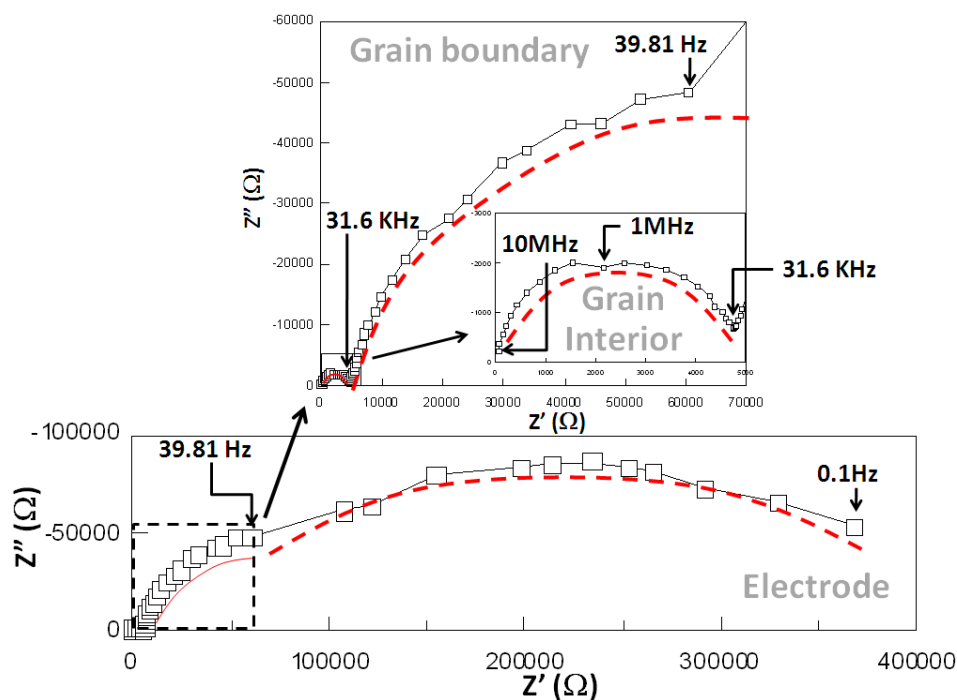


Figure 25. Typical complex impedance plot showing three semi-circles corresponding to grain interior, grain boundary and electrode processes for GDC1017 sample measured at 523K.



Figure 26 shows a typical variation in impedance spectra as function of measurement temperatures. It is clear from figure that all three contributions go on decreasing with an increase in measurement temperatures. At high temperatures (>673K), the semi-circle corresponding to grain interior contribution becomes undetectable and only a semi-circle due to grain boundary (comparably short span on real axis) and a semi-circle or linear spike due to electrode process is observed.

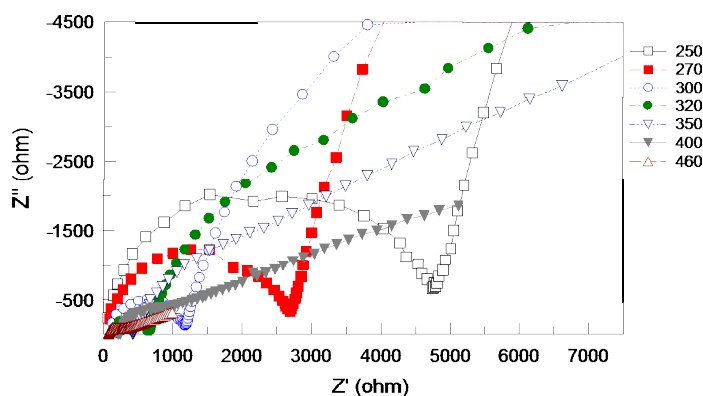


Figure 26. Typical variations in complex impedance spectrum for GDC1017 samples as function of measuring temperatures (523–773K; legends are in °C).

The impedance spectrum of the  $Ce_{1-x}Gd_xO_{2-\delta}$  ceramics were similar to those of other typical polycrystalline ion conducting materials such as Ytria-stabilized zirconia. Figure 27 shows the impedance spectra of Gd-doped ceria solid solutions, measured at 573K in air. The contributions of the grain interior and grain boundary behavior can be clearly identified from the figure. The sample with high Gd contents has a large grain boundary (GB) arc, implying that the blocking effect of grain boundaries dominates the total conductivity at 573K.



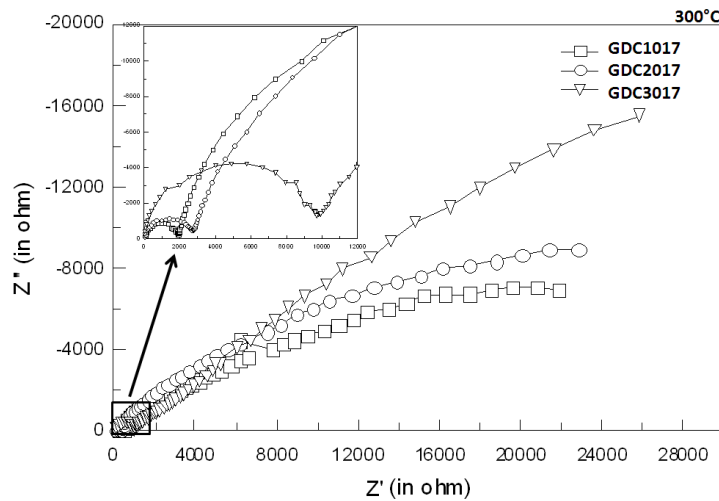


Figure 27. Isothermal complex impedance spectra for GDC1017, GDC2017 and GDC3017 samples measured at 573K.

The impedance data were analyzed by impedance analysis software (ZView Version 2.4 a) and used to extract the grain interior ( $R_g$ ) and grain boundary ( $R_{gb}$ ) impedances. The typical fit result from the analysis is shown in figure 28, for GDC1017 measured at 523K. Insets of the figure 28 shows model used to fit the data and the values obtained from the analysis.

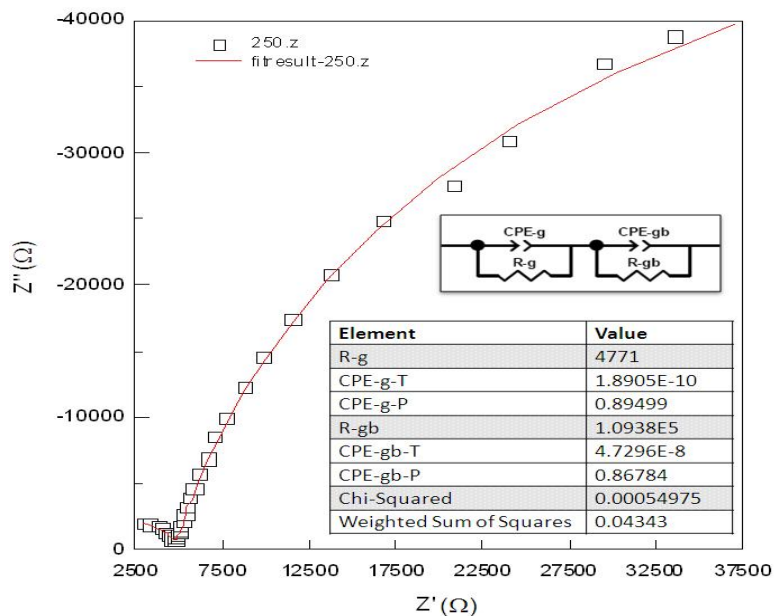


Figure 28. The typical fit results from the analysis of complex impedance plot for GDC1017 sample measured at 523K.





The extracted parameter for  $R_g$  and  $R_{gb}$  were used to calculate ac conductivities which were then fitted to the Arrhenius relation for thermally activated conduction. Figure 29 shows variation of  $\ln(\sigma T)$  as function of  $1000/T$  for GDC1017, GDC2017 and GDC3017 samples. In figure 29, 'Gr' and 'GB' stands for grain interior and grain boundary conductivities calculated for respective samples.

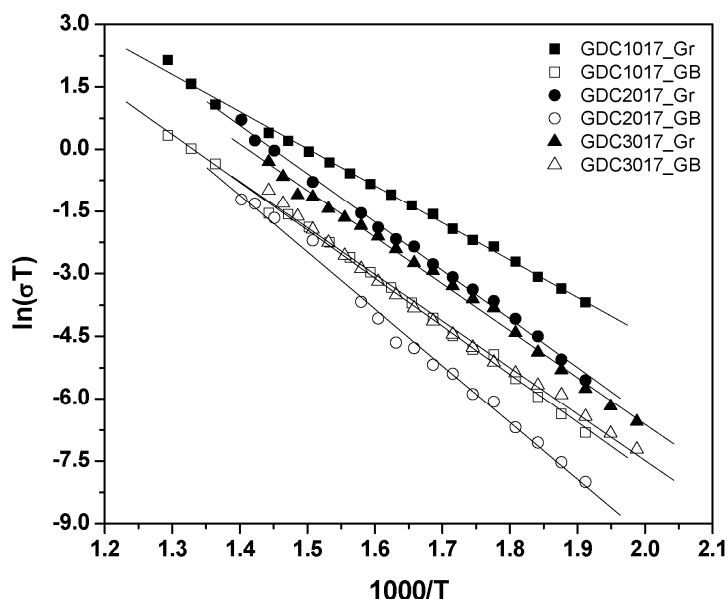


Figure 29. Arrhenius plot of grain interior (filled symbols) and grain boundary (empty symbols) conductivities measured in the temperature range from 250°C to 500°C.

It can be seen that grain interior conductivity ( $\sigma_g$ ) for GDC1017 is maximum while that of for GDC2017 and GDC3017 were in decreasing order, which is in line with earlier reported works in the literature [20, 51]. However, grain boundary conductivity ( $\sigma_{gb}$ ) in case of GDC2017 was observed to be least for all the measured range of temperature while for GDC1017 and GDC3017 it was comparable. At 773K, the grain boundary conductivity ( $\sigma_{gb}$ ) calculated from complex impedance spectrum is observed to decrease from  $1.8 \times 10^{-3}$  S/cm for GDC1017 to  $1.6 \times 10^{-3}$  S/cm for GDC2017 and again increases to  $1.8 \times 10^{-3}$  S/cm for GDC3017. The values of  $\sigma_g$ ,  $\sigma_{gb}$  with respective activation energies (i.e.  $E_g$  and  $E_{gb}$ ) along with activation energies ( $E_t$ ) for total conduction are listed in table 8.



Sample ID	$\sigma_g$ (S/cm)	$\sigma_{gb}$ (S/cm)	$E_g$ (eV)	$E_{gb}$ (eV)	$E_t$ (eV)
GDC1017	0.0109	0.001809	0.75	0.97	0.96
GDC2017	0.0036	0.001607	1.01	1.14	1.14
GDC3017	0.0029	0.001810	0.96	0.99	0.98

Table 8. Variation in conductivities and activation energies of GDC samples. Grain interior ( $\sigma_g$ ) and grain boundary conductivities ( $\sigma_{gb}$ ) were measured at 773K and  $E_g$ ,  $E_{gb}$  and  $E_t$  are activation energies for grain interior, grain boundary and total conductivities, respectively.

It is well documented in literature that in high-purity raw materials (i.e.  $\text{SiO}_2$  content is less than 50ppm), the grain boundary behavior is usually attributed to intrinsic blocking behavior space charge effect [50, 52]. Additionally, for the impure raw materials (i.e.  $\text{SiO}_2$  contents is greater than 200ppm) the blocking effect due to presence of siliceous phase along the grain boundary is dominant. Typically the  $\text{SiO}_2$  content in the commercial raw powders is 200ppm [53], which is same for the present work. Based on the space-charge layer theory as discussed in references [50, 52], a grain boundary consists of a grain boundary core and two adjacent space-charge layers of both sides. In the Gd-doped ceria solid solutions, effectively negatively charged  $Gd'_{Ce}$  species segregate at the grain boundaries, in which positively charged  $V_o^{\bullet\bullet}$  are depleted. Therefore, the space-charge layers formed by the negatively charged  $Gd'_{Ce}$  resist the movement of  $V_o^{\bullet\bullet}$  across the grain boundaries. Thus the presence of the siliceous film at the grain boundaries could be a major factor dominating the grain boundary conductivity in addition to the space-charge effect leading to low GB conductivities.

With an increase in Gd content from 10 to 20%, the decrease in GB conductivity could be attributed to the blocking behavior originated from the thin siliceous film in addition to segregated negatively charged  $Gd'_{Ce}$  species along the grain boundary. However, for high Gd content (30% Gd), grain boundary conductivity was increased, which could be attributed to the decreased GB blocking behavior. The decrease in GB blocking would be due to presence of excess negatively charged  $Gd'_{Ce}$  species (30%Gd) along the grain boundary which, according to Guo et al. [52], decreases the space charge potential.



According to T.S. Zhang et al [54], for a polycrystalline oxygen-ion electrolyte, the activation energy for total ionic conduction should come from three sources, that is, the enthalpy of migration of oxygen ions ( $\Delta H_m$ ), the association enthalpy of complex defects ( $\Delta H_a$ ), and the activation energy for the grain boundary conduction ( $E_{Gb}$ ). However, in a low temperature range (e.g.  $\leq 500^\circ\text{C}$ ); these three sources simultaneously limit the total ionic conductivity. Moreover, T.S. Zhang et al [54] further cleared that with increasing temperature, the grain boundary effect and the association enthalpy of complex defects (e.g.  $Gd_{ce}^I - V_o^{**}$ ) gradually disappears. As a result, only the enthalpy of migration of oxygen ions ( $\Delta H_m$ ) plays a major role in limiting the total ionic conductivity and thus the activation energy at high temperatures e.g.  $500\text{--}700^\circ\text{C}$  could be further smaller than that of at  $250\text{--}500^\circ\text{C}$  (employed in present case). However, the activation energies estimated in the present work well matches with the earlier reported work for all the three compositions. Among the three compositions, GDC1017 (i.e. 10%Gd doped ceria) sample showed the least activation energy for conduction through grain and grain boundaries and least activation energy for total conduction.

#### 4.4. Conclusions

The optimization of processing parameters of ceramic route to prepare GDC solid electrolyte for the implementation in IT-SOFC results in following conclusions: The 'electrolyte-quality' GDC samples could be prepared using the ceramic route. By modifying the conventional procedure of ceramic route i.e. by implementing 5-step process (additional pre-sintering step) could avoid the reduction of ceria at high sintering temperatures. The high enough sintering temperature for GDC samples to form the lattice structure approaching to the standard one with the relative density of 99% is 1773K (8h). It has also been observed that the longer the sintering duration higher the densification of samples. Apart from these sintering parameters, the thickness of the samples also plays the critical role in impeding the electrical performance of samples. It was observed that the electrical performance of solid electrolyte is inversely proportional to thicknesses of the samples.

The optimization of doping concentration of Gd in ceria enabled us to point out the doping % desirable for best solid electrolyte. With an increase in doping



concentration of Gd, the grain growth rate of GDC was observed to reduce leading to a decrease in average grain size. Further, the linear variation of lattice parameter for GDC solid solution with Gd doping concentration confirms the dissolution of Gd in ceria. The electrical characterization confirmed that the grain boundary conductivities showed the ion blocking behavior due to existing impure phases in commercially available raw powders. However, the GDC10 composition showed the highest grain interior ionic conductivity in addition to total conductivity with activation energy of 0.75eV.

Thus, the optimized process parameters for ceramic route to prepare Gd doped ceria based solid electrolyte with intention to use it in IT-SOFC, would use 10% doping of Gd in ceria to form the solid electrolyte composition. While synthesizing the solid electrolyte using solid state reaction the ceramic route with binder added step (5 – step) should be followed and thickness of the solid electrolytes should be maintained below 0.15 cm (electrolyte supported cell configuration). Finally the sample should be processed at optimized sintering temperature ( $\geq 1773\text{K}$  and  $< 1873\text{K}$ ) and duration ( $\geq 8\text{h}$ ).

## References

- [1] B.C.H. Steele, NATO ASI Series, Series E, *App. Sci.* 368 (1997) 323.
- [2] H. Huang, X. Feng, W. Zhu, Y. Zhang, T. Wen, T. Tang, *J. Phys. Condens. Matter.*, 15 (2003) 5689.
- [3] B.C.H. Steele, *Solid State Ionics* 134 (2000) 3.
- [4] M. Sahibzada, B.C.H. Steele, K. Hellgardt, D. Barth, A. Effendi, D. Mantzavinos, I.S. Metcalfe, *Chem. Eng. Sci.* 55 (2000) 3077.
- [5] B.C.H. Steele, *J. Mater. Sci.* 36 (2001) 1053.
- [6] S. Zha, Q. Fu, Y. Lang, C. Xia, G. Meng, *Mater. Lett.* 47 (2001) 351.
- [7] C. Peng, Y. Zhang, Z.W. Cheng, X. Cheng, J. Meng, *J. Mater. Sci.* 13 (2002) 757.
- [8] S. Zha, C. Xia, G. Men, *J. Power Sources* 115 (2003) 44.
- [9] B. C. H. Steele, *Solid State Ionics* 134 (2000) 3.
- [10] L.D. Jadhav, S.H. Pawar, M.G. Chourashiya, *Bull. Mater. Sci.* 97 (2007) 30.
- [11] S. W. Zha, Q. X. Fu, Y. Lang, C. R. Xia, G. Y. Meng, *Mater. Lett.* 47 (2001) 351.



- [12] W Huang, P. Shuk, M. Greenblatt, *Solid State Ionics* 100 (1997) 23.
- [13] C. Xia, M. Liu, *Solid State Ionics* 152 (2002) 423.
- [14] K. Wang, R. S. Ticky, J. B. Goodenough, *J. Am. Ceram. Soc.* 81 (1998) 2565.
- [15] T. S. Zhang, L B. Kong, Z Q. Zeng, H.T. Huang, P. Hing, Z.T. Xia, J. A. Kilner, *J. Solid State Electrochem.* 7 (2003) 348.
- [16] A.D. Brailsford, D.K. Hohnke, *Solid State Ionics* 11 (1983) 133.
- [17] M. Kleitz, L. Dessemond, M.C. Steil, *Solid State Ionics* 75 (1995) 107.
- [18] C.S. Chen, M.M.R. Boutz, B.A. Boukamp, A.J.A. Winnubst, K.J. de Vries, A.J. Berggraaf, *Mater. Sci. Eng.* 168 (1993) 231.
- [19] Brian D. Madsen, Scott A. Barnett, *Solid State Ionics* 176 (2005) 2545.
- [20] G.B. Balazs, R.S. Glass, *Solid State Ionics* 76 (1995) 155.
- [21] T.S. Zhang, J. Ma, H.T. Huang, P. Hing, Z.T. Xia, S.H. Chan, J.A. Kilner, *Solid State Sci.* 5 (2003) 1505.
- [22] A.L. Stuijts, C. Kooy, *Sci. Ceram.*, 2 (1967) 231.
- [23] Muthukkumaran, P. Kuppusami, E. Mohandas, V.S. Raghunathan, S. Selladurai, *Int. Symp. Res. Students on Mater. Sci., Eng., Chennai, India* (2004) 1.
- [24] M. Mogensen, N.M. Sammes, G.A. Tompsett, *Solid State Ionics* 129 (2000) 63.
- [25] H. Inaba, T. Nakajima, H. Tagawa, *Solid State Ionics* 106 (1998) 263.
- [26] W.D. Kingery, H.K. Bowen, D.R. Uhlmann, *Introduction to Ceramics, 2nd ed.*, John Wiley, New York (1976) 456.
- [27] S. Hwang, I. Chen, *J. Am. Ceram. Soc.* 73 (1990) 3269.
- [28] M.M.R. Boutz, A.J.A. Winnubst, A.J. Berggraaf, *J. Eur. Ceram. Soc.* 13 (1994) 89.
- [29] D.D. Upadhyaya, R. Bhat, S. Ramanathan, S.K. Roy, H Schubert, G. Petzow, *J. Eur. Ceram. Soc.* 14 (1994) 337.
- [30] M.M.R. Boutz, C.S. Chen, L. Winnubst, A.J. Berggraaf, *J. Am. Ceram. Soc.* 77 (1994) 2632.
- [31] G.S.A.M. Theunissen, A.J.A. Winnubst, A.J. Berggraaf, *J. Mater. Sci.* 27 (1992) 5057.
- [32] H. Inaba, *Proc. of Powder Metallurgy World Congress, Kyoto* (1993) 381.
- [33] T. Ikegami, M. Tsutsumi, S. Matsuda, S. Shirasaki, H. Suzuki, *J. Appl. Phys.* 49 (1978) 4238.
- [34] G.C. Kuczynski, *Trans. AIME* 185 (1949) 169.
- [35] R.L. Coble, *J. Appl. Phys.* 32 (1961) 787.

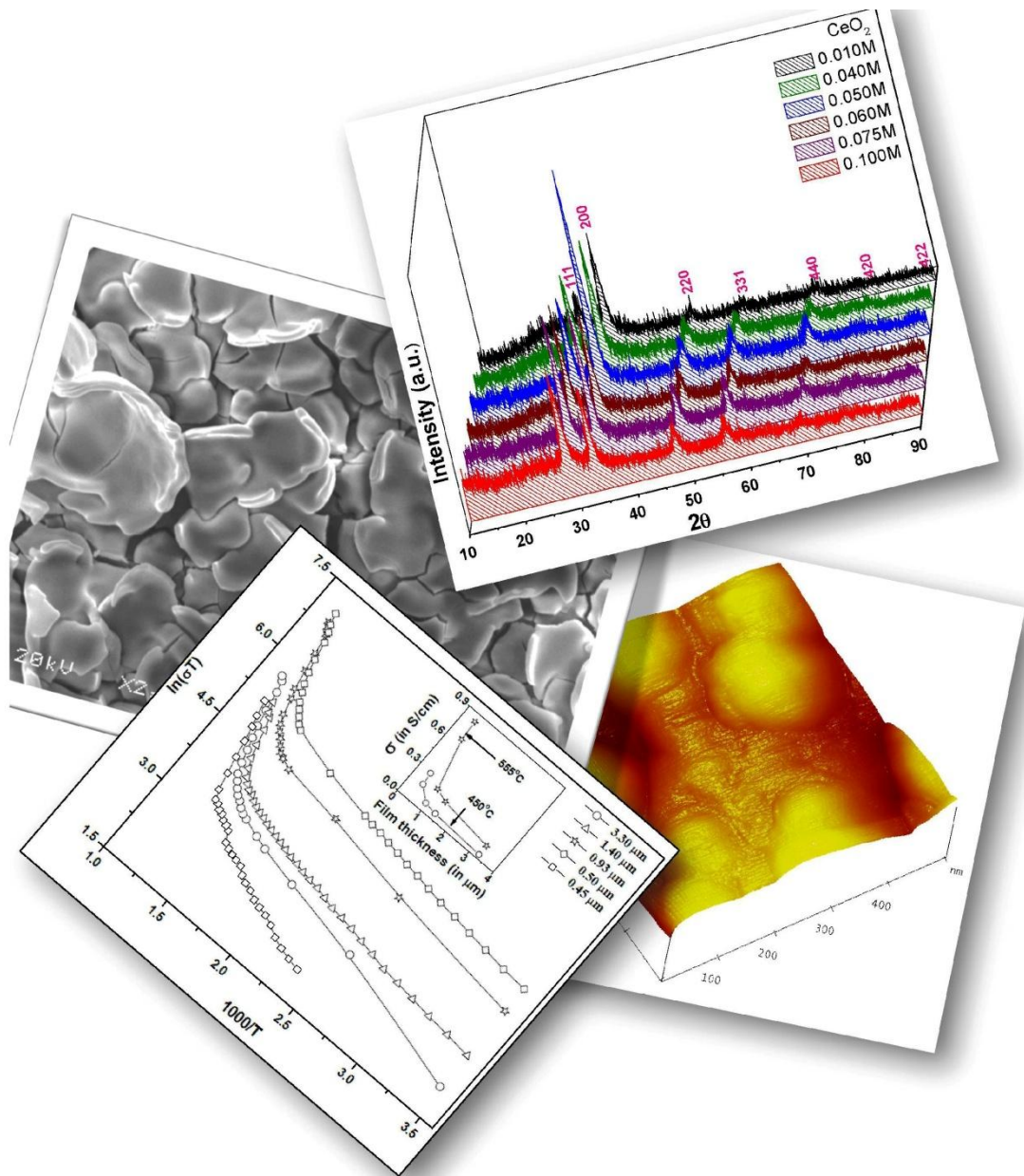


- [36] R.L. Coble, *J. Appl. Phys.* 32 (1961) 793.
- [37] J.A. Kilner, CD. Walters, *Solid State Ionics* 6 (1982) 253.
- [38] H. Yahiro, Y. Eguchi, K. Eguchi, H. Arai, *J. Appl. Electrochem.* 18 (1988) 527.
- [39] X.J. Chen, K.A. Khor, S.H. Chan, L.G. Yu, *Mater. Sci. Eng. A* 335 (2002) 246.
- [40] Butler, V., et al., *Solid State Ionics* (1983), 8, 109
- [41] Minervini, L., et al., *Solid State Ionics* (1999), 116, 339
- [42] J. A. Kilner, *Solid State Ionics* (2000), 129 (1-4), 13
- [43] D.L. Maricle, T.E. Swarr, S. Karavolis, *Solid State Ionics* 52 (1992) 173
- [44] J. Ma, T.S. Zhang, L.B. Kong, P. Hing, S.H. Chen, *J. Power sources* 132 (2004) 71.
- [45] V. Espositow, E. Traversa, *J. Am. Ceram. Soc.* 91 (2008) 1037.
- [46] M.G. Chourashiya, J.Y. Patil, S.H. Pawar, L.D. Jadhav, *Mater. Chem. Phy.* 109 (2008) 39.
- [47] V. N. Morris, R. A. Farrell, A. M. Sexton, M. A. Morris, *J. Phy. Conf. Series: Imaging, Analysis and Fabrication on the Nanoscale* 26 (2006) 119.
- [48] K. Eguchi, T. Setoguchi, T. Inoue, H. Arai, *Solid State Ionics* 52 (1992) 165.
- [49] H. Inaba, H. Tagawa, *Solid State Ionics* 83 (1996) 1.
- [50] X. Guo, *Solid State Ionics* 81 (1995) 235.
- [51] Steele B.C.H., *Solid State Ionics* 129 (2000) 95.
- [52] Guo X., W. Sigle, J. Maier, *J. Am. Ceram. Soc.* 86 (2003) 77.
- [53] M. Aoki, Y.M. Chiang, I. Kosacki, L.J. Lee, H. Y. Tuller Liu, *J. Am. Ceram. Soc.* 79 (1996) 1169.
- [54] T.S. Zhang, J. Ma, H. Cheng, S.H. Chan, *Mater. Res. Bull.* 41 (2006) 563.



# Chapter five:

*Synthesis and characterization of 10%Gd doped ceria thin films using spray pyrolysis technique.*







# Chapter five

## CONTENTS

5. SYNTHESIS AND CHARACTERIZATION OF 10%GD DOPED CERIA (GDC10) THIN FILMS USING SPRAY PYROLYSIS TECHNIQUE. ....	186
Keywords: CeO <sub>2</sub> and GDC10 thin films, Spray pyrolysis technique, XRD, EDAX, SEM, AFM, effect of thickness on electrical properties.....	186
5.1. Introduction .....	187
5.2. Experimental.....	188
5.2.1. Introduction .....	188
5.2.2. CeO <sub>2</sub> (ceria) thin films:.....	190
5.2.2.1. Synthesis of ceria thin films:.....	190
5.2.2.2. Characterizations and optimizations .....	190
5.2.3. GDC10 thin films.....	190
5.2.3.1. Synthesis of GDC10 thin films:.....	190
5.2.3.2. Characterizations and optimizations .....	191
5.3. Results and discussions .....	192
5.3.1. Introduction .....	192
5.3.2. TG-DTA of cerium nitrate (Ce(NO <sub>3</sub> ) <sub>3</sub> .6H <sub>2</sub> O).....	192
5.3.3. Synthesis and characterizations of CeO <sub>2</sub> thin films on glass substrate.....	194
5.3.3.1. Effect of precursor solution concentrations:.....	194
5.3.3.2. Effect of annealing on crystalline nature of ceria thin films: .....	197
5.3.4. Synthesis and characterizations of GDC10 (Ce <sub>0.9</sub> Gd <sub>0.1</sub> O <sub>2-δ</sub> ) thins films.....	198
5.3.4.1. Optimization of substrate temperature.....	199
5.3.4.2. Optimization of precursor solution concentration .....	206
5.4. Conclusions.....	215
References.....	216

## 5. SYNTHESIS AND CHARACTERIZATION OF 10%Gd DOPED CERIA (GDC10) THIN FILMS USING SPRAY PYROLYSIS TECHNIQUE.

### Abstract:

Gd doped ceria (GDC) films are of great importance in concern with its applications in intermediate temperature (IT) or low temperature (LT) solid oxide fuel cells (SOFCs). Since, the use of thin film GDC electrolyte in SOFC keeps the ohmic losses at minimum level and allows the SOFC to operate at lower temperature (~773K). The 10%Gd doped ceria (GDC10) is characterized by highest ionic conduction properties among the other doping concentrations. Here, the spray pyrolysis technique (SPT) is employed to prepare GDC10 thin films. The preparative parameters of SPT such as substrate temperatures, precursor's concentrations, annealing temperature, etc. were varied to obtain dense, adherent and uniform depositions of GDC10 thin films (on glass substrates).

Initially, the CeO<sub>2</sub> (host material) were deposited and optimized by varying the preparative parameters of SPT. Substrate temperature (i.e. decomposition temperature) was determined from TG-DTA of host precursor. The solution concentration was optimized by analyzing the XRD patterns obtained for various films prepared using different precursor concentrations. Post annealing treatment has found to improve the crystalline nature of films and hence was assumed to be a mandatory step in processing of GDC10 thin films. These initial optimized preparative parameters of SPT for CeO<sub>2</sub> films were taken as seed parameters to obtain GDC10 thin films. The substrate temperature and solution concentration were varied about seed parameters to obtain smooth, uniform and dense GDC10 films. These GDC10 films were characterized by XRD and EDAX for structural and elemental characterization while SEM and AFM were employed to characterize the micron and atomic level morphologies, respectively. From fractured SEM it was revealed that the maximum thickness on glass substrate was ~3.3μm. Finally, electrical characterizations of GDC10 films were carried out using two probe dc conductivity measurements. The effect of film thickness on electrical properties of films was also investigated. The dc conductivity decreases with an increase in thickness of the films. The dc conductivity was observed to be ~0.5 S/cm at 623 K, which is five times than that of YSZ at 1273K (0.1S/cm)<sup>†</sup>.

**Keywords:** CeO<sub>2</sub> and GDC10 thin films, Spray pyrolysis technique, XRD, EDAX, SEM, AFM, effect of thickness on electrical properties.

<sup>†</sup> This work is published in *Applied Surface Science*.



## 5.1. Introduction

Besides having an excellent ionic conduction behavior, Gd doped ceria (GDC) has a relatively narrow region of oxide ion conductivity as an electronic component is introduced on reduction [1]. When the ceria based electrolyte is subjected to low partial pressure of oxygen, typically associated with the anode side of a fuel cell, its electronic contribution to the overall conductivity increases. This increase in electronic conduction, due to the reduction of  $\text{Ce}^{4+}$  to a  $\text{Ce}^{3+}$  state, shorts out the electrolyte results in failure of the electrolyte [2]. However, thin film technology could enable Gd doped ceria electrolytes to be operated at further reduced temperature, thereby eliminating the negative aspect of reducing behavior (observed only above 973K) [3].

Therefore, GDC in thin film form could be of great importance in concern with its applications in intermediate temperature (IT) or low temperature (LT) solid oxide fuel cells (SOFCs). Since, the use of thin film GDC electrolyte in SOFC keeps the ohmic losses at minimum level and allows the SOFC to operate at lower temperatures (~773K). The high ionic conductivity of GDC (bulk samples) at 773-923K than that of conventional solid electrolyte, Ytria stabilized Zirconia (YSZ), make it appropriate to implement in IT-SOFCs. Further, if GDC is fabricated in thin film forms it would show a possibility of further reduction in operating temperature thereby allowing its use in LT-SOFCs (673-773K). The reduction of operating temperature offers number of advantages as it solves the problems related to reliability, efficiency and cost of manufacturing of the oxygen permeable devices (OPDs) e.g. SOFCs, etc.

Lowering the operating temperature of OPDs assures the following advantages:

- Metallic interconnects can be used
- Easier sealing is possible
- Smaller thermal mismatch between constituent components
- Less insulation material is required
- Rapid startup with less energy consumption is possible

To reduce the electrolyte thickness, various thin film deposition methods have been applied so far e.g. electrochemical vapor deposition (EVD) [4], physical vapor deposition (PVD) [5], vacuum plasma spraying [6], tape casting [7], screen printing



[8], slurry dip coating technique [9], chemical spray technique [10], aerosol-assisted metal-organic chemical vapor deposition (AA-MOCVD) technique [11], etc. Earlier investigations [12-17] have revealed strong promise of chemical spray deposition techniques for the fabrication of thin electrolyte films. This technique has the potential to prepare the dense and 2-20 $\mu\text{m}$  thin films which are the essential requirements of materials to be used as solid electrolytes (to be operated in low temperature regime) in any OPD's. SPT has the advantage of being simpler, cost effective and well known for the deposition of metal oxide thin films [18, 19]. In addition to its simplicity it possesses following advantages:

- Unlike closed vapor deposition method, spray pyrolysis neither requires high quality targets and/or substrates nor does it require vacuum at any stage.
- SPT can produce films even on less robust material because it operates at moderate temperature (100-550°C) and at ambient pressures.
- By changing composition of the spray solution during the spray process, it can be used to make layered films and the films having composition gradients throughout the thickness.
- It offers an extremely easy way to dope films with any element in any proportion by merely adding it in some form to the spray solution.
- The deposition rate and the thickness of the films can be easily controlled over a wide range by changing the spray parameters
- Unlike high power methods such as radio frequency magnetron sputtering (RFMS), it do not cause local over-heating that can be harmful for materials to be deposited. There are virtually no restrictions on substrate material, dimension or its surface profile.

## 5.2. Experimental

### 5.2.1. Introduction

As discussed in chapter 3, there are different preparative parameters of SPT which can directly or indirectly affect the film's chemical compositions, surface morphologies, adherence, density, etc. Hence to obtain the thin films with desired properties one has to optimize the preparative parameters. The effect of each of the preparative parameter is described in detail in chapter 3 and a general scheme of



optimization is also discussed. As there are six to eight preparative parameters in a SPT, it is cumbersome task to optimize all. Hence, it is strongly recommended to fix some of them and vary as few as possible parameters. Here the type of salt used for fabrication of thin films was nitrate of respective metals, the substrate to nozzle distance was kept fixed to 25cm and nozzle cyclic motion was fixed to a rate of 1cm/sec (linear traversing length was 30cm).

The remaining preparative parameters such as solution concentration, substrate temperature, solution spray rate (by controlling air pressure and solution quantity), were optimized by preparing the thin films for different parameter values and characterizing the same with different characterization techniques. The process of optimization and film formation of CeO<sub>2</sub> (host material) and GDC10 composition are discussed here. The characterized properties of films (CeO<sub>2</sub> and GDC10) were analyzed during every step of optimization and are presented in detail in next sections. The glass substrates were employed for this study. The glass substrates were cleaned prior the deposition by employing the five-step procedure, flow chart of which is given in figure 1.

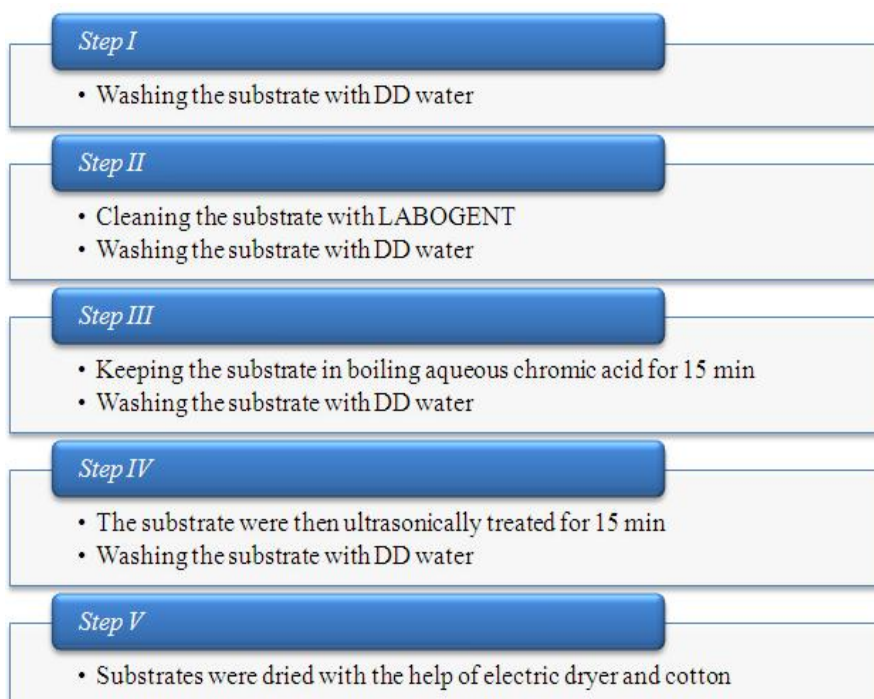


Figure 1. Flow chart of five-step procedure employed to clean the glass substrates.



### 5.2.2. $CeO_2$ (ceria) thin films:

#### 5.2.2.1. Synthesis of ceria thin films:

An aqueous solution of cerium nitrate ( $Ce(NO_3)_3 \cdot 6H_2O$ , 99.9% Pure; ALFA AESAR) was used for the deposition of ceria thin films. The concentration of precursor solution was varied from 0.01M to 0.1M. The solution was sprayed using air-blast type of glass nozzle with air as carrier gas on preheated glass substrates (set at decomposition temperature of cerium nitrate).

#### 5.2.2.2. Characterizations and optimizations

Thermo-gravimetric analysis (TGA) and differential thermal analysis (DTA) were carried out using a PerkinElmer TG-DTA-DSC instrument to determine the decomposition temperature. This decomposition temperature of cerium nitrate was then used as substrate temperature for depositions. Films prepared for different concentrations was then analyzed by XRD using PHILIPS PW-3710 XRD diffractometer with Cu-K $\alpha$  as radiation source and then optimum concentration was selected for further studies. The films prepared with optimum concentration was post annealed at 450°C for 2h in air and effect on crystallization of films were studied using XRD. Thus, the optimized solution concentration, substrate temperature from TG-DTA and annealing temperature (for glass substrate) for  $CeO_2$  films (i.e. host material) were determined and were used as 'seed' parameters for deposition of GDC10 thin films on glass substrates.

### 5.2.3. GDC10 thin films

#### 5.2.3.1. Synthesis of GDC10 thin films:

To deposit GDC10 ( $Ce_{0.9}Gd_{0.1}O_{1.95}$ ) the aqueous solution of cerium nitrate and gadolinium nitrate ( $Gd(NO_3)_3 \cdot 6H_2O$ , 99.9% Pure; ALFA AESAR) was mixed, according to the stoichiometry of the desired phase. While depositing the thin films equi-molar solutions of both the precursors were employed and the amount of mixing was in proportion of 9:1. For deposition of GDC10 thin films the solution



concentration and substrate temperature were varied about the ‘seed’ parameters obtained during synthesis of CeO<sub>2</sub> thin films. The crystallization of the thin film material was achieved by subsequent annealing at 450°C.

### 5.2.3.2. Characterizations and optimizations

The prepared films were then characterized for their structural, elemental, morphological and electrical properties. The structural properties of prepared films were determined using X-ray diffractometer. Elemental and morphological properties were analyzed using scanning electron microscope (SEM, JEOLJSM-6360) with attached EDS unit.

The morphology of the grain growth was examined using ‘Atomic Force Microscopy, Nanoscope-E’ of ‘Digital Instruments, USA’ in contact mode, with ‘V’ shape silicon nitride cantilever of length 100µm and spring constant of 0.58 N/m. The surface roughness was determined from the AFM images, using the formula given below,

$$R_q = \sqrt{\sum (Z_i - Z_{avg})^2 / N} \quad (5.1)$$

It gives the RMS surface roughness of a particular image area. This is the standard deviation of the  $Z$  value (height value) within the given area. Where,  $Z_{avg}$  is the average of the  $Z$  values within the given area,  $Z_i$  is the height value at particular point and  $N$  is the number of points within the given area.

The dc conductivity measurements were done using two-probe technique. Activation energies ( $E_a$ ) were calculated by fitting the conductivity data to the Arrhenius relation for thermally activated conduction, which is given as

$$\sigma = (\sigma_0 / T) \exp(E_a / KT), \quad (5.2)$$

where,  $E_a$  is the activation energy for conduction,  $T$  the absolute temperature,  $K$  the Boltzmann constant and  $\sigma_0$  the pre-exponential factor.



### 5.3. Results and discussion

#### 5.3.1. Introduction

Initially the optimization to determine the 'seed' parameters for GDC10 thin films were carried out using synthesis and characterizations of ceria (host material) thin films. Since, cerium nitrate was used as precursor for deposition of ceria thin films, its decomposition temperature was determined using TG-DTA. This temperature was expected to be used as substrate temperature for the deposition of ceria. After some trails, it was found that the surface of glass substrate is not exactly at the temperature of hot plate. The temperature of surface of glass substrate was about 20°C less than that of hot plate, obviously due to temperature gradient produced by substrate. Thus the depositions on glass substrate were carried out at a substrate temperature which is sum of decomposition temperature and the temperature difference (gradient) produced by substrate. Later, the precursor concentration was optimized for ceria by characterizing the as deposited and annealed films using XRD.

After determination of seed parameters (i.e. optimized preparative parameters for ceria thin films), the preparative parameters of SPT were varied about the seed parameters to deposit GDC10 thin films. This variation was to account the change of precursor solution (mixed with gadolinium source) which is known to affect the boiling point and decomposition of precursor solution. The GDC10 films were characterized using XRD, SEM, EDAX and dc conductivity and the optimum preparative parameters of SPT for GDC10 films on glass substrate were determined. The detailed analysis of characterizations done at each step of optimization during deposition of CeO<sub>2</sub> and GDC10 thin films is presented in consequent sections.

#### 5.3.2. TG-DTA of cerium nitrate (Ce(NO<sub>3</sub>)<sub>3</sub>.6H<sub>2</sub>O)

TG-DTA was carried out to study the decomposition behavior of the cerium nitrate hexa-hydrate (Ce(NO<sub>3</sub>)<sub>3</sub>.6H<sub>2</sub>O) precursor and the results are shown in figure 2. The endothermic peaks at 57.82 and 88.55°C with weight loss of ~4.6% are due to the dehydration. The endothermic peak observed at 191.21°C along with weigh loss ~11.5% may be due to dissociation of nitrous group from crystallized cerium (III) anhydrous nitrate. Further with an increase in temperature a weight loss of ~8%





occurs which may corresponds to evolution of oxygen from the nitrous group. A comparatively broader endothermic peak in the range 270-290°C with a fast mass loss refers to the decomposition of residual material. The total weight loss (59.86%) for the decomposition of precursor from the thermal gravimetric curve was almost similar to the calculated weight loss (60.36%) for cerium oxide formation. The data of thermal analysis clearly indicate that the decomposition occurs at about 280°C. The absence of peaks after the major peak in DTA curve (at ~280 °C) indicates that the crystallization process also occurs at the same temperature together with the decomposition process. However, the weight loss data shows the slight reduction in weight up to 450°C after which there was no much weight loss was observed till 1000°C.

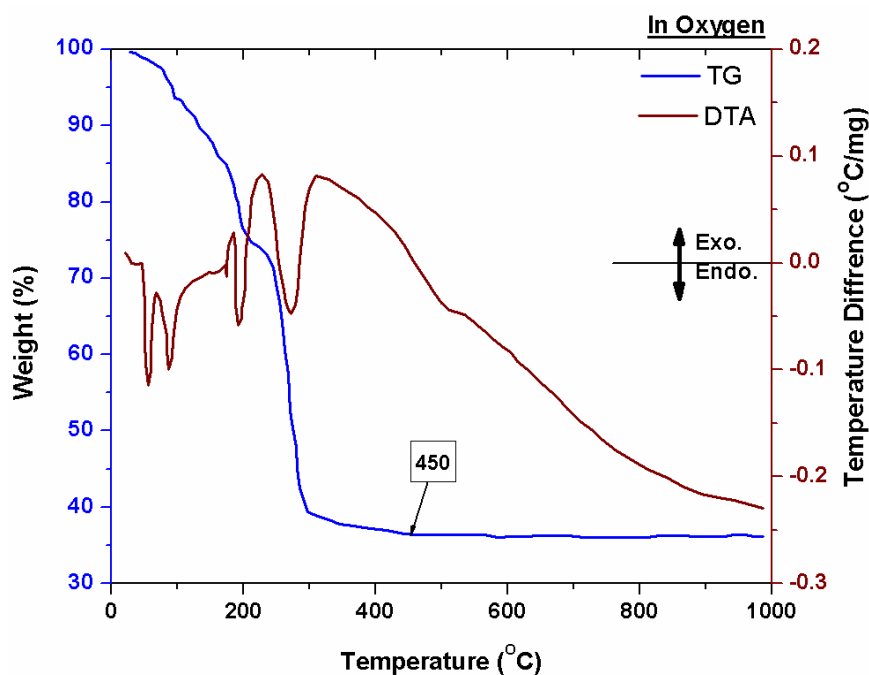
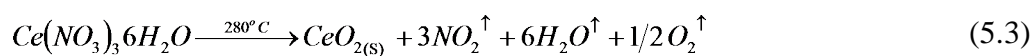


Figure 2. TG-DTA of cerium nitrate hexa-hydrate ( $\text{Ce}(\text{NO}_3)_3 \cdot 6\text{H}_2\text{O}$ ) precursor.

The possible chemical reaction for this thermal decomposition can be given as follows:



The analysis of TG-DTA curves shows that the complete decomposition of precursor occurs at 280°C. Hence, the minimum substrate temperature at which the decomposition of sprayed precursor would be possible is 280°C. However, the phase stability is observed at 450°C from TG curves and hence it signifies that the thin films deposited at 280°C require further heat treatment i.e. post annealing at 450°C.

### 5.3.3. Synthesis and characterizations of CeO<sub>2</sub> thin films on glass substrate

#### 5.3.3.1. Effect of precursor solution concentrations:

Figure 3 shows the XRD patterns of ceria thin films prepared with aqueous solution cerium nitrate having different concentrations. These films were prepared at substrate temperature (ST) of 300°C for 100 ml solution. The XRD patterns were compared with JCPDS PDF No. 81-0792 for ceria and were indexed accordingly. It can be seen in figure 3 that all the XRD patterns showed the presence of (111), (200), (220), (331), (440), (420) and (422) diffraction peaks in 2θ range of 10-90°. There were no unidentified peaks in XRD patterns, confirming the formation of single phase polycrystalline ceria thin films.

The intensity profile of ceria thin films prepared with 0.05M precursor solution was comparatively highest. It signifies that more crystalline film formations are possible for 0.05M precursor solution. The lattice parameter of ceria thin films was calculated using formula,

$$a = d \cdot \sqrt{h^2 + k^2 + l^2}, \quad (5.4)$$

where,  $a$  is lattice parameter of cubic system, ' $hkl$ ' are miller indices and  $d$  is inter-planer distance, while crystallite sizes were determined using Scherrer's formula which is given as,

$$D = \frac{0.9 \cdot \lambda}{\beta \cos \theta}, \quad (5.5)$$

where,  $\lambda$  is wavelength of X-ray radiation (1.5406 Å),  $\beta$  is FWHM of the strongest peak in XRD and  $\theta$  is the half of corresponding diffraction angle (2θ).



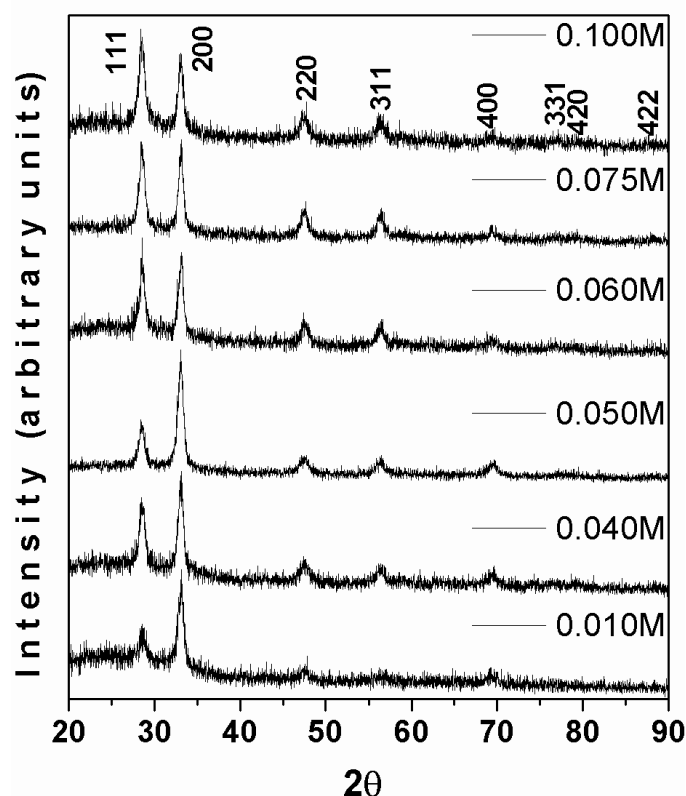


Figure 3. XRD patterns of ceria thin films prepared from precursor solution of different concentrations.

The calculated lattice parameters and crystallite sizes for ceria thin films prepared from precursors with different concentrations are listed in table 1. From table 1 it can be clearly seen that the lattice parameter of ceria film prepared from 0.05M solution is exactly same as the standard lattice parameter (5.412 Å) from JCPDS PDF.

Concentration	Lattice parameter (Å)	Crystallite size (nm)
0.010M	5.390	121
0.040M	5.409	138
0.050M	5.412	123
0.060M	5.408	137
0.075M	5.408	144
0.100M	5.416	136

Table 1. Lattice parameters and crystallite sizes for ceria thin films prepared from precursor solution of different concentrations.



The grain orientations as a function of precursor solution concentrations for ceria films are shown in figure 4. The peak intensity ratio  $I(111)/I(200)$  is calculated for precursor solution concentrations. The change of the grain orientations for different precursor solution concentrations is indicated by changes in the proportion of the different peak intensities.

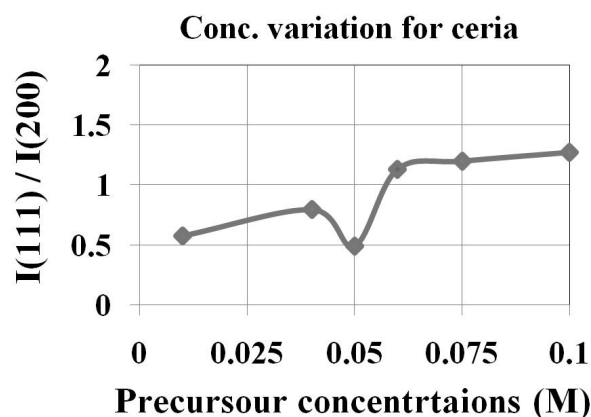


Figure 4. Grain orientations (peak intensity ratio  $I(111)/I(200)$ ) as a function of precursor solution concentrations for ceria films.

The peak intensity ratio,  $I(111)/I(200)$ , increases with an increase in solution concentration. For lower solution concentration the grain orientation is along (200). It is true up to 0.05M where the (200) peak dominance is highest one; (200) peak holds double intensity values than that of (111) peak. Preferred (200) grain orientation perpendicular to the substrate developed lead to highly crystalline thin films in as deposited state, which was further improved by post heat treatments. For solution concentration above 0.05 M, the ratio  $I(111)/I(200)$  become greater than one, implying change of grain orientation along (111).

This structural characterization of prepared ceria thin films confirms that films prepared from 0.05M precursor solution gives good quality thin films as per the lattice parameter and crystalline nature of films. Hence, 0.05M precursor concentration was treated as optimum concentration for other fixed preparative parameters employed in this study.



### 5.3.3.2. Effect of annealing on crystalline nature of ceria thin films:

Figure 5 shows XRD pattern of as deposited and annealed (at 450°C for 2h in air) ceria thin film. The crystalline nature of ceria thin films has been enhanced after annealing however no effect on lattice parameter was observed. The crystallite size has been increased from 123nm for as deposited films to 130nm for annealed films. The annealing temperature of ceria thin films was restricted to 450°C as higher temperature could lead to softening of glass substrate. These softening in substrate may produce stresses in the films and could lead to warping of films.

It was observed that if as prepared films (without annealing) were kept in open air for few hours, film material peel-off leading to powder formation on to the substrate. It can be attributed to the residual water trapped in the films. For the preparation of dense electrolyte films it is mandatory to keep the films wet in its as deposited state (details are in chapter 3). Since the residual water trapped in the films and intentionally held wet films for densification may attract atmospheric water vapors which cause its physio-absorption on the surface of film. Furthermore, the physio-absorbed water gets diffused into the film by capillary action and after few hours the water content in the films may exerts pressure on to the material network leading to peel-off of the films. However, this effect was not seen in case of annealed films. Hence, the post heat treatment is necessary to evaporate residual water content in the films, which further densify the films. This evaporation of trapped residual water in the films makes the films completely dry and the physio-absorbed water onto the surface of the films may not enter the film (since films are dense now) and thereby avoids the peeling of films. Such films remain intact even after a month of deposition.

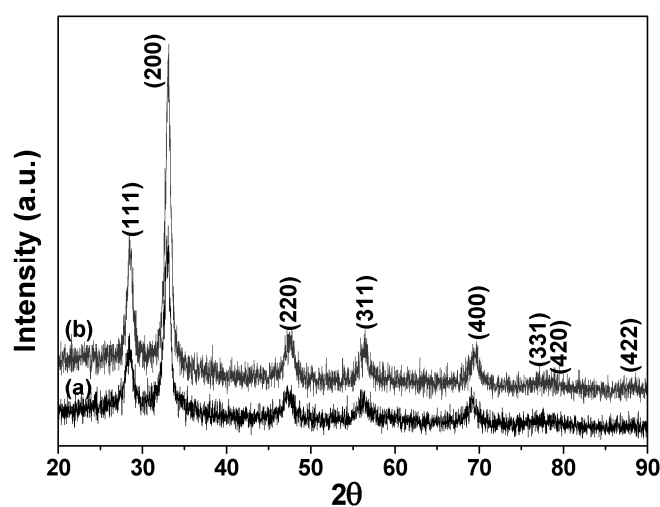


Figure 5. XRD pattern of ceria thin film (a) as deposited and (b) annealed at 450°C for 2h in air.



The optimization of preparative parameters of SPT was scrutinized by selecting those parameters which supports our desired characteristics or would support the same in further studies. The desired characteristics include highly crystalline thin films in its as deposited state, which was seen for 0.05M precursor solution. Thus, the optimized preparative parameters of SPT for ceria thin films on glass substrate are shown in table 2.

<b>Fixed parameter:</b>	
<i>Type of salt</i>	<i>Meal nitrate</i>
<i>Atomization type</i>	<i>Air-blast</i>
<i>Nozzle to substrate distance</i>	<i>25 cm</i>
<i>Nozzle motion</i>	<i>1cm/second</i>
<i>Linear distance traversed by nozzle</i>	<i>20 cm</i>
<i>Temperature controller</i>	<i>+4°C cycle</i>
<b>Optimized parameters for CeO<sub>2</sub> on glass substrate:</b>	
Solution quantity	100 ml
Substrate temperature	300°C (for glass substrate)
Solution concentration	0.05M
Annealing (post heat treatment)	≥ 450° for ≥ 2h

Table 2. The optimized preparative parameters of SPT for ceria thin films on glass substrate.

#### 5.3.4. Synthesis and characterizations of GDC10 (Ce<sub>0.9</sub>Gd<sub>0.1</sub>O<sub>2-δ</sub>) thins films

The parameters obtained in the formation of ceria thin films would not be suitable to implement directly for the deposition of GDC10 thin films. The precursor solution for the deposition of ceria films consists of cerium nitrate while that for GDC10 was mixture of cerium nitrate and gadolinium nitrate (in a proportion of 9: 1). This mixing of two salts in a proportion may vary the decomposition temperature. Thus it is well known that such variation of decomposition temperature may affect the preparative parameters of SPT. Thus it was decided to vary the substrate temperature and solution concentration for the deposition of GDC10. However, as the large part of



mixture consist cerium nitrate the variation was carried out about the optimized preparative parameters (seed parameters) for ceria.

The synthesis of GDC10 films were carried out at different ST in the range of 250-450°C. It was observed that the film formation at substrate temperature below 300°C was not complete. At substrate temperatures less than 300°C droplets traveling from spray nozzle to substrate remain in un-vaporized state and may contain large amount of water and hence caused spitting of droplets on the substrate and at extreme cracking of glass substrates was observed. Hence the deposition below 300°C was discarded. However, the deposition of GDC10 films at substrate temperatures greater than 400°C revealed that the film formations were made no variation in substrate surface. This is because of the complete decomposition of spray solution prior to reaching the substrate surface. Completely decomposed sprayed matter consists only of dried precipitate particles of size of nano-scale. When these dried particles reach to the surface of hot substrate, it experiences large thermophoretic forces leading to complete fly-away of precipitates. To clarify the same, the bare substrates (without spray) were heat treated at the same deposition temperature and were compared with those used for depositions. Both the substrates showed the same surface textures. Thus the discussion involves the substrate temperatures ranging from 300 to 400°C. While optimizing the substrate temperature, the solution concentration was kept fixed (0.05M).

After optimization of substrate temperature, the variation in solution concentration was carried out and its optimization was done on the basis of adherence and surface roughness of the films. The concentration of solution was varied as 0.04M, 0.05M and 0.1M.

#### *5.3.4.1. Optimization of substrate temperature*

##### *a. Structural characterizations:*

Figure 6 shows the XRD patterns of the thin films prepared at different substrate temperatures (ST). It can be clearly seen in the XRD pattern that the polycrystalline phase of GDC10 is only observed in case of ST equal to 300°C.



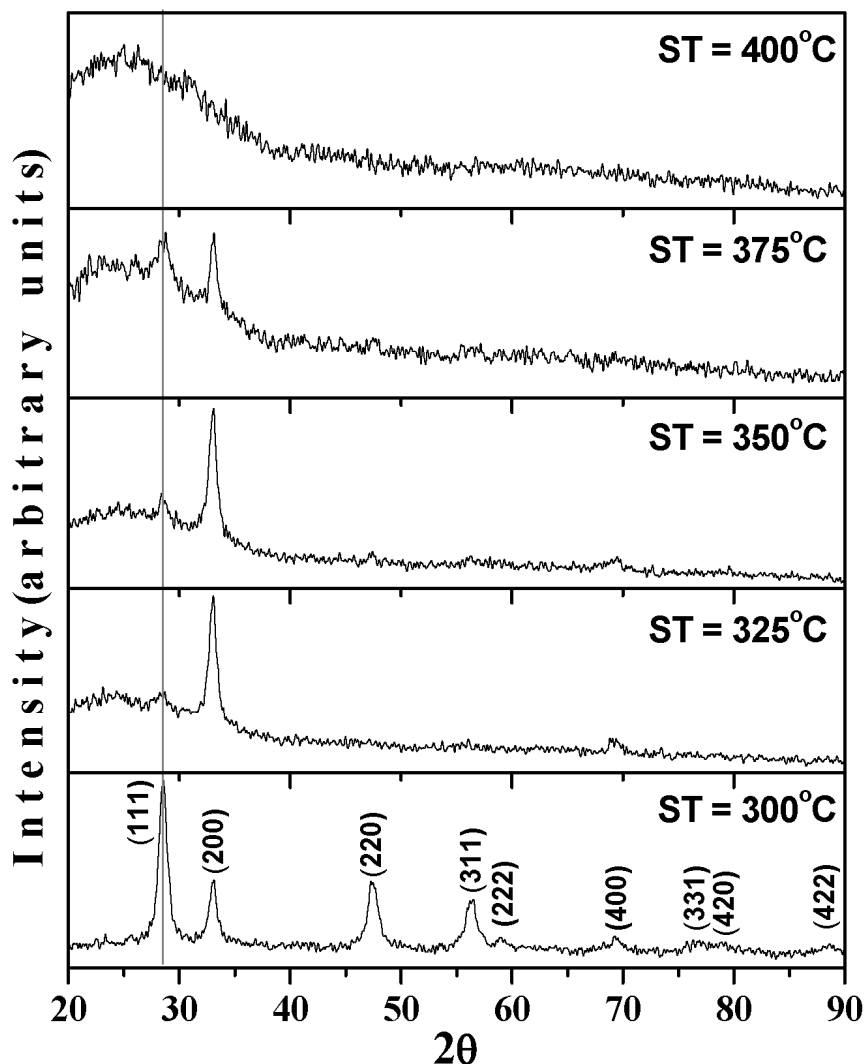


Figure 6. XRD patterns of the thin films prepared at different substrate temperatures.

As observed in the XRDs presented in figure 6, hump due to the glass substrate dominates the crystallinity of the films with an increase in substrate temperature. Further no materials peak was observed for the thin films deposited at 400°C, instead there was only a glass hump in XRD due to amorphous nature of glass substrate. This observation leads to affirmation that there was no deposition of material onto substrate at ST of 400°C.

The XRD pattern of thin films deposited at ST of 300°C was compared with JCPDS PD file 75-0161. The intensity profile of JCPDS file and that of XRD pattern of GDC10 thin film prepared at ST of 300°C were well in agreement with each other (table 3). The margin of error % was attributed to texture of films i.e. oriented grains.





Peaks	From JCPDS (Rel. Intensity)	Observed (Rel. Intensity)	Error %
(111)	999	999	0
(200)	279	516	24
(220)	446	592	15
(311)	328	412	8
(222)	60	208	15
(400)	52	237	19
(331)	103	220	12
(420)	65	208	14
(422)	84	179	10

Table 3. Comparison of relative intensity profile of JCPDS and observed data for GDC10 thin films prepared at substrate temperature of 300°C

The grain orientation was found to be a function of substrate temperature as shown for GDC10 films in figure 7. The peak intensity ratio  $I(111)/I(200)$  is calculated for various substrate temperatures. The preferred orientation was observed to be along (111) for the substrate temperature of 300°C, while it is along (200) for the other substrate temperatures.

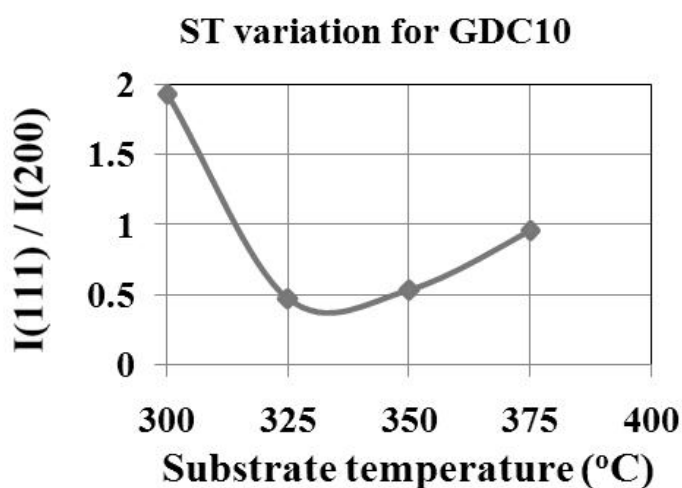


Figure 7. The grain orientations (intensity ratio  $I(111)/I(200)$ ) as a function of substrate temperature for GDC10 films.



For the substrate temperature of 300°C, the (111) peak is the highest intense peak and (200) the second highest ( $I(111)/I(200) > 1$ ). At substrate temperature of 325°C, the intensity of (200) peak drastically dominates over the (111) reflection ( $I(111)/I(200) < 1$ ). Preferred (200) grain orientation perpendicular to the substrate develops during further higher substrate temperatures from 325°C to 375°C. The data point for substrate temperature of 400°C is missing as corresponding XRD pattern did not revealed any reflection peaks.

The GDC10 thin films for different ST were further characterized for their morphological and elemental characterizations to verify the optimization of substrate temperature.

*b. Morphological and elemental characterizations:*

Figure 8, shows the SEM images of thin films prepared for various substrate temperatures and a typical EDAX pattern of film prepared at substrate temperature of 300°C.

SEM of thin films prepared at ST of 300°C shows that the dense material has been grown onto substrate while surfaces of the films prepared at ST greater than 300°C showed rings and some spherical particles of deposit material onto substrates. These rings and spherical particles of deposit onto substrates are due to imperfect decomposition of sprayed solution on to substrate. Also from SEM images, it can be clearly seen that the densities of rings onto substrate decreases with an increase in substrate temperature. This may be attributed to the fact that with increase in substrate temperature the amount of fly-away of droplets before reaching the substrates increases. Thus less amount of deposit is seen onto substrates at higher substrate temperatures. The materials content on the films has been decreased with an increase in substrate temperature.



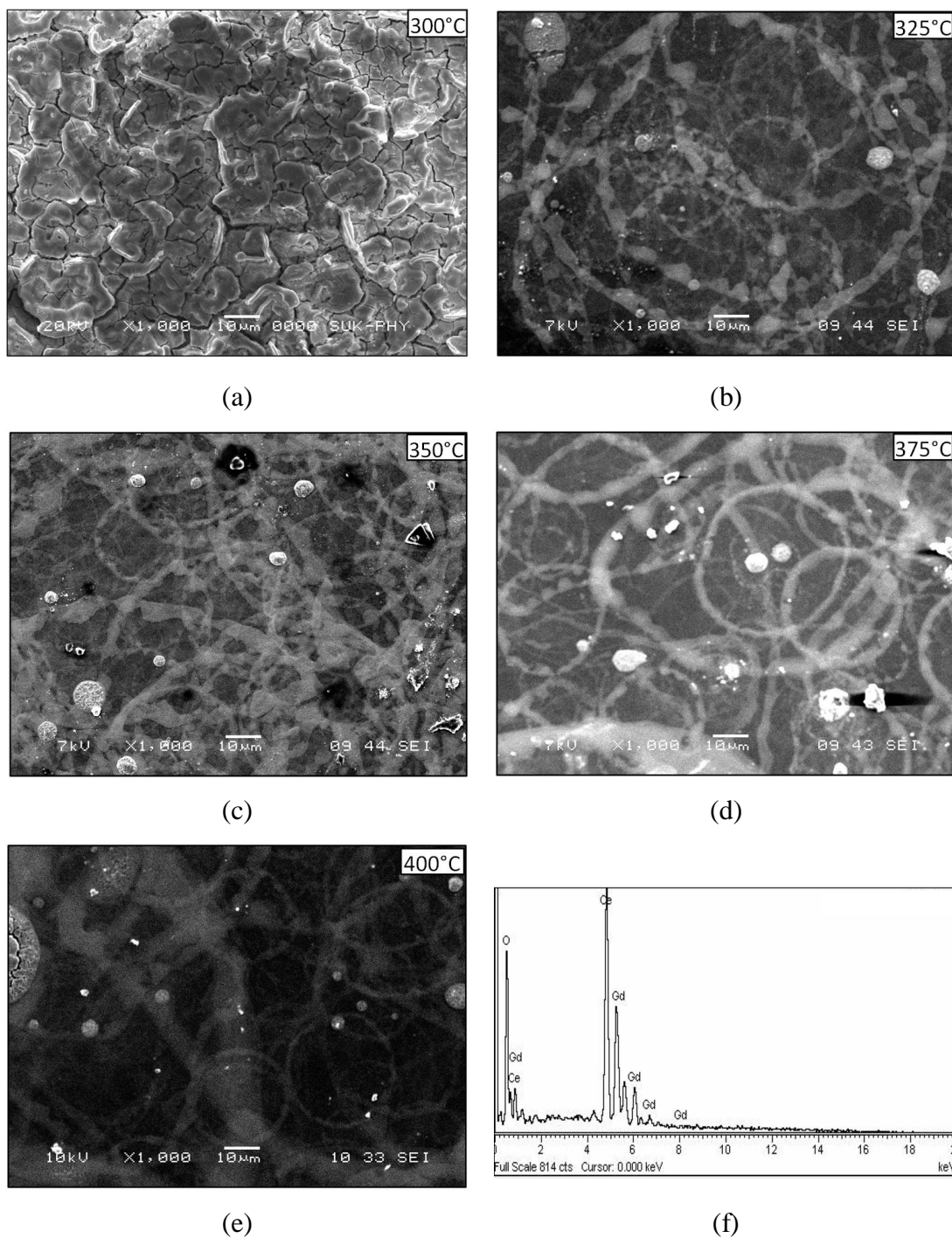


Figure 8.. SEM of the thin films prepared at substrate temperature (ST) equal to (a) 300°C, (b) 325°C, (c) 350°C, (d) 375°C and (e) 400°C. (f) Typical EDAX pattern of GDC10 film prepared at ST = 300°C.

During the deposition, aerosol produced by atomizer flies from nozzle to substrate and undergo a process in a sequence as (i) breaking of droplets at nozzle (due to pressurized air through nozzle), (ii) pyrolysis of droplets (forms precipitate



during fly) and (iii) decomposition of precipitate at substrate (due to large temperature gradient). When the precipitate reaches the substrate, it undergoes decomposition and nucleation. Many processes occur simultaneously when a droplet hits the surface of substrate, which includes, evaporation of residual solvent, spreading of the droplet and salt decomposition.

According to D. Perednis [20], five possible droplet impacts with substrate surface are shown in figure 9a. While describing the “*decomposition of the precursor on the substrate...*” in chapter 3, how these impacts leads to different film formation and grain growth mechanisms are explained in detail. Thus correlating those mechanisms and observed SEM for films prepared with different substrate temperature is explained as follows.

The GDC10 films prepared at ST of 300°C are dense and crystalline which is due to the spreading of droplets, while for ST between 300°C to 420°C, ‘spread & contract’ and ‘stick’ type of impacts have been observed. The ‘spread & contract’ impact results in ring type of deposit while that of ‘stick’ type impact leads to spherical particles on substrate. However, for the films prepared at ST of 400°C, morphology might have originated from ‘rebound’ type of impact in addition to ‘spread & contact’ and ‘stick’ type of impacts, as the existence of materials on glass substrate is negligible.

The ‘spread’ droplets onto substrates forms disks and these disks pile-up to form a dense structure as shown in figure 9b. Hence, for fixed preparative parameters of SPT, GDC10 thin film prepared at ST of 300°C leads to dense film formation. However, in case of ST greater than 300°C, the ‘spread & contact’ type of impact gives ring type structures on the substrates. Apart from this, few droplets (comparably small in size) gets evaporated before reaching the substrate and becomes completely dry. When these dry particle impacts on the substrate, it sticks to substrates. Hence ring type structure along with spherical particles is observed for substrate temperature between 300°C to 400°C.

Thus, when the impacting droplet contains just sufficient amount of solvent, it spreads over the substrate surface and forms a disk shaped splat, which are responsible for dense film formation. With increasing temperature (for  $ST > 300^\circ\text{C}$ ), the impacting droplets contain less and less solvent. These nearly dry-droplets will stick on the substrate without spreading, and consequently more stick-particles will occur on the film. Finally, at high deposition temperatures ( $ST \geq 400^\circ\text{C}$ ), the droplets



evaporates before reaching the substrate, and leads to powder formation or nearly bare substrate could be obtained. We could see decreased number of rings and almost the glass substrate exposed in figure 8e for substrate temperature of 400°C. This observation was confirmed by elemental analysis.

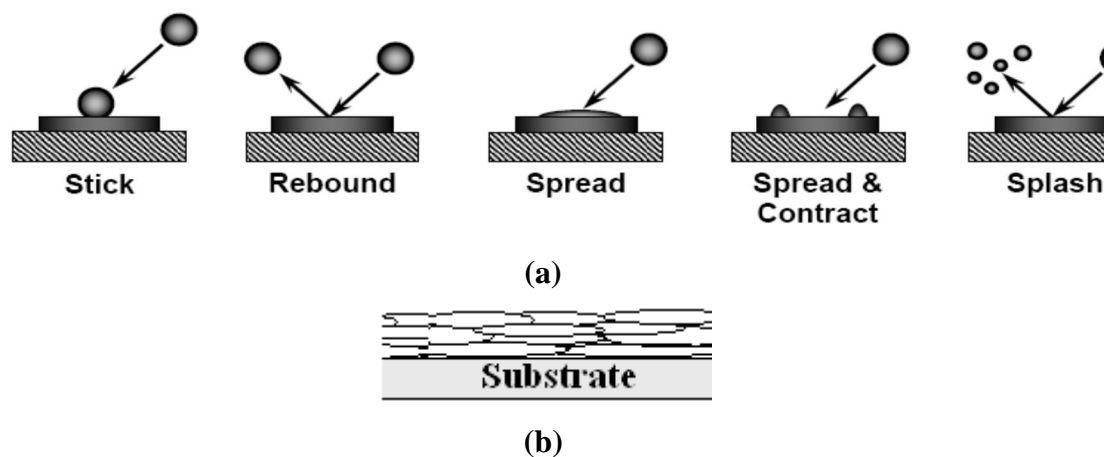


Figure 9. (a) Five possible droplet impacts on heated substrate and (b) schematic showing how the spread droplet forms dense films.

Table 4 shows the atomic percentage of Ce and Gd content extracted from EDAX pattern. It is evident that the films prepared at ST of 300°C shows the desired stoichiometry of Ce and Gd. However, for ST of 400°C, Na content from glass substrate appears in the EDAX pattern and analysis showed that its percentage is about 63% while remaining is Gd. There was no indication of Ce in the films prepared at ST of 400°C.

With an increase in the substrate temperature the rate of cerium ion to fly away from the substrate increases. However, only gadolinium ions (since its decomposition temperature is 408°C) could reach the substrate and form rings by 'spread and contract' mechanism along with some spherical particles. The presence of Na in the EDAX pattern confirms the formation of discrete islands of materials for ST of 400°C exposing the bare substrate during EDAX studies. This observation supports that the droplet impact occurred during deposition at ST of 400°C is also of 'rebound' or 'splash' type (figure 9a).



Element ↓	At%		
	ST →	300°C	400°C
Na		-	63.76
Ce		89.95	-
Gd		10.05	36.24
<b>Total</b>		100.00	100.00

Table 4. Typical atomic % of Na, Ce and Gd for the films prepared at 300 and 400°C.

Thus from the structural, morphological and elemental characterization, it was confirmed that the GDC10 films prepared with 0.05M precursor with ST of 300°C is able to give well grown, dense, polycrystalline and stoichiometric films. Hence ST of 300°C was chosen as optimum substrate temperature for deposition of GDC10 thin films (on glass substrates) for further studies.

#### 5.3.4.2. Optimization of precursor solution concentration

Now keeping the substrate temperature constant, the solution concentration was varied as 0.04M, 0.05M<sup>‡</sup> and 0.1M, to observe its effect on structural and morphological properties.

##### a. Structural characterizations

Figure 10 shows the XRD patterns for the thin films prepared using precursor solution of different concentrations. The XRD patterns matches well with JCPDS PD file no. 75-0161 for GDC10 composition and were indexed accordingly. From these patterns lattice parameter were found to be very close to that of standard value i.e. 5.418Å. The estimated crystallite size for films prepared using 0.04, 0.05 and 0.1M solution were 165nm, 127nm and 162nm, respectively.

<sup>‡</sup> The same samples which were studied during optimization of substrate temperature.



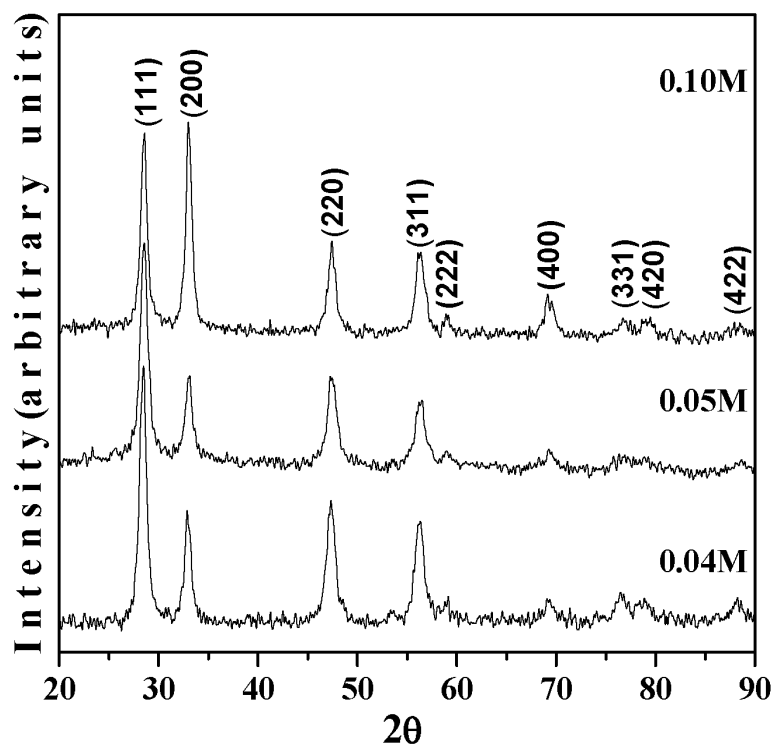


Figure 10. XRD patterns of GDC10 thin films prepared using precursor solution of different concentrations at ST equal to 300°C.

The grain orientations as a function of precursor solution concentration for GDC10 thin films are shown in table 5. The peak intensity ratio  $I(111)/I(200)$  is calculated for films prepared using different precursor solution concentrations.

Solution concentration (M)	Intensity ratio $I(111)/I(200)$
0.04	1.762
0.05	1.943
0.10	0.960

Table 5. Grain orientations as a function of precursor solution concentration for GDC10 thin films.

For solution concentration of 0.05M and 0.04M the (111) peak dominates the (200) peak, while in the case of 0.1M solution the peak intensity of (200) is higher than that of (111) peak i.e.  $I(111)/I(200) < 1$ . Thus for 0.04 and 0.05M concentration, the preferred (111) grain orientation perpendicular to the substrate is developed and it



is in line with standard values (JCPDS PDF No. 75-0161) for GDC10 composition, where the ratio holds the value of 3.5. This standard value of  $I(111)/I(200)$  could be achieved through further heat treating the samples at higher annealing temperatures.

*b. Morphological characterizations*

Figure 11 shows the SEM of the films prepared from different solution concentration. It can be seen that the size of clusters of grains increases with an increase in solution concentration, while the compactness in the surface goes on decreasing.

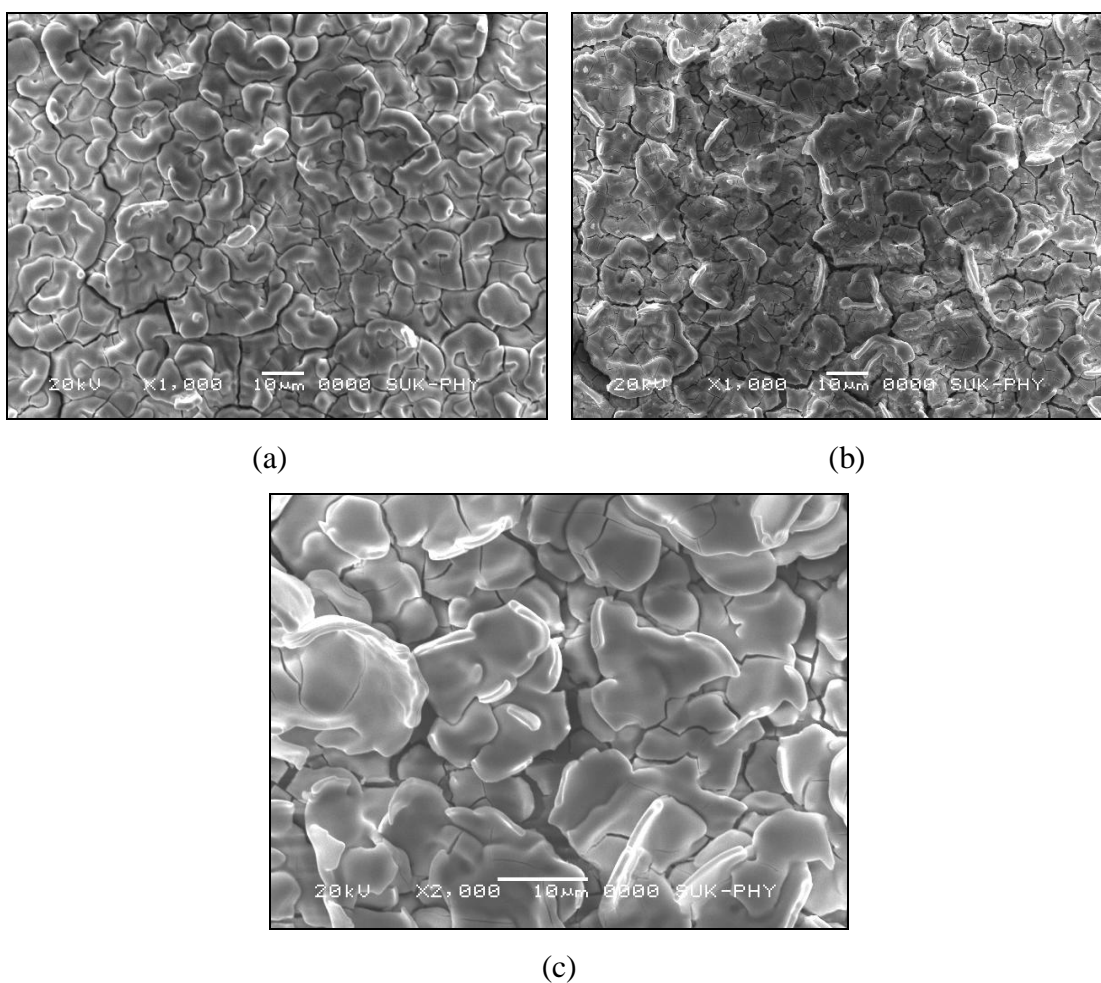


Figure 11. SEM images of GDC10 thin films prepared with precursor solution; (a) 0.04M, (b) 0.05M and (c) 0.10M; ST = 300°C.

The reduction in compactness of the film observed for 0.1M leads to almost negligible adherence to the substrate and the deposit easily flakes off from the





substrate. This morphology might be originated from the ‘stick’ type of impacts during deposition which leads to further grain growth around the loosely stick particle. This type of grain growth results in formation large clusters of grains onto the surfaces, which does not have the adequate adherence with the substrate (figure 11c).

During the deposition, for higher solution concentration (0.1M) the amount of deposit reaching to substrate is comparatively large and hence leads to formation of large number of nucleation centers. These nucleation centers further lead to fast grain growth compared to lower concentrated solutions. Therefore as observed, the grain growth is fast for 0.1M solution and finally results in large clusters onto substrates. However, this rapid grain growth leads to low adherence to the substrate and deposit may flakes off easily. As the desired properties of electrolyte films demand dense and adherent films, for further studies the samples prepared using 0.1M solution were discarded.

*c. Atomic force microscopy (AFM)*

AFM studies were carried out to determine grain size and surface roughness of the films prepared using 0.04 and 0.05M solution. The estimated mean surface roughness (Rq) and average grain size are listed in table 6.

	Concentration of the precursor	
	0.04M	0.05M
Mean surface roughness (Rq)	4.75 nm	2.75 nm
Average grain size	98.00 nm	88.00 nm

Table 6. Estimated mean surface roughness (Rq) and average grain size from AFM.

Figure 12 shows the AFM images of the GDC10 films. The GDC10 films prepared from 0.04M precursor solution are rough compared to the films prepared from 0.05M precursor solution. Moreover, the average grain size is found to be relatively large for films prepared using 0.04M solution. The larger grain size results into increased roughness in films. The enhanced grain size observed is might be due



to lower concentration (0.04M) resulting in the formation of comparably less number of nucleation centers and clusters. Since, less number of nucleation centers and clusters in unit area allows the precipitate reaching to substrate to grow more than that of large number of nucleation centers and clusters (as in case of 0.05M).

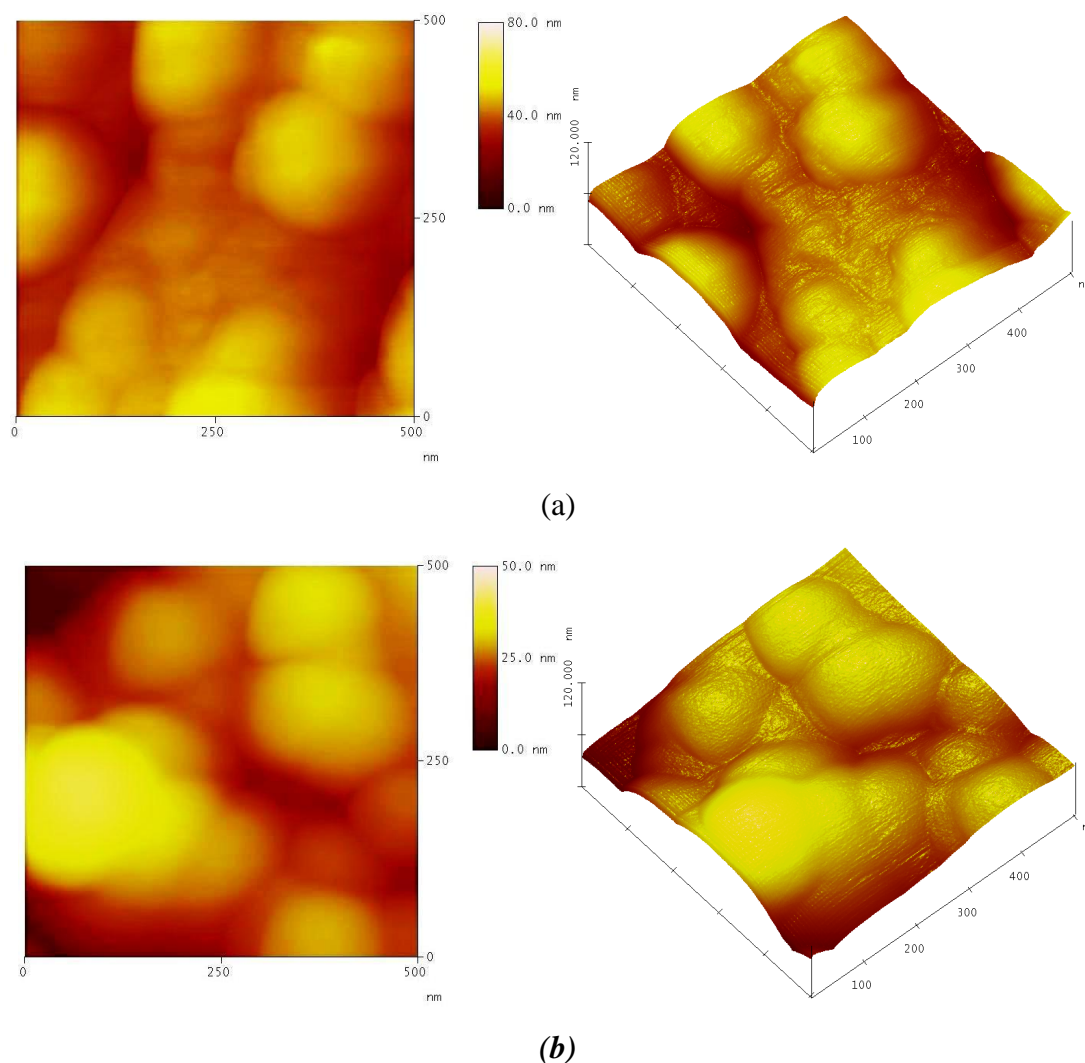


Figure 12. AFM images of GDC10 thin films prepared using precursor solution (a) 0.04M and (b) 0.05M concentrations; ST = 300°C.

From above discussion, it can be obviously thought that the films prepared from still less concentrated solution ( $< 0.04\text{M}$ ) would give further large grains. However, this is not true since solution with concentration  $< 0.04\text{M}$  leads to widely placed nucleation centers on to substrates. Thus in this case, to form a connected grain structures comparably large deposition time is necessary, otherwise it may leads the



formation of islands of materials on to the substrates. Thus 0.04M solution was found to be optimum for the GDC10 films with large grains.

In GDC10 electrolyte materials, the large number of grain boundaries offers high impedance to ionic hopping and it is recommended to have samples with less number of grain boundaries or in other words with large grains. Since, it is obvious when the grains are of bigger in sizes the number of grain boundaries per unit area would be less. Therefore, for electrical characterizations of GDC10 films the samples prepared from 0.04M solution were preferred instead of samples prepared using 0.05M solution.

*d. Electrical properties as function of thickness of GDC10 films*

- *Thickness measurements:*

Conventionally the thicknesses of the thin films were determined by gravimetric method in which the thickness was determined by using the weight difference of bare and coated substrate. With known weight difference, surface area and density of deposit the thickness of the film could be easily calculated. However, this method requires a balance with high precision, since the thickness of the thin film is in range of microns. Small error in determination of the weight difference could leads to confusing results. Hence in this study the surface profiler is used to determine the thickness. This measurement needs the formation of step on to the substrate involving bare and coated substrate. When the tip of surface profiler moves over this step, it recognizes the change in height while moving over the step. This change in height is related to the thickness of the film. The other way to form the step involves scratching of coated substrate by sharp edge.

The results of surface profiler were cross checked by SEM. The average thickness measured by surface profiler is 3.3 $\mu\text{m}$ . The typical fractured morphology of the also shows average thickness of 3.3 $\mu\text{m}$  as shown in figure 13. Thus the surface profiler can also be used to determine the film thickness provided the step must be formed carefully.



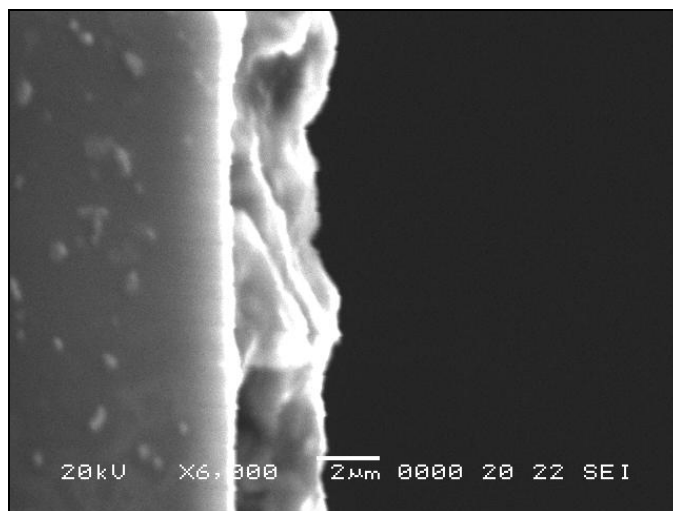


Figure 13. Typical SEM image used to determine thickness of the sample.

- *Electrical characterizations:*

The thin films deposited onto glass substrate were characterized for their electrical properties using two-probe dc conductivity measurement technique. Two silver electrodes separated by 1cm were marked on GDC10 thin films using silver paste and were heat treated at 500°C for 2h (figure 14a). Two pressure point contacts were made from these two silver strips onto films, to apply the voltage bias and to measure the current. The current and voltage were used to calculate the resistance of the thin film, which further used to determine its resistivity and conductivity.

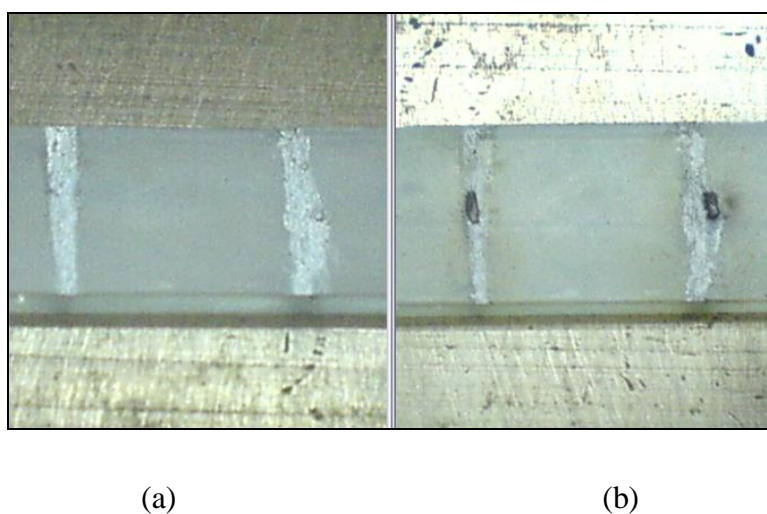


Figure 14. Photograph of GDC10 thin film on glass substrate showing the silver electrodes (a) before and (b) after the dc conductivity measurements.



Figure 15 shows the variation of conductivity values measured at 555°C and 450°C, for different film thickness. The dc conductivity was observed to be ~0.5 S/cm at 450°C, which is five times than that of YSZ at 1000°C (0.1S/cm). The conductivity for 3.3μm thick film is 0.03S/cm at 450°C and 0.12 S/cm at 555°C. On the contrary, GDC10 bulk sample (thickness = 1.78mm) sintered at 1500°C shows the conductivity of 0.0011 S/cm at 555°C. The results are compared with more details in chapter seven.

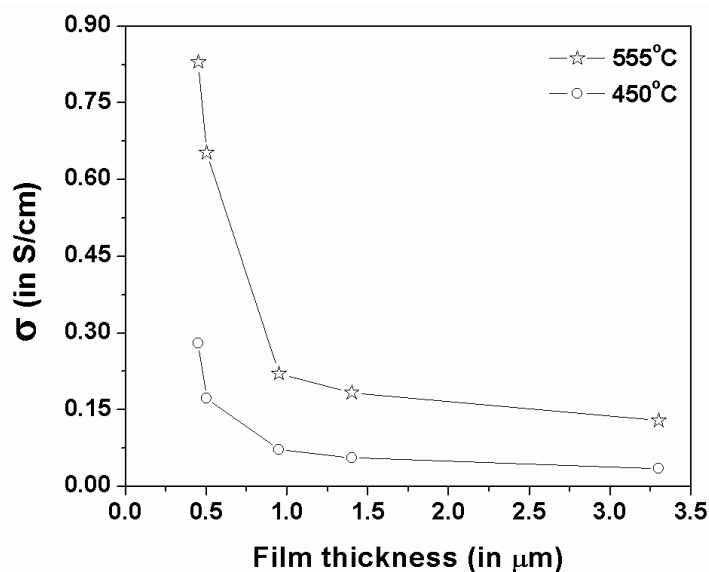


Figure 15. Variation of conductivity values of GDC10 films measured at 555 and 450°C with film thicknesses.

Chemical composition perpendicular to the film surface is an important property of the thin films. During spray pyrolysis deposition, the first droplets arriving on the heated substrate remain at temperature for a longer time than droplets deposited on top of the thin film. This might result in a gradient of the chemical composition and, therefore, a gradient of the amount of point defects, resulting in differences in the electrical conductivity with film thickness. In this regard, Rupp et al [21] investigated the chemical homogeneity of spray-pyrolyzed gadolinia-doped ceria electrolyte thin films and observed that films show a surprisingly stable and constant dopant concentration as a function of film thickness. Therefore, a constant oxygen ion vacancy migration over the film thickness can be assumed for applications like electrolyte films in solid oxide fuel cells. However, in their case the pyrolysis process was not completed during the spray pyrolysis deposition at 350°C, which could be attributed to the precursor employed by them (cerium nitrate and gadolinium



chloride). Residues of the spray pyrolysis precursors such as carbon from the organic solvents and chlorine and water from the used salts were even present after thermal treatment at 1000°C. Certainly, the residues in the films may affect the electrical properties of the GDC. However, Rupp et al [21] have not reported the effect of residues present in the films on the electrical properties of gadolinia-doped ceria. In our case, however, as the aqueous solution of both metal nitrates was employed, the decomposition would have completed at the substrate/deposition temperature without any organic residues. Thus the higher dc conductivity observed in our studies could be attributed to chemically homogenous GDC films without any impure organic phases. Moreover, the phase analysis has not shown the presence of Ce (III) even for 0.45  $\mu\text{m}$  thick films, which has been otherwise the source electronic contribution to the total conductivity. Further as the measurements are carried out in air and at temperature < 1000°C, the possibility of high conduction due to release of electrons on reduction of Ce(IV) to Ce(III) to the total conductivity is neglected.

Figure 16 shows the variation of  $\ln(\sigma T)$  with  $1000/T$  for GDC10 thin films with different thicknesses. As the thickness of film goes on increasing plots of  $\ln(\sigma T)$  with  $1000/T$  shifts to lower values leading to decrease in conductivity values. The thickness dependant conduction is obvious in ionic materials, since in these materials electrical (ionic) conduction is observed due to defect assisted hopping mechanism.

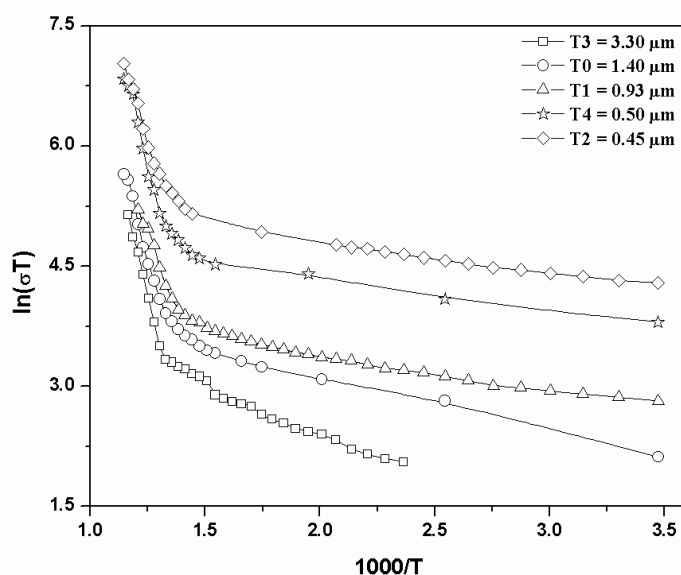


Figure 16. Variation of  $\ln(\sigma T)$  with  $1000/T$  for the GDC10 thin films having different thicknesses.



As the thickness of the sample increases, the probability of successful hopping of ions gets reduced. Also, the ohmic losses in thick samples will be more compared to thin samples [22]. Therefore, as observed, the plot of  $\ln(\sigma T)$  with  $1000/T$  shifts to lower values for comparatively thick films. However, the observed fact that the inflexion point does not show any dependence on the thickness of the films (inflexion point (change of slope) is nothing but the point of initiation of ionic diffusion in the films [23]), and is, in general, decided by the composition of sample. The change in the slopes for all the films is observed at  $480^\circ\text{C}$ .

However, with an increase in film thickness the slopes of both the regions in the plot i.e. before and after the inflexion point decreases which leads to decreased activation energies for the conduction. Table 7 shows the estimated activation energy for the high temperature regime. The higher activation energy of  $0.98\text{eV}$  was observed for  $3.3\mu\text{m}$  thick film, which decreases to  $0.61\text{eV}$  for  $0.45\mu\text{m}$  thick film.

Film thickness ( $\mu\text{m}$ )	$E_a$ (eV)
3.30	0.98
1.40	0.79
0.93	0.73
0.50	0.71
0.45	0.61

Table 7. Estimated activation energies ( $>480^\circ\text{C}$ ) of GDC10 thin films having different thicknesses.

#### 5.4. Conclusions

The suitability of spray pyrolysis technique (SPT) to deposit the GDC solid electrolyte thin films has been tested. The preparative parameters of SPT for the deposition of ceria and 10%Gd doped ceria films were optimized. The GDC10 films synthesized in the present work, showed the phase pure fluorite structure with lattice parameter well matched with that of standard. In addition to that the films were highly dense with smoother morphology. The dc conductivity was observed to decrease with an increase in thickness of the films. The dc conductivity was observed to be  $\sim 0.5\text{ S/cm}$  at  $623\text{ K}$ , which is five times than that of YSZ at  $1273\text{ K}$  ( $0.1\text{ S/cm}$ ). However,



the GDC10 thin films synthesized on glass substrate could not be implemented for its application as device, since the substrate side puts limitations. Thus the deposition of GDC10 thin films on electrode (ceramic) substrate is desirable.

The optimized preparative parameters for the deposition of GDC10 thin films on glass substrates are as follows:

#### Fixed parameter:

Type of salt	Meal nitrate
Atomization type	Air-blast
Nozzle to substrate distance	25 cm
Nozzle motion	1cm/second
Linear distance traversed by nozzle	20 cm
Temperature controller	+4°C cycle

#### Optimized parameters for GDC10 on glass substrate:

Solution quantity	100 ml
Substrate temperature	300°C (for glass substrate)
Solution concentration	0.04M
Annealing (post heat treatment)	≥ 450° for ≥ 2h

## References

- [1] N. M. Sammes, Z. Cai, *Solid State Ionics*, 100 (1997) 39.
- [2] Petterson, Jeffrey, *Alfred University, Doctoral Thesis, Alfred Ny*, (2003).
- [3] C. Xia, M. Liu, *Solid State Ionics*, 152 (2002) 423.
- [4] M.F. Carolan, J.N. Michaels, *Solid State Ionics* 37 (1990) 189.
- [5] K. Honegger, E. Batawi, C. Sprecher, R. Diethelm, in: *U. Stimming, S.C. Singhal, H. Tagawa, W. Lehnert (Eds.), Proc. 5th Int. Symp. Solid Oxide Fuel Cells, Electrochemical Society, Pennington, NJ*, 97 (1997) 321.
- [6] M. Lang, R. Henne, S. Schaper, G. Schiller, *J. Therm. Spray Technol.* 10 (2001) 618.
- [7] N.Q. Minh, K. Montgomery, in: *U. Stimming, S.C. Singhal, H. Tagawa, W. Lehnert (Eds.), Proc. 5<sup>th</sup> Int. Symp. Solid Oxide Fuel Cells, Electrochemical Society, Pennington, NJ*, 97 (1997) 153.





- [8] J. van Herle, R. Ihringer, R.V. Cavieres, L. Constantin, O. Bucheli, *J. Eur. Ceram. Soc.* 21 (2001) 1855.
- [9] Tuong Lan Nguyen, Kenichi Kobayashi, Takeo Honda, Youko Iimura, Ken Kato, Akira Neghisi, Ken Nozaki, Fabrizio Tappero, Kazuya Sasaki, Hiroshi Shirahama, Kenichiro Ota, Masayuki Dokiya, Tohru Kato, *Solid State Ionics* 174 (2004) 163.
- [10] P. Bohac, L. Gauckler, *Solid State Ionics* 119 (1999) 317.
- [11] Y.J. Leng, S.H. Chan, S.P. Jiang, K.A. Khor, *Solid State Ionics* 170 (2004) 9.
- [12] H.Z. Song, H.B. Wang, S.W. Zha, D.K. Peng, G.Y. Meng, *Solid State Ionics* 156 (2003) 249.
- [13] T. Setoguchi, M. Sawano, K. Eguchi, H. Arai, *Solid State Ionics* 37 (1990) 502.
- [14] E.M. Kelder, O.C.J. Nijs, J. Schoonman, *Solid State Ionics* 68 (1994) 5.
- [15] A.A. Van Zomeren, E.M. Kelder, J.C.M. Marijnissen, J. Schoonman, *J. Aerosol. Sci.* 25 (1994) 1229.
- [16] C.H. Chen, A.A.J. Buysman, E.M. Kelder, J. Schoonman, *Solid State Ionics* 80 (1995) 1.
- [17] K.L. Choy, In: W.E. Lee (Ed.), *British Ceramic Proceedings, Ceramic Films, Coatings, The Institute of Materials* 54 (1995) 65.
- [18] K.L. Choy, W. Bai, B.C.H. Steele, In: A.J. Mcevoy, K. Nisancioglu (Eds.), *Materials, Processes, 10th SOFC Workshop, Les Diablerets, Int. Energy Agency*, (1997) 233.
- [19] N.H.J. Stelzer, C.H. Chen, L.N. Van Rij, J. Schoonman, In: A.J. Mcevoy, K. Nisancioglu (Eds.), *Materials, Processes, 10th SOFC Workshop, Les Diablerets, Int. Energy Agency* (1997) 236.
- [20] K.L. Choy, W. Bai, in: A.J. Mcevoy, K. Nisancioglu (Eds.), *Materials, Processes, 10th SOFC Workshop, Les Diablerets, Int. Energy Agency* (1997) 252.
- [21] S.K. Pawar, S.H. Pawar, *Mater. Res. Bull.* 18 (1983) 211.
- [22] P.S. Patil, *Mater. Chem. Phys.* 59 (1999) 185.
- [23] D. Perednis, "Thin film deposition by spray pyrolysis and the application in solid oxide fuel cells", Ph.D. Thesis, Swiss Federal Institute of Technology, Zurich, 2003.
- [24] J.L.M. Rupp, T. Drobek, A. Rossi, L.J. Gauckler, *Chem. Mater.* 19 (2007) 1134.

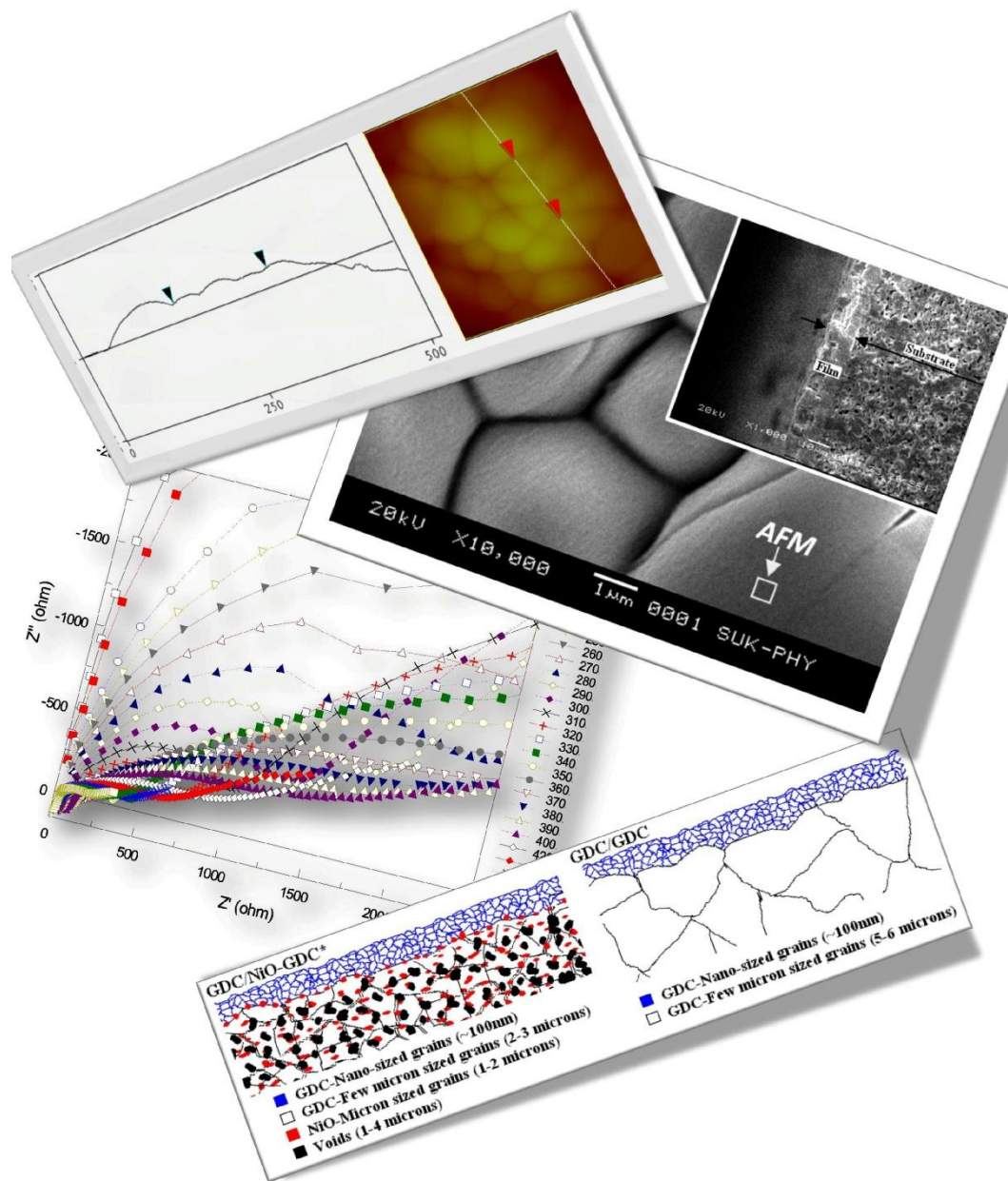


- [25] H.Z. Song, H.B. Wang, S.W. Zha, D.K. Peng, G.Y. Meng, *Solid State Ionics* 156 (2003) 249.
- [26] S. Zha, C. Xia, G. Meng, *J. Power Sources* 115 (2003) 44



# Chapter six:

*Synthesis and characterization of 10%Gd doped ceria (GDC10) thin films on ceramic substrates.*





# Chapter six

## CONTENTS

<b>6. SYNTHESIS AND CHARACTERIZATION OF 10%GD DOPED CERIA (GDC10) THIN FILMS ON CERAMIC SUBSTRATES.....</b>	<b>220</b>
<b>Keywords:</b> GDC, Thin film, NiO-GDC, Spray pyrolysis, Impedance spectroscopy.....	220
<b>6.1. Introduction .....</b>	<b>221</b>
<b>6.2. Experimental .....</b>	<b>222</b>
<b>6.2.1. Synthesis of GDC and NiO-GDC ceramics substrates .....</b>	<b>222</b>
<b>6.2.2. Synthesis of GDC/GDC and GDC/NiO-GDC structures .....</b>	<b>223</b>
<b>6.2.3. Characterizations .....</b>	<b>224</b>
<b>6.3. Results.....</b>	<b>225</b>
<b>6.3.1. Micro-structural and electrical properties of GDC/GDC structures.....</b>	<b>225</b>
<b>6.3.2. Micro-structural properties of NiO-GDC substrates at different stages of its processing and electrical properties of NiO-GDC* substrate.....</b>	<b>232</b>
<b>6.3.3. Micro-structural and electrical properties of GDC deposited on NiO-GDC* substrate .....</b>	<b>238</b>
<b>6.4. Discussion .....</b>	<b>243</b>
<b>6.4.1. Atomic force microscopy of GDC films deposited on ceramic substrates .....</b>	<b>243</b>
<b>6.4.2. Formation of nano-crystalline GDC thin films.....</b>	<b>246</b>
<b>6.4.3. Effect of substrates on film thickness .....</b>	<b>246</b>
<b>6.4.4. Electrical characterizations.....</b>	<b>248</b>
<b>6.5. Conclusions .....</b>	<b>252</b>
<b>References: .....</b>	<b>253</b>

## 6. SYNTHESIS AND CHARACTERIZATION OF 10%Gd DOPED CERIA (GDC10) THIN FILMS ON CERAMIC SUBSTRATES.

### Abstract:

Commercialization of solid oxide fuel cells (SOFCs), a forthcoming high efficient energy generation device, is not successful yet because of its high operating temperature. Hence, intermediate and low temperature SOFCs (operated below 700°C) has attracted much attention in recent years. It's potential to reduce the cost of the materials and cell fabrication in addition with improved reliability, portability and operational life, makes it most suitable prospective energy generation device for commercial realization. The ceria based electrolytes (10%Gd doped ceria – GDC10 or simply GDC) has the potential characteristic properties to be used in IT-SOFCs. This promising solid electrolyte can be further extended to use in LT-SOFCs by implementing the same in thin film form. In addition, if these films are prepared onto functional ceramic substrates (an electrode), the formed structure leads to electrode supported half cell of SOFCs. As in previous chapter it is well demonstrated that the spray pyrolysis technique is a suitable technique to prepare the solid electrolytes with desired properties and hence we have extended the same to prepare the half cell of SOFCs. Spray pyrolysis technique with optimized preparative parameters to deposit GDC on glass substrate was implemented as seed parameters to synthesize GDC thin films on ceramic substrates. The ceramic substrates, namely GDC and 30%NiO-70%GDC10 (NiO-GDC) were prepared by conventional ceramic route. The prepared ceramic substrates and structures were characterized for their structural, morphological and electrical properties using XRD, SEM and impedance spectroscopy.

Either of ceramic substrates employed shown their own advantages over the others. GDC substrate showed effect of substrate oriented grain growth in GDC films while that of NiO-GDC substrate provided well connected grains of GDC films with thickness  $\sim 13\mu\text{m}$ . The interface studied using impedance spectroscopy showed that the grain boundary activation energy is high (1.40eV) for conduction in the case of GDC substrate while it is comparably small (0.93eV) for NiO-GDC substrate. The activation energy for grain interior conduction estimated for the system formed by films on either ceramic substrate is of the same order ( $\sim 1.02\text{eV}$ ). In view of application of GDC films as solid electrolyte for SOFC, the GDC films on NiO-GDC ceramic substrate showed the desirable characteristic along with an advantage that the substrate could also act as anode for SOFC<sup>†</sup>.

**Keywords:** GDC, Thin film, NiO-GDC, Spray pyrolysis, Impedance spectroscopy.

<sup>†</sup> This work is submitted to the journal *Materials Chemistry and Physics*.



## 6.1. Introduction

Solid Oxide Fuel Cell (SOFC) is well known forthcoming high efficient power generation devices (operating temperature ( $T_{OP}$ ) is  $1000^{\circ}\text{C}$ ), as it converts gaseous fuel electrochemically into electricity with a very efficient (greater than 60%) and eco-friendly manner. In recent years, to overcome commercialization related problems of SOFCs, such as its cost of fabrication, reliability, durability etc., researchers gradually has been shifted towards the development of intermediate and low temperature (IT and LT) SOFCs (operated below  $700^{\circ}\text{C}$ ). IT or LT-SOFCs has inherent potential of reduction in the cost of the cell fabrication materials by allowing use of standard quality sealant, interconnects, etc. instead of high quality materials for the same. In addition to reduction in cost of fabrication, it also offers better reliability, portability and operational life. These advantageous over HT-SOFCs ( $T_{OP} > 800^{\circ}\text{C}$ ) would certainly make IT and LT-SOFC, a most appropriate prospective power generation device for commercial realization.

There are three strategies which should be stressed to overcome the bottleneck for operating temperatures of SOFCs [1-3]. The strategies to be dealt with are as follows: (i) use of alternate solid electrolyte having high ionic conductivity at reduced temperature should be preferred over the conventional solid electrolyte; thereby  $T_{OP}$  kept below  $700^{\circ}\text{C}$ . (ii) The thickness of electrolyte should be decreased to such an extent that it would offer less ohmic losses for ionic conduction but should not allow fuel cross over. It is reported that the thin film with relative density of the order of 90% with 10-20 $\mu\text{m}$  thickness would suffice the purpose. (iii) It is observed from earlier research that the reduction of  $T_{OP}$  increases the electrode potentials across the electrode/electrolyte interface and thus reduction of electrode-electrolyte interfacial resistance is suggested. Thus to tackle these strategies, search of new electrolyte material was obligatory. During the search of alternate material for solid electrolytes, 10% Gadolinia doped ceria (GDC) was an exciting discovery due to its high ionic conductivity at relatively low temperatures that make it an ideal candidate for IT-SOFC (operating at  $550\text{--}650^{\circ}\text{C}$ ) and has been extensively studied [2, 4-8]. In order to increase the ionic conductivity at further reduced temperatures, reduction in the thickness of the GDC electrolyte (10-20 $\mu\text{m}$ ) would be advantageous [9]. Further reduction in  $T_{OP}$  in addition to improved ionic conductivity, would be helpful to avoid the well known transition of GDC from ionic to electronic conductor (by  $\text{Ce}^{4+} \rightarrow$



Ce<sup>3+</sup>) in a typical fuel cell condition [10]. To employ the thin film electrolyte in SOFCs, it has to be supported by some kind of substrate and if the substrate itself acts as an electrode for SOFC, it would be an added advantage.

In this particular study, an attempt has been made to conquer these strategies simultaneously through employing spray pyrolysis technique (SPT) to prepare GDC thin films. The SPT is a well known method to prepare tailored metal oxide thin films on either conducting or non-conducting substrates, with an added advantage of easier way of doping. Using SPT, doping of films with any element in any proportion is possible by merely adding it in some form to the spray solution. The versatility of the SPT and requirement of fabrication of dense, thin solid electrolyte film on functional ceramic substrates makes SPT a most suitable technique for development of electrode/electrolyte structures (half cell) [11-17]. Moreover, SPT can be further extended to prepare the multilayered structures even. Here, GDC thin films were deposited on two types of ceramic substrates namely GDC and NiO-GDC (composite), which were prepared by conventional ceramic route. In general, the chemical deposition methods are sensitive to the surface structure of the substrates hence to investigate the substrate effect we employed two types of ceramic substrates; dense structured GDC and porous structured NiO-GDC. The micro-structural and electrical characterization of 'film/substrate' structures and that of bare substrates were carried out. Impedance spectroscopy was employed for electrical characterizations of GDC/GDC and GDC/NiO-GDC structures.

## 6.2. Experimental

In this work, GDC thin films have been deposited on to two types of ceramic substrates namely, GDC (same as that of the deposit material) and 30%NiO-70%GDC (referred as NiO-GDC hereinafter). Both the ceramic substrates were prepared by conventional ceramic route.

### 6.2.1. Synthesis of GDC and NiO-GDC ceramics substrates

The ceramic GDC substrate was prepared by mixing Gd<sub>2</sub>O<sub>3</sub> (AR grade, 99.9 %) and CeO<sub>2</sub> (AR grade, 99.9 %) from HIMEDIA Inc., in 1: 9 proportion in an agate mortar. The mixed powder was then calcined at 1200°C/4h in air. The calcined





powder was reground and mixed with organic binder (Poly-Vinyl Alcohol – PVA). The binder added powder was pelletized with the help of hydraulic press machine, which were further heat treated at 800°C/2h for binder removal. After binder removal step the samples were finally sintered at 1500°C/8h in air [18].

The NiO-GDC ceramic substrates were prepared by mixing NiO (Extra pure, AR grade from HIMEDIA Inc.) and calcined powder of GDC (at 1200°C), to obtain the desired composite phase of (NiO)<sub>30</sub>-(GDC)<sub>70</sub>. The selection of ceramic composition of NiO<sub>30</sub>-GDC<sub>70</sub> (precursor composite for Ni-GDC anode) substrate was done on the basis of their viability in prospective use as an anode of half cell for SOFC [19, 20]. Similar synthesis procedure, as that followed for GDC, was employed to prepare NiO-GDC composite samples. However, the binder removal step was not applied and the final sintering was carried out at 1400°C/8h in air, since, the binder removal step and high sintering temperature is usually employed to obtain dense ceramic bodies and here we are looking for porous structured NiO-GDC substrates.

The dimensions of the sintered substrates were 0.12cm in thickness and 2.5cm in diameter. The NiO-GDC substrates were heat treated in reducing atmosphere of 5%H<sub>2</sub>-95%Ar with gas flow rate of 500ml/min at 900°C for 5h. The reduction treatment leads to formation of porous structured Ni-GDC composite (referred as Ni-GDC hereinafter) ceramic substrates.

### 6.2.2. Synthesis of GDC/GDC and GDC/NiO-GDC structures

To prepare GDC thin films, cerium nitrate ( $Ce(NO_3)_3 \cdot 6H_2O$ , 99.9% Pure; ALFA AESAR) and gadolinium nitrate ( $Gd(NO_3)_3 \cdot 6H_2O$ , 99.9% Pure; ALFA AESAR) were dissolved separately in double distilled water to form solution with same concentrations. The equi-molar aqueous solution of cerium nitrate and gadolinium nitrate was mixed in desired proportion (i.e. 9: 1) to form the spray solution. This spray solution was then sprayed by air-blast type of nozzle on ceramic substrates, kept on a hot plate with controlled preset temperature. In this study, preparative parameters of SPT for deposition of GDC thin films were optimized for ceramic substrate while the detailed optimization procedure for the glass substrate is reported in chapter 5 [21]. Our attempts to deposit GDC thin films on NiO-GDC ceramic substrate were resulted into non-adherent films. Instead the GDC films



deposited on Ni-GDC ceramic substrate were adherent and thick, as the rough surfaced Ni-GDC substrates facilitated relatively more nucleation centers than of comparatively dense NiO-GDC. The optimized preparative parameters of SPT for the deposition of GDC films are listed in table 1 and are same for both the ceramic substrates except substrate/deposition temperature. The post heat treatment at 450°C/2h was employed for both the ceramic substrates. Further, crystallization of GDC films and improvement in film/substrate interface were achieved by subsequent heat treating the structure at 1000°C/8h in air, which transformed the Ni-GDC phase of substrate to NiO-GDC (referred as NiO-GDC\* hereinafter).

Preparative parameters ↓	Substrates→	Glass [21]	GDC	Ni-GDC
Solution concentration (M)		0.4	0.4	0.4
Solution flow rate (ml/min)		3 ± 0.2	3 ± 0.2	3 ± 0.2
Deposition time (h)		0.5	0.5	0.5
Substrate temperature (°C)		<b>300</b>	<b>280</b>	<b>250</b>
Post-annealing to avoid peel-off (°C)		450	450	450
Sintering to improve the interface with the substrate (°C)		-	1000	1000*

\* Transformed the Ni-GDC phase of substrate to NiO-GDC.

Table 1. Optimized preparative parameters of SPT for deposition of GDC films on different substrates.

### 6.2.3. Characterizations

The phase formation of prepared structure and ceramic substrates were studied using PHILIPS X-ray diffractometer (PW-3710) with Cu-K $\alpha$  radiation source. The XRD patterns were compared with their respective JCPDS PDFs to confirm the phase formations in the samples. The surface and fractured morphologies of the samples were imaged using scanning electron microscope (SEM, JEOL-JSM-6360, Japan). The electrical characterization was carried out by ac impedance measurements using impedance analyzer (SOLARTRON 1260 Impedance Analyzer; 1mHz – 32 MHz). Impedance measurements were obtained as a function of frequency (1Hz-10MHz) for



various temperatures ranging from 250°C to 500°C. Prior to measurements, the samples were coated with platinum paste (MaTeck GmbH, Germany) and heat treated at 200°C for 2h in air for drying. The platinum coated sample was sandwiched between two platinum electrodes. Collected impedance data were analyzed by impedance analysis software (ZView Version 2.4a) and used to extract the grain interior and grain boundary impedances, which further used to calculate ac conductivities. Obtained ac conductivities were then fitted to the Arrhenius relation for thermally activated conduction [22].

### 6.3. Results

#### 6.3.1. Micro-structural and electrical properties of GDC/GDC structures

Figure 1 shows the XRD patterns of GDC/GDC structure (annealed at 1000°C) and of bare substrate.

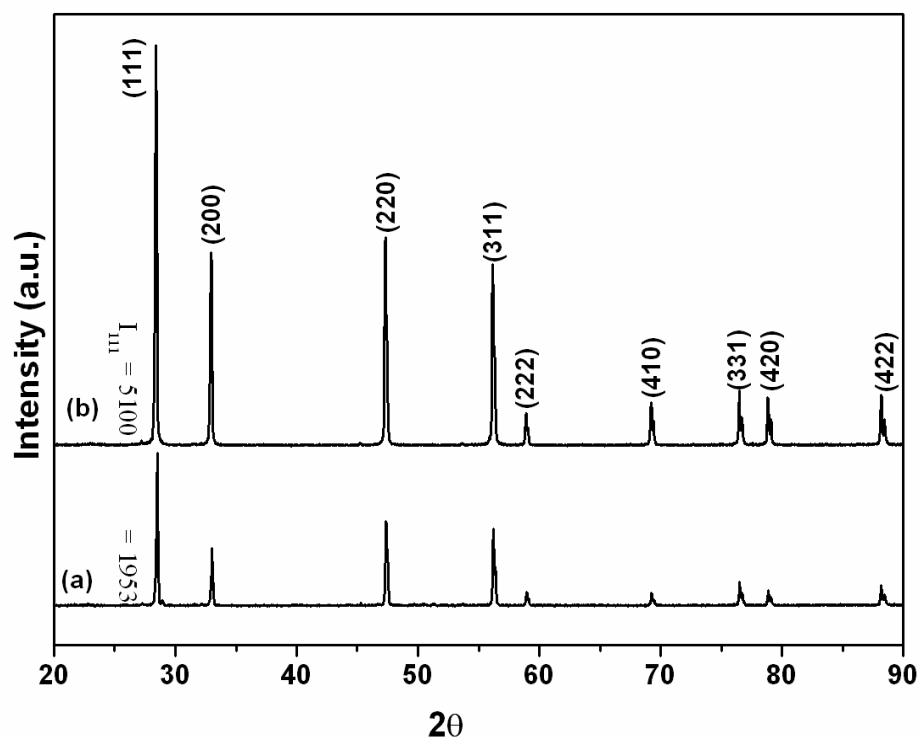


Figure 1. The XRD patterns of (a) GDC ceramic substrate and (b) GDC film on GDC ceramic substrate.  $I_{111}$  showing the intensity counts of (111) peak in XRD pattern.



The intensities of all the peaks of bare GDC substrate have been doubled for GDC/GDC structure which could be due to enhanced density of Bragg planes. These observations reveal that GDC substrate promotes the crystal growth of GDC film (“substrate effect”), which is obvious in chemical deposition techniques. This is because the lattice parameter of depositing material and the substrate is same, therefore, the free energy exchange between them facilitates more nucleation centers along substrate crystallites and hence permit added rate of crystallite formation during film deposition (thickness  $\sim 2\mu\text{m}$ ).

The GDC films deposited on ceramic substrates were annealed to improve crystallization of films and the quality of film/substrate interface. The films annealed at temperature of  $450^\circ\text{C}$  are “less adhered” to the substrate and surface grains are discontinuous (figure 2a-b). Such interface and discontinuous grains could lead to additional interfacial resistance to the total structure. It is reported in literature that high temperature sintering of GDC thin films could be employed to fill-up the 2-3  $\mu\text{m}$  cracks in thin films. Hence to avoid interfacial resistance in the total system and to improve the film/substrate interface, the post heat treatment at  $1000^\circ\text{C}$  in air was carried out.

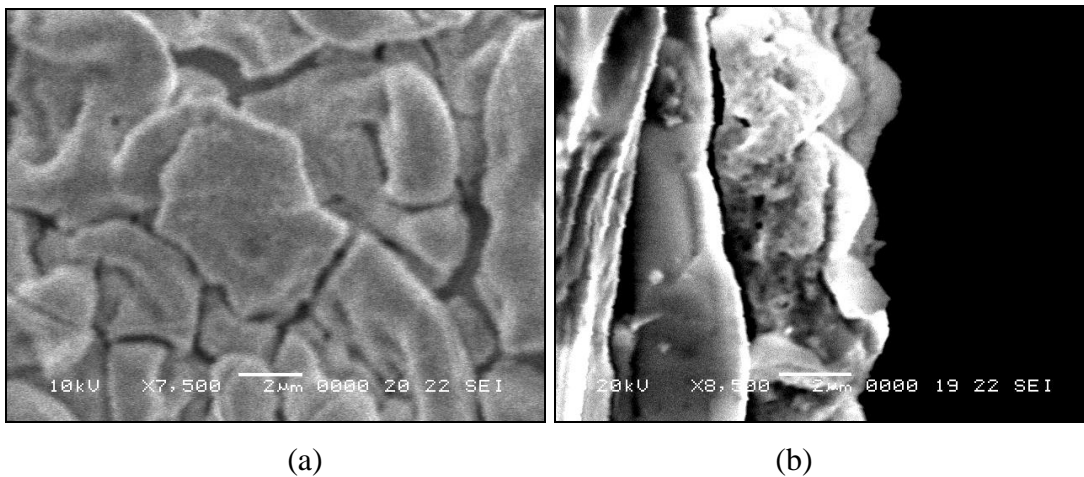
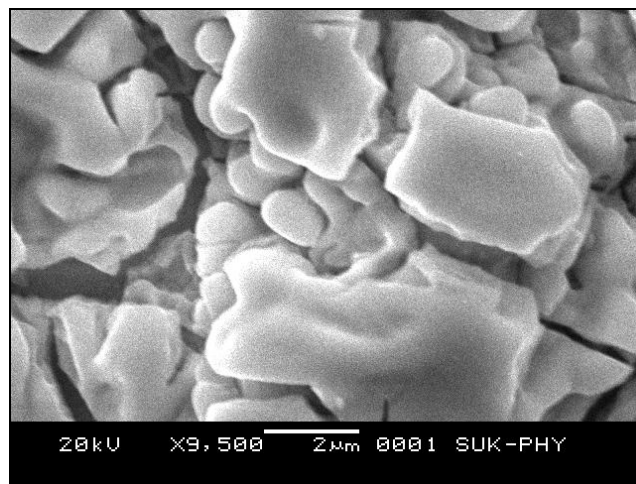


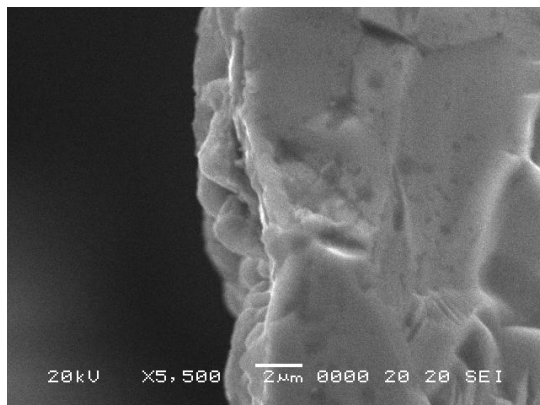
Figure 2. SEM of GDC films deposited on GDC ceramic substrate and annealed at  $450^\circ\text{C}$  for 3h in air; (a) surface and (b) the interface of GDC/GDC structure. (Bar length is  $2\mu\text{m}$ ).



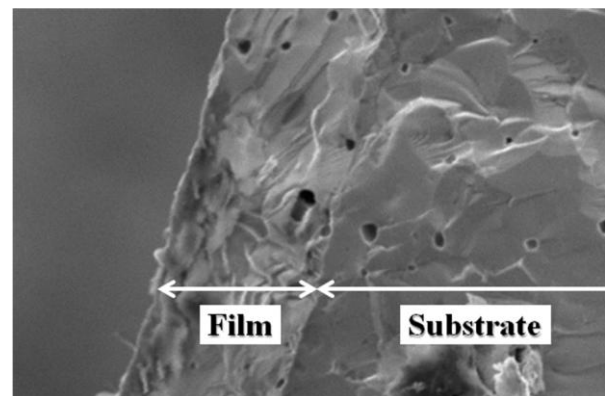
The post heat treatment (at 1000°C) leads to uniform and adherent film/substrate interface in addition to improved surface morphology of the film (depicted in figure 3a-b). The physical separation, considered being only due to dissimilar morphology of film and substrate, is reduced to a negligible level. Besides this, density of the GDC films is observed to be of the order of GDC substrate sintered at 1500°C (relative density is greater than 98%; figure 3c). This higher density achieved at 1000°C was attributed to the presence of nano-granules (avg. grain size 83-85nm), explained in detail in the next section.



(a)



(b)

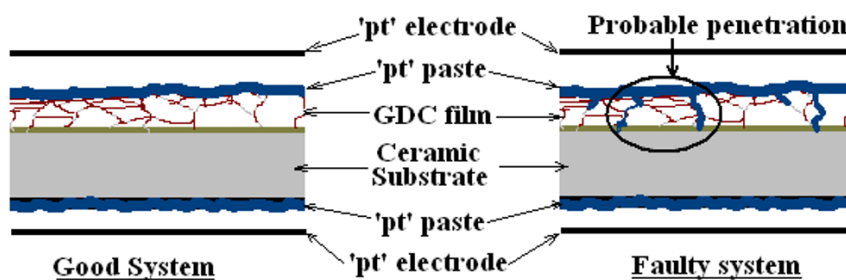


(c)

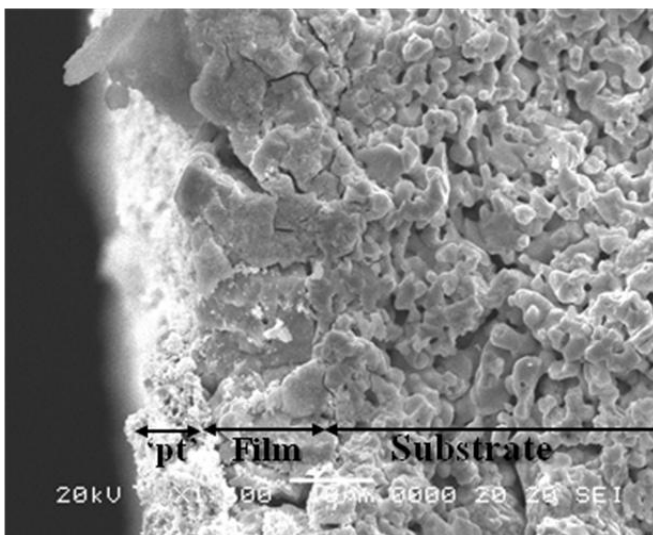
Figure 3. SEM of GDC films deposited on GDC ceramic substrate, annealed at 1000°C for 8h in air; (a) surface and (b) the interface of GDC/GDC structure. (Bar length is 2µm). (c) Fractured SEM of GDC/GDC structure for density comparison.



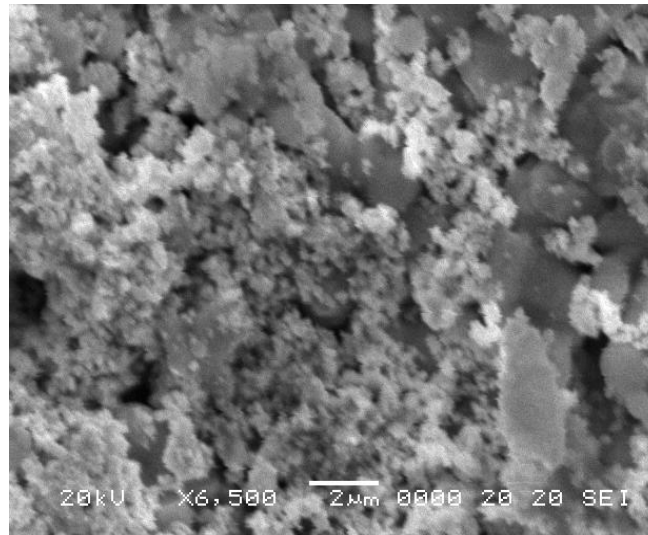
The electrical characterization of bare substrate and GDC/GDC structure was carried out using impedance measurements (1Hz-10MHz) in temperature range 250-500°C. The direct contact of 'pt' electrodes with the substrate from either side (illustrated in figure 4a) may short the sample under investigation during the impedance measurements and could lead to incorrect measurements. However, the fractured SEM image of platinum coated structure, imaged after the impedance measurements (figure 4b) shows that the platinum paste has remained on the surface of the film and has not penetrated/diffused into the film to short with substrate surface. Figure 4c shows the uniform coating of platinum paste over the surface of GDC films.



(a)



(b)

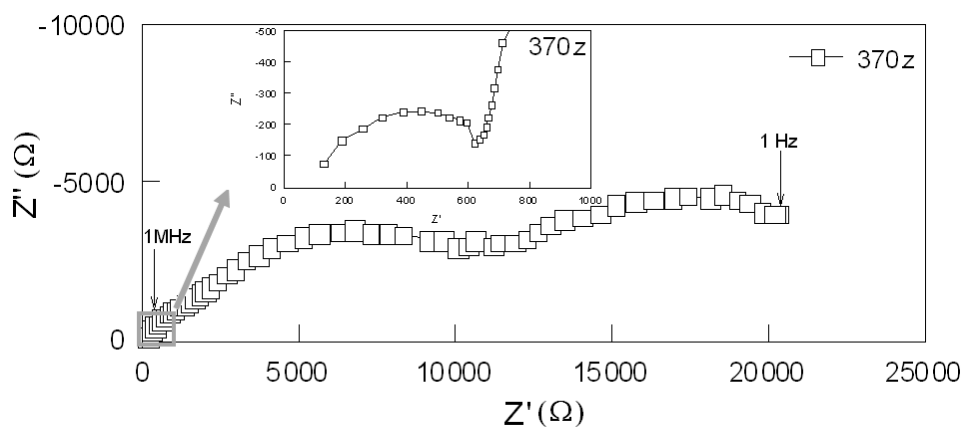


(c)

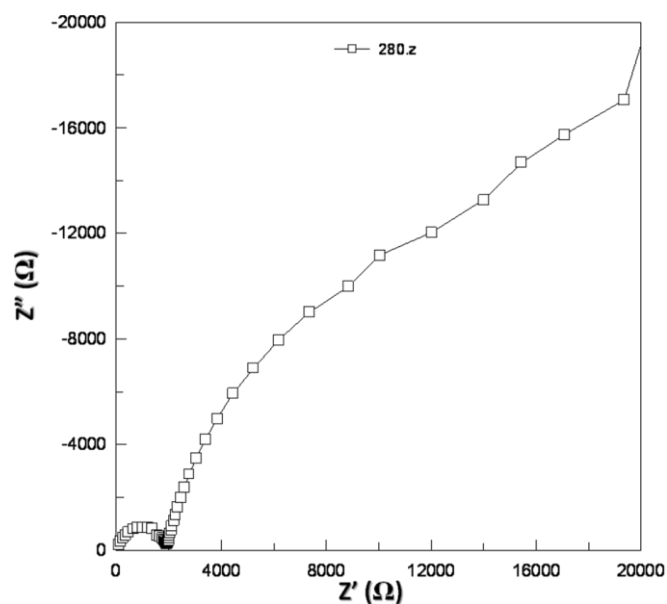
Figure 4. (a) Schematic of system formed by 'pt' electrode/film-substrate/'pt' electrode for impedance measurement. Right image shows the doubtful penetration of 'pt' paste. (b) SEM of tri-layer of 'pt' paste/film/substrate, (c) 'pt' paste coated onto surface of substrate.



The complex impedance plot of GDC/GDC structure and that of bare substrate recorded at 370°C and 280°C, respectively is shown in figure 5. It showed usual trend of three semicircles in complex impedance plots corresponding to electrode, grain boundary (GB) and grain interior (GI) impedance contributions to total impedance of the system.



(a)



(b)

Figure 5. Nyquist plot of (a) GDC film deposited on GDC substrate and (b) GDC substrate. Inset: Magnified view to show grain interior impedance contribution.

Complex impedance plots of bare substrate and GDC/GDC structure showed the gradual decrease in impedances originating from all the three contributions with an increase in measurement temperature. However, the common behavior of disappearance of the semi-circle originating due to GI impedance contribution was



observed at 440-460°C for both the systems i.e. of GDC/GDC structure and GDC substrate.

The impedance data were analyzed by impedance analysis software (ZView Version 2.4a) and used to extract the grain interior ( $R_g$ ) and grain boundary impedances ( $R_{gb}$ ). While analyzing the impedance data, the data points corresponding to electrode contribution was skipped to avoid the complexities in extraction of  $R_g$  and  $R_{gb}$ . In accordance with Duncan and Laxia [23], the use of 2CPE circuit is employed here to obtain the best fit for observed impedance data, which adequately allowed us to determine the resistance of system under investigation. This fitting cannot be considered for interpretation of the exact physical processes that would occur in such systems. At present GDC\GDC system forms a complex tri-layer structure we would have to consider other complex circuit elements to simulate the exact processes taking place in the system. However, it requires further studies and which is out of scope this thesis. Thus the extracted  $R_g$  and  $R_{gb}$  determined were used to outline the electrical performance of grain interior and grain boundaries of samples under investigation. The fit result from the analysis, for GDC film on GDC substrate is shown in figure 6.

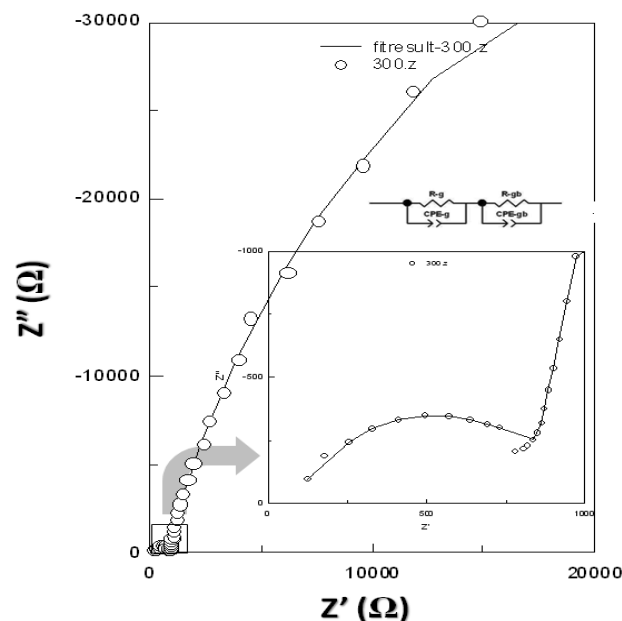
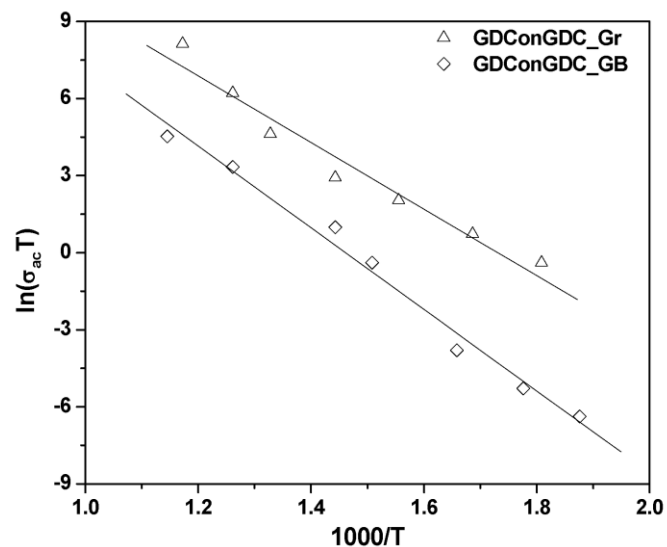


Figure 6. The typical fit result from the analysis of impedance data collected for GDC film on GDC substrate at 300°C.

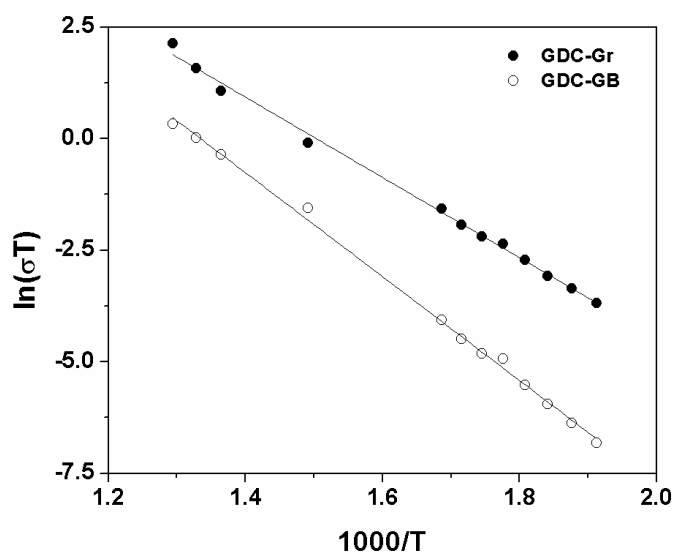




The values of  $R_g$  and  $R_{gb}$  obtained from the fit parameters were used to calculate ac conductivities and were further fitted to the Arrhenius relation. Figure 7 shows the Arrhenius plot for GDC/GDC structure and GDC substrate.



(a)



(b)

Figure 7. Variation of  $\ln(\sigma_{ac}T)$  as function of  $1000/T$  for (a) GDC/GDC and (b) GDC substrate.

The values of GI and GB conductivity and respective activation energies calculated from Arrhenius plots for GDC/GDC structure and GDC substrate are listed in table 2. The GI conductivity of GDC substrate was higher than that of GDC/GDC



structure while GB conductivity was high for GDC/GDC structure. These results are discussed in the next section of this chapter.

Samples ↓	$\sigma_g$ (S/cm)	$\sigma_{gb}$ (S/cm)	$E_g$	$E_{gb}$
<b>GDC substrate</b>	0.035	0.0017	0.77	1.09
<b>GDC/GDC</b>	0.027	0.0028	1.07	1.40

Table 2. Values of grain interior (GI) and grain boundary (GB) conductivities at 500°C in air along with respective activation energies for GDC/GDC structure and GDC substrate.

### 6.3.2. Micro-structural properties of NiO-GDC substrates at different stages of its processing and electrical properties of NiO-GDC\* substrate

In the early stage of work of the work we have planned to deposit GDC on NiO-GDC to form GDC/NiO-GDC structures, which were further planned to reduce in-situ to get electrolyte/anode structures. However, an attempt to deposit GDC films onto NiO-GDC substrate results into less adherent and films with thickness much less than 2 $\mu$ m. An electrolyte is supposed to have the thickness of the order of 10 $\mu$ m [2]. We have decide to reduce the NiO-GDC substrate to obtain porous material and then to deposit GDC film on it.

Figure 8 shows the XRD patterns of NiO-GDC (sample sintered at 1400°C/8h), Ni-GDC (sample reduced in H<sub>2</sub> atmosphere at 900°C/5h) and NiO-GDC\* (sample heat treated at 1000°C/8h in air) ceramic samples. In all three states of processed NiO-GDC substrates, the absence of peaks corresponding to Gd<sub>2</sub>O<sub>3</sub> and comparatively larger lattice parameter (~5.419Å) than that of the host lattice of ceria (5.410Å) confirms the complete dissolution of Gd<sub>2</sub>O<sub>3</sub> in ceria lattice, to form GDC [24].

The XRD pattern of NiO-GDC was compared with JCPDS PDF no. 75-0161 (10%Gd doped Ceria) and 78-0643 (Cubic NiO) to confirm the individual phase peaks and was accordingly indexed in figure 8a. All the reflection peaks could be either indexed with NiO or GDC, confirming formation of composite. In addition to that the lattice parameters calculated for each of phase are in well agreement with that



of respective standard values. The average lattice parameters are 5.419Å and 3.540Å, respectively for GDC and NiO phase. These observations affirm that NiO phase remains separate and does not diffuse into the GDC lattice to form the undesirable phase. The average crystallite size estimated for GDC and NiO phases are 581nm 343nm, respectively.

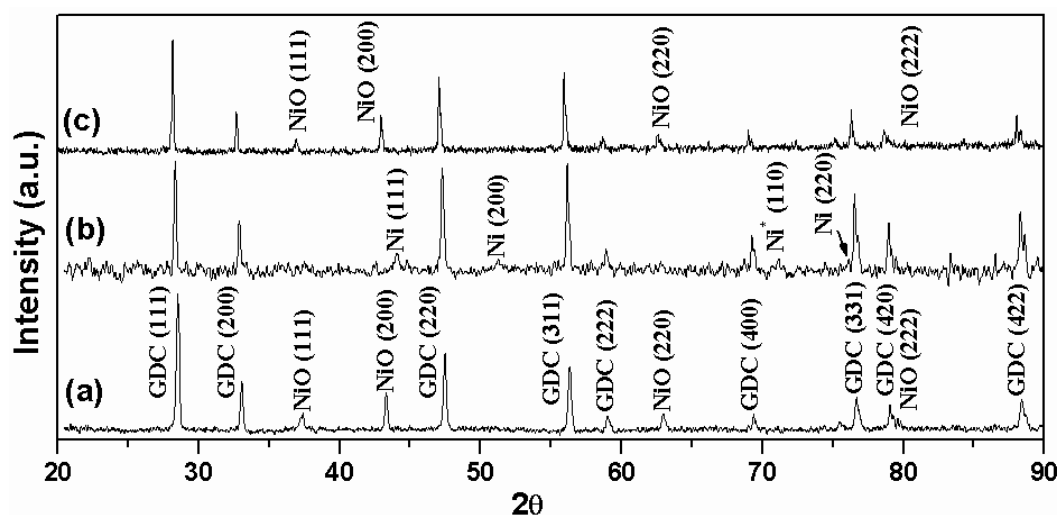


Figure 8. XRD patterns of ceramic samples, (a) NiO-GDC, (b) Ni-GDC and (c) NiO-GDC\*.

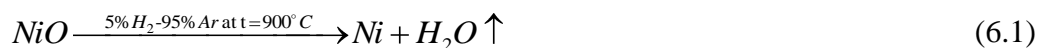
The XRD pattern of reduced sample i.e. of Ni-GDC (figure 8b) was compared with JCPDS PDF no. 75-0161 (10%Gd doped Ceria) and 04-0850 (Cubic Ni). In addition, it was also compared with JCPDS PDF no 78-0643 for the presence of cubic NiO remained in the sample due to un-reduced state of NiO-phase. The peaks are indexed accordingly in the figure 8b (GDC peaks are not indexed to avoid the complication in the figure) and no peaks corresponding to NiO-phase were observed, confirming the complete reduction of sample under investigation. The average lattice parameters calculated for GDC and Ni phases are 5.418Å and 4.169Å, respectively. The average crystallite size calculated using Scherrer's formula for GDC and Ni phases are 575nm 403nm, respectively.

The reduced samples employed to synthesize the GDC/Ni-GDC structure and further heat treated in air for improvement of crystallinity in the film and quality of the interface. Upon heat treatment, the Ni-GDC substrates were supposed to get oxidized and become NiO-GDC\*, which was confirmed by comparing its XRD



pattern with JCPDS PDF no. 75-0161 (10%Gd doped Ceria) and 78-0643 (Cubic NiO) (figure 8c). No reflection peak due to Ni was observed in the XRD pattern, which confirms the complete oxidation of Ni to NiO. Again the lattice parameters calculated for each of phase are in well agreement with that of respective standard values from JCPDS. The average lattice parameters for GDC and NiO phases are 5.419Å and 3.541Å, respectively, which are in good agreement with the standard (JCPDS) values. Apart from the similarities in lattice parameters as that of NiO-GDC and NiO-GDC\*, the crystallite size obtained for NiO-GDC\* case are slightly higher for GDC (610nm) and NiO-GDC (443nm) phases.

Figure 9 shows the SEM images of the NiO-GDC ceramic substrates at different stages. The surface morphology of the NiO-GDC (sintered at 1400°C/8h) is comparatively porous (figure 9a) than that of GDC samples sintered at 1500°C/8h. The porous nature of NiO-GDC samples is attributed to comparably low sintering temperature in addition to the procedure employed to for its synthesis (4-step ceramic route; without binder removal step). One can also attribute the porous nature of NiO-GDC samples to its composition, as the composition involves two phases (composite) either of which avoids the lattice diffusion (which is the major process of densification) at particular sintering temperature. These porous NiO-GDC (green in color) ceramic samples, upon reduction in H<sub>2</sub> atmosphere at 900°C, turns into more porous Ni-GDC (dark black in color) structure (figure 9b). The increased porosity is attributed to the fact that the heating the NiO-GDC in reducing environment eliminates the oxygen from the NiO phase by forming H<sub>2</sub>O. The probable reaction during this process could be



GDC thin films were deposited on this porous Ni-GDC substrate followed by annealing at 1000°C for 8h in air. This leads to re-oxidation of Ni into NiO phase, confirmed by XRD analysis (figure 1d),



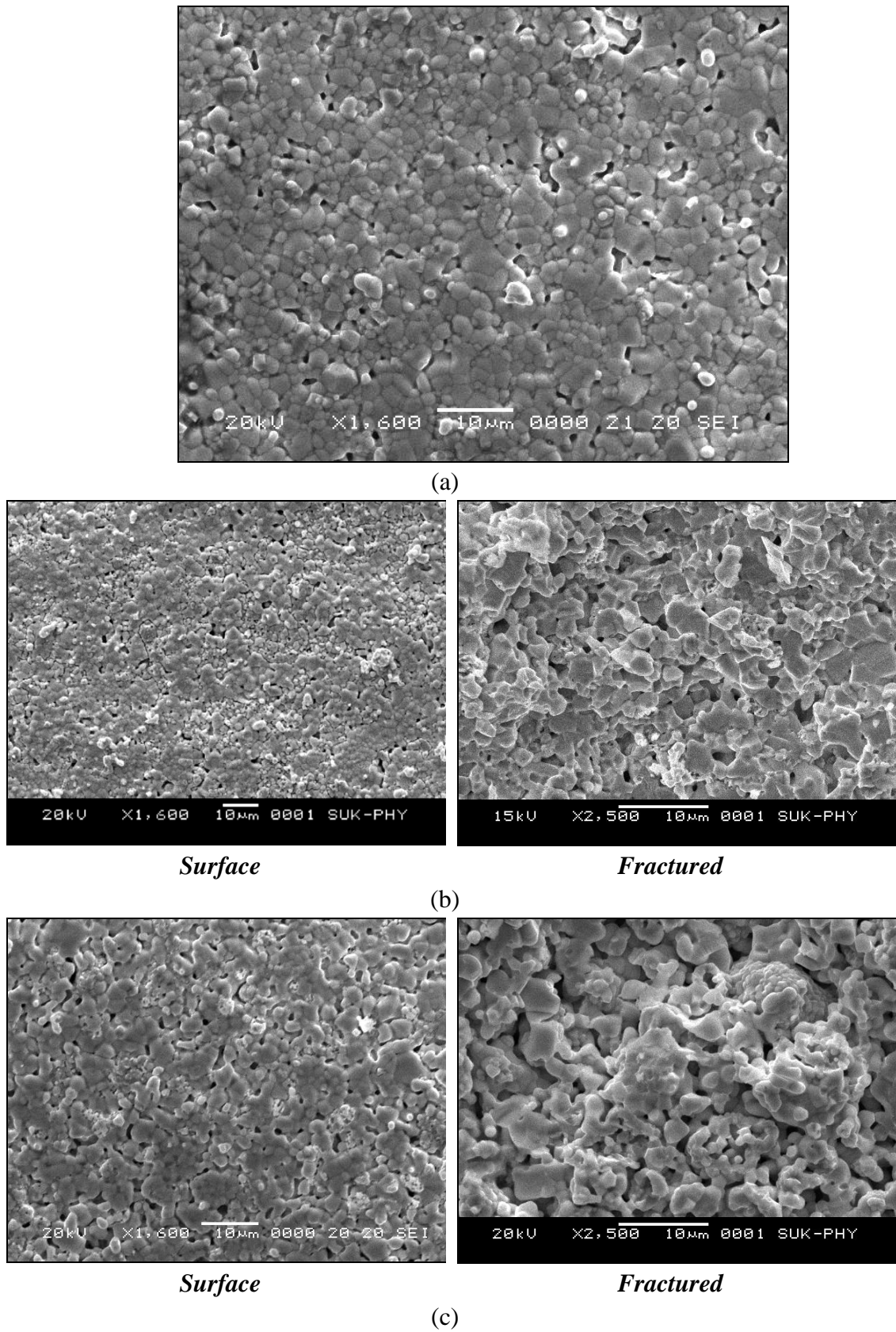


Figure 9. SEM of NiO-GDC ceramic samples at different stages. (a) NiO-GDC, (b) Ni-GDC and (c) NiO-GDC\*.



The SEM image of NiO-GDC\* is shown in figure 9c. The grain growth pattern has not been changed drastically for NiO-GDC to Ni-GDC and to NiO-GDC\*, however, the NiO-GDC\* showed comparatively larger grains than NiO-GDC. The careful observation of the micrographs of composite substrate (figure 9a-c) reveals that, there are two types of grains, as expected, one is of GDC phase and other is of NiO phase. As we have prepared the composites with 30%NiO, the less continuous grains would be of NiO (in NiO-GDC) or Ni (in Ni-GDC) phase. The grains of NiO in NiO-GDC (figure 9a) sample undergo decrease in size after reduction treatment and can be seen as clusters of comparatively smaller Ni grains embedded in GDC grains. Further when the Ni-GDC composite is heat treated in air at 1000°C, the transformation of Ni to NiO leads to increase in grain size of NiO (figure 9c). However, in NiO-GDC\* the agglomeration of grains takes place and leads to formation of comparatively large clusters and pores in the sample. Apart from these morphological dissimilarities, the relative densities of composite samples varied with change of compositions. The Ni-GDC sample possesses least relative density of 71%, while that of NiO-GDC and NiO-GDC\* possesses approximately same relative density of 79%.

The complex impedance plot of NiO-GDC\* recorded at 290°C is shown in figure 10. It shows the usual trend of three semicircles in complex impedance plots corresponding to electrode, grain boundary (GB) and grain interior (GI) impedance contributions to total impedance of the system.

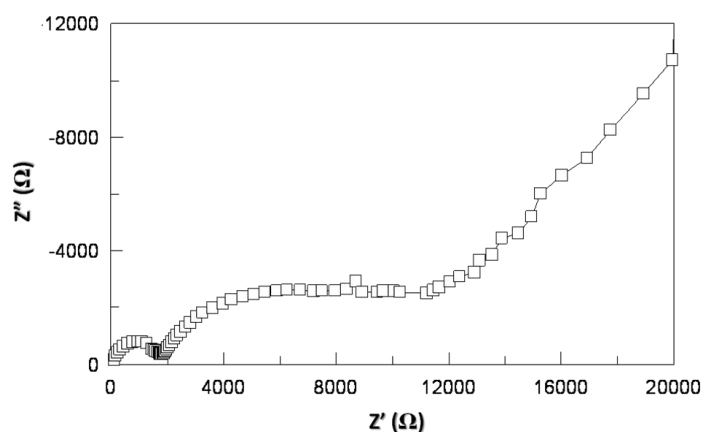


Figure 10. Complex impedance plot of NiO-GDC\* substrate measured at 290°C.



In line with other polycrystalline samples complex impedance plots for substrates showed the gradual decrease in impedances with an increase in measurement temperature. The semi-circle originating due to GI impedance contribution was also observed to disappear at 440-460°C for NiO-GDC\* substrate. It is interesting to note that the presence of NiO phase in NiO-GDC\* substrate does not vary the temperature of fading of semi-circle originating due to GI impedance. Therefore, this observation implies that onset temperature (~460°C) of fading of GI impedance response is the intrinsic property of GDC.

The impedance data were further analyzed by impedance analysis software to extract the grain interior ( $R_g$ ) and grain boundary impedances ( $R_{gb}$ ), with the criteria mentioned while analyzing impedance data for GDC/GDC structure. The values of  $R_g$  and  $R_{gb}$  obtained from the fit parameters were used to calculate ac conductivities and were further fitted to the Arrhenius relation. Figure 11 shows the Arrhenius plot for NiO- GDC substrate.

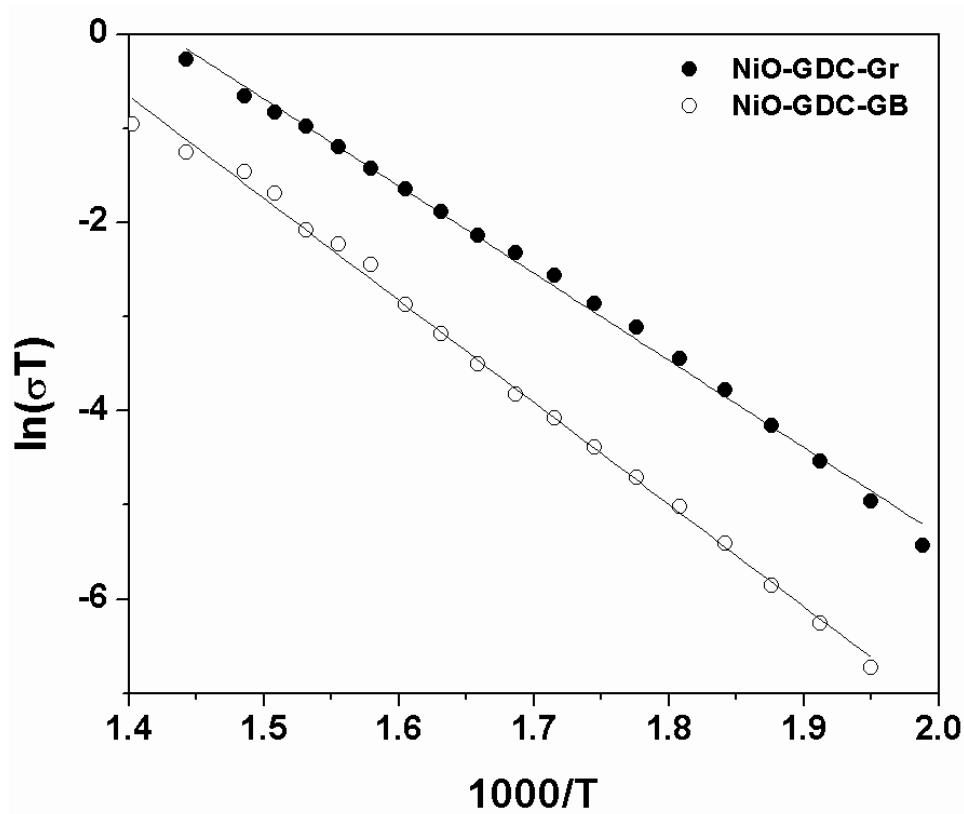


Figure 11. Variation of  $\ln(\sigma_{ac}T)$  as function of  $1000/T$  for NiO-GDC\* substrate.



The values of GI and GB conductivity measured at 500°C for NiO-GDC\* substrate are 0.107S/cm and 0.0009 S/cm. respectively. These GI conductivity obtained for NiO-GDC\* is much higher than that of GDC substrate and that of GDC/GDC structure. The high value of GI conductivity could be due to the presence of NiO-phase in substrate. Besides this, comparably less GB conductivity of NiO-GDC\* substrate is attributed to the increased hetero-contacts between GDC and NiO phase. This aspect is more clearly discussed in discussions section. The activation energies calculated from Arrhenius plots for NiO-GDC\* substrate for GI and GB conductivity is 0.81eV and 0.9eV, respectively. Comparably less activation energy obtained than that of GDC substrate and GDC/GDC structure was attributed to presence of NiO-phase in sample as NiO possesses comparatively lesser activation energies for both the contributions than that of single GDC phase. The results are discussed at length in the ‘discussions’ section of this chapter.

### 6.3.3. Micro-structural and electrical properties of GDC deposited on NiO-GDC\* substrate

Figure 12 shows the XRD patterns of GDC/NiO-GDC\* structure (annealed at 1000°C) and of bare substrate.

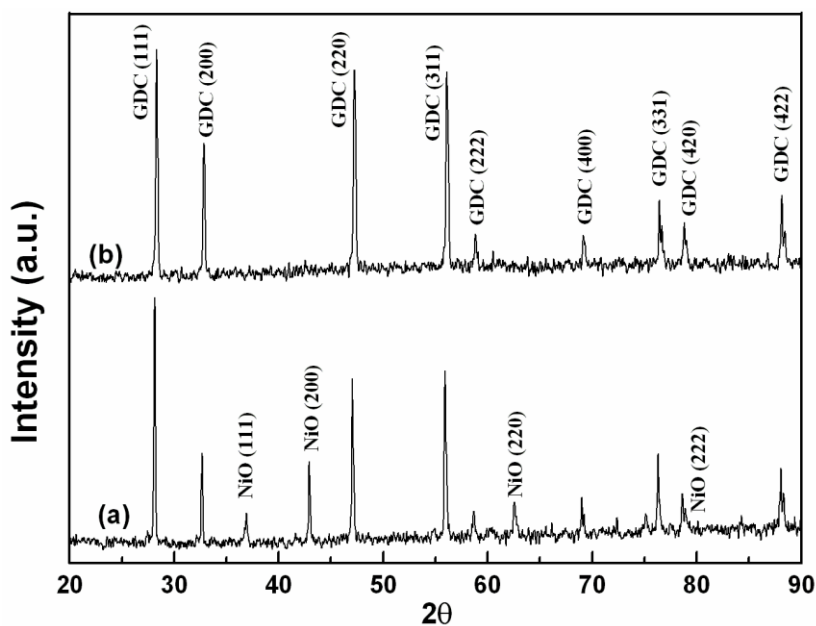


Figure 12. The XRD patterns of (a) NiO-GDC\* ceramic substrate and (b) GDC film on NiO-GDC\* ceramic substrate.





As mentioned for GDC/GDC structure, if the lattice parameter of depositing material and the substrate is same, it leads to added rate of crystallite formation during film deposition. As a consequence, all the intensity of almost all the reflection peaks was doubled. However, such added rate of crystallite formation during film deposition is not observed for the GDC/NiO-GDC\* structure (figure 12), instead it showed higher grain growth leading to higher thickness ( $\sim 13\mu\text{m}$ ). Further, as the film thickness was large ( $\sim 13\mu\text{m}$ ), the peaks originating from substrate were not seen in the XRD pattern of film (figure 12b).

The thermal treatment employed for the GDC/GDC structure was repeated for the GDC/NiO-GDC\* structure to improve the grain connectivity and interface. Figure 13 shows the SEM of GDC/NiO-GDC\* structure annealed at  $450^\circ\text{C}$ .

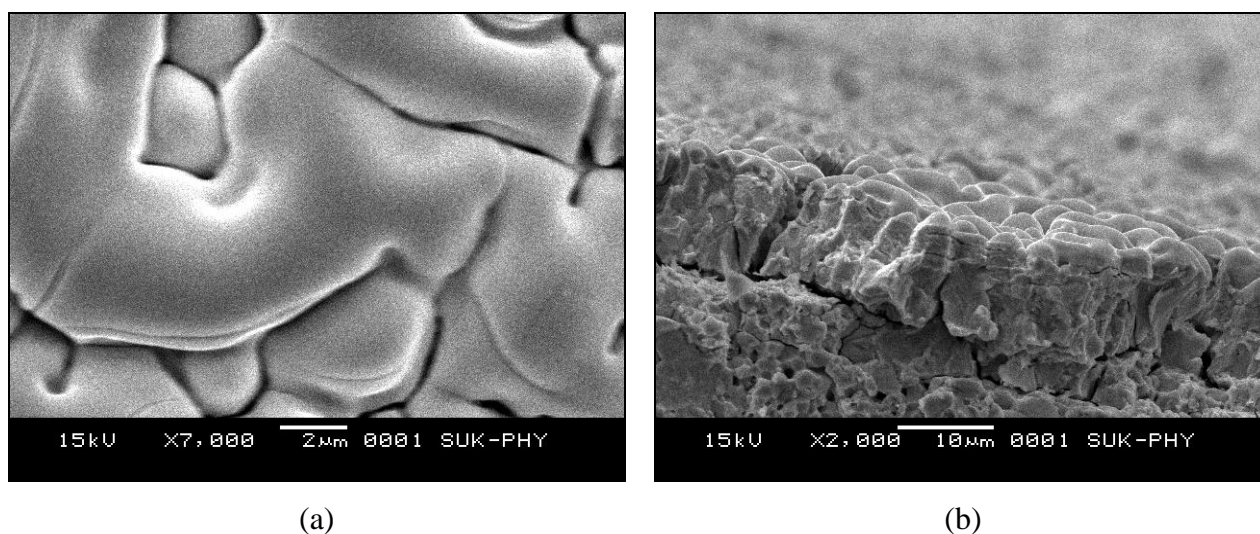
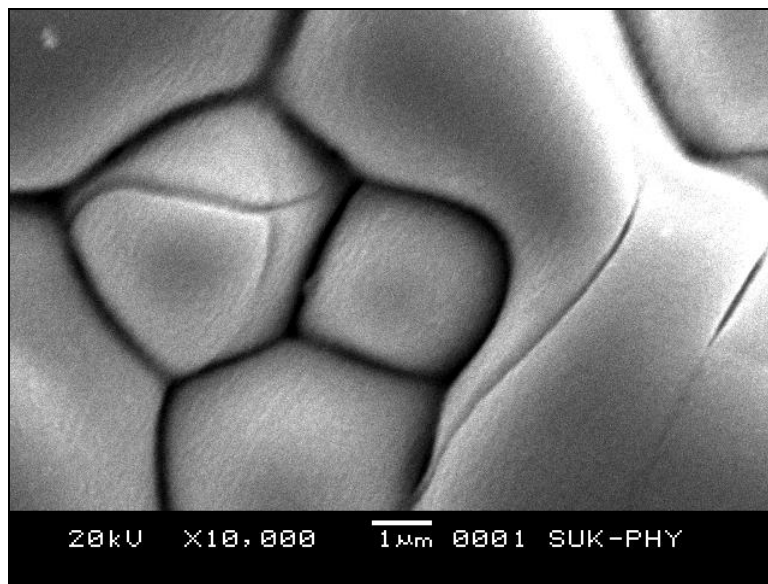


Figure 13. SEM of GDC films deposited on NiO-GDC\* substrates and annealed at  $450^\circ\text{C}$  for 3h in air; (a) surface morphology and (b) fractured morphology.

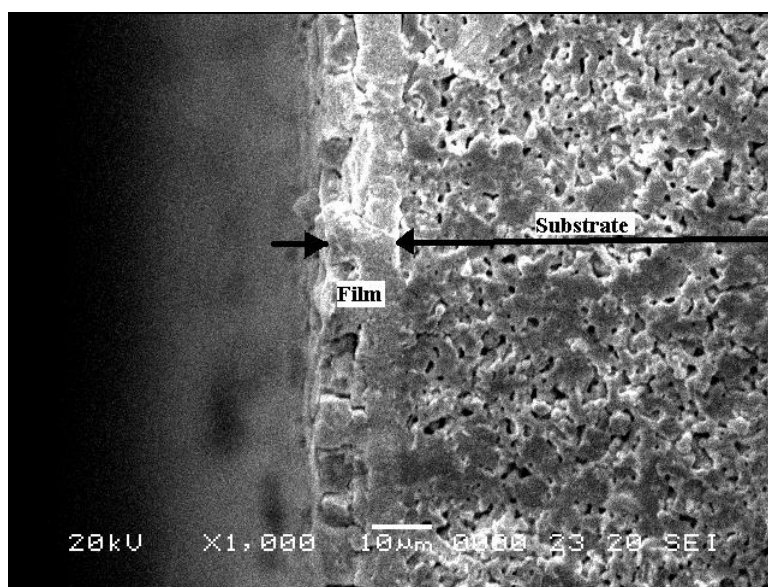
The surface morphology of GDC/NiO-GDC\* structure shows comparably compact and uniform surface than that of GDC/GDC structure annealed at the same temperature. However, the interface of GDC film with NiO-GDC\* is not adherent and shows discontinuous grains, similar to GDC/GDC structure. Thus to improve the interface and adherence of film with substrate the post heat treatment at  $1000^\circ\text{C}$  was employed and it leads to uniform and adherent film/substrate interface in addition to improved surface morphology of the film (depicted in figure 14a-b). The physical separation is reduced to a negligible level (figure 14b). Besides this, relative density



of the GDC film is observed to be greater than 98%. This higher density achieved at 1000°C was attributed to the presence of nano-granules formed during the synthesis of GDC thin films using spray pyrolysis technique. This aspect is discussed in detail in discussions section.



(a)



(b)

Figure 14. SEM of GDC films deposited on NiO-GDC\* substrate and annealed at 1000°C/8h in air; (a) surface and (b) fractured morphology.



The electrical characterization of GDC/NiO-GDC\* structures was carried out using impedance measurements (1Hz-10MHz) in temperature range 250-500°C. The typical complex impedance plot of GDC/NiO-GDC\* structure recorded at 340°C is shown in figure 15. It also showed the usual trend of three semicircles in complex impedance plots.

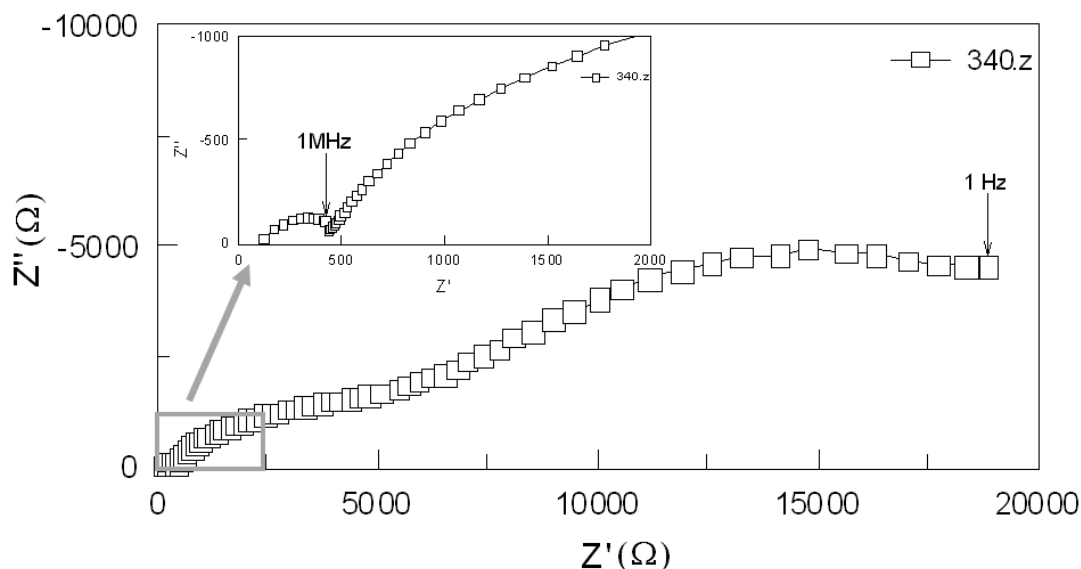


Figure 15. Complex impedance plot of GDC/NiO-GDC\* structure. Inset shows magnified view of grain interior impedance contribution.

The similar trend of the gradual decrease in impedances originating from all the three contributions with an increase in measurement temperature was observed for GDC/NiO-GDC\* structure. The semi-circle originating due to GI impedance contribution disappears at 440-460°C, which is again attributed to the inherent property of GDC. The impedance data were analyzed by impedance analysis software (ZView Version 2.4a) and used to extract the grain interior ( $R_g$ ) and grain boundary impedances ( $R_{gb}$ ). The typical fit result from the analysis, for GDC film on NiO-GDC\* substrate is shown in figure 16.



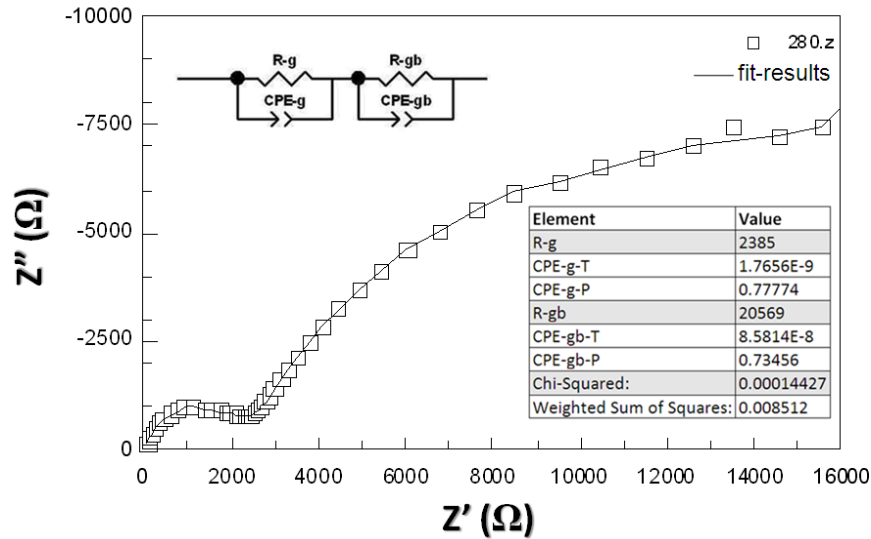


Figure 16. The typical fit result from the analysis, for GDC film on NiO-GDC\* substrate.

The values of  $R_g$  and  $R_{gb}$  obtained from the fit parameters were used to calculate ac conductivities and were further fitted to the Arrhenius relation (figure 17).

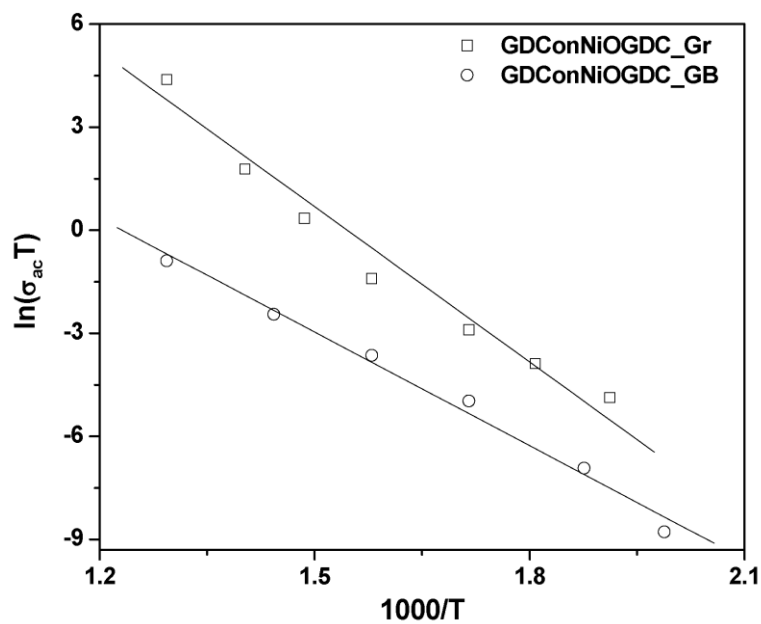


Figure 17. Variation of  $\ln(\sigma_{ac} T)$  as function of  $1000/T$  (Arrhenius plots) for GDC film on NiO-GDC\* substrate.



The GI and GB conductivity for GDC film on NiO-GDC\* substrate at 500°C are 0.103 S/cm and 0.0005S/cm, respectively. The decrease in these values compared to those for substrates are attributed to the increased number of hetero-contacts (discussed in detail in *discussions* section). The calculated activation energies for GI and GB conductivity are 1.02eV and 0.93eV, respectively.

#### **6.4. Discussion**

The potential of spray pyrolysis to synthesize the phase pure and dense GDC film on ceramic substrates with aim to develop half cell for IT or LT-SOFC has been demonstrated in the present work. The optimized preparative parameters more precisely, substrate temperatures are different for the ceramic substrates, which are obvious, as the ceramic substrates do carry different micro-structures and structural properties. Structural characterization revealed that GDC substrate enhances the crystallite formation in GDC film while it was not seen in GDC/NiO-GDC\* structure. However, the film thickness was much higher for NiO-GDC\* than that GDC substrates.

Apart from this, after heat treatment the fractured density for both the structures is comparable to that of GDC ceramic substrate sintered at 1500°C/8h (relative density is greater than 98%). This was attributed to the presence of nano-granules in the films, which not only affected the morphological properties of films but also affected the electrical performance of structures. The presence of nano-granules and surface roughness of these films were characterized by AFM.

##### **6.4.1. Atomic force microscopy of GDC films deposited on ceramic substrates**

Figure 18 shows the AFM of GDC films deposited on GDC and NiO-GDC\* ceramic substrate. Even after post heat treatment at 1000°C, GDC/GDC showed discontinuous and fractured grain morphology (figure 3) while GDC/NiO-GDC\* showed the better grain growth and grain connectivity (figure 14). Nonetheless, AFM showed reasonably smooth surfaced grains of GDC films deposited on both the ceramic substrates (table 3).



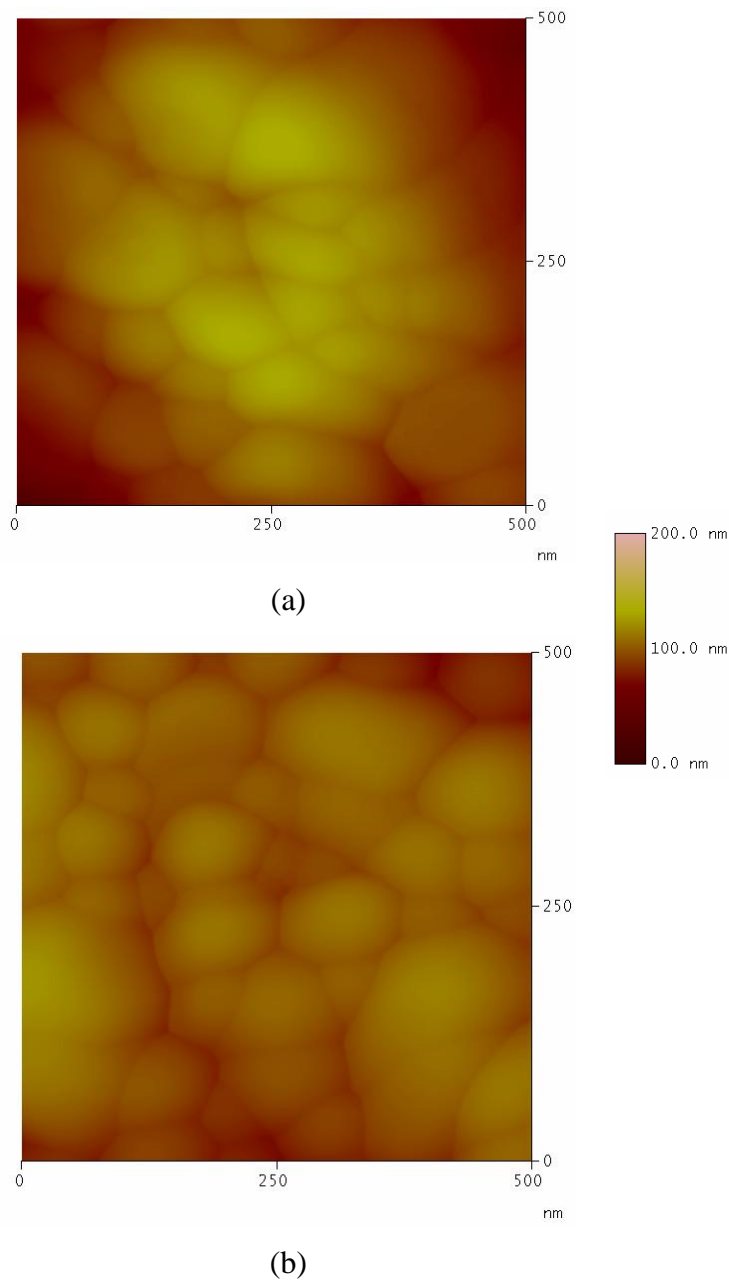


Figure 18. AFM of GDC films deposited on (a) GDC and (b) NiO-GDC\* substrate.

The surface roughness of the GDC films deposited on ceramics substrates examined using AFM were calculated using formula,

$$R_q = \sqrt{\frac{\sum (Z_i - Z_{avg})^2}{N}} \quad (6.3)$$

It shows the RMS surface roughness of a particular image area. This is the standard deviation of the Z value (height value) within the given area. Where  $Z_{avg}$  is



the average of the Z values within the given area,  $Z_i$  is the height value at particular point and N is the number of points within the given area. From the values in table 3, estimated mean surface roughness ( $R_q$ ) is low for larger grain size and vice-a-versa. As the surface roughness is standard deviation of height values from its mean height values, the wider grain size distribution for films on GDC substrates would be the major cause of higher surface roughness estimation. Typical section of AFM image used to determine surface roughness is shown in figure 19. Numbers of such sections were used to determine average surface roughness of films.

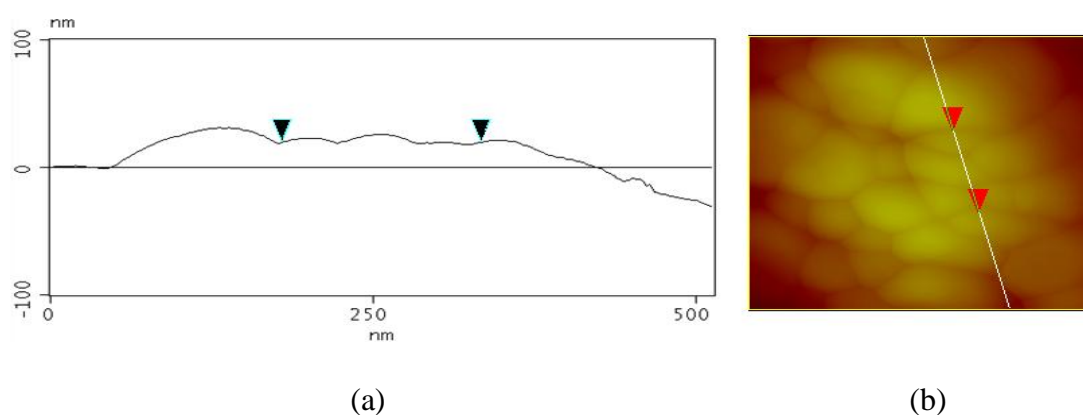


Figure 19. Typical section of AFM image used to determine the surface roughness of the films; (a) variation of height values about its mean along the line drawn in the (b) corresponding AFM image.

For GDC/GDC structure, there were granules with size as large as 250nm compared to their smaller counterparts in the range 30-40nm. The size distribution of granules in the GDC films deposited on GDC substrate is comparatively wider than that of on NiO-GDC\* substrate (table 3).

GDC films on	Surface roughness	Avg. grain size	Min. grain size	Mix. grain size	Grain size Distribution
GDC	18.64nm	83 nm	30-40 nm	250 nm	Wider
NiO-GDC*	8.86 nm	85 nm	60-70 nm	150 nm	Moderate

Table 3. Surface roughness and average grain size estimated from AFM images of GDC thin films on different ceramic substrates.



### 6.4.2. Formation of nano-crystalline GDC thin films

Formation of nano-crystallites during thin film deposition is the characteristic of SPT, which can be explained as follows: The spray solution, containing metal ions in desired proportion, when sprayed using air-blast nozzle, undergoes droplet formation. The droplets directed towards the heated substrate undergo subsequent decomposition during its flight and eventually gets partially dehydrated. This partially dehydrated solid particles when approaches to substrate experience high thermal-gradient at substrate and get rapidly pyrolyzed. After the pyrolysis, the decomposed solid particle on reaching to substrate finds/forms a nucleation center for further grain growth. These solid particles, in general, possess the dimensions of few nanometers. The continued spray of solution leads to accumulation of such solid particles on the substrate and the maximum of thickness of film is decided by surface properties of the substrate, provided the spray parameters are fixed (table 1), except the substrate temperature (explained in next section). These accumulated nanometer sized particles undergo sintering and partial grain-growth at deposition temperature. Further crystallization and grain growth in films occurs upon the post-annealing treatment, But the grain remains still in nano-meter size with improved compactness (figure 18a-b). The SEM images (figure 3 and figure 14) show the clusters of such nano-granules.

### 6.4.3. Effect of substrates on film thickness

The set point (substrate/deposition temperature – ST) for Ni-GDC and GDC substrates were 250°C and 280°C, respectively. Here we have employed two different substrate temperatures to account the different temperature gradients produced by substrates due to their thermal conductivities. Higher the thermal conductivity of substrate, the set point of deposition temperature would be further lower (reaching to decomposition temperature ( $T_d$ ) of solution). Further the surface of substrate could attain the temperature of hot plate (deposition temperature – set point) very easily (table 1). Hence the preset temperature is not required to set above the desired value (decomposition temperature of solution).

The decomposition temperature of GDC as confirmed from TG-DTA analysis [21] is 280°C. Now the deposition temperature would be closer to decomposition temperature for highly thermal conducting substrate i.e. Ni-GDC substrate of the





present work. However, the optimized substrate temperature for the growth of GDC film on Ni-GDC is 250°C ( $< T_d = 280^\circ\text{C}$ ). It is observed fact that the presence of metallic species in the substrate (e.g. Ni in case of Ni-GDC) at elevated temperatures (greater than room temperatures) hinders the stabilization of sprayed droplets on to the substrate. Hence the substrate temperature was decreased to 250°C. And to get the films deposited on to such substrates an approach of *wet-film-formation* during spray pyrolysis was employed. In this approach, the films are deposited at temperatures lower than decomposition temperature (i.e. at  $250^\circ\text{C} < T_d = 280^\circ\text{C}$ ) of precursor and subsequently heat treated to a higher temperature to complete the decomposition of deposited materials. This is not a good practice to prepare the films by SPT as it involves the high amount of incorporation of solvent (water in our case) and which might lead to cracking or peeling-off of the films during heat treatment. However, on the other hand it may results in higher thickness ( $\sim 13\mu\text{m}$ ) in a single run, as the wet droplets pile up for comparably high length. The decreased substrate temperature for highly thermal conducting substrate is also reported in literature [25]; however, its interpretation was not presented.

As mentioned in the *formation of nano-crystalline GDC film*, when the dehydrated solid particle reaches to the substrate, it *forms* or *finds* the nucleation sites for its stabilization and then further grain growth occurs. In the former case, the rate of grain growth becomes delayed as the formation of nucleation sites by the sprayed particle requires its stabilization and hence leads to less efficient graining during its deposition. In this case the nucleation sites would be along the crystallites of substrate leading to improved rate of crystallite formation, as observed in case of GDC substrate (figure 1). As the surface of GDC substrate is smoother (average grain size  $\sim 11\mu\text{m}$ ), the probable nucleation sites would be only along the crystallites as these are the only sites where the sprayed droplet can stabilize for further grain growth. The process being less efficient for graining, the film cannot grow to large thickness. On the other hand, if sprayed particle *finds* available nucleation sites on substrate, in the form of irregular and rough structured surfaces (as in Ni-GDC substrate), there will be enhanced grain growth leading to higher thickness ( $\sim 13\mu\text{m}$ ), however, improved crystallite formation could not be seen (figure 12).



#### 6.4.4. Electrical characterizations

For both the structures (GDC/GDC and GDC/NiO-GDC\*) and substrates (GDC and NiO-GDC\*), the magnitudes of GI conductivity were remained higher than that of GB conductivity. Earlier research done for ceria systems [26, 27] showed that the “grain boundary effect” was greater for dilute solid solutions like 10%Gd doped ceria (GDC), with which our results agrees well.

The comparably decreased electrical conduction observed for GDC/GDC and GDC/NiO-GDC\* structure than that of respective bare substrates could be assigned to the existing various phase contacts in the samples. The various phase contacts are feasible among micron sized grains of GDC, NiO and voids from the substrates and nano sized GDC grains in the film. It is valid to consider that the homo phase-contacts offer less opposition than that of hetero phase-contacts for a particular process. The possible micro-structural phase contacts for GDC/GDC and GDC/NiO-GDC\* structures are schematically illustrated in figure 20 and originating number of total contacts are listed in table 4.

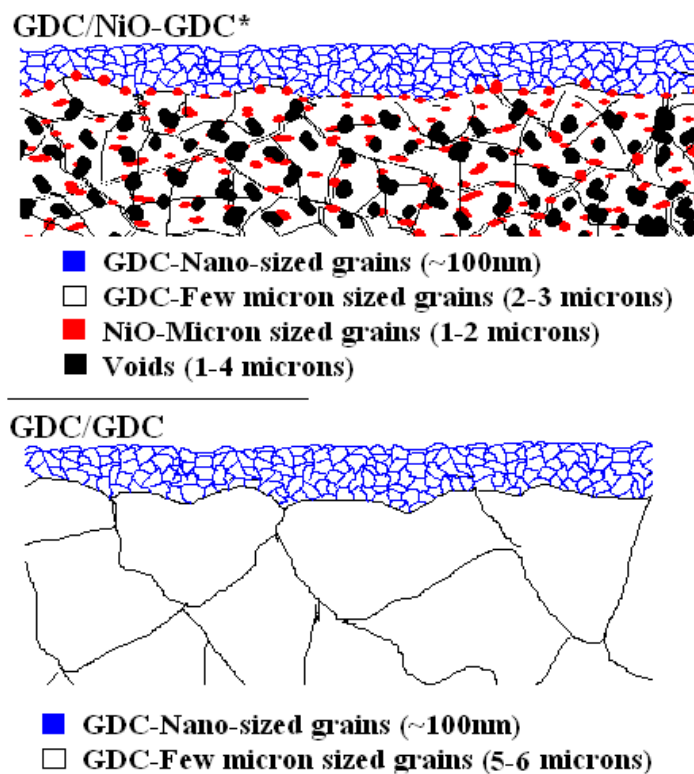


Figure 20. Schematic of micro-structural phase contacts for GDC/NiO-GDC\* and GDC/GDC structures.



Samples ↓	Probable phase contact types	Number of phase contacts
GDC substrate	MG-MG	1
GDC/GDC structure	MG-MG; NG-NG; MG-NG;	3
NiO-GDC* substrate	MG-MG; MN-MN; MG-MN;	5
	MN;	
	MV-MG; MN-MV;	
GDC/NiO-GDC* structure	MG-MG; MG-MN; MG-MV;	9
	MG-NG; MN-MN; MN-MV;	
	MN-NG; MV-NG; NG-NG;	

*MG – micron sized grains of GDC from the substrates*  
*MN – micron sized grains of NiO from the substrates*  
*MV – micron sized voids from the substrates and*  
*NG – nano sized grains of GDC from films*

Table 4. Various phase contacts for different systems.

#### 6.4.4.1. Variation in grain interior (GI) and grain boundary (GB) conductivities

The possible phase-contacts in GDC/GDC structure could be only of ‘nano/micron grains of GDC (NG-MG)’ type and only at film/substrate interface, as the presence of voids (relative density is greater than 98%) and other impurities (phase pure by XRD; impurity could be less than 0.1%), might not be realistic for this case. Thus the inability of GDC/GDC structure to surmount the GI conductivity of bare substrate can be attributed to the only existing phase-contact of NG-MG type, as the grain size distributions of film and substrate are different. The change of electrical properties of samples with variation in grain size distribution is discussed further in next section while explaining the variation in activation energies of the structures.

According to Ruiz-Trejo et al. [28], nano-ceramics have conduction paths along the grain boundaries. In the same regard, Bellino and co-workers [29] emphasizes that in nano-ceramics of doped ceria, oxygen migration can take place along the grain boundaries resulting in an enhanced GB ionic conductivity. In agreement with their observation our data showed enhancement in GB conductivity



for GDC/GDC structure by virtue of nano-ceramic GDC film on GDC substrate (table 2). It should be noted that though apparently the thickness ratio of the substrate and the top layer is high; the actual grain boundary length could vary for nano-ceramics. The ratio of GB of substrate to GB of film is calculated (table 5) and is found to be only 3 to 5. This ascertains the contribution of GB from nano-ceramics to the GB conductivity of total structure.

	Apparent thickness (t) ( $\mu\text{m}$ )	Avg. grain size (d) ( $\mu\text{m}$ )	GB/length ( $D = 1/d$ ) ( $\mu\text{m}$ )	Total GB $T = A \times t \times D$	Apparent 't' ratio	Actual GB (T) ratio
GDC	1200	11	9.1E-08	= 109.09 x a		
GDC film on GDC substrate	2	0.083	1.3E-05	= 24.096 x a	600	4.527273
NiO-GDC*	1200	2.5	4.0E-07	= 480 x b		
GDC film on NiO-GDC* substrate	13	0.085	1.2E-05	= 152.94 x b	92	3.138462

Where, 'a' and 'b' are surface area (A) of the samples, which was same for the G-G and G-N pair, respectively.

Table 5. Calculations of the apparent thickness (t) and actual GB (T) ratios (0.8–1.2 % error). The calculation assumes isotropic grain boundaries throughout the specimen.

The GI conductivity of NiO-GDC\* is found to be higher than that of GDC. Park and Choi [30] carried out detailed study on ionic conduction for complete range of  $(\text{NiO})_x\text{-(YSZ)}_{1-x}$  composite and found that additions of NiO in YSZ steadily increases the GI conduction. While explaining the conduction process in NiO-YSZ composite, they divided the entire composition range into three regions depending upon the type of charge carriers. According to them, for less than 30 mol% NiO in YSZ (region I), the charge carriers are ionic, for greater than 65 mol% NiO (region III) they are electronic, while for NiO content in between 30 to 65 mol% (region II) they are mixed conductors [31]. The NiO-GDC\* (30: 70 mol %) prepared in the present work resides at the beginning of II region. Therefore, the conduction is considered to be due to NiO grains in addition to GDC grains, resulting in higher GI conductivities. This assures that GDC and NiO grains are well distributed through the substrate with a three dimensional connectivity contributing improved GI



conductivity. Similar results were also observed for GI conductivity of GDC/NiO-GDC structure, however, the slight decrease in GI conduction than that of bare substrate could be attributed to added contact of 'NG-MG' type.

However, when the GB conduction of NiO-GDC\* and GDC/NiO-GDC\* were considered, very low values of GB conductivities were observed. The well connected GDC and NiO grains form GDC-NiO hetero-contacts, which offer more GB impedances. In addition to NiO-GDC contacts, other hetero-contacts present in the structure (table 4) would also be responsible to lower the GB conductivity. The hetero-contacts in GDC/NiO-GDC\*, in addition to those observed for NiO-GDC\*, are formed at film/substrate interface. All the mentioned contacts add-up together to form apparent GB impedance of GDC/NiO-GDC\* structure and led to further decrease in GB conduction.

#### 6.4.4.2. Variation in activation energies ( $E$ )

The activation energy for bare GDC substrate is in well agreement with the earlier reported values in literature [5, 20, 32]. Also it is well established for dilute doped ceria systems that the activation energy for conductivity along the GB ( $E_{gb}$ ) remains higher than that of GI ( $E_g$ ) conductivity. The value of  $E_g$  and  $E_{gb}$  for GDC is 0.77 and 1.09 eV, respectively.

Rupp et al [33] has compared the activation energies for nano-grained GDC films and micron-grained GDC bulk samples. The activation energy increases with grain size up to 200 nm while it remains constant for grain sizes greater than 200nm. The results by Rupp et al shows that the activation energy for total conduction increases from 0.77eV for average grain size of 29nm to 1.04eV for average grain size of 76 nm. In the present work, the average grain size of nano-crystalline GDC films over GDC is 83 nm. Therefore, the higher values of activation energy for GDC/GDC than the GDC may be attributed to the modification of electrical conduction phenomena from micron grained process to nano-grained process, for both the type of conduction (GI and GB), at the interface. The similar results were also reported by S.H. Jo et al [34]; however, their results were for nano-crystalline bulk samples.



Apart from effect of grain size distribution on conduction process, the comparatively lower values of activation energies for GDC/NiO-GDC\* structure than that of GDC/GDC structures could be attributed to the presence of NiO phase along with GDC phase in the substrate (composite), in addition to the electrically less impeding and homogeneously adherent interface.

## 6.5. Conclusions

The potential of spray pyrolysis technique (SPT) to synthesize solid electrolyte thin film on to ceramic substrates has been successfully demonstrated in this study. Optimization of preparative parameters for SPT to prepare the GDC coatings on ceramic substrates having different micro-structures and morphological properties leads to different structural and morphological properties of thin films. The GDC film coated on GDC electrolyte-grade ceramic substrate leads to comparably less thick films ( $\sim 2.2\mu\text{m}$ ) than that of on NiO-GDC anode-grade ceramic substrate ( $\sim 13\mu\text{m}$ ).

Apart from application of GDC thin films as solid electrolyte for IT-SOFCs, it could also act as a protective layer in conventional HT-SOFCs. The commercialization of conventional HT-SOFCs is mainly obstructed by the non-reliability of conventional electrolytes (e.g. YSZ) as it forms the undesirable phases at electrode interfaces (e.g. cathodes employing lanthanum-strontium-magnate – LSM system) during its operation over a time span. Thus to avoid this, a protective coating of very thin layer ( $\sim 100\text{-}500\text{nm}$ ) between electrolyte and cathode materials is mandatory. Thus from our investigation on GDC/GDC structure, it is possible to deposit the GDC as a protective layer with desired thickness on to electrolyte-like-ceramic substrates (i.e. on YSZ). Thus the cost-effective SPT could be employed to deal with the interfacial problems which are hindering the commercialization of SOFCs. The GI conductivity of such structure (here GDC/GDC) is  $0.027\text{S/cm}$  at  $500^\circ\text{C}$ , which perhaps could reach the desired conductivity value ( $\sim 0.1\text{S/cm}$ ) at the operation temperature of YSZ ( $\sim 800^\circ\text{C}$ ) electrolyte.

The GDC films deposited over NiO-GDC substrate have thickness between  $10\text{-}20\mu\text{m}$  with relative density of 98% which are the desirable characteristics of thin solid electrolytes to be used in IT-SOFCs. The GDC deposited over NiO-GDC provides a half cell onto which a suitable cathode material could be deposited and tested for inter-mediate temperature solid oxide fuel cell applications. The grain



interior conductivity of such a half cell is  $\sim 0.1\text{S/cm}$  at  $500^\circ\text{C}$ . Distinctly, the SPT synthesized highly sinterable (consisting of nano-granules) and dense (relative density is greater than 98%) GDC films prepared on anode with less impeding interface, offers an added advantage of co-sintering at as low as  $1000^\circ\text{C}$ . This ability of co-sintering at lower temperature avoids the electrode/electrolyte interfacial problems during fabrication of complete cell and thereby allows better and reliable electrical performance. Therefore, these outcomes definitely would support the prospective strategies for the commercialization of SOFCs.

### References:

- [1] S.C. Singhal, *Solid State Ionics* 135 (2000) 305.
- [2] B.C.H. Steele, *Solid State Ionics* 129 (2000) 95.
- [3] M. Mogensen, N.M. Sammes, G.A. Tompett, *Solid State Ionics* 129 (2000) 63.
- [4] I. S. Wang, T. Kato, S. Nagata, T. Kaneko, N. Iwashita, T. Honda, Dokiya M., *Solid State Ionics* 477 (2002) 152.
- [5] B. C. H. Steele, *Solid State Ionics* 134 (2000) 3.
- [6] T. S. Zhang, J. Ma, L. B. Kong, P. Hing, J. A. Kilner, *Solid State Ionics* 167 (2004) 191.
- [7] Y. J. Leng, S. H. Chan, S. P. Jiang, K. A. Khor, *Solid State Ionics* 170 (2004) 9.
- [8] C. Hatchwell, N. M. Sammes, I. W. M. Brown, *Solid State Ionics* 126 (1999) 201.
- [9] T. Fukui, K. Murata, S. Ohara, H. Abe, M. Naito, K. Nogi, *J. Power Sources* 125 (2004) 17.
- [10] J.B. Goodenough, *Ann. Rev. Mat. Res.* 33 (2003) 91.
- [11] T. Setoguchi, M. Sawano, K. Eguchi, H. Arai, *Solid State Ionics* 37 (1990) 502.
- [12] E.M. Kelder, O.C.J. Nijs, J. Schoonman, *Solid State Ionics* 68 (1994) 5.
- [13] A.A. Van Zomeren, E.M. Kelder, J.C.M. Marijnissen, J. Schoonman, *J. Aerosol. Sci.* 25 (1994) 1229.
- [14] C.H. Chen, A.A.J. Buysman, E.M. Kelder, J. Schoonman, *Solid State Ionics* 80 (1995) 1.



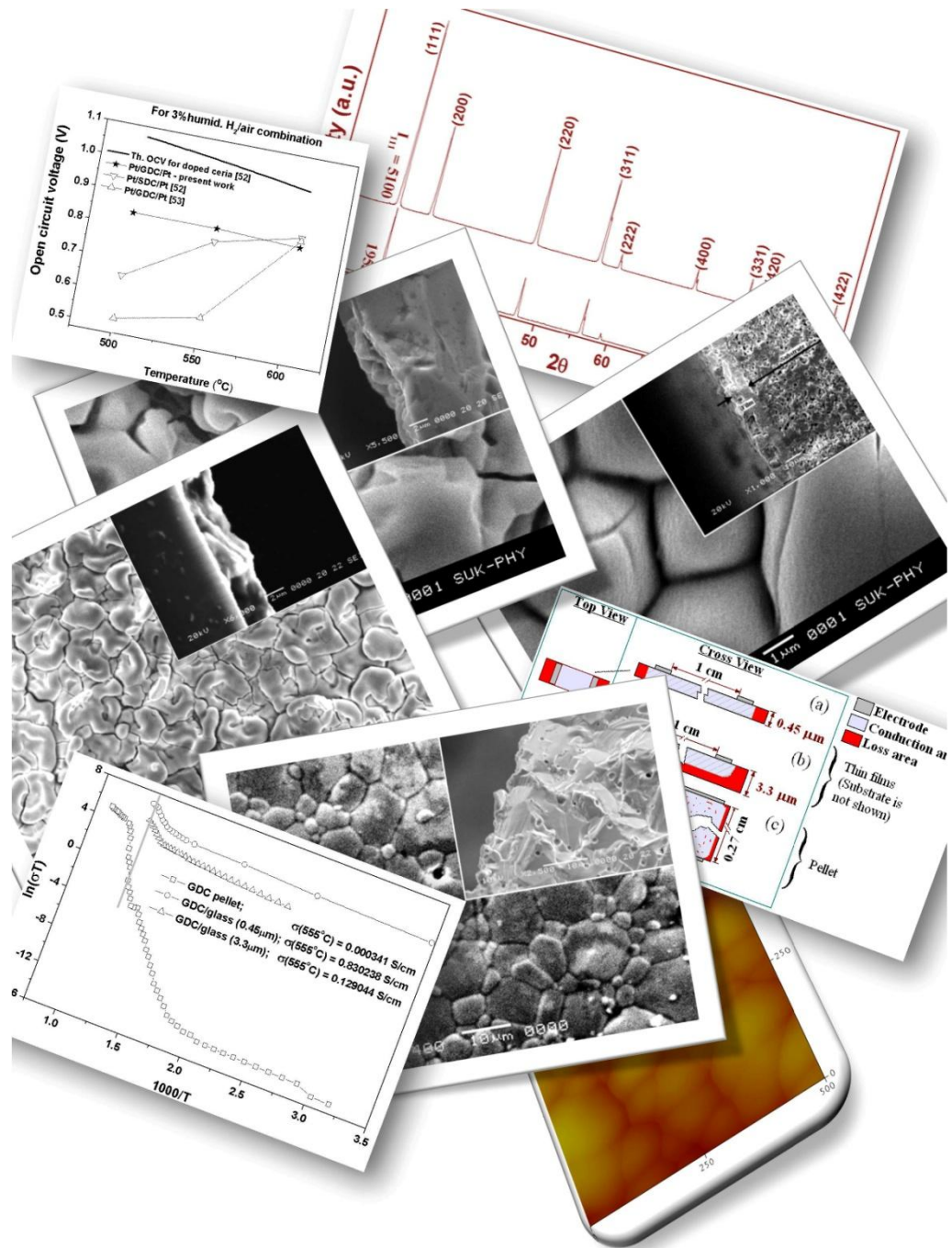
- [15] K.L. Choy, In: W.E. Lee (Ed.), *British Ceramic Proc., Ceramic Films, Coatings, The Institute of Materials* 54 (1995) 65.
- [16] K.L. Choy, W. Bai, B.C.H. Steele, In: A.J. Mcevoy, K. Nisancioglu (Eds.), *Materials, Processes, 10<sup>th</sup> SOFC Workshop, Les Diablerets, Int. Energy Agency*, (1997) 233.
- [17] N.H.J. Stelzer, C.H. Chen, Rij Van, L.N. J. Schoonman, In: A.J. Mcevoy, K. Nisancioglu (Eds.), *Materials, Processes, 10<sup>th</sup> SOFC Workshop, Les Diablerets, Int. Energy Agency*, (1997) 236.
- [18] M.G. Chourashiya, J. Y. Patil, S.H. Pawar, L.D. Jadhav, *Mat. Chem. Phy.* 109 (2008) 39.
- [19] C.R. Xia, F.L. Chen, M.L. Liu, *Electrochem. Solid-State Lett.* 4 (2001) A52.
- [20] C. Xia, M. Liu, *Adv. Mater.* 14 (2002) 521.
- [21] M.G. Chourashiya, S.H. Pawar, L.D. Jadhav, *App. Surf. Sci.* 254 (2008) 3431.
- [22] J.A. Kilner, B.C.H. Steele, in: O.T. Sorensen (Ed.), *Non-Stoichiometric Oxides, Academic Press, New York*, 1981.
- [23] H. Duncan, A. Laxia, *Solid State Ionics* 176 (2005) 1429.
- [24] R.V. Wandekar, M. Ail (Basu), B.N. Wani, S. R Bharadwaj., *Mat. Chem. Phy.* 99 (2006) 289.
- [25] K.Y. Rajpure, C.H. Bhosale, *Mater. Chem. Phys.* 64 (2000) 14.
- [26] D.Y. Wang, A. S. Nowick, *J. Solid State Chem.* 35 (1980) 325.
- [27] K.E. Adham, A. Hammou, *Solid State Ionics* 9/10 (1983) 905.
- [28] E. Ruiz-Trejo, J. Santoyo-Salazar, R. Vilchis-Morales, A. Benitz-Rico, F. Gomex-Garcia, C. Flores-Morales, J. Chavez-Carvayar, G. Tavizon, *J. Solid State Chem.* 180 (2007) 3093.
- [29] M.G. Bellino, D.G. Lamas, N.E. Walsoe de Reca, *Adv. Functnl. Mater.* 16 (2006) 107.
- [30] Y.M. Park, G.M. Choi, *Solid State Ionics* 120 (1999) 265.
- [31] Y.M. Park, G.M. Choi, *J. Electrochem. Soc.* 146 (1999) 1046.
- [32] J.M. Ralph, *A study of doped ceria electrolyte, Ph.D. Thesis, University of London*, February 1998.
- [33] J.L.M. Rupp, L.J. Gauckler, *Solid State Ionics* 177 (2006) 2513.
- [34] S.H. Jo, P. Muralidharan, D.K. Kim, *Solid State Ionics* 178 (2008) 1990.





# Chapter seven:

*Gd doped ceria in bulk and thin film form as solid electrolyte for IT -solid oxide fuel cells*





# Chapter seven

## CONTENTS

<b>7. Gd DOPED CERIA IN BULK AND THIN FILM FORM AS SOLID ELECTROLYTE FOR IT-SOLID OXIDE FUEL CELLS.....</b>	<b>256</b>
<b>7.1. Introduction.....</b>	<b>257</b>
7.1.1. <i>A general consideration of thin films.....</i>	257
7.1.2. <i>Importance of thin films in solid oxide fuel cells: .....</i>	260
<b>7.2. Discussion.....</b>	<b>261</b>
7.2.1. <i>Structural comparison .....</i>	261
7.2.2. <i>Comparison of surface and fractured morphologies.....</i>	263
7.2.3. <i>Comparative elemental analysis .....</i>	266
7.2.4. <i>Comparison of electrical performance of optimized GDC samples.....</i>	267
7.2.4.1. <i>Comparison of dc conductivity measurement of bulk GDC and GDC/glass substrate.....</i>	268
7.2.4.2. <i>Comparison of ac conductivity measurements of bulk GDC and GDC/ceramic substrate.....</i>	271
7.2.5. <i>Open circuit voltage (OCV) measurements.....</i>	272
7.2.5.1. <i>Fundamentals of fuel cell performance.....</i>	272
7.2.5.2. <i>Experimental for OCV measurements.....</i>	276
7.2.5.3. <i>OCV measurements in different fuel cell conditions.....</i>	277
7.2.5.4. <i>Comparison of OCV data with reported values.....</i>	279
<b>7.3. Conclusions .....</b>	<b>281</b>
<b>References:.....</b>	<b>281</b>

**7. Gd DOPED CERIA IN BULK AND THIN FILM FORM AS SOLID ELECTROLYTE FOR IT-SOLID OXIDE FUEL CELLS.**



## **7.1. Introduction**

Research carried out in this work includes synthesis and characterization of GDC in bulk and thin film form with varying process parameters. Optimization of Gd doping concentration in ceria revealed that 10% Gd doped ceria (hereinafter it is referred as GDC) sintered at 1500°C (8h) leads to comparatively good structural and electrical performance over the other process parameter and doping concentrations. Further thin films of GDC with optimized doping concentration of Gd were synthesized by spray pyrolysis technique and the processing parameters of the technique were optimized to obtain dense, smooth and adherent films onto various substrates, which include glass and two types of ceramic substrates, namely GDC and NiO-GDC composite ceramic substrate.

This chapter reviews and compares the physicochemical properties of bulk and thin film samples of GDC synthesized with optimum process parameters. The significance of these samples is discussed in view of its use as solid electrolyte in IT-SOFC. A brief review of thin films and the necessity of thin films in commercialization of SOFC are presented.

### **7.1.1. A general consideration of thin films**

Any solid or liquid system possesses at most two-dimensional order or periodicity, called “thin film”. The conventional bulk material is characterized by three-dimensional order in which the constituent atoms or molecules are found. This order or periodicity is responsible for the structure/nature of the material, which is, in general responsible for distinct physicochemical properties of the materials. In case of thin films, the system possesses at most two dimensional order or periodicity, this accounts for distinct physicochemical properties from their bulk counterpart. This difference in properties of thin films is due to surface and interface effects, which may dominate the overall behavior of film material. These effects are briefly discussed in following section with the help of various defects in solids.

Repetition of a particular geometric pattern of atoms without interruption or mistake leads to a perfect crystal structure, which in reality does not find great existence. Although there are materials—carefully grown silicon single crystals, for example—that have virtually perfect crystallographic structures extending over



macroscopic dimensions, this is not generally true in bulk materials. In thin crystalline films, the presence of defects not only serves to disrupt the geometric regularity of the lattice on a microscopic level, but it also significantly influences many film properties, such as chemical reactivity, electrical conduction, and mechanical behavior. There are two types of irregularities namely grain boundaries and dislocations, which causes the changes in thin film materials properties over bulk counterpart [1].

**Grain Boundaries:** Grain boundaries are surface or area defects that constitute the interface between two single-crystal grains of different crystallographic orientation. The atomic bonding, in particular grains, terminates at the grain boundary where more loosely bound atoms exist. Atoms on surfaces, they are necessarily more energetic than those within the grain interior. This causes the grain boundary to be a heterogeneous region where various atomic reactions and processes, such as solid-state diffusion and phase transformation, precipitation, corrosion, impurity segregation, and mechanical relaxation, are favored or accelerated. In addition, electronic transport in metals is impeded through increased scattering at grain boundaries, which also serve as charge recombination centers in semiconductors. Grain sizes in films are typically from 0.01 to 1.0  $\mu\text{m}$  in dimension and are smaller, by a factor of more than 100, than common grain sizes in bulk materials. For this reason, thin films tend to be more reactive than their bulk counterparts. The fraction of atoms associated with grain boundaries of thin film is approximately  $3a/l$ , where 'a' is the atomic dimension and 'l' is the grain size. For  $l = 1000\text{\AA}$ , this corresponds to about 5 in 1000. Grain morphology and orientation in addition to size control are not only important objectives in bulk materials but are quite important in thin-film technology. For example, a major goal in microelectronic applications is to eliminate grain boundaries.

**Dislocations:** Dislocations are line defects ('edge' and 'screw' dislocations) that bear a definite crystallographic relationship to the lattice. A state of internal stress exists around each dislocation. However, the stresses differ around 'edge' and 'screw' dislocations because of different lattice distortions. Close to the dislocation axis the stresses are high, but they fall off with distance (r) according to  $1/r$  dependence.



Dislocations are important because they are at the bottom of mechanical phenomena and properties in all classes of crystalline solids. Thus the knowledge of dislocations helps us to explain why metals are weak and can be deformed at low stress levels and paradoxically, dislocations can also explain why metals get stronger when they are deformed. These justifications require the presence of large quantity of dislocations in solids. Many deposited polycrystalline metal thin films also have high dislocation densities.

Apart from these understandings, the role of dislocations in thin films is diverse. As an example, consider the deposition of atoms onto a single-crystal substrate in order to grow an epitaxial single-crystal film. If the lattice parameter in the film and substrate differ, films of high crystalline perfection are not obtained. For this reason, a good match of lattice parameters is required for epitaxial growth. If the substrate has screw dislocations emerging normal to the surface, depositing atoms may continue the extension of the dislocation spiral into the growing film. Like grain boundaries dislocations can be sites of charge recombination or generation as a result of uncompensated "dangling bonds". Film stress, thermally induced mechanical relaxation processes and diffusion in films are all influenced by dislocations.

***The characterizations:*** The changes in physicochemical properties of thin films over bulk materials not only affect the above mentioned technologically important properties but also offer specific necessities for characterizations. For example consider the characterization of materials for their structural properties. In bulk solids large diffraction effects occur at many values of  $\theta$ . In thin films, however, very few atoms are present to scatter X-rays into the diffracted beam when  $\theta$  is large. For this reason the intensities of the diffraction lines or spots will be unacceptably small unless the incident beam strikes the film surface at a near-glancing angle. This, in effect, makes the film look thicker. This thickness limitation in thin films is turned into great advantage, however, in the transmission electron microscope. Here electrons must penetrate through the material under observation, and this can occur only in thin films or specially thinned specimens. The short wavelength of the electrons employed enables high-resolution imaging of the lattice structure as well as diffraction effects to be observed.



### 7.1.2. Importance of thin films in solid oxide fuel cells:

Solid oxide fuel cells (SOFCs) rely on oxygen ion conduction through ceramic electrolytes. The transport rates of oxygen ions of known electrolytes is, however, presently too low to allow for practical devices at temperatures much below 500°C. This lower temperature limit is determined not only by the conductivity of the electrolyte but also by electrode performance and by the advantageous ability to extract additional energy from the fuel cell exhaust gases. Temperatures above 800°C lead to rapid electrode reactions and exhaust gases that may be used in turbine bottoming cycles. Unfortunately, such temperatures severely restrict the materials that are compatible and can resist the operating conditions for long times. While high-temperature systems (i.e., above 950°C) have demonstrated extended performance, their economic viability remains a persistent concern.

Reducing the temperature of operation to below 800°C greatly extends the choice of compatible materials. The reduced temperatures require the use of thin solid electrolytes, typically less than 25µm thick, to reduce the ionic resistance of the electrolyte. Such electrolytes are not sufficiently robust by themselves and must therefore be produced on either the anode or cathode of the fuel cell, where this electrode provides a mechanical support function in addition to its electrical function. The production of supported thin film solid oxide electrolytes on a porous support electrode in an economically viable manner is, therefore, one of the essential aspects of reduced-temperature thin film SOFCs. The fabrication process itself subjects the materials to conditions that differ significantly from those of the fuel cell operating environment, and significant challenges can be encountered in assuring that promising materials combinations survive the processing steps.

The vast majority of the thin film SOFCs uses Yttria-stabilized zirconia (YSZ) as an electrolyte. This material has been extensively examined and has the advantage of high stability and compatibility with the broadest range of electrode materials. In thin film form, it is suitable down to approximately 650°C. For lower temperatures, alternative electrolytes with higher oxygen ion conductivity can be considered (e.g., Ceria-based ones), although many of these introduce new difficulties such as higher reactivity, electronic conductivity, or thermal expansion mismatch [2].





## 7.2. Discussion

In this research work, two different synthesis techniques have been employed, namely solid state reaction method and spray pyrolysis technique (SPT). Among these, SPT has demonstrated its appropriateness for quality synthesis, since SPT allows atomic level precursor mixing and thereby results in expected intimate final product.

### 7.2.1. Structural comparison

Figure 1 shows the XRD patterns of GDC samples prepared with optimized process parameters in bulk and thin film form. In figure 'I<sub>111</sub>' indicates the intensity counts of (111) plane of respective XRD pattern. For uncoated glass substrate, max intensity count observed for glass hump is represented by 'I<sub>max</sub>' (amorphous).

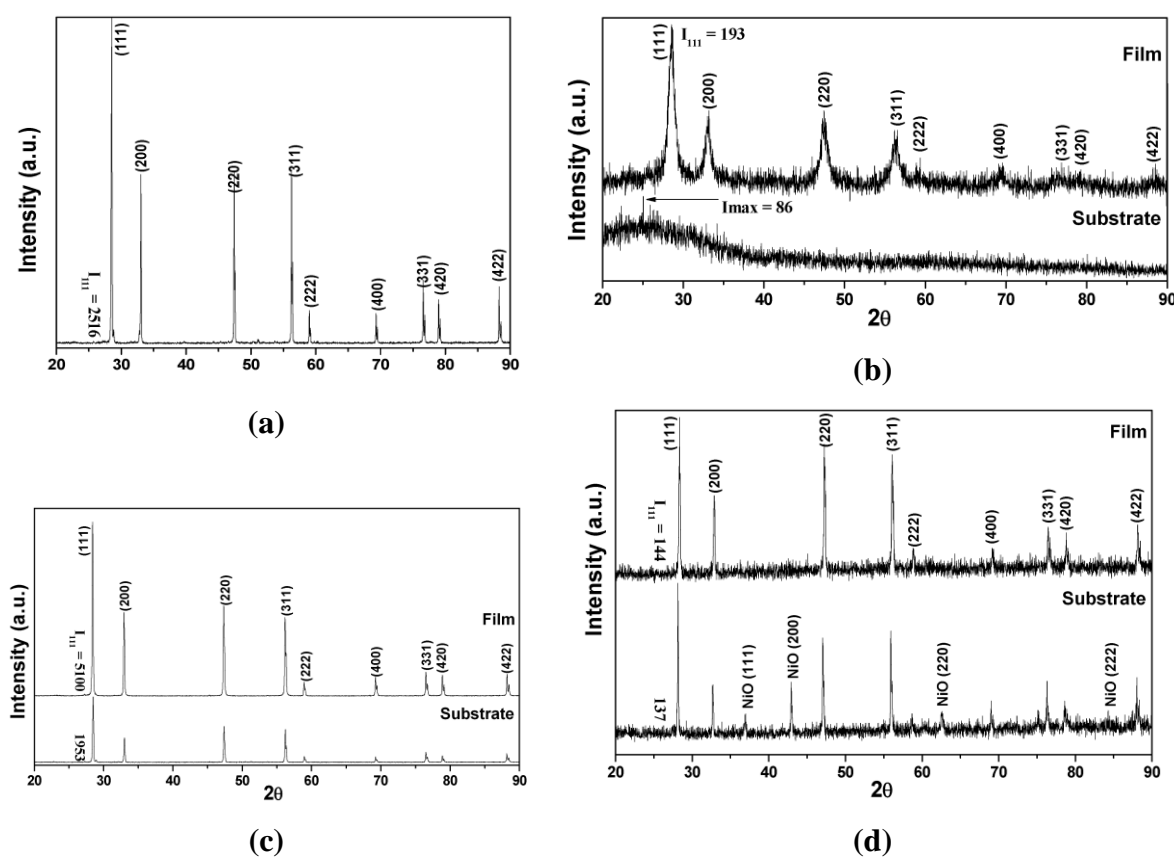


Figure 1. XRD patterns of GDC samples prepared with optimized process parameters.

(a) Bulk GDC sample (pellet), GDC films on (b) glass, (c) GDC and (d) NiO-GDC substrate along with respective uncoated substrates.



Effect of substrates on lattice parameter and crystallite size can be clearly seen in table 1. The lattice parameter of the GDC films on glass and NiO-GDC substrate is observed to deviate from its standard value (5.418 Å) while that of GDC substrate it matches exactly. The deviation is of order of 0.002Å and 0.001Å for glass and NiO-GDC substrate, respectively. Comparison of lattice parameter reveals that the deviation of respective lattice parameter from standard is more for higher amount of lattice mismatch between substrate and deposit. Lattice mismatch in case of NiO-GDC could have originated from the presence of 30%NiO.

Overall observation of the four optimized samples clears that the crystallinity in case of GDC bulk sample and GDC film on GDC ceramic substrate is higher. This observed higher crystallinity is attributed to the heat treatment employed during final sintering (1500°C/8h) for bulk sample (figure 1a) and the post heat treatment for thin films (1000°C/8h – figure 1c). Conversely, the same heat treatment (1000°C/8h) employed in case of GDC films on NiO-GDC substrate gives the crystallite size of 395nm, but thickness of film was high enough (~13µm) to suppress the substrate peaks in XRD pattern (figure 1d). In case of GDC films on GDC, maximum thickness achieved was ~3µm. The XRD patterns of GDC films on glass substrate showed broader reflection peaks confirming the formation of nano-crystallites on glass substrates. However, the thickness of the GDC film again was thick enough (~2.2µm) to hide the amorphous nature of glass substrate.

Structure		Lattice parameter	Crystallite size	
<b>THIN FILMS</b>	GDC/Glass	Substrate	-	
		Film	<b>5.420 Å</b>	
	GDC/GDC	Substrate	5.418 Å	
		Film	5.418 Å	
	GDC/NiO-GDC	Substrate	70%-GDC	5.418 Å
			30%-NiO	4.169 Å
Film		<b>5.419 Å</b>	<b>395 nm</b>	
<b>BULK</b>	GDC	-	5.418 Å	
			598 nm	

Table 1. Lattice parameter and crystallite sizes for optimized GDC bulk and thin film samples.



The bulk GDC were prepared by solid state route, which involve sintering of green pellets at 1500°C/8h. Therefore, the XRD pattern is sharply defined with large count reflection peaks among the all. The crystallite size was 570nm. The same order of crystallinity is retained by the GDC films deposited on ceramic substrates while the HDV films deposited on glass has crystallite size of 127 nm. This difference originated due to the difference in the nature of substrates. The later substrate is amorphous in nature while the former one is highly polycrystalline. Further the broader reflection peaks for GDC/GDC confirms the nano-crystalline growth of GDC films.

Another aspect which contributes to crystallinity is the annealing applied to the GDC films deposited on glass and ceramic substrates. GDC films on glass were annealed about 450°C (since higher annealing temperature could lead to glass (substrate) softening and would generate stresses into the films), while those on ceramic substrate were annealed at as high as 1000°C. Further the crystallite size of (554nm) GDC on GDC is higher than that of GDC on NiO-GDC. This could be attributed to free energy exchange between the deposit and substrate during deposition. In both cases of ceramic substrates, the GDC is present as part of substrate which has exactly equal lattice parameter as that of depositing material (GDC thin film). The maximum free energy exchange between substrate and GDC material, to be deposited, may occur in case of GDC substrate which in turn facilitated more nucleation centers along substrate crystallites and results in improved crystallization. However, the presence of NiO in NiO-GDC substrate may affect the free energy exchange between substrate and film leading to crystallite size of 395nm, beside the same sintering schedule. The thickness of GDC film on GDC is 2.2µm and that on NiO-GDC is 13µm.

### ***7.2.2. Comparison of surface and fractured morphologies***

Figure 2 shows the SEM of surface and fractured morphologies of optimized GDC samples. The SEM images of the films deposited onto different substrates shows the presence of well interconnected grains of few micron sizes. But these are the clusters of nano-granules as can be seen in the respective AFM images (figure 3a-c). In case of thin film samples, the fractured morphologies illustrate the density of films and substrate, and quality of physical interface of films with the substrate.



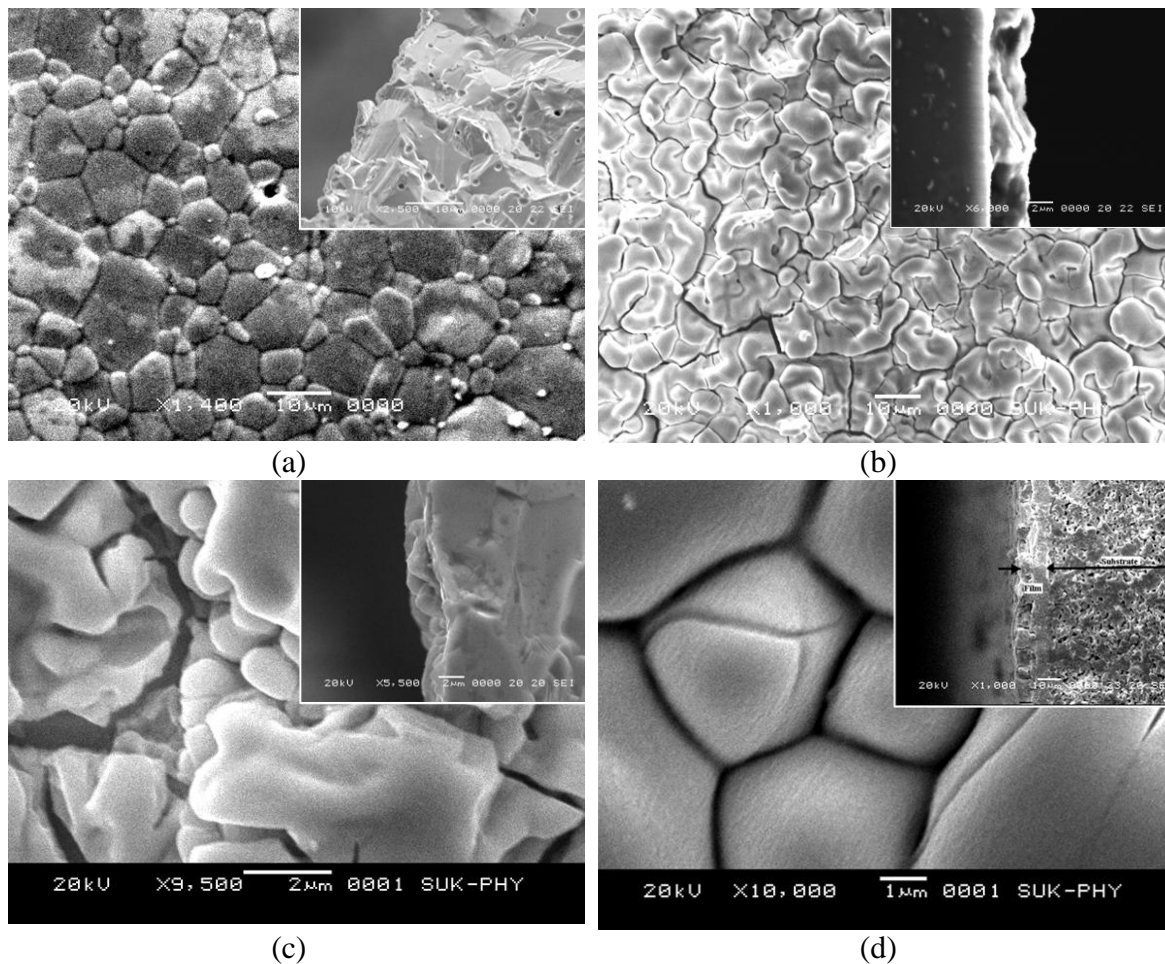


Figure 2. SEM of surface and fractured morphologies of optimized GDC samples; (a) GDC pellet (b) GDC film on glass, (c) on GDC and (d) on NiO-GDC substrate

The surface morphology of each of these optimized GDC samples shows well connected surface grains, except for GDC films on GDC substrate. However closer look (SEM at higher magnification) in surface as well as fractured morphology of GDC films on GDC substrate reveals the existence of grain connectivity.

The relative density of GDC pellet sintered at 1500°C for 8h was about 98% of its theoretical value. The fractured SEM image of the same is shown in the inset of figure 2a. If we compare the fractured SEM image of GDC films grown on different substrates, we can see that the relative densities of the films are nearly same as that of



GDC pellet. Thus highly dense films onto different substrate are possible at 1000°C (films was heat treated at 1000°C/8h). The dense film at reduced heat treatment is entirely attributed to the presence of nano sized granules (~100nm – figure 3a-c) in the GDC films.

Figure 3 shows the AFM images of optimized GDC thin film deposited on different substrates. These images clearly show that the GDC films consist of nano-granules. The average grain size and mean surface roughness of GDC films on different substrates are listed in table 2.

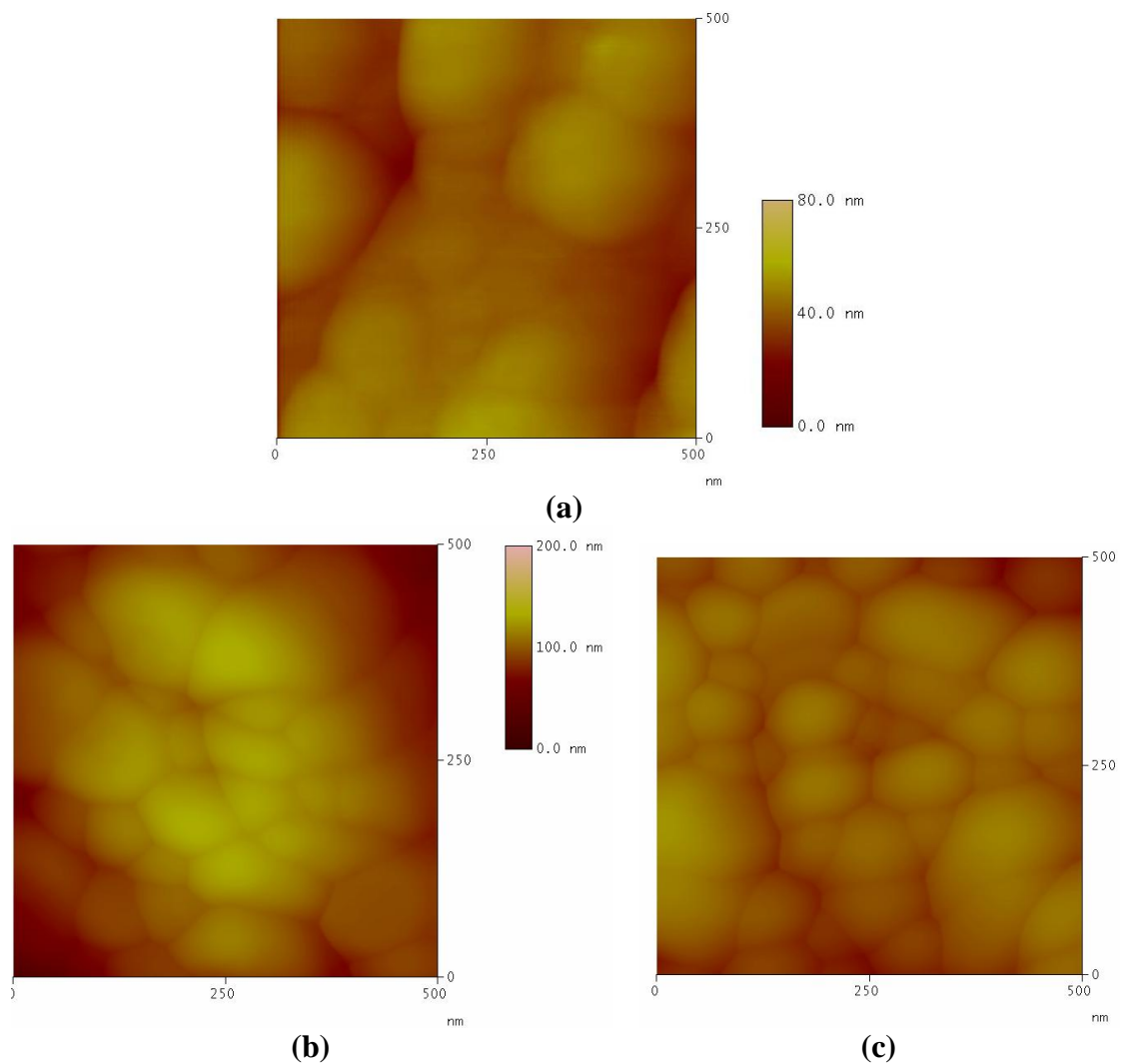


Figure 3. AFM of GDC film deposited on (a) glass (scale bar 0-80nm) (b) GDC (scale bar 0-200nm) and (c) NiO-GDC (scale bar 0-200nm) substrate.



	GDC films on		
	GDC (in nm)	NiO-GDC (in nm)	Glass (in nm)
Mean surface roughness (in nm)	18.64	8.86	4.75
Average grain size (in nm)	83.00	85.00	98.00

Table 2. Estimated grain size and surface roughness of GDC films.

The estimated grain size of GDC films on glass substrate is largest of three substrates used for the depositions but with least surface roughness. The least surface roughness obtained for glass substrate could be due to the smoothness of substrate surface which was not possible in case of ceramic substrates. The mean surface roughness is nothing but the standard deviation of height values from mean height values; therefore, the larger surface roughness for GDC films on GDC substrate would be caused by its wider grain size distribution while surface roughness is moderate for GDC films on NiO-GDC substrate.

### 7.2.3. Comparative elemental analysis

The presence of stoichiometry in the material plays the key role. Further this decides the optimum electrical behavior. The metal atomic percentage in the film and bulk sample was estimated from elemental analysis (using EDAX) of optimized GDC samples and is shown in table 3. All the optimized GDC samples have the nearly expected atomic % of ‘Ce’ and ‘Gd’ (90: 10). Thus the optimized GDC samples in thin as well as bulk form have maintained the desired stoichiometry. Here it is noteworthy that the GDC films prepared using spray pyrolysis technique (SPT) maintains the stoichiometry, even after heat treating the films at 1000°C in air.



		Atomic % of	
		Ce	Gd
GDC pellet		90.2	9.8
GDC thin films on	Glass	89.9	10.1
	GDC	90.5	9.5
	NiO-GDC	90.1	9.9

Table 3. Estimated atomic % of ‘Ce’ and ‘Gd’ in optimized GDC samples.

#### 7.2.4. Comparison of electrical performance of optimized GDC samples

The electrical properties of optimized GDC samples were determined using ac and dc conductivity measurement techniques. The types of measurement techniques employed to determine the electrical performance are listed in table 4.

		Conductivity measurements	
		ac	dc
GDC pellet		YES	YES
GDC thin films on	Glass	NO	YES
	GDC	YES	NO
	NiO-GDC	YES	NO

Table 4. Type of conductivity measurement carried out for optimized GDC samples.

For ionic materials such as Gd doped ceria, it is recommended that study of its electrical performance must be carried out using ac conductivity measurements instead of dc conductivity measurements. The ac conductivity measurements not only determine total ionic conductivity but also allow us to separate out the extent of contributions originated from grain interior and grain boundaries of samples. Because of inability to probe the electrode on the substrate side for the case of GDC films on glass substrate, the electrical performance of GDC/glass system were done by two probe (surface) dc conductivity measurements. To compare the electrical performance of GDC/glass system, the GDC pellets were also characterized by the same technique. Different sample holdings for conductivity measurements are illustrated in figure 4.



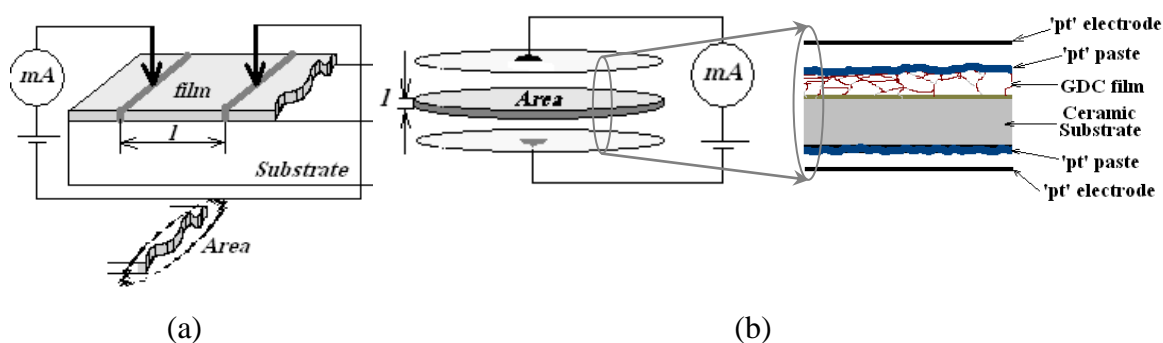


Figure 4. Sample holding for (a) GDC film on glass substrate (for dc measurements) and (b) GDC films on ceramic substrates & GDC pellets (for ac and dc measurements); explaining the structure.

#### 7.2.4.1. Comparison of dc conductivity measurement of bulk GDC and GDC/glass substrate

Figure 5 shows the comparative plot of  $\ln(\sigma_{dc}T)$  vs.  $1000/T$  for GDC bulk and GDC/glass system. It is evident from figure that the conduction values for GDC/glass system is much higher than that of GDC bulk samples. As shown in figure 4, the different measurement geometries were applied to record conductivities of bulk and film. Therefore, direct comparison of results would not be possible. However, in case of GDC films, the larger values of conductivities observed at lower temperatures could be attributed to reduced ohmic losses, which is obvious for the ionic solid materials. The another probability of observing large conduction at lower temperatures (in dc conductivity measurement) could be due to electronic conduction produced by the presence of  $Ce_2O_3$  species in the film or reduction of the film during measurements. However, the XRD of the GDC films has not shown any impure phase (e.g.  $Ce_2O_3$ ) and the conductivity measurements were carried out in air (temperature <  $600^\circ C$ ). Therefore, the possibility of larger electrical conduction due to electronic conduction (instead of ion hopping mechanism) can be ruled out.





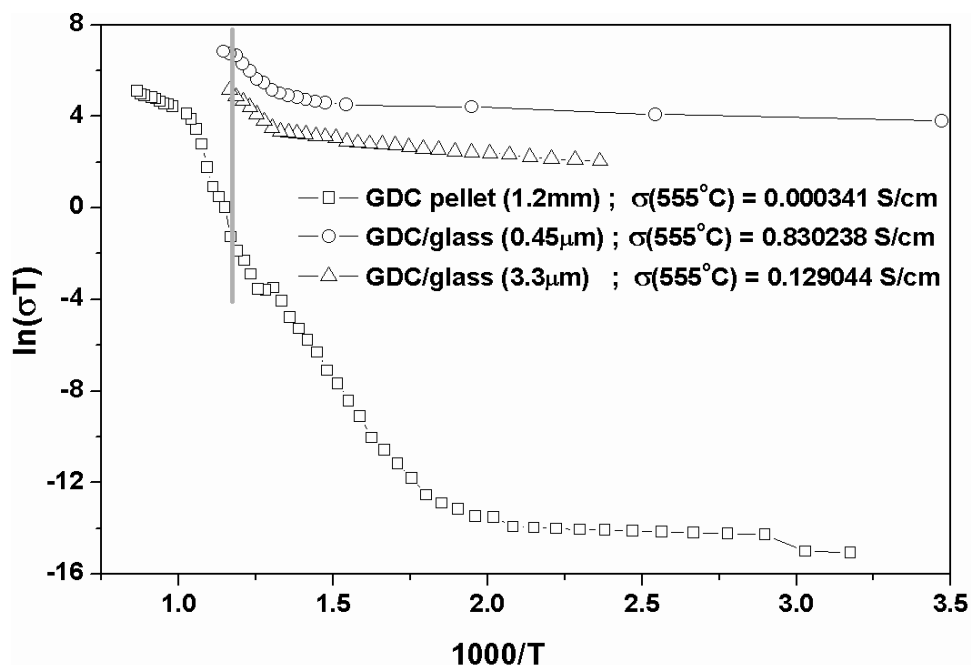


Figure 5. Comparative plot of  $\ln(\sigma_{dc}T)$  with  $1000/T$  for GDC pellets and GDC/glass system (for films with different thicknesses)

The point of change of slope (inflexion point) in case of GDC thin films on glass was observed at  $450^\circ\text{C}$  while for GDC pellet it was about  $300^\circ\text{C}$ . This difference of inflexion points can be attributed to total amount of defects in the samples, which would be obviously larger for GDC pellets and hence comparatively earlier initiation of ionic diffusion occurs (at  $300^\circ\text{C}$ ). However, due to comparatively larger ohmic losses in GDC pellets, the desired amount of conductivity ( $0.1\text{S/cm}$ ) is observed at temperatures as high as  $750^\circ\text{C}$  while for GDC/glass system same values were observed at  $555^\circ\text{C}$ .

The activation energies determined in ionic diffusion region of the plot i.e. for  $T >$  inflexion point, were  $0.8\text{eV}$  for GDC pellet,  $0.61\text{eV}$  for  $0.45\mu\text{m}$  thick film on glass substrate and  $0.98\text{eV}$  for  $3.3\mu\text{m}$  thick film on glass substrate. This difference in values of  $E_a$  for pellet and thin films with different thicknesses could be explained using figure 6, which illustrate the dependence of conduction path, loss area and geometry of electrodes employed during measurements.



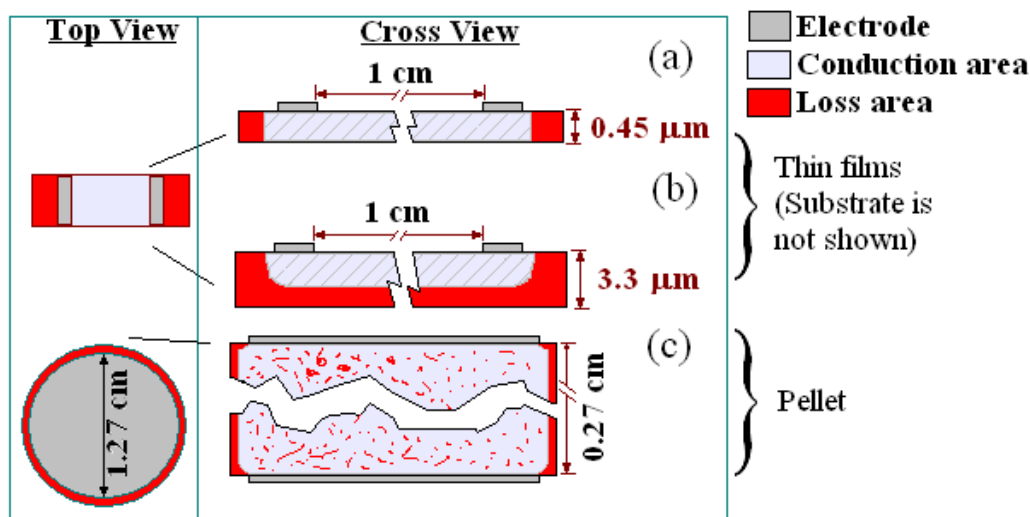


Figure 6. Schematic illustration of the cause of variations in activation energies.

Red marked area in figure 6 shows the location of losses for particular sample, which would be highest in case of pellet sample as it (i) involves larger defect concentration which could trap the mobile species during the applied field (figure 6c – red spots inside the conduction area of pellet). Such defects would also be present in thin film samples; however their number would be comparatively less. In addition to this, while (ii) traversing from one electrode to other the mobile ionic or electronic species may loss in zero potential biasing region (figure 6-Top view (see left image) – red area). Further, if (iii) the thickness of conducting path is larger than the critical thickness, the zero potential biasing region would extend below the critical thickness also (see figure 6b). Now, the average energy required for successful journey from electrode to electrode i.e. activation energy ( $E_a$ ), would also depend upon the three locations mentioned above. The critical thickness under the employed measurement conditions for GDC thin films may be of  $0.45\mu\text{m}$ , for this particular study. Therefore, for GDC/glass; having film thickness of  $0.45\mu\text{m}$ ,  $E_a$  is least ( $0.61\text{eV}$ ) as there would be neither the ‘extended’ zero biasing region nor the large amount of trapping defects. For GDC bulk samples, because of possibility of high number of trapping defects present in the area of conduction, it might have showed moderate value of activation energy ( $0.8\text{eV}$ ). Finally, for GDC/glass; having film thickness of  $3.3\mu\text{m}$ ,  $E_a$  is observed to be highest ( $0.98\text{eV}$ ), which could be ascribed to higher area of zero biasing region (loss area) extended below the critical thickness of the film.



However, it must be noted that in addition to above mentioned spots of losses, area of electrode and its geometry plays the critical role in deciding the phenomenon of conduction in samples during the dc measurements.

#### 7.2.4.2. Comparison of ac conductivity measurements of bulk GDC and GDC/ceramic substrate

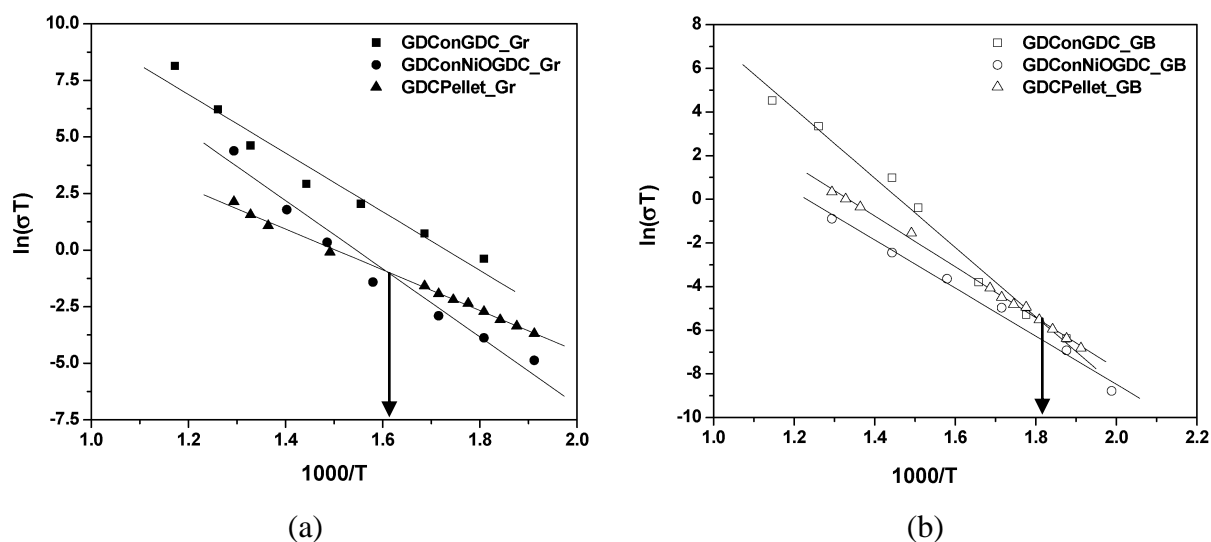


Figure 7. Comparative plots of  $\ln(\sigma_{ac}T)$  with  $1000/T$  originated due to (a) grain interior contribution and (b) grain boundary contribution.

Figure 7 shows the Arrhenius plot of grain interior (GI) and grain boundary (GB) conductivity contributions of GDC samples. It can be seen from the plots that the GI contribution to conductivity is in general two orders higher than that of the GB contributions. This reveals that the conductivity phenomenon in all three samples is mainly enforced by GI mechanisms and the GB conduction phenomenon possesses comparatively higher impedance to the ionic conduction. The higher impedance to GB conduction phenomenon is attributed to the segregated impurities, as it acts like a partial ion blocking layer at the grain boundaries.

In figure 7, conduction due to GB and GI is lower for GDC/NiO-GDC system compared to GDC/GDC system which can be attributed to the presence of NiO phase in substrate. However, the ionic conduction originated from GB and GI of GDC bulk samples lies between GDC/GDC and GDC/NiO-GDC system. The GDC/ceramic substrates shows higher GI ionic conductivity even it were sintered at less sintering



temperature (1000°C) than that employed for the synthesis of bulk GDC (1500°C). This higher GI ionic conductivity of films is attributed to the well sintered and nano-crystalline nature of ceramic thin films (figure 3).

The activation energy ( $E_a$ ) estimated from conductivity data of GDC/GDC and GDC/NiO-GDC reveals that  $E_a$  for GI conduction was nearly same for both systems while it differs by ~0.5eV for GB conduction, with lower value for GDC/NiO-GDC system. This lesser activation energy (0.93eV) observed is attributed to the well connected interface of substrate and film, which can be clearly seen in its fractured SEM image (figure 2d). The activation energy of GDC pellet estimated for GI and GB ionic conduction was 0.75eV and 0.98eV, respectively. The comparable values of  $E_a$  for GB ionic conduction for GDC/NiO-GDC and GDC pellet imply that the interface of substrate and film in addition to its respective GB regions are as good and clean as that of GDC pellet's GB region.

### 7.2.5. Open circuit voltage (OCV) measurements

The samples prepared with optimized process parameters and optimum doping % of Gd was tested for its fuel cell performance by measuring open circuit voltage (OCV). Here OCV measurements were carried out for GDC bulk sample. The other optimized samples, electrical performance were characterized by recording impedance measurements to decide its suitability for its prospective application in IT-SOFCs as solid electrolyte. The GDC/glass system was ruled out on the basis of non-conducting substrate which may crack at elevated temperatures, while GDC/GDC and GDC/NiO-GDC structures require further studies to accomplish the formation of complete cell for testing in a fuel cell environment (future scope of this research).

#### 7.2.5.1. Fundamentals of fuel cell performance

During the operation of fuel cell, chemical energy is transformed into electrical energy and is expressed mathematically as the product of the cell's electromotive force (emf) and the electrical charge transferred through the external circuit.

$$\text{Electrical energy} = E_{\text{cell}} \times C_{\text{trans}}$$

where,  $E_{\text{cell}}$  is the cell potential measured in volts (V) and  $C_{\text{trans}}$  is the cell current integrated over time and measured in coulombs (C).  $C_{\text{trans}}$  can also be



determined by multiplying the total number of electrons transferred (measured in moles) times Faraday's constant,  $F = 96,485 \text{ C/mole}$ .

The emf of the cell at zero current is the maximum possible emf, also called open circuit voltage (OCV). It is used to calculate the maximum possible electrical energy that could be obtained from fuel cell. This energy is referred to as electrical work and is expressed by the following equation:

$W_{\max} = W_{\text{electrical}} = -nFE_{\text{cell}}$ , where, work is defined as positive into the system.

Since the free energy is the maximum amount of work that can be extracted from a system, one can write:

$$\Delta G = -nFE_{\text{cell}}$$

A positive cell potential gives a negative change in Gibbs free energy. This is consistent with the cell production of an electric current flowing from the cathode to the anode through the external circuit (fuel cell). If the current is driven in the opposite direction by imposing an external potential, then work is done on the cell to drive electrolysis.

A spontaneous electrochemical reaction (change in Gibbs free energy less than zero i.e. negative) can be used to generate an electric current, in electrochemical cells. This is the basis of all batteries and fuel cells. For example, gaseous oxygen ( $\text{O}_2$ ) and hydrogen ( $\text{H}_2$ ) can be combined in a fuel cell to form water and energy, typically a combination of heat and electrical energy. Conversely, non-spontaneous electrochemical reactions can be driven forward by the application of a current at sufficient voltage. The electrolysis of water into gaseous oxygen and hydrogen is a typical example.

The relation between the equilibrium constant,  $K$ , and the Gibbs free energy for an electrochemical cell is expressed as follows:

$$\Delta G^{\circ} = -RT \ln K = -nFE_{\text{cell}}^{\circ}$$

Rearranging to express the relation between standard potential and equilibrium constant yields,

$$E_{\text{cell}}^{\circ} = \frac{RT}{nF} \ln K.$$

Standard reduction potentials for different  $\text{H}_2/\text{O}_2$  chemical reactions are listed in *appendix III*.



### ***Nernst Equation***

The standard potential of an electrochemical cell requires standard conditions for all of the reactants. When reactant concentrations differ from standard conditions, the cell potential will deviate from the standard potential. In the 20<sup>th</sup> century German chemist Walther Hermann Nernst proposed a mathematical model to determine the effect of reactant concentration on electrochemical cell potential.

In the late 19<sup>th</sup> century Josiah Willard Gibbs had formulated a theory to predict whether a chemical reaction is spontaneous based on the free energy

$$\Delta G = \Delta G^{\circ} + RT \ln Q$$

Where:

$\Delta G$  = change in Gibbs free energy,

T= absolute temperature,

R = gas constant,

ln = natural logarithm,

Q = reaction quotient.

Gibbs' key contribution was to formalize the understanding of the effect of reactant concentration on spontaneity. Based on Gibbs' work, Nernst extended the theory to include the contribution from electric potential on charged species. As shown earlier, the change in Gibbs free energy for an electrochemical cell can be related to the cell potential. Thus, Gibbs' theory becomes

$$nF\Delta E = nF\Delta E^{\circ} - RT \ln Q$$

Where:

n = number of electrons/mole product,

F = Faraday constant (coulombs/mole), and

$\Delta E$  = cell potential.

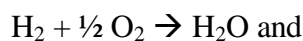
Finally, Nernst divided through by the amount of charge transferred to arrive at a new equation which now bears his name:

$$\Delta E = \Delta E^{\circ} - \frac{RT}{nF} \ln Q .$$



***Ideal performance of a fuel cell***

The ideal performance of a fuel cell is defined by its Nernst potential represented as cell voltage. The overall cell reactions for H<sub>2</sub>/O<sub>2</sub> fuel cell and corresponding form of the Nernst equation is given as,



$$E = E^\circ + (RT/2F) \ln \left[ \frac{P_{\text{H}_2}}{P_{\text{H}_2\text{O}}} \right] + (RT/2F) \ln \left[ P_{\text{O}_2}^{1/2} \right], \text{ respectively.}$$

Where, P - Gas pressure, R - Universal gas constant, E - Equilibrium potential and T – absolute temperature.

The Nernst equation provides a relationship between the ideal standard potential (E°) for the cell reaction and the ideal equilibrium potential (E) at other temperatures and partial pressures of reactants and products. Once the ideal potential at standard conditions is known, the ideal voltage can be determined at other temperatures and pressures through the use of these equations. According to the Nernst equation for hydrogen reaction, the ideal cell potential at a given temperature can be increased by operating at higher reactant pressures.

The ideal standard potential of an H<sub>2</sub>/O<sub>2</sub> fuel cell (E°) is 1.229 volts with liquid water product and 1.18 volts water with gaseous product. The potential force also can be expressed as a change in Gibbs free energy for the reaction of hydrogen and oxygen. The change in Gibbs free energy increases as cell temperature decreases and that the ideal potential of a cell, is proportional to the change in the standard Gibbs free energy.

Figure 2-1 shows the relation of E° to cell temperature. Because the figure shows the potential of higher temperature cells, the ideal potential corresponds to a reaction where the water product is in a gaseous state. Hence, E° is less than 1.229 at standard conditions when considering gaseous water product.



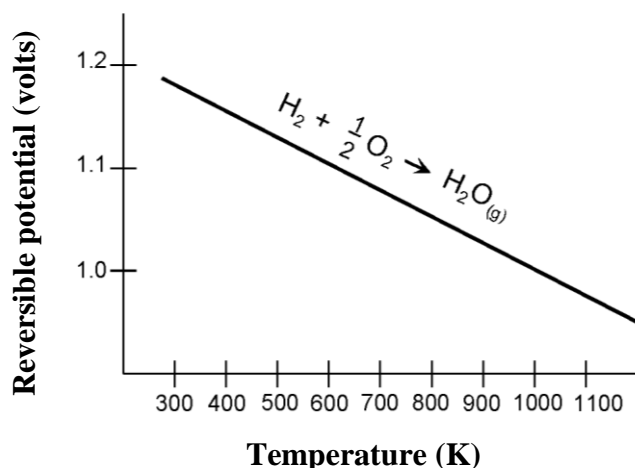


Figure 8.  $H_2/O_2$  fuel cell ideal potential as a function of temperature

The impact of temperature on the ideal voltage,  $E$ , for the oxidation of hydrogen is shown in table 5.

Temperature	25°C (298K)	80°C (353K)	100°C (273K)	205°C (478K)	650°C (923K)	800°C (1073K)	1100°C (1373K)
Cell Type		PEFC	AFC	PAFC	MCFC	ITSOFC	SOFC
Ideal Voltage (V)	1.18	1.17	1.16	1.14	1.03	0.99	0.91

Table 5. Ideal voltage as a function of cell temperature.

#### 7.2.5.2. Experimental for OCV measurements

OCV measurements of 10%Gd doped ceria bulk sample were carried out by sandwiching it between two platinum electrodes (i.e. in symmetrical cell configuration). OCV measurements for four different fuel/oxidizer combinations were conceded. Even the SOFCs are known to possess the fuel flexibility; here we have employed pure  $H_2$  to test its performance for symmetrical cell configuration (“pt/GDC/pt”). Four combinations of fuel/oxidizer combination were paired by utilizing 3% humidified  $H_2$  and dry  $H_2$  as fuel while pure oxygen and air as oxidizer. Each of the OCV measurement was done at 500-600°C.





The samples for OCV measurements were prepared using optimized processing parameters and doping concentration. The dimensions, composition and preparation history of the sample is as follows:

Thickness	≈	<b>1.2 mm</b>
Diameter	≈	<b>16 mm</b>
Composition	–	<b><math>Ce_{0.9}Gd_{0.1}O_{1.95}</math> – GDC10</b>
Pre-sintered at	–	<b>1273K for 2 hrs in air</b>
Sintered at	–	<b>1773K for 8 hrs in air</b>
Relative density	–	<b>98.9%</b>

The OCV measurements were involving five items as mentioned below:

- The symmetrical cell → pt/GDC/pt (... abbreviated as cell hereinafter)
- Humidified H<sub>2</sub> → 3%H<sub>2</sub>O + H<sub>2</sub>
- Dry H<sub>2</sub> → Argon + H<sub>2</sub>
- Pure oxygen → 100% O<sub>2</sub>
- Air → compressed air containing 21% O<sub>2</sub>

Four experimental conditions employed for characterization of symmetrical cell are:

<i>Anode side</i>	<i>Symmetrical Cell</i>	<i>Cathode side</i>
<i>Dry H<sub>2</sub></i>	→ <i>pt/GDC/pt</i> ←	<i>Pure O<sub>2</sub></i>
<i>Dry H<sub>2</sub></i>	→ <i>pt/GDC/pt</i> ←	<i>Air</i>
<i>3%Humidified H<sub>2</sub></i>	→ <i>pt/GDC/pt</i> ←	<i>Pure O<sub>2</sub></i>
<i>Humidified H<sub>2</sub></i>	→ <i>pt/GDC/pt</i> ←	<i>Air</i>

### 7.2.5.3. OCV measurements in different fuel cell conditions

In the presence of 3% humidified-H<sub>2</sub>, the cell showed very stable OCV values for both the oxidizing atmospheres. However, for dry H<sub>2</sub>, the OCV values decreases with time. There was no significant variation in OCV measurements after interchanging the atmospheres on the sides of the GDC electrolyte. The presence of water



content in fuel is well known to decrease the polarization losses at the electrodes and hence it is essential while operating the fuel cells. However, to compare the effect of humidified fuel, OCV measurements were also carried out in the presence of dry fuel.

Figure 9 shows the variation of OCV as function of operating temperature of cell for different fuel/oxidizer pair. For '3%humidified H<sub>2</sub>/pure O<sub>2</sub>' and '3%humidified H<sub>2</sub>/air' combinations the OCV is observed to decrease with an increase in operating temperature, which could be attributed to loss of humidification of fuel for higher operating temperatures. In contrast to these, the 'dry H<sub>2</sub>/pure O<sub>2</sub>' and 'dry H<sub>2</sub>/air' combinations showed increase in OCV with the operating temperature. However, these OCV values are comparably less than 3%humidified H<sub>2</sub>/oxidizer combinations. As no humidification of fuel is employed, the polarizations at each electrode/electrolyte interface leads to great decrease in OCV. But with an increase in operating temperature, polarizations at each electrode/electrolyte interface starts to decrease and lead to an increase in OCV for higher operating temperatures.

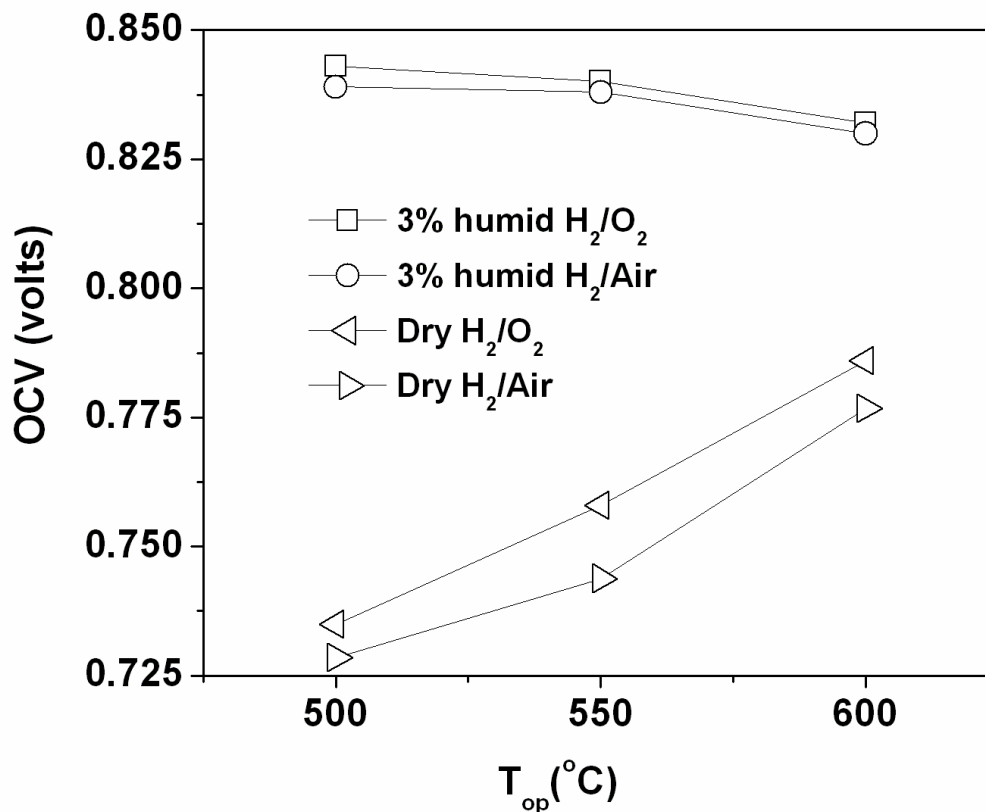


Figure 9. The variation of OCV for different fuel/oxidizer combinations.



#### 7.2.5.4. Comparison of OCV data with reported values

The OCV of fuel cells is generally described by the Nernst equation. However, the Nernst potential is reduced if the electrolyte shows a non-negligible electronic conduction. For doped ceria such as GDC, electronic conduction appears in reducing conditions due to the electrons generated by the reduction reaction as shown in eq. (7.1)



In this reaction, the electronic defect ( $e'$ ) is due to the Ce reduction ( $Ce^{4+} \rightarrow Ce^{3+}$ ). The electronic conductivity ( $\sigma_e$ ) is dependent on  $P(O_2)$  when the oxygen vacancy concentration is fixed by acceptor doping. Thus, the total conductivity ( $\sigma_t$ ) can be expressed by the sum of ionic ( $\sigma_i$ ) and electronic ( $\sigma_e$ ) conductivity.

$$\sigma_t = \sigma_i + \sigma_e = \sigma_i + \sigma_e^o P(O_2)^{-1/4} \quad (7.2)$$

The calculated OCV of fuel cells employing doped ceria as electrolytes can be described as [3],

$$E = \frac{RT}{4F} \int_{\ln P(O_2)_{fuel}}^{\ln P(O_2)_{air}} \frac{\sigma_i}{\sigma_i + \sigma_e^o P(O_2)^{-1/4}} d \ln P(O_2) \quad (7.3)$$

Where  $P(O_2)_{(fuel)}$  and  $P(O_2)_{(air)}$  are the oxygen partial pressures in fuel and air, F and R are the Faraday constant and the gas constant, respectively.

In figure 10, the OCV data of the present work is compared with the reported one [3, 4]. The theoretical OCV data, as in [3], decreases with operating temperature. We have obtained the similar variations with low OCV values. However, the OCV values reported for Pt/SDC/Pt [3] and Pt/GDC/Pt [4] increases with the temperature. The OCV values of the present work, though slightly deviated from theoretical one, are higher than the [5] and [4].



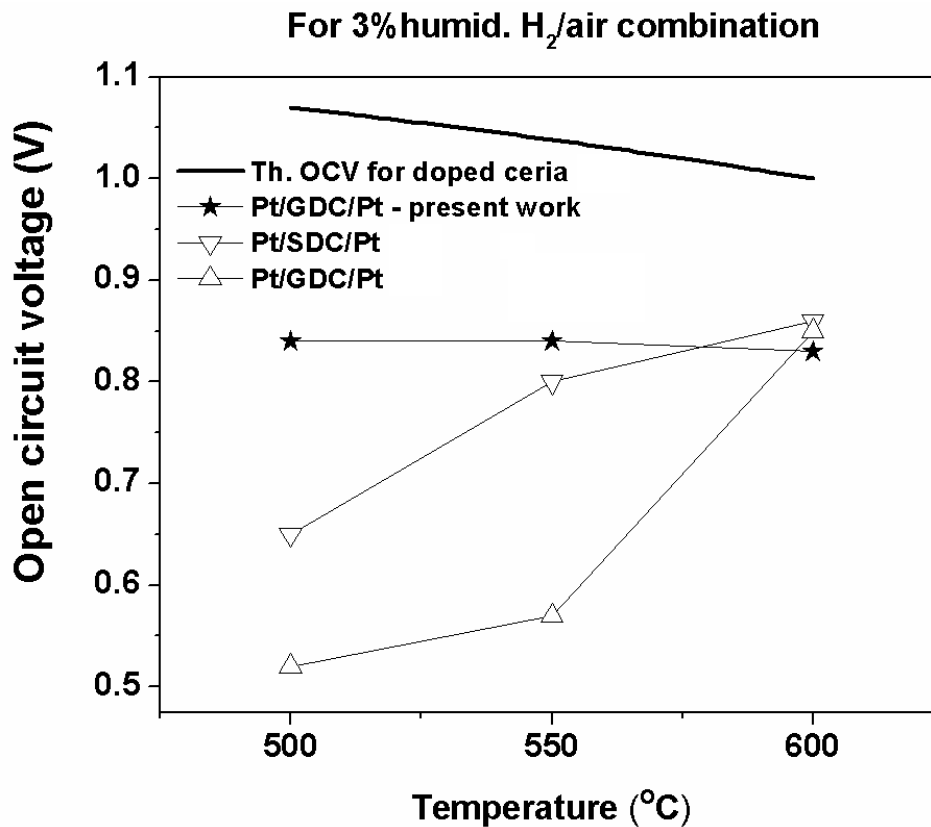


Figure 10. Comparison of OCV of Pt/GDC/Pt cell with Pt/SDC/Pt [3] and Pt/GDC/Pt [4] as a function of temperature. Theoretical (Th.) OCV curve of doped ceria using eq. (7.3) [3] is also shown in figure.

The low OCV, in general, originates from the several different factors, including the gas leakage due to sealing problems, possible structural defects in the GDC electrolytes, an internal short-circuit due to the partial electronic conductivity, the permeation of oxygen due to the electronic conduction, or low electrode kinetics [5]. As the samples employed in this study have relative density greater than 98%, there would be no possibility of gas leakage. Thus, the low OCV is most likely due to the poor electrode kinetics of Pt electrodes in this study. This may be explained by the slow electrode reaction of Pt at low temperature [3]. The strong dependence of OCV on electrode materials was also observed in YSZ electrolyte for CO or H<sub>2</sub> gases below 600°C [6]. Thus the enhanced OCV is expected if highly active electrodes such as the Ba- or La-based cobaltite, etc. are used instead of Pt [5, 7]. The fabrication of a highly active cathode and the anode of porous structure will also enable the measurement of high power density of thin film SOFC.



### 7.3. Conclusions

The comparative analysis of micro-structural and electrical properties of bulk and films samples reveals that the films showed the better performance over the bulk samples. However, combining both the studies together one could prepare good quality half cell of SOFC. After the fabrication of half cell, other coating technique (e.g. spin coating, screen printing, etc.) could be employed to coat the cathode layer over it. The formed cell can be co-sintered at comparatively lower temperature as the spray synthesized electrolyte has the desired density. Thus co-sintering ability of cell at lower temperature could be easily achieved and thereby formation of un-desirable phases at the interface could be avoided.

For typical fuel cell conditions, the open circuit voltage (OCV) of 10%Gd doped ceria bulk sample was of the order of 0.84 volts at 500°C, which is higher than that of reported values in literature for symmetrical cell configuration.

#### References:

- [1] M. Ohring, "*The material science of thin films*", Academic Press, London, 1992.
- [2] L. C. De Jonghe, C. P. Jacobson, S. J. Visco, *Annu. Rev. Mater. Res.* 33 (2003).169.
- [3] T. Matsui, T. Kosaka, M. Inaba, A. Mineshige, Z. Ogumi, *Solid State Ionics* 176 (2005) 663.
- [4] Jong Hoon Joo, Gyeong Man Choi, *Solid State Ionics* 178 (2007) 1602.
- [5] X. Zhang, M. Robertson, C. Deces-Petit, W. Qu, O. Kesler, R. Maric, D. Ghosh, *J. Power Sources* 164 (2007) 668.
- [6] J.H. Joo, G.M. Choi, *J. Electroceram.* 17 (2006) 1019.
- [7] Z. Shao, S.M. Haile, *Nature* 431 (2004) 170.

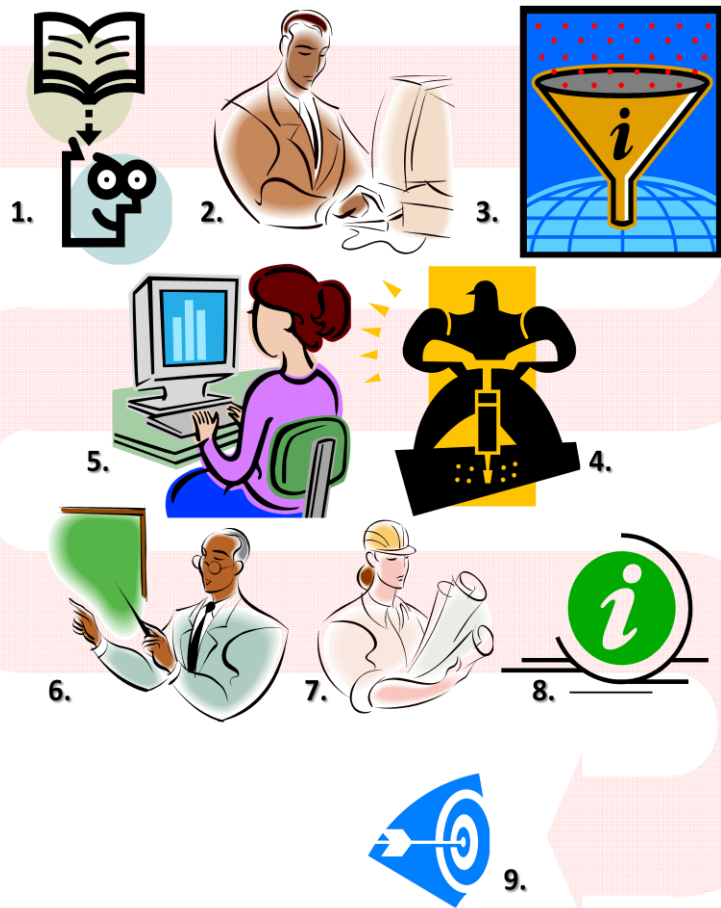




# Chapter eight:

## *Summary and Conclusions*

1. Literature survey
2. Review of research problem
3. Defining the problem and setting the goals
4. Executing the experimental and characterizations
5. Analysis and interpretation of results
6. Peer reviewed publications
7. Final documentations
8. Addition Knowledge
9. Achievements







# **Chapter eight**

## **CONTENTS**

<b>8. SUMMARY AND CONCLUSIONS.....</b>	<b>284</b>
<b>Major achievements of the research .....</b>	<b>291</b>
<b>FUTURE SCOPE .....</b>	<b>292</b>

## 8. SUMMARY AND CONCLUSIONS

Before the discovery of solid electrolytes, it was generally believed that a solid material with a rigid crystal structure cannot obviously conduct much electrical current due to ionic movements. However, the discovery of unexpectedly large electrical conductivity in AgI (1934) and in doped zirconia (1943) due to ionic conduction completely changed the scenario. These materials were termed as “solid electrolytes”, to account its physical property (solid) and its ability of electrical conduction through the motion of ions (electrolytes). Solid electrolytes are characterized by high ionic conductivity and negligible electronic conduction.

Solid electrolytes due to their inherent properties find extensive applications in different areas. Few to mention are given below,

- Energy storage by new types of high-performance batteries,
- Efficient energy conversion by fuel cells,
- Generation of hydrogen fuel by electrolysis,
- Chemical sensors,
- Solar cells,
- Electro-chromic windows or displays, etc.

As these applications are directly related to our standard of living, its success will have tremendous impact on many aspects of our life, environment and economy.

More recently, and particularly in the past two decade, the pace of research has been rapidly driven by the requirements for new clean energy sources, sensors, and high energy density batteries. Because of the promise of important technological devices, a subgroup of anionic conducting materials exhibiting oxygen ion conductivity has been continually developed. However, the conventional oxygen ion conducting solid electrolytes (e.g. Ytria stabilized zirconia – YSZ) requires high operating temperatures (~1000°C) and thereby leads to bottleneck for its commercialization. Therefore, the formulations of materials having the property of solid electrolytes with lower operating temperature are believed to play the key role in its commercialization. Initially, by the curiosity for understanding and later due to



interest of industrial applications, apprehensive research on the solid electrolytes has led to enormous literature.

The search of alternate materials to replace the conventional solid electrolytes has resulted into exciting discovery of gadolinium doped ceria (GDC). The high ionic conduction of GDC at comparably lower temperature made it an ideal candidate to be used as solid electrolyte for intermediate temperature solid oxide fuel cell (IT-SOFC – operating at 550–650°C). In order to increase the ionic conductivity at further lower temperatures, the thickness of the GDC electrolyte (10-20µm) would be reduced to 10-20µm. Because further reduction in operating temperature ( $T_{OP}$ ) in addition to improved ionic conductivity would be helpful to avoid the well known transition of GDC from ionic to electronic conductor (by  $Ce^{4+} \rightarrow Ce^{3+}$ ) in a typical fuel cell condition. To employ the thin film electrolyte in SOFCs, it has to be supported by some kind of substrate and if the substrate itself acts as an electrode for SOFC, it would offer advantage. Therefore, keeping all these assumption and earlier results in mind, systematic research was planned and executed.

As the material system selected for research is gadolinium doped ceria it was mandatory to determine the optimum doping % of dopant (Gd) in the host system ( $CeO_2$  – ceria). In literature there is uncertainty about the optimum doping level of Gd in ceria. Hence initially it was decided to optimize the doping level. For this, the cost effective solid state reaction route was selected, as it is simple and allows easier way to synthesize various desirable composition, with high accuracy. The ceramic process parameters were also optimized to achieve the desirable result in the final products and to fabricate the ceramic substrates. After optimization of Gd doping level in ceria, the material was synthesized in thin film form. Review of very recent literature reveals that the spray pyrolysis technique (SPT) could be a promising technique. Therefore, SPT was employed to prepare the thin films of GDC on glass substrates to and on to ceramics substrates. The optimization of process parameters of SPT was done so as to achieve the films of GDC with desirable characteristics.

The details of theoretical aspect of synthesis and characterization techniques employed during the research along with the detailed results and discussion on various measurements carried out has been provided in seven chapters.



**Chapter one** starts with brief introduction to solid electrolytes with its concise history and probable impact on our standard of living, environment, and economy. In subsequent sections a few application of the materials exhibiting oxygen ion conductivity (oxygen ion conductors - OICs) were explained. However, the fabrication and operation of these technologically important devices experienced various commercialization related dilemmas. Few of them are mentioned in section 1.4 along with possible resolution over these problems. In the next section, the literatures were surveyed systematically and the most important research work is presented. The importance of pure and doped ceria is discussed. One of the best doped cerias is Gd doped ceria (GDC) and in-spite of its excellent electrical properties it suffers from some shortfalls when used as solid electrolyte. This is discussed at length with the help of relevant literature. The synthesis of GDC by the cost effective ceramic route and of GDC thin films by different thin film preparation techniques is briefly reviewed and presented in chapter one. The **chapter one** ends with the scope of the research work

**Chapter two** discusses the fundamental aspect of solid electrolytes. The first half of chapter two is focused on the general consideration of ion conduction mechanisms in solid electrolytes. A basic model of ion transport to describe conduction in solid electrolytes is presented. The model is based on the isolated hopping of the mobile ions. In addition, brief aspects of the influence of ion interactions between both the mobile and immobile ions of the solid lattice are explained. It is likely that in solid electrolytes, such ion interactions and cooperative ion movements are important and must be taken into account if a quantitative description of ionic conductivity is to be attempted. All these aspects were systematically described and finally were applied to oxygen ion conductor, as an example. The second half of **chapter two** dealt with the crystal structure of pure and doped ceria, where it's theoretical (defect-free – ideal) and real (with defect) crystal structure is described. Finally, while explaining the electrical behavior of pure and doped ceria, the effect dopant concentration and temperature dependence is also considered.



**Chapter three** covers the theoretical aspect of techniques employed for the synthesis and characterization of materials. The synthesis of the Gd doped ceria in bulk and thin film form has been carried out using solid state ceramic route and spray pyrolysis technique (SPT), respectively. The details of ceramics route and SPT were discussed in first two sections of this chapter. These sections involve the general steps included in synthesis of materials along with its importance and its influence on the final product. The accepted reports found in literature regarding the theory of formation of materials in ceramic route and SPT, for example, grain growth, film formation, phase formation, densification, etc. were referred and discussed. A brief introduction of characterization techniques employed to characterize the prepared materials is also given. The characterization techniques include (i) density measurements, (ii) thickness and surface roughness measurements using surface profiler, (iii) Thermo-gravimetric and Differential thermal analysis (iv) X-ray diffraction, (v) Scanning electron microscopy, (vi) Energy dispersive X-ray analysis (vii) Atomic force microscopy, (viii) DC conductivity measurements and (ix) AC conductivity measurements using impedance spectroscopy.

**Chapter four** describes the study of optimization of doping percentage of Gd in ceria (bulk form) to lead to the best electrical performance. Various compositions of Gd doped ceria were synthesized for different preparative parameters of solid state reaction method. The chapter describes experimental procedure employed and the results obtained, which are discussed with relevant reasoning. The samples with different content of Gd were prepared at different processing parameters. All the samples were studied for their structural, morphological and electrical properties. The host lattice of GDC, ceria, expands upon doping with Gd, since Gd has size (0.1nm) slightly greater than Ce(IV) (0.096nm). All the samples showed the presence of (111), (200), (220), (311), (222), (400), (331), (420) and (422) reflection peaks. The variation of Gd in ceria obeys the Vegard's rule.

With an increase in Gd content in ceria, the grain growth rate of GDC was observed to reduce, leading to a decrease in average grain size. The electrical characterization confirmed that the grain boundary conductivities were of ion blocking behavior due to existing impure phases like SiO<sub>2</sub> at 300 ppm level in commercially available raw powders. However, the GDC10 composition showed the



highest grain interior ionic conductivity, in addition to total conductivity with activation energy of 0.75eV.

The optimization of processing parameters has suggested the use of five step ceramic route (binder removal step), which has shifted the process of reduction of ceria at high sintering temperature by about 100°C. Further, the relative density was found to be a function of sintering temperature and duration. The relative density of 99% of theoretical value was obtained for sintering temperature of 1773K and sintering duration of 8h. The grain growth, as observed in SEM, was also a function of sintering temperature.

Apart from these sintering parameters, the thickness of the samples also plays the critical role in impeding the electrical performance of samples. It was observed that the electrical performance of solid electrolyte is inversely proportional to thicknesses of the samples. Thus we could develop electrolyte quality GDC10 samples (samples with required ionic conductivity and relative density) by a ceramic route.

*Chapter five* deals with synthesis and characterization of 10%Gd doped ceria (GDC10) thin films deposited on glass substrate using spray pyrolysis technique (SPT). The optimized Gd doping level from bulk study was chosen for thin film studies and, as primary attempts, was deposited on glass substrate.

Initially, un-doped ceria films were deposited onto glass substrates. One of the spray pyrolysis preparative parameters, precursor solution concentration, was varied by keeping the other parameters constant. The phase purity of the films was confirmed by XRD. All the samples showed the fluorite structure with lattice parameters,  $a = 5.412\text{\AA}$ . The optimized preparative parameters for the deposition of ceria on glass substrate are listed in the table below.

Then 10mol%Gd doped ceria was deposited onto glass substrate. The films showed the fluorite structure with (111), (200), (220), (311), (222), (400), (331), (420) and (422) reflection peaks and elemental composition, as confirmed by EDAX, was as expected i.e. Ce: Gd :: 0.9:0.1. The SEM pictures of the films showed the micron size grains, which were actually clusters made up of nano-sized grains as observed in AFM. The grain growth, surface morphology and structural morphology were



discussed as a function of preparative parameters such as solution concentration, substrate temperature of SPT. The optimized parameters are listed in table below.

<b>Fixed parameter:</b>	<b>Values</b>	
<i>Type of salt</i>	<i>Metal nitrate</i>	
<i>Atomization type</i>	<i>Air-blast</i>	
<i>Nozzle to substrate distance</i>	<i>25 cm</i>	
<i>Nozzle motion</i>	<i>1cm/second</i>	
<i>Linear distance traversed by nozzle</i>	<i>20 cm</i>	
<i>Temperature controller</i>	<i>+4°C cycle</i>	
<b>Optimized parameters for glass substrate</b>	<b>For Ceria</b>	<b>For 10%Gd doped ceria</b>
Solution quantity	100 ml	100 ml
Substrate temperature	300°C	300°C
Solution concentration	<b>0.05M</b>	<b>0.04M</b>
Annealing (post heat treatment)	≥ 450° for ≥ 2h	≥ 450° for ≥ 2h

The dc conductivity was observed to decrease with an increase in thickness of the films. The dc conductivity was ~0.5 S/cm at 623 K, which is five times larger than that of YSZ at 1273K (0.1S/cm). However, the GDC10 thin films as synthesized on glass substrate could not be employed for application in oxygen permeable devices. Thus the spray pyrolysis technique (SPT) is a promising technique to deposit thin GDC solid electrolytes and the deposition of GDC10 thin films on electrode (ceramic) substrate is desirable.

**Chapter six** elaborates further the suitability of SPT for the deposition of GDC thin films on ceramic substrates. The experimental procedure of fabrication of dense, thin solid electrolyte film on functional ceramic substrates using SPT for development of electrode/electrolyte structures (half cell) are discussed in detail. Here, GDC thin films were deposited on two types of ceramic substrates namely GDC and NiO-GDC (composite), which were prepared by conventional ceramic route employing the optimized process parameters obtained from chapter four. These substrates were



characterized by XRD to study their phase purity and surface morphology. The GDC substrates were denser than the NiO-GDC. Surface modification of NiO-GDC substrate was carried out using reduction treatment in H<sub>2</sub> atmosphere.

GDC films were deposited onto these substrates and were characterized by XRD, SEM, cross sectional SEM and electrical properties etc. GDC substrate showed effect of substrate oriented grain growth in GDC films while that of NiO-GDC substrate provided well connected grains of GDC films. With this technique, we could be able to deposit films of thickness of the order of 2 $\mu$ m and 13 $\mu$ m onto GDC and NiO-GDC substrate. The later has the ability to provide the anode supported cell after being coated with suitable cathode on electrolyte, since its relative density was of the order of 96% with required ionic conductivity. While the former can be used to form a protective layer of GDC onto YSZ, for use in conventional SOFCs, to avoid the undesirable phase formation at electrode interface.

The interface studied using impedance spectroscopy showed that the grain boundary activation energy is high (1.40eV) for conduction in the case of GDC substrate while it is comparably small (0.93eV) for NiO-GDC substrate. The activation energy for grain interior conduction estimated for the system formed by films on either ceramic substrate is of the same order (~1.02eV).

Further there was only nominal decrease in overall ionic conduction of the GDC/NiO-GDC structure over the bare substrate, indicating that the interface formed by spray deposited GDC films onto NiO-GDC substrate was well adherent. After the fabrication of half cell, other coating technique (e.g. spin coating, screen printing, etc.) could be employed to coat the cathode layer over it. The formed cell can be co-sintered comparatively at lower temperatures as the density of spray synthesized electrolyte has already reached to its desirable value during the formation of half cell (anode/electrolyte). This ability of co-sintering of cell at lower temperature is an added advantage; as it avoids the formation of un-desirable phases at the interface.

Thus the spray pyrolysis technique (SPT) has the potential to synthesize the solid electrolyte grade GDC thin films on to NiO-GDC ceramic substrates.

*Chapter seven* discusses the significance of Gd doped ceria in bulk and thin film form as solid electrolyte for IT-solid oxide fuel cells. Importance of thin films in





IT-SOFC has been discussed in the chapter seven. The results obtained for the bulk and thin film GDC samples prepared with optimized preparative parameters were compared.

Chapter seven ends with fuel cell characterization of GDC sample. The samples prepared with optimized preparative parameters were tested in a symmetrical cell configuration for four different fuel cell conditions. For a typical fuel cell condition, the open circuit voltage (OCV) was of the order of 0.84 volts at 500°C, which is comparatively higher than the values reported in literatures.

**Thus in conclusion, the major achievements of the research work done are:**

1. The process parameters of ceramic route were optimized to obtain dense ‘electrolyte-grade’ Gd doped ceria bulk samples. The ceramic route was understood completely in order to control porosity, grain growth and surface morphology. We have successfully avoided the reduction of  $Ce^{4+}$  to  $Ce^{3+}$  at high sintering temperatures and obtained a solid electrolyte grade material.
2. These understanding allowed us to prepare GDC sample for high open circuit voltage (OCV) than reported values in a symmetrical cell configuration. The open circuit voltage of **0.85 V** was recorded at 500°C
3. We have prepared, for the first time, GDC thin films from **aqueous precursors** using spray pyrolysis technique. Thereby there was **no organic contamination** in the films.
4. We have also optimized the process parameters of spray pyrolysis technique to obtain dense ‘electrolyte-grade’ Gd doped ceria thin films.
5. We have deposited 13µm GDC films onto **electrode-grade** NiO-GDC substrate with **least impeding interface**. These could be used as a half cell and after depositing suitable cathode could be tested for cell characteristics in a typical fuel cell conditions. This proposes the co-sintering of cell components at low temperature.



6. Also, the GDC films of 2 $\mu$ m on a dense GDC substrate could be employed as a protective layer of the same on traditional electrolyte materials to enhance the electrode interface.

***“Overall conclusions and achievements of research would assist the commercialization of ceria based solid oxide fuel cells for intermediate or low temperature operation”.***

—————***Mr. Muralidhar Girish Chourashiya***

---

### ***FUTURE SCOPE OF RESEARCH***

---

#### ***For GDC in bulk form***

---

1. The optimized process parameter for ceramic route could be used to prepare “electrolyte-grade” GDC electrolyte
2. This GDC electrolyte should be coated by electrode materials using suitable coating technique to form a complete cell of electrolyte supported cell configuration
3. The cell formed could be evaluated by placing the cell in a typical fuel cell environment and recording the power curve

---

#### ***For GDC films on ceramic substrates***

---

1. The GDC films on electrode substrate could be used to prepare “electrode/electrolyte” assembly
2. The assembly further would be coated by using a suitable coating technique to coat the another electrode material (electrode supported cell configuration)
3. The complete cell formed would further be evaluated by placing the cell in a typical fuel cell environment and recording the power curve



---

# Appendix

---

**Appendix I-A: Powder synthesis techniques** [i]

---

**Appendix I-B: Green body formation** [ix]

---

**Appendix II: Some useful definitions** [xvii]

---

**Appendix III: Standard reduction potentials** [xxxii]  
for different H<sub>2</sub>-O<sub>2</sub> chemical reactions

---



## Appendix – I-A: Powder synthesis techniques

To make the best use of the potential properties of ceramics, new ceramic powders with high chemical purity, uniform distribution of constituent starting chemicals and fine particle size are necessary. Table 1 gives an overview of the various methods for powder synthesis. These methods are generally broken into four categories:

- Solid phase reactant
- Liquid phase reactant
- Gas phase reactant.
- Miscellaneous synthesis methods

<b>Solid phase reaction</b>	<b>Liquid phase reactant</b>	<b>Gas phase reaction</b>	<b>Miscellaneous synthesis methods</b>
<ul style="list-style-type: none"> <li>• Solid state reactants</li> <li>• Thermal decompositions of a solids</li> <li>• Oxidation or reduction of a solids</li> </ul>	<ul style="list-style-type: none"> <li>• Precipitation</li> <li>• Solution heating or cooling.</li> <li>• Evaporative salting-out</li> <li>• Chemical reaction with insoluble product</li> <li>• Hydrothermal synthesis</li> <li>• Forced insolubility</li> <li>• Dissolution re-precipitation</li> </ul>	<ul style="list-style-type: none"> <li>• Evaporative condensation</li> <li>• Gas phase reaction with solid product</li> <li>• Thermal decompositions</li> <li>• Oxidation or reduction reaction</li> <li>• Combination reaction with a solid product</li> </ul>	<ul style="list-style-type: none"> <li>• Solvent removal</li> <li>• Spray drying</li> <li>• Freeze drying</li> <li>• Spray roasting</li> <li>• Sol-gel synthesis</li> <li>• Melt solidification</li> </ul>

Table 1. Ceramic powder synthesis methods.

### *a) Ceramic powder synthesis with solid phase reactant*

There are two types of reactions are included in this type of synthesis, namely, the fluid-solid reaction and solid-solid reactions. A solid is a reactant in two general

types of powder synthesis reactions. One type is a fluid-solid reaction, where the fluid is either a liquid or a gas. The other type is a solid-solid reaction. Fluid-solid reactions can be represented by

- $A \text{ (fluid)} + b B \text{ (solid)} \rightarrow d D \text{ (solid)}$
- $A \text{ (fluid)} + b B \text{ (solid)} \rightarrow d D \text{ (solid)} + e E \text{ (fluid)}$
- $b B \text{ (solid)} \rightarrow d D \text{ (Solid)} + e E \text{ (fluid)}$

With each of these reactions, a solid of one type (B) is the reactant and a solid of another type is the product (D). A fluid is also a reactant or a product of the reaction. In some cases, the solid product (D) forms a shell on the outside of particle B, giving a diffusion barrier for further reaction. This type of reaction is modeled as a shrinking core (figure 1).

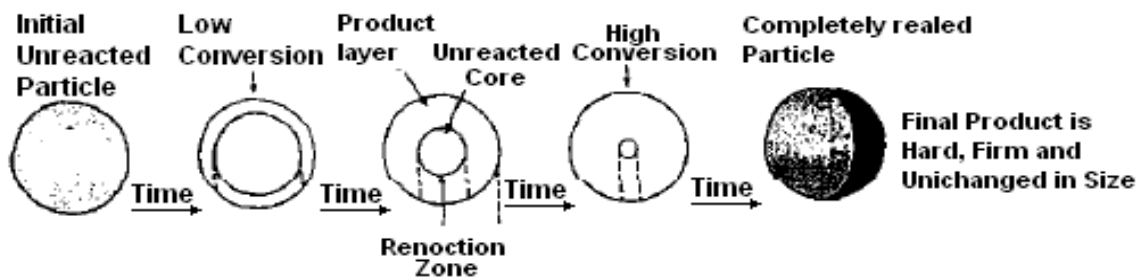


Figure 1: Shrinking core model.

In other cases, the product D flakes off the surface of particle B, because there is a large difference in the molar volume of reactant B and product D. This type of reaction is modeled as a shrinking sphere as seen in Figure 2. Fluid-solid reactions include thermal decomposition of minerals, roasting (oxidation) of sulfide ores, reduction of metal oxides with hydrogen, nitridation of metals, and carburization of metals.

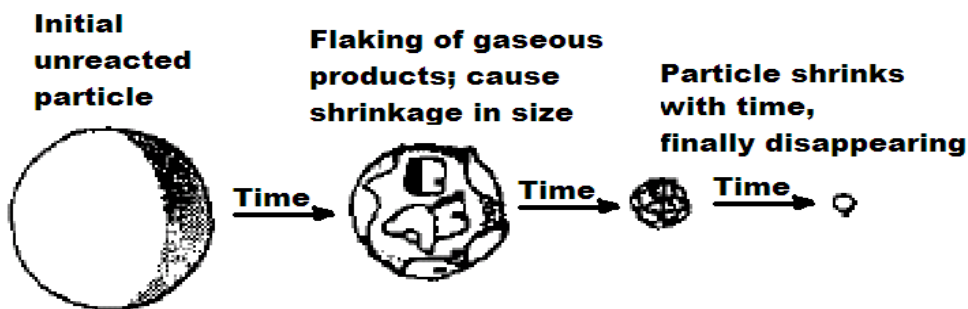


Figure 2: Shrinking sphere model.

The reaction between two (or more) types of solid is frequently practiced to produce multi-component ceramic powders. Solid-solid synthesis reactions operate by different mechanisms, which include solid state diffusion and chemical reaction. In mechanism of solid inter-diffusion, where the two solid state reactants inter-diffuse at the points of powder particle contact and produces mixed oxide ceramic powders. However, diffusion in ceramic solids is always ionic in nature and depends on defect or hole diffusivity, as well as, electron conductivity. Once the ionic reactants are in close association, chemical reactions can take place. Obviously, this mechanism is not truly a solid-solid reaction. It involves the vaporization of one of the reactants and then reaction of this vapor with the other solid.

*b) Ceramic powder synthesis with liquid phase reactant (precipitation)*

In most cases, the production of ceramic powders from liquid phase reactants are produced by precipitation of ceramic powder precursors such as sulfates, carbonates, oxalates, hydroxides, etc. These powders must be thermally decomposed to their oxides in a separate step that frequently maintains their precipitated particle morphology although some degree of particle sticking (agglomeration) often occurs. The precipitation includes fundamental steps of nucleation, growth, and aggregation, which controls the particle morphology and size distribution in the final ceramic powder product.

The main reason behind the use of precipitation is to make ceramic powders is that it gives a pure solid product, rejecting to the most of the impurities floating over the surface of precipitate (solid product). In addition, with precipitation the particle morphology and the particle size distribution can be controlled to some degree. Precipitation has the disadvantage that the powders must be separated from their supernatants and dried, as well as, frequently thermally decomposed to the desired ceramic material. This drying and calcinations often leads to aggregates that are cemented together. Special precautions must be made to prevent aggregate formation during drying and calcinations (e.g. calcinations in very dry atmospheres).

The precipitation of powders involves nucleation and growth from a supersaturated solution. There are several ways to cause a solution to become supersaturated to induce nucleation and growth. For systems in which the solubility is not a strong function of temperature, evaporation is used to cause super-saturation.

---

For those in which solubility increases with temperature, cooling is used to supersaturate the solution. High pressures are also used to precipitate a particular crystal phase that may not be stable at ambient pressure. The use of high pressure precipitation is referred to as hydrothermal synthesis. Super-saturation can also be produced by adding another component in which the solute is insoluble. Although these methods can be used to generate ceramic powders, the most common method, reactive precipitation, occurs when a chemical reaction produces an insoluble species. Reaction-induced super-saturation is often very high, giving high nucleation rates. With the high number densities of nuclei produced, agglomeration is an important growth mechanism leading to spherical particles that are either polycrystalline or amorphous.

*c) Ceramic Powder Synthesis with Gas Phase Reactants*

There are four methods of gas phase ceramic powder synthesis: by flames, furnaces, lasers and plasmas. In each case, the reaction thermodynamics and kinetics are similar, but the reactor design is different. To account for the particle size distribution produced in a gas phase synthesis reactor, the population balance must account for nucleation, atomistic growth (also called vapor condensation) and particle-particle aggregation. To obtain narrow size distribution ceramic powders by gas phase synthesis, dispersion must be minimized because it leads to a broadening of the particle size distribution. Finally the gas must be quickly quenched or cooled to freeze the ceramic particles, which are often liquid at the reaction temperature, and thus prevent further aggregation.

Gas phase reactors are used to produce the purest ceramic powders because it is relatively easy to obtain purified reactant gases with purities at the ‘ppm’ to ‘ppb’ level. Dopants can be easily added to the ceramic powder in a controlled way by simply mixing in another reactant gas. Depending on the reaction kinetics these dopants may not homogeneously distributed within the resulting ceramic powder. In addition, gas phase reactors are typically continuous reactors that can be controlled very precisely by inexpensive methods. Gas phase reactors produce, for the most part, very fine ceramic powders and narrow particle size distributions, which is an advantage; however, these particles can also be fractal structures that are strongly agglomerated together. In process sintering of these fractal aggregates can sinter to

---



give a roughly spherical particle. Important disadvantages of Gas phase reactors is that it produces very fine ceramic particles ( $<0.5 \mu m$ ) at low volume fraction. These particles are difficult to separate from the large volume of gas, and as a result, a significant fraction of the cost of producing gas phase ceramic particles is spent on particle-gas separation.

	Reaction energy	Heat transfer in by	Max. temp.
Flame synthesis	Exothermic	-	2500 K
Furnace synthesis	Endothermic*	Radiation, Convection	2300 K
Plasma synthesis	Endothermic*	Ions and electrons <sup>#</sup>	10000 K
Laser synthesis	Endothermic*	Lasers; $\lambda =$ Molecular vibration <sup>#</sup>	1800 K

\* Exothermic reactions are also possible. <sup>#</sup> Standard methods of heat transfer are also possible.

Table 2: gas phase powder synthesis routes

In gas phase reactions to produce ceramic powders one can make use of exothermic and endothermic chemical reaction mechanisms. Those reactions which are exothermic require no external energy source to keep them going after the reaction has been initiated, e.g. using flames. However, for endothermic reactions, gas phase powder synthesis can be performed with an external energy source to provide the necessary heat for reaction. This external energy source can be provided by a furnace, laser, or plasma (direct current, dc arc, or radio frequency, RF). In a furnace, conduction, radiation and convection provide the energy. The ions and electrons of the plasma provide the energy in plasma synthesis. The wavelength of the laser must be coupled with a molecular vibration of one of the reactants or the carrier gas to provide the energy necessary for reaction in laser synthesis. On an industrial scale, only flame and furnace reactors are used. Much research is being done to perfect laser and plasma reactors for future ceramic powder synthesis. Gas phase ceramic synthesis is the subject of several review papers [5-7]. Each of the gas phase powder synthesis methods is summarized in Table 2. The accessible maximum temperatures are also listed.

*d) Ceramic Powder Synthesis with Miscellaneous methods*

These ceramic powder synthesis processes are not easily classified in the solid, liquid and gas phase synthesis schemes. These methods include spray drying, spray roasting, freeze drying, metal-organic decomposition, sol-gel synthesis, and melt and flux solidification.

- Spray drying:

Spray drying is an industrial process used very often in the generation of dry powders from liquids or suspensions. A basic description of the preferred techniques can be found in *Spray Drying Handbook* by Masters [8]. Spray drying is also a method of ceramic powder production that uses either a concentrated metal salt solution, powder dispersion (a sol) with a polymeric binder or a gel solution as a feed material. The feed material is introduced into the top of a dryer by some method of atomization. The atomization results in (1) many droplets of the feed material, increasing its surface to volume ratio to aid in drying, and (2) forms droplets that will give the desired particle size distribution for the dried product.

- Spray roasting:

Spray roasting is simply an extension of spray drying to higher temperatures, where thermal decomposition of the sprayed salt takes place. The steps involved are, atomization of a salt solution, mixture of droplets with a heated gas, evaporation of the solvent (often water) and thermal decomposition of the dried salt particles in the heated part of the equipment.

- Metal organic decomposition for ceramic films:

Solutions of metal organics can also be spray roasted to give ceramic powders as mentioned earlier. But by far the most interesting use of metal organic decomposition is for the manufacture of ceramic thin films. In this case, metal organic solutions can be dip coated or spin coated onto a substrate. After drying, a metal

organic coating is obtained, which can then be thermally decomposed to a ceramic. These metal organic solutions can also be used to put coatings on other ceramic powders to make a layered composite powder.

- Freeze drying:

Freeze drying is used to dry either salt solutions or ceramic suspensions in a gentle way, avoiding thermal decomposition of the metal salts and aggregation of the particles. There are four steps in freeze drying:

- i) Either a mixture of soluble salts containing the desired ratio of metal ions is dissolved in a solvent or a ceramic powder suspension is made.
- ii) The solution is sprayed into droplets between 0.1 and 0.5 mm in diameter and rapidly frozen by a cold fluid (liquid or gas) so that no compositional segregation or aggregation can occur and the solvent crystals that nucleate are very small.
- iii) The solvent is removed by vacuum sublimation being careful not to form any liquid phase that could cause chemical segregation.
- iv) The resulting powder is either used directly or the metal salts are calcined at a temperature that decomposes the crystallized salts and converts them to very fine crystallites of the desired ceramic powder.

- Sol-Gel Synthesis:

The earliest routes for forming ceramics from sol-gel solutions involved the precipitation of metal oxide particles from solutions. These form a true colloidal suspension: a sol. Upon destabilization of this sol, aggregation takes place and a rigid network is formed: a gel. A gel is intermediate between a solid and a liquid. The term sol-gel has since been used by the materials science community to describe, virtually all chemical processing of ceramics from solutions (e.g., metal oxide particle precipitation or metal-organic decomposition).

- Melt solidification:

Large grained ceramic powders can be produced by the melt solidification processes. An electric arc is passed between the electrode and through the ceramic powder. After a sufficient current has passed the ceramic powder melts. The steel vessel is protected from the melt by a layer of solidified ceramic powder. After melting the electrode is removed, and the vessel is set aside to cool. Solidification then begins. In some cases the cooling rate is increased by passing cooling water over the surface of the steel vessel. Even under these conditions, the melt is slowly cooled, crystallizing rather large crystals (e g 0.1-5 cm). Ceramic and abrasive powders are produced from these crystals by grinding and classification.

## Appendix – I-B: Green body formation

---

### *Green body formation – Pressing of the homogenized powder in desired shape*

A green body can be made from a ceramic suspension, a ceramic paste or from a dry ceramic powder. It is molded into a shape with forces applied to either the individual particles, as in drag and gravitational forces, or to the mass of particles as, in ramming a dry powder onto a die or extruding a paste. After drying, the ceramic green body contains (1) the ceramic components; (2) a polymeric binder system including dispersant, binder, and plasticizer, and (3) residual solvent used to make the initial ceramic suspension or paste or used to spray dry the ceramic powder before dry pressing.

The mechanical properties of ceramic powders are important in designing the equipment necessary to process the ceramic suspensions, pastes, and dry powders into ceramic green bodies. Each of the different raw materials for green body formation is used with different methods of ceramic green body formation. For example, (1) ceramic suspensions are used with slip casting, drain casting, tape casting, dip coating, filter pressing, and electro-deposition; (2) ceramic pastes are used with extrusion and injection molding; and (3) dry ceramic powders are used in die pressing, dry bag isostatic pressing, and wet bag isostatic pressing.

The uniformity in green body formation is essential for its uniform sintering. Any differences in the packing density of the ceramic powder will cause different shrinkage during sintering, which leads to warping or cracking of the shape during sintering. Depending on the initial state of the ceramic material, which can be either, a dry powder, a suspension or a paste, there are different methods of shape manufacture.

Particular attention must be paid to the uniformity of powder packing, binder distribution, and solvent distribution because these play an important role in the next phases of processing: drying, binder burnout and sintering. In-homogeneities in these properties will lead to deforming and cracking of the ceramic piece during further processing.

#### *A. Green body formation with ceramic suspensions*

A ceramic suspension consists of ceramic powder, a solvent, often a dispersant to stabilize the ceramic powder against agglomeration, a polymeric binder to provide

---

green strength after the green body has been dried, and often a plasticizer to lower the glass transition of the polymeric binder. All these additives must be compatible so the ceramic suspension has the desirable properties needed for green body fabrication.

- Slip Casting

With slip casting, a porous mold is used to give shape to the green body. Slip casting can be performed with two options, drain casting or solid casting. In drain casting, the mold is filled with a dilute slip, typically less than 5% solids, and a portion is dewatered by the porous mold giving a cast layer on the mold wall. The excess suspension is drained from the mold, and the cast layer is allowed to dry and shrink away from the mold. In solid casting, a thick slip is poured into the mold, where it completely dewateres. In both drain and solid casting, the mold is filled with a ceramic suspension, and a combination of hydrostatic pressure and capillary suction dewateres the ceramic suspension adjacent to the mold.

- Filter pressing (figure 1)

In pressure filtration, a piston is used with a frit bottom to allow the excess liquid to leave the chamber, catching the ceramic powder on the frit. The permeability of the cake of consolidated ceramic powder and frit permeability decreases as the applied pressure increases, due to an increase in the packing density.

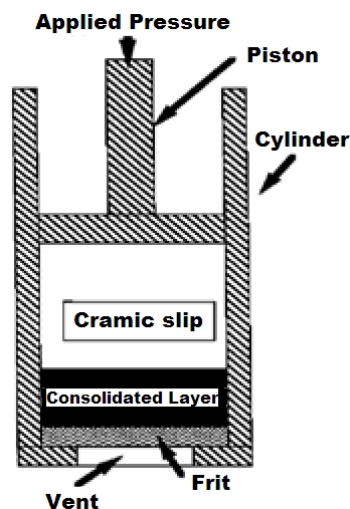


Figure 1. Filter pressing.

- Tape Casting

Tape casting is used to produce a green body which consists of a thin layer of a dried ceramic suspension. These green layers can be cut into a near-net shape and sintered to give a useful ceramic object. In addition, these thin ceramic layers can be layered to produce a multilayer structure.

A tape casting machine consists of a moving belt onto which ceramic powder slurry is spread by a stationary doctor blade, generally with a rectangular form. Control of the thickness of the cast is of critical importance in tape casting. This is done by first precisely controlling the solids concentration in the thick suspension. Typical solids loading are between 10 and 50% by volume. To determine the cast thickness, it is necessary to know the velocity profile in the gap between the doctor blade and the moving belt.

- Sedimentation Casting and Centrifugal Casting

In sediment casting, a suspension of ceramic powder is placed in a vessel and allowed to settle until a cake is formed. The supernatant is removed and the wet green body is allowed to dry. Depending on the colloid stability, different types of settling behavior will be observed. When the particles are well dispersed, the settling is slow and persistent, giving a high density cake that resists re-dispersion. The supernatant is cloudy for dilute free settling suspensions but will be clear for high volume fractions when hindered settling takes place. For centrifugal casting, the same process occurs in a centrifugal field which is used to speed up the cake (green body formation) formation.

- Electrodeposition

Electrodeposition was introduced into ceramics processing to make green bodies more quickly. During sedimentation casting and slip casting of very fine particles, long time periods are required to build up a deposit. An electric field is used to enhance the deposition rate of ceramic particles in the cake.

- Dip Coating

In dip coating, a nonporous substrate is dipped into a dilute ceramic suspension and removed at a constant velocity. The removal of substrate at constant velocity results into formation of ceramic thin film formation on substrate. The equipment made for this purpose has the assembly of the electric motor with high precision to satisfactorily achieve the constant and steady velocity of removal of substrate. The thickness of the film on substrate is depends on factors like the viscosity of the suspension, surface tension of suspension, removal velocity of the substrate, angle of dipping of substrate, etc.

*B. Extrusion and Injection Molding of Ceramic Pastes*

Extrusion and injection molding are typically used in polymer processing. They are also used in ceramic green body manufacture. In extrusion, a ceramic paste is continuously pushed through a die in the shape of a cylindrical drainage tile or a honey comb channel shape. Because of the high shear rates imposed upon this viscous mass of ceramic paste temperatures high enough to soften or melt the polymeric binder are often obtained. Upon leaving the die, the paste is no longer under shear and it solidifies into the desired shape. With injection molding, the extrudate flows into a mold. When the mold is filled, the mold is either removed from the extruder and another empty mold is put in its place or the extruder is stopped. In some cases, an extrude-able and inject-able paste may consist of 65% vol. ceramic powder and 35% vol. polymeric binder.

*C. Green Body Formation with Dry Powders — Dry Pressing*

There are two types of dry pressing, isostatic and die pressing.

- Isostatic pressing:

In isostatic pressing, the dry powder is allowed to flow into a rubber mold. Then the material is vibrated or tapped to give uniform particle packing density

---



distribution. After tapping, the mold is sealed and then placed into a fluid (oil) bath. The pressing action takes place when the fluid is placed under hydrostatic pressure. With isostatic pressing, the pressure is evenly distributed over all the surface of the green body inside the rubber mold. After a relatively short period of time at pressure, the pressure is released and the mold removed from the oil and the green body, now much smaller than that of the mold cavity, is released from the mold cavity. Isostatically pressed green bodies can be of any geometry because the only limitation is that of shaping the rubber mold which is quite easily modified as per the requirements.

- Die pressing:

In die pressing, the dry ceramic powder is allowed to flow into a hardened steel mold. Then the materials are pressed by a die. This pressing action can be either uniaxial or biaxial, depending on the type of press. After a short period of time under pressure, the pressing action is decreased and the pressure is used to eject the green body from the press. Large production runs are almost always made with die pressing and not isostatic pressing.

In addition, there is a hybrid form of pressing called ramming (figure 3). In this case, a ceramic powder is placed in a thick walled rubber mold and a steel mandrel (rod or bar) is rammed into the mold, forcing the powder into a gap between the steel mandrel and the now deformed rubber mold. The pressure acting on the powder particles is a result of the elasticity of the rubber mold. To have uniform pressure acting on the ceramic powder, the wall thickness of the mold must be designed appropriately. Ramming is often used for the fabrication of crucible shaped ceramic objects.

Ramming, die pressing, and isostatic pressing have several aspects which are similar, however two aspects are different. One is the tapping or vibration step used in isostatic pressing, and the other is the type of force used in pressing. The isostatic force is a uniform pressure on the surface of the green body in the mold but die pressing is either a uniaxial or biaxial force on green body. Ramming is a combination of both types.

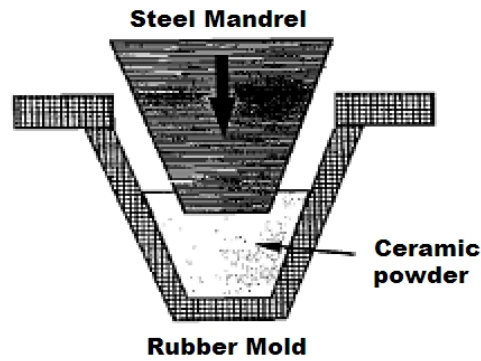


Figure 3: Schematic diagram of ramming of ceramic powders.

*D. Brief information on important steps in die pressing:*

1. Tapping step in Dry pressing: A crucial step to enhance the density

In dry press green body formation tapping provides a method to (1) increase the packing density and (2) eliminate any in-homogeneities in the packing, which is by far the more important consideration in view of prospective properties of final product. If the mold is not filled homogeneously, the final pressed shape will be very different from that of the mold.

2. Die Pressing

With die pressing, a powder after flowing into a mold is subjected to high pressure. When this powder is compacted, it first reorganizes into a close packed structure (figure 4b). At higher pressure, it undergoes plastic deformation of the agglomerates to further increase the packing density (figure 4c). At still higher pressure, the remaining pores are filled by comminution (size reduced fine particles) products (figure 4d). This series of structural reorganizations is schematically shown in Figure 4.

When the localized forces on the particles are sufficiently large, particle comminution starts as depicted in figure 4 (d). The pressures required for stage (c) in figure 4, compaction depend on the choice of polymeric binder system used. The hardness of a binder system is related to its mechanical properties. These mechanical properties of a polymer depend on the molecular weight of the polymer, its molecular weight distribution, and its chemistry. One important property is the glass transition

temperature of the binder system. Above the glass transition temperature for the binder system, the polymer flows easily. Below the glass transition temperature, the polymer is brittle. The glass transition temperature of a binder system can be lowered by lower molecular weight additives, which are called plasticizers.

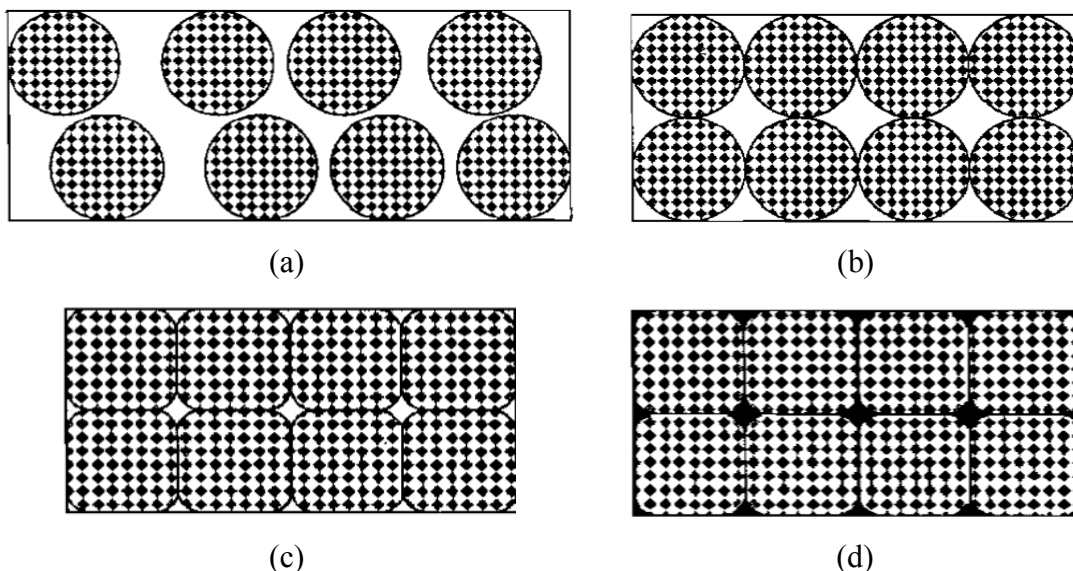


Figure 4: Schematic of series of structural reorganizations (a) Loose packing as die is filled, (b) After structural re-organization to removed packing holes, (c) Deformation of aggregates and d) Comminution of agglomerates filling the voids with fine particles

### 3. Die ejection and wall friction

After compaction, the green body must be ejected from the die. During the ejection the green body is released from compression at high pressure to very low pressure and then pushed out the mold. Wall friction depends on the roughness of die wall and its lubrication. For walls with a scale of roughness larger than the diameter of the powder, the wall friction is essentially the same as the internal friction of the powder. This is because the rough wall traps small amount of the powder in its rough surface and the sliding of this powder mass against the trapped powder produce the effective wall friction. If the wall has a scale of roughness smaller than the diameter of the powder, the wall friction is controlled by particle-wall friction. In both the cases the wall friction can be decreased by lubricants applied to the die wall prior to pressing. The thickness of the lubricant plays an important role in reducing the wall friction. If the wall roughness is smaller than the diameter of the particles, the

thickness of the lubrications layer need only exceed the diameter of the particles to forms the lubricated powder layer against the wall and thus decrease the wall friction. When the wall roughness is larger than the diameter of the particles, the thickness of the lubrications layer needs to exceed the wall roughness to decrease the wall friction. In many cases it is need not to put lubricants in the press, instead the binder in the powder itself can act as lubricant.

## Appendix – II: Definitions of some useful scientific terms

### Index

<b>A</b>	Absorptance (a), Absorption coefficient (a), Absorption coefficient, molar (e), Acceleration, Acceleration due to gravity (g)*, Acid, Activation energy*, Adiabatic process, Admittance (Y), Adsorption, Ampere (A)*, Ampere's law, Ångström (Å), Angular velocity (w), Are (a), Anion, Arrhenius equation, Atomic mass*, Atomic mass unit (u)*, Atomic number (Z), Atomic weight (Ar)*,
<b>B</b>	Boltzmann constant (k)*, Boltzmann distribution, Bragg angle, Bravais lattices*,
<b>C</b>	Capacitance (C), Carnot cycle, Catalyst, Cation, Ceramic, Chalcogens, Chemical potential, Chromatography*, Colloid, Conductance (G)*, Conductivity, electrical (s)*, Coulomb's law, Covalent bond,
<b>D</b>	Defect, Density (r)*, Dislocation, Dispersion, Dissociation constant*, Dissociation energy (De)*,
<b>E</b>	Einstein, Electric charge (Q), Electric current (I), Electric displacement (D), Electric field strength (E), Electric potential (V), Electrochemical series*, Electrode potential*, Electrolysis, Electromotive force (emf), Electron*, Electron affinity*, Electron volt (eV)*, Electro, Electrophoresis, Energy gap*, Enthalpy (H)*, Enthalpy of combustion*, Enthalpy of formation, standard*, Enthalpy of fusion*, Enthalpy of sublimation, Enthalpy of vaporization*, Entropy (S)*,
<b>F</b>	Farad (F)*, Faraday constant (F)*, Faraday effect*, Fermi level, Ferrimagnetism*, Ferrite, Ferroelectricity*, Ferromagnetism*, Frequency (n)*,
<b>G</b>	Gallon (US), Gallon (UK, Imperial), Gel, Gibbs energy (G)*, Glass transition temperature*, Grain (gr), Grain boundary,
<b>H</b>	Hall effect*, Hardness*, Heat capacity*, Heisenberg uncertainty principle, Helmholtz energy (A), Henry (H)*, Hertz (Hz), Holography, Hydrocarbon, Hydrolysis, Hysteresis*,
<b>I</b>	Ideal solution, Ignition temperature*, Impedance (Z), Inductance, Insulator, International System of Units (SI)*, Ion, Ion exchange, Ionization constant*, Ionization potential*, Isotherm, Isothermal process,
<b>J</b>	Joule (J)*,
<b>K</b>	Kelvin (K)*, Kilogram (kg)*,
<b>L</b>	Lattice constants*, Lattice energy*, Liter (L)*, Lux (lx)*,
<b>M</b>	Mass (m)*, Mass fraction (wB), Mass number (A), Mass spectrometry, Mean free path*, Melting point*, Metal, Meter (m)*, Mho, Micelle, Micron (m), Mie scattering, Miller indices (hkl), Millimeter of mercury (mmHg), Mobility (m)*, Molality (m), Molar mass, Molar quantity, Molarity (c), Mole (mol)*, Mole fraction (xB), Molecular weight (Mr)*, Monomer, Mössbauer effect,
<b>N</b>	Nernst effect, Neutrino, Neutron*, Newton (N)*, Nyquist theorem,
<b>O</b>	Oersted (Oe), Ohm (W)*, Ohm's law, Osmosis, Osmotic coefficient (f), Osmotic pressure (P), Ostwald dilution law, Ounce (oz), Over,
<b>P</b>	Parsec (pc), Pascal (Pa)*, Pauli exclusion principle, Permeability (m), Permittivity (e), pH*, Phosphoresence, Photoelectric effect, Photon, Planck constant (h)*, Planck function, Plasma, Point group*, Poiseuille's equation, Poisson ratio (m), Polymer, Pound (lb), Power (P), Pressure*, Proton*,
<b>Q</b>	Quality factor (Q), Quasicrystal,
<b>R</b>	Rad, Radiance (L), Radiant intensity (I), Radicals, Raman effect, Rankine cycle, Rankine temperature, Reactance (X), Relative humidity*, Resistance (R), Resistivity (r), Rheology,
<b>S</b>	Salt, Second (s)*, Seebeck effect, Semiconductor, SI units*, Siemens (S)*, Skin effect, Snell's law, Soliton, Solubility*, Solubility product constant (Ksp)*, Space group*, Specific gravity, Specific heat, Specific quantity, Stacking fault, Standard reduction potential (E°), Stark effect, Stoichiometric number (n), Stokes (St), Stokes' law, Strain, Stress, Structure factor, Superconductor, Superfluid, Surface tension (g,s)*, Surfactant, Susceptance (B), Svedberg,
<b>T</b>	Tensile strength*, Tesla (T)*, Thermal conductivity*, Thermal diffusivity, Thermal expansion coefficient (a)*, Thermodynamic laws, Thermoelectric power, Thomson coefficient (m, t), Tonne (t), Torque (T), Torr, Transducer, Transistor,
<b>U</b>	Unified atomic mass unit (u)*, Universal time (tU, UT),
<b>V</b>	Vacancy, Van der Waals' equation*, Van der Waals' force, Vapor pressure*, Velocity (v), Viscosity (h)*, Volt (V)*, Volume fraction (fj),
<b>W</b>	Watt (W)*, Weight, Work (W), Work function (F)*,
<b>X</b>	X unit (X),
<b>Z</b>	Zeta potential (z)

**A**

**Absorptance ( $\alpha$ )** - Ratio of the radiant or luminous flux in a given spectral interval absorbed in a medium to that of the incident radiation. Also called absorption factor. [1]

**Absorption coefficient ( $a$ )** - The relative decrease in the intensity of a collimated beam of electromagnetic radiation, as a result of absorption by a medium, during traversal of an infinitesimal layer of the medium, divided by the length traversed. [1]

**Absorption coefficient, molar ( $\epsilon$ )** - Absorption coefficient divided by amount-of-substance concentration of the absorbing material in the sample solution ( $\epsilon = a/c$ ). The SI unit is  $\text{m}^2/\text{mol}$ . Also called extinction coefficient, but usually in units of  $\text{mol}^{-1}\text{dm}^3\text{cm}^{-1}$ . [2]

**Acceleration** - Rate of change of velocity with respect to time.

**Acceleration due to gravity ( $g$ )\*** - The standard value ( $9.80665 \text{ m/s}^2$ ) of the acceleration experienced by a body in the earth's gravitational field. [1]

**Acid** - Historically, a substance that yields an  $\text{H}^+$  ion when it dissociates in solution, resulting in a  $\text{pH} < 7$ . In the Brønsted definition, an acid is a substance that donates a proton in any type of reaction. The most general definition, due to G.N. Lewis, classifies any chemical species capable of accepting an electron pair as an acid.

**Activation energy\*** - In general, the energy that must be added to a system in order for a process to occur, even though the process may already be thermodynamically possible. In chemical kinetics, the activation energy is the height of the potential barrier separating the products and reactants. It determines the temperature dependence of the reaction rate.

**Adiabatic process** - A thermodynamic process in which no heat enters or leaves the system.

**Admittance ( $Y$ )** - Reciprocal of impedance.  $Y = G + iB$ , where  $G$  is conductance and  $B$  is susceptance. [1]

**Adsorption** - A process in which molecules of gas, of dissolved substances in liquids, or of liquids adhere in an extremely thin layer to surfaces of solid bodies with which they are in contact. [10]

**Ampere ( $A$ )\*** - The SI base unit of electric current. [1]

**Ampere's law** - The defining equation for the magnetic induction  $\mathbf{B}$ , viz.,  $d\mathbf{F} = I d\mathbf{l} \times \mathbf{B}$ , where  $d\mathbf{F}$  is the force produced by a current  $I$  flowing in an element of the conductor  $d\mathbf{l}$  pointing in the direction of the current.

**Ångström ( $\text{Å}$ )** - A unit of length used in spectroscopy, crystallography, and molecular structure, equal to  $10^{-10} \text{ m}$ .

**Angular velocity ( $\omega$ )** - The angle through which a body rotates per unit time.

**Are ( $a$ )** - A unit of area equal to  $100 \text{ m}^2$ . [1]

**Anion** - A negatively charged atomic or molecular particle.

**Arrhenius equation** - A key equation in chemical kinetics which expresses the rate constant  $k$  as  $k = A \exp(-E_a/RT)$ , where  $E_a$  is the activation energy,  $R$  the molar gas constant, and  $T$  the temperature.  $A$  is called the pre-exponential factor and, for simple gas phase reactions, may be identified with the collision frequency.

**Atomic mass\*** - The mass of a nuclide, normally expressed in unified atomic mass units ( $u$ ).

**Atomic mass unit ( $u$ )\*** - A unit of mass used in atomic, molecular, and nuclear science, defined as the mass of one atom of  $^{12}\text{C}$  divided by 12. Its approximate value is  $1.66054 \times 10^{-27} \text{ kg}$ . Also called the unified atomic mass unit. [1]

**Atomic number ( $Z$ )** - A characteristic property of an element, equal to the number of protons in the nucleus.

**Atomic weight ( $A_r$ )\*** - The ratio of the average mass per atom of an element to 1/12 of the mass of nuclide  $^{12}\text{C}$ . An atomic weight can be defined for a sample of any given isotopic composition. The standard atomic weight refers to a sample of normal terrestrial isotopic composition. The term relative atomic mass is synonymous with atomic weight. [2]

## **B**

**Boltzmann constant (k)\*** - The molar gas constant R divided by Avogadro's constant.

**Boltzmann distribution** - An expression for the equilibrium distribution of molecules as a function of their energy, in which the number of molecules in a state of energy E is proportional to  $\exp(-E/kT)$ , where k is the Boltzmann constant and T is the temperature.

**Bragg angle** - Defined by the equation  $n\lambda = 2d\sin\theta$ , which relates the angle  $\theta$  between a crystal plane and the diffracted x-ray beam, the wavelength  $\lambda$  of the x-rays, the crystal plane spacing d, and the diffraction order n (any integer).

**Bravais lattices\*** - The 14 distinct crystal lattices that can exist in three dimensions. They include three in the cubic crystal system, two in the tetragonal, four in the orthorhombic, two in the monoclinic, and one each in the triclinic, hexagonal, and trigonal systems.

## **C**

**Capacitance (C)** - Ratio of the charge acquired by a body to the change in potential. [1]

**Carnot cycle** - A sequence of reversible changes in a heat engine using a perfect gas as the working substance, which is used to demonstrate that entropy is a state function. The Carnot cycle also provides a means to calculate the efficiency of a heat engine.

**Catalyst** - A substance that participates in a particular chemical reaction and thereby increases its rate but without a net change in the amount of that substance in the system. [3]

**Cation** - A positively charged atomic or molecular particle.

**Ceramic** - A nonmetallic material of very high melting point.

**Chalcogens** - The Group VIA elements (oxygen, sulfur, selenium, tellurium, and polonium). Compounds of these elements are called chalcogenides. [7]

**Chemical potential** - For a mixture of substances, the chemical potential of constituent B is defined as the partial derivative of the Gibbs energy G with respect to the amount (number of moles) of B, with temperature, pressure, and amounts of all other constituents held constant. Also called partial molar Gibbs energy. [2]

**Chromatography\*** - A method for separation of the components of a sample in which the components are distributed between two phases, one of which is stationary while the other moves. In gas chromatography the gas moves over a liquid or solid stationary phase. In liquid chromatography the liquid mixture moves through another liquid, a solid, or a gel. The mechanism of separation of components may be adsorption, differential solubility, ion-exchange, permeation, or other mechanisms. [6]

**Colloid** - Molecules or polymolecular particles dispersed in a medium that have, at least in one direction, a dimension roughly between 1 nm and 1  $\mu\text{m}$ . [3]

**Conductance (G)\*** - For direct current, the reciprocal of resistance. More generally, the real part of admittance. [1]

**Conductivity, electrical (s)\*** - The reciprocal of the resistivity. [1]

**Coulomb's law** - The statement that the force F between two electrical charges  $q_1$  and  $q_2$  separated by a distance r is  $F = (4\pi\epsilon_0)^{-1}q_1q_2/r^2$ , where  $\epsilon_0$  is the permittivity of a vacuum.

**Covalent bond** - A chemical bond between two atoms whose stability results from the sharing of two electrons, one from each atom.

## **D**

**Defect** - Any departure from the regular structure of a crystal lattice. A Frenkel defect results when an atom or ion moves to an interstitial position and leaves behind a vacancy. A Schottky defect involves either a vacancy where the atom has moved to the surface or a structure where a surface atom has moved to an interstitial position.

**Density (r)\*** - In the most common usage, mass density or mass per unit volume. More generally, the amount of some quantity (mass, charge, energy, etc.) divided by a length, area, or volume.

**Dislocation** - An extended displacement of a crystal from a regular lattice. An edge dislocation results when one portion of the crystal has partially slipped with respect to the other, resulting in an extra plane of atoms extending through part of the crystal. A screw dislocation transforms successive atomic planes into the surface of a helix.

**Dispersion** - Splitting of a beam of light (or other electromagnetic radiation) of mixed wavelengths into the constituent wavelengths as a result of the variation of refractive index of the medium with wavelength.

**Dissociation constant\*** - The equilibrium constant for a chemical reaction in which a compound dissociates into its constituent parts.

**Dissociation energy ( $D_e$ )\*** - For a diatomic molecule, the difference between the energies of the free atoms at rest and the minimum in the potential energy curve. The term bond dissociation energy ( $D_0$ ), which can be applied to polyatomic molecules as well, is used for the difference between the energies of the fragments resulting when a bond is broken and the energy of the original molecule in its lowest energy state. The term bond strength implies differences in enthalpy rather than energy.

## **E**

**Einstein** - A non-SI unit used in photochemistry, equal to one mole of photons.

**Electric charge (Q)** - The quantity of electricity; i.e., the property that controls interactions between bodies through electrical forces.

**Electric current (I)** - The charge passing through a circuit per unit time. [1]

**Electric displacement (D)** - A vector quantity whose magnitude equals the electric field strength multiplied by the permittivity of the medium and whose direction is the same as that of the field strength.

**Electric field strength (E)** - The force exerted by an electric field on a point charge divided by the electric charge. [1]

**Electric potential (V)** - A scalar quantity whose gradient is equal to the negative of the electric field strength.

**Electrochemical series\*** - An arrangement of reactions which produce or consume electrons in an order based on standard electrode potentials. A common arrangement places metals in decreasing order of their tendency to give up electrons.

**Electrode potential\*** - The electromotive force of a cell in which the electrode on the left is the standard hydrogen electrode and that on the right is the electrode in question. [2]

**Electrolysis** - The decomposition of a substance as a result of passing an electric current between two electrodes immersed in the sample.

**Electromotive force (emf)** - The energy supplied by a source divided by the charge transported through the source. [1]

**Electron\*** - An elementary particle in the family of leptons, with negative charge and spin of  $1/2$ .

**Electron affinity\*** - The energy difference between the ground state of a gas-phase atom or molecule and the lowest state of the corresponding negative ion.

**Electron volt (eV)\*** - A non-SI unit of energy used in atomic and nuclear physics, equal to approximately  $1.602177 \times 10^{-19}$  J. The electron volt is defined as the kinetic energy acquired by an electron upon acceleration through a potential difference of 1 V. [1]

**Electro-negativity\*** - A parameter originally introduced by Pauling which describes, on a relative basis, the power of an atom or group of atoms to attract electrons from the same molecular entity. [3]

**Electrophoresis** - The motion of macromolecules or colloidal particles in an electric field. [3]

**Energy gap\*** - In the theory of solids, the region between two energy bands, in which no bound states can occur.



**Enthalpy (H)\*** - A thermodynamic function, especially useful when dealing with constant-pressure processes, defined by  $H = E + PV$ , where  $E$  is energy,  $P$  pressure, and  $V$  volume. [1]

**Enthalpy of combustion\*** - The enthalpy change in a combustion reaction. Its negative is the heat released in combustion.

**Enthalpy of formation, standard\*** - The enthalpy change for the reaction in which a substance is formed from its constituent elements, each in its standard reference state (normally refers to 1 mol, sometimes to 1 g, of the substance).

**Enthalpy of fusion\*** - The enthalpy change in the transition from solid to liquid state.

**Enthalpy of sublimation** - The enthalpy change in the transition from solid to gas state.

**Enthalpy of vaporization\*** - The enthalpy change in the transition from liquid to gas state.

**Entropy (S)\*** - A thermodynamic function defined such that when a small quantity of heat  $dQ$  is received by a system at temperature  $T$ , the entropy of the system is increased by  $dQ/T$ , provided that no irreversible change takes place in the system. [1]

## **F**

**Farad (F)\*** - The SI unit of electric capacitance, equal to  $C/V$ . [1]

**Faraday constant (F)\*** - The electric charge of 1 mol of singly charged positive ions; i.e.,  $F = N_A e$ , where  $N_A$  is Avogadro's constant and  $e$  is the elementary charge. [1]

**Faraday effect\*** - The rotation of the plane of plane-polarized light by a medium placed in a magnetic field parallel to the direction of the light beam. The effect can be observed in solids, liquids, and gasses.

**Fermi level** - The highest energy of occupied states in a solid at zero temperature. Sometimes called Fermi energy. The Fermi surface is the surface in momentum space formed by electrons occupying the Fermi level.

**Ferrimagnetism\*** - A type of magnetism in which the magnetic moments of atoms in a solid are ordered into two nonequivalent sublattices with unequal magnetic moments, leading to a nonzero magnetic susceptibility.

**Ferrite** - A ferrimagnetic material of nominal formula  $MFe_2O_4$ , where  $M$  is a divalent metal; widely used in microwave switches and other solid state devices.

**Ferroelectricity\*** - The retention of electric polarization by certain materials after the external field that produced the polarization has been removed.

**Ferromagnetism\*** - A type of magnetism in which the magnetic moments of atoms in a solid are aligned within domains which can in turn be aligned with each other by a weak magnetic field. Some ferromagnetic materials can retain their magnetization when the external field is removed, as long as the temperature is below a critical value, the Curie temperature. They are characterized by a large positive magnetic susceptibility.

**Frequency ( $\nu$ )\*** - Number of cycles of a periodic phenomenon divided by time. [1]

## **G**

**Gallon (US)** - A unit of volume equal to 3.785412 L.

**Gallon (UK, Imperial)** - A unit of volume equal to 4.546090 L.

**Gel** - A colloidal system with a finite, but usually rather small, yield stress (the sheer stress at which yielding starts abruptly). [3]

**Gibbs energy (G)\*** - An important function in chemical thermodynamics, defined by  $G = H - TS$ , where  $H$  is the enthalpy,  $S$  the entropy, and  $T$  the thermodynamic temperature. Sometimes called Gibbs free energy and, in older literature, simply "free energy". [2]

**Glass transition temperature\*** - The temperature at which an amorphous polymer is transformed, in a reversible way, from a viscous or rubbery condition to a hard and relatively brittle one. [10]

**Grain (gr)** - A non-SI unit of mass, equal to 64.79891 mg.

---

**Grain boundary** - The interface between two regions of different crystal orientation.

## I

**Hall effect\*** - The development of a transverse potential difference  $V$  in a conducting material when subjected to a magnetic field  $H$  perpendicular to the direction of the current. The potential difference is given by  $V = R_H B J t$ , where  $B$  is the magnetic induction,  $J$  the current density,  $t$  the thickness of the specimen in the direction of the potential difference, and  $R_H$  is called the Hall coefficient.

**Hardness\*** - The resistance of a material to deformation, indentation, or scratching. Hardness is measured on various scales, such as Mohs, Brinell, Knoop, Rockwell, and Vickers. [10]

**Heat capacity\*** - Defined in general as  $dQ/dT$ , where  $dQ$  is the amount of heat that must be added to a system to increase its temperature by a small amount  $dT$ . The heat capacity at constant pressure is  $C_p = (\partial H / \partial T)_p$ ; that at constant volume is  $C_v = (\partial E / \partial T)_v$ , where  $H$  is enthalpy,  $E$  is internal energy,  $p$  is pressure,  $V$  is volume, and  $T$  is temperature. An upper case  $C$  normally indicates the molar heat capacity, while a lower case  $c$  is used for the specific (per unit mass) heat capacity. [1]

**Heisenberg uncertainty principle** - The statement that two observable properties of a system that are complementary, in the sense that their quantum-mechanical operators do not commute, cannot be specified simultaneously with absolute precision. An example is the position and momentum of a particle; according to this principle, the uncertainties in position  $\Delta q$  and momentum  $\Delta p$  must satisfy the relation  $\Delta p \Delta q \geq h/4\pi$ , where  $h$  is Planck's constant.

**Helmholz energy ( $A$ )** - A thermodynamic function defined by  $A = E - TS$ , where  $E$  is the energy,  $S$  the entropy, and  $T$  the thermodynamic temperature. [2]

**Henry (H)\*** - The SI unit of inductance, equal to Wb/A. [1]

**Hertz (Hz)** - The SI unit of frequency, equal to s<sup>-1</sup>. [1]

**Holography** - A technique for creating a three-dimensional image of a object by recording the interference pattern between a light beam diffracted from the object and a reference beam. The image can be reconstructed from this pattern by a suitable optical system.

**Hydrocarbon** - A compound containing only carbon and hydrogen. [5]

**Hydrolysis** - A reaction occurring in water in which a chemical bond is cleaved and a new bond formed with the oxygen atom of water.

**Hysteresis\*** - An irreversible response of a system (parameter  $A$ ) as a function of an external force (parameter  $F$ ), usually symmetric with respect to the origin of the  $A$  vs.  $F$  graph after the initial application of the force. A common example is magnetic induction vs. magnetic field strength in a ferromagnet.

## I

**Ideal solution** - A solution in which solvent-solvent and solvent-solute interactions are identical, so that properties such as volume and enthalpy are exactly additive.

**Ignition temperature\*** - The lowest temperature at which combustion of a material will occur spontaneously under specified conditions. Sometimes called autoignition temperature, kindling point. [10]

**Impedance ( $Z$ )** - The complex representation of potential difference divided by the complex representation of current. In terms of reactance  $X$  and resistance  $R$ , the impedance is given by  $Z = R + iX$ . [1]

**Inductance** - The ratio of the electromagnetic force induced in a coil by a current to the rate of change of the current.

**Insulator** - A material in which the highest occupied energy band (valence band) is completely filled with electrons, while the next higher band (conduction band) is empty. Solids with an energy gap of 5 eV or more are generally considered as insulators at room temperature. Their conductivity is less than 10<sup>-6</sup> S/m and increases with temperature.

**International System of Units (SI)\*** - The unit system adopted by the General Conference on Weights and Measures in 1960. It consists of seven base units (meter, kilogram, second, ampere, kelvin, mole, candela), plus derived units and prefixes. [1]

**Ion** - An atomic or molecular particle having a net electric charge. [3]

**Ion exchange** - A process involving the adsorption of one or several ionic species accompanied by the simultaneous desorption (displacement) of one or more other ionic species. [3]

**Ionization constant\*** - The equilibrium constant for a reaction in which a substance in solution dissociates into ions.

**Ionization potential\*** - The minimum energy required to remove an electron from an isolated atom or molecule (in its vibrational ground state) in the gaseous phase. More properly called ionization energy. [3]

**Isotherm** - A line connecting points of equal temperature on a graphical representation of a physical system.

**Isothermal process** - A thermodynamic process in which the temperature of the system does not change.

## **J**

**Joule (J)\*** - The SI unit of energy, equal to N m. [1]

## **K**

**Kelvin (K)\*** - The SI base unit of thermodynamic temperature. [1]

**Kilogram (kg)\*** - The SI base unit of mass. [1]

## **L**

**Lattice constants\*** - Parameters specifying the dimensions of a unit cell in a crystal lattice, specifically the lengths of the cell edges and the angles between them.

**Lattice energy\*** - The energy per ion pair required to separate completely the ions in a crystal lattice at a temperature of absolute zero.

**Liter (L)\*** - A synonym for cubic decimeter. [1]

**Lux (lx)\*** - The SI unit of illuminance, equal to cd sr m<sup>-2</sup>. [1]

## **M**

**Mass (*m*)\*** - Quantity of matter. Mass can also be defined as “resistance to acceleration”.

**Mass fraction (*w<sub>B</sub>*)** - The ratio of the mass of substance B to the total mass of a mixture. [1]

**Mass number (*A*)** - A characteristic property of a specific isotope of an element, equal to the sum of the number of protons and neutrons in the nucleus.

**Mass spectrometry** - An analytical technique in which ions are separated according to the mass/charge ratio and detected by a suitable detector. The ions may be produced by electron impact on a gas, a chemical reaction, energetic vaporization of a solid, etc. [6]

**Mean free path\*** - The average distance a gas molecule travels between collisions.

**Melting point\*** - The temperature at which the solid and liquid phases of a substance are in equilibrium at a specified pressure (normally taken to be atmospheric unless stated otherwise).

**Metal** - A material in which the highest occupied energy band (conduction band) is only partially filled with electrons. The electrical conductivity of metals generally decreases with temperature.

**Meter (m)\*** - The SI base unit of length. [1]

**Mho** - An archaic name for the SI unit siemens (reciprocal ohm).

**Micelle** - A particle formed by the aggregation of surfactant molecules (typically, 10 to 100 molecules) in solution. For aqueous solutions, the hydrophilic end of the molecule is on the

surface of the micelle, while the hydrophobic end (often a hydrocarbon chain) points toward the center. At the critical micelle concentration (cmc) the previously dissolved molecules aggregate into a micelle.

**Micron ( $\mu$ )** - An obsolete name for micrometer.

**Mie scattering** - The scattering of light by spherical dielectric particles whose diameter is comparable to the wavelength of the light.

**Miller indices ( $hkl$ )** - A set of indices used to label planes in a crystal lattice. [2]

**Millimeter of mercury (mmHg)** - A non-SI unit of pressure, equal to 133.322 Pa. The name is generally considered interchangeable with torr.

**Mobility ( $\mu$ )\*** - In solid state physics, the drift velocity of electrons or holes in a solid divided by the applied electric field strength. The term is used in a similar sense in other fields.

**Molality ( $m$ )** - A measure of concentration of a solution in which one states the amount of substance (i.e., number of moles) of solute per kilogram of solvent. Thus a 0.1 molal solution (often written as 0.1 m) has  $m = 0.1$  mol/kg.

**Molar mass** - The mass of one mole of a substance. It is normally expressed in units of g/mol, in which case its numerical value is identical with the molecular weight (relative molecular mass). [1]

**Molar quantity** - It is often convenient to express an extensive quantity (e.g., volume, enthalpy, heat capacity, etc.) as the actual value divided by amount of substance (number of moles). The resulting quantity is called molar volume, molar enthalpy, etc

**Molarity ( $c$ )** - A measure of concentration of a solution in which one states the amount of substance (i.e., number of moles) of solute per liter of solution. Thus a 0.1 molar solution (often referred to as 0.1 M) has a concentration  $c = 0.1$  mol/L.

**Mole (mol)\*** - The SI base unit of amount of substance. [1]

**Mole fraction ( $x_B$ )** - The ratio of the amount of substance (number of moles) of substance B to the total amount of substance in a mixture. [1]

**Molecular weight ( $M_r$ )\*** - The ratio of the average mass per molecule or specified entity of a substance to 1/12 of the mass of nuclide  $^{12}\text{C}$ . Also called relative molar (or molecular) mass. [1]

**Monomer** - A substance consisting of molecules which can undergo polymerization, thereby contributing constitutional units to the essential structure of a macromolecule. [8]

**Mössbauer effect** - The recoilless emission of  $\gamma$ -rays from nuclei bound in a crystal under conditions where the recoil energy associated with the  $\gamma$  emission is taken up by the crystal as a whole. This results in a very narrow line width, which can be exploited in various types of precise measurements.

## N

**Nernst effect** - The production of an electric field in a conductor subject to an applied magnetic field and containing a transverse temperature gradient. The electric field is perpendicular to the magnetic field and the temperature gradient.

**Neutrino** - A stable elementary particle in the lepton family. Neutrinos have zero (or at least near-zero) rest mass and spin 1/2.

**Neutron\*** - An elementary particle on spin 1/2 and zero charge. The free neutron has a mean lifetime of 887 seconds. Neutrons and protons, which are collectively called nucleons, are the constituents of the nucleus.

**Newton (N)\*** - The SI unit of force, equal to  $\text{m kg s}^{-2}$ . [1]

**Nyquist theorem** - An expression for the mean square thermal noise voltage across a resistor, given by  $4RkT\Delta f$  where  $R$  is the resistance,  $k$  the Boltzmann constant,  $T$  the temperature, and  $\Delta f$  the frequency band within which the voltage is measured.

**O**

**Oersted (Oe)** - A non-SI unit of magnetic field ( $H$ ), equal to 79.57747 A/m.

**Ohm ( $\Omega$ )\*** - The SI unit of electric resistance, equal to V/A. [1]

**Ohm's law** - A relation among electric current  $I$ , potential difference  $V$ , and resistance  $R$ , viz.,  $I = V/R$ . The resistance is constant at constant temperature to high precision for many materials.

**Osmosis** - The flow of a solvent in a system in which two solutions of different concentration are separated by a semi-permeable membrane which cannot pass solute molecules. The solvent will flow from the side of lower concentration to that of higher concentration, thus tending to equalize the concentrations. The pressure that must be applied to the more concentrated side to stop the flow is called the osmotic pressure.

**Osmotic coefficient ( $\phi$ )** - Defined by  $\phi = \ln a_A / (M_A \Sigma m_B)$ , where  $M_A$  is the molar mass of substance A (normally the solvent),  $a_A$  is its activity, and the  $m_B$  are molalities of the solutes. [1]

**Osmotic pressure ( $\Pi$ )** - The excess pressure necessary to maintain osmotic equilibrium between a solution and the pure solvent separated by a membrane permeable only to the solvent. In an ideal dilute solution  $\Pi = c_B R T$ , where  $c_B$  is the amount-of-substance concentration of the solute,  $R$  is the molar gas constant, and  $T$  the temperature. [1,2]

**Ostwald dilution law** - A relation for the concentration dependence of the molar conductivity  $\Lambda$  of an electrolyte solution, viz.,

$$\frac{1}{\Lambda} = \frac{1}{\Lambda^\circ} + \frac{\Lambda c}{K(\Lambda^\circ)^2}$$

where  $c$  is the solute concentration,  $K$  is the equilibrium constant for dissociation of the solute, and  $\Lambda^\circ$  is the conductivity at  $c\Lambda = 0$ .

**Ounce (oz)** - A non-SI unit of mass. The avoirdupois ounce equals 28.34952 g, while the troy ounce equals 31.10348 g.

**Over-potential ( $\eta$ )** - In an electrochemical cell, the difference between the potential of an electrode and its zero-current value.

**P**

**Parsec (pc)** - A unit of distance defined as the distance at which 1 astronomical unit (AU) subtends an angle of 1 second of arc. It is equal to 206264.806 AU or  $3.085678 \times 10^{16}$  m.

**Pascal (Pa)\*** - The SI unit of pressure, equal to N/m<sup>2</sup>. [1]

**Pauli exclusion principle** - The statement that two electrons in an atom cannot have identical quantum numbers; thus if there are two electrons in the same orbital, their spin quantum numbers must be of opposite sign.

**Permeability ( $\mu$ )** - Magnetic induction divided by magnetic field strength; i.e.  $\mu = B/H$ . The relative permeability  $\mu_r = \mu/\mu_0$ , where  $\mu_0$  is the permeability of a vacuum. [1]

**Permittivity ( $\epsilon$ )** - Ratio of the electric displacement in a medium to the electric field strength. Also called dielectric constant. [1]

**pH\*** - A convenient measure of the acid-base character of a solution, usually defined by  $\text{pH} = -\log [c(\text{H}^+)/\text{mol L}^{-1}]$ , where  $c(\text{H}^+)$  is the concentration of hydrogen ions. The more precise definition is in terms of activity rather than concentration. [2]

**Phosphorescence** - The process by which a molecule is excited by light to a higher electronic state and then undergoes a radiationless transition to a state of different multiplicity from which it decays, after some delay, to the ground state. The emitted light is normally of longer wavelength than the exciting light because vibrational energy has been dissipated.

**Photoelectric effect** - The complete absorption of a photon by a solid with the emission of an electron.

**Photon** - An elementary particle of zero mass and spin 1/2. The photon is involved in electromagnetic interactions and is the quantum of electromagnetic radiation.

**pK\*** - The negative logarithm (base 10) of an equilibrium constant  $K$ . For  $pK_a$ , see Acid dissociation constant.

**Planck constant ( $h$ )\*** - The elementary quantum of action, which relates energy to frequency through the equation  $E = h\nu$ .

**Planck function** - A thermodynamic function defined by  $Y = -G/T$ , where  $G$  is Gibbs energy and  $T$  thermodynamic temperature. [2]

**Plasma** - A highly ionized gas in which the charge of the electrons is balanced by the charge of the positive ions, so that the system as a whole is electrically neutral.

**Point group\*** - A group of symmetry operations (rotations, reflections, etc.) that leave a molecule invariant. Every molecular conformation can be assigned to a specific point group, which plays a major role in determining the spectrum of the molecule. **Poise (P)** - A non-SI unit of viscosity, equal to 0.1 Pa s.

**Poiseuille's equation** - A formula for the rate of flow of a viscous fluid through a tube:

$$\frac{dV}{dt} = \frac{(p_1^2 - p_2^2)\pi r^4}{16l\eta p_0}$$

where  $V$  is the volume as measured at pressure  $p_0$ ;  $p_1$  and  $p_2$  are the pressures at each end of the tube;  $r$  is the radius and  $l$  the length of the tube; and  $\eta$  is the viscosity.

**Poisson ratio ( $\mu$ )** - The absolute value of the ratio of the transverse strain to the corresponding axial strain resulting from uniformly distributed axial stress below the proportional limit (i.e., where Hooke's law is valid). [10]

**Polymer** - A substance composed of molecules of high relative molecular mass (molecular weight), the structure of which essentially comprises the multiple repetition of units derived, actually or conceptually, from molecules of low relative molecular mass. A single molecule of a polymer is called a macromolecule. [8]

**Pound (lb)** - A non-SI unit of mass, equal to 0.4535924 kg.

**Power (P)** - Rate of energy transfer. For electrical circuits, this is equal to the product of current and potential difference,  $P = IV$ . [1]

**Pressure\*** - Force divided by area. [1]

**Proton\*** - A stable elementary particle of unit positive charge and spin 1/2. Protons and neutrons, which are collectively called nucleons, are the constituents of the nucleus.

## Q

**Quality factor (Q)** - The ratio of the absolute value of the reactance of an electrical system to the resistance; thus a measure of the energy stored per cycle relative to the energy dissipated.

**Quasicrystal** - A solid having conventional crystalline properties but whose lattice does not display translational periodicity.

## R

**Rad** - A non-SI unit of absorbed dose of radiation, equal to 0.01 Gy.

**Radiance (L)** - The radiant intensity in a given direction from an element of a surface, divided by the area of the orthogonal projection of this element on a plane perpendicular to the given direction. [1]

**Radiant intensity (J)** - The radiant energy flux leaving an element of a source within an element of solid angle, divided by that element of solid angle. [1]

**Radicals** - Molecular entities possessing an unpaired electron, such as  $\cdot\text{CH}_3$ ,  $\cdot\text{SnH}_3$ ,  $\cdot\text{Cl}$ . (In these formulas the dot, symbolizing the unpaired electron, should be placed so as to indicate the atom of highest spin density, if this is possible). [5]

**Raman effect** - The inelastic scattering of light by a molecule, in which the incident photon either gives up to, or receives energy from, one of the internal vibrational modes of the molecule. The scattered light thus has either a lower frequency (Stokes radiation) or higher frequency (anti-Stokes radiation) than the incident light. These shifts provide a measure of the normal vibrational frequencies of the molecule.

**Rankine cycle** - A thermodynamic cycle which can be used to calculate the ideal performance of a heat engine that uses a condensable vapor as the working fluid (e.g., a steam engine or a heat pump).

**Rankine temperature** - A thermodynamic temperature scale based on a temperature interval  $^{\circ}\text{R} = (5/9) \text{ K}$ ; i.e.,  $T/^{\circ}\text{R} = (9/5)T/\text{K} = t/^{\circ}\text{F} + 459.67$ .

**Reactance ( $X$ )** - The imaginary part of impedance. For an inductive reactance  $L$  and a capacitive reactance  $C$  in series, the reactance is  $X = L\omega - 1/(C\omega)$ , where  $\omega$  is  $2\pi$  times the frequency of the current. [1]

**Relative humidity\*** - The ratio of the partial pressure of water vapor in air to the saturation vapor pressure of water at the same temperature, expressed as a percentage. [10]

**Resistance ( $R$ )** - Electric potential difference divided by current when there is no electromotive force in the conductor. This definition applies to direct current. More generally, resistance is defined as the real part of impedance. [1]

**Resistivity ( $\rho$ )** - Electric field strength divided by current density when there is no electromotive force in the conductor. Resistivity is an intrinsic property of a material. For a conductor of uniform cross section with area  $A$  and length  $L$ , and whose resistance is  $R$ , the resistivity is given by  $\rho = RA/L$ . [1]

**Rheology** - The study of the flow of liquids and deformation of solids. Rheology addresses such phenomena as creep, stress relaxation, an elasticity, nonlinear stress deformation, and viscosity.

## **S**

**Salt** - An ionic compound formed by the reaction of an acid and a base.

**Second (s)\*** - The SI base unit of time. [1]

**Seebeck effect** - The development of a potential difference in a circuit where two different metals or semiconductors are joined and their junctions maintained at different temperatures. It is the basis of the thermocouple.

**Semiconductor** - A material in which the highest occupied energy band (valence band) is completely filled with electrons at  $T = 0 \text{ K}$ , and the energy gap to the next highest band (conduction band) ranges from 0 to 4 or 5 eV. With increasing temperature electrons are excited into the conduction band, leading to an increase in the electrical conductivity.

**SI units\*** - The International System of Units adopted in 1960 and recommended for use in all scientific and technical fields. [1]

**Siemens (S)\*** - The SI unit of electric conductance, equal to  $\Omega^{-1}$ . [1]

**Skin effect** - The concentration of high frequency alternating currents near the surface of a conductor.

**Snell's law** - The relation between the angle of incidence  $i$  and the angle of refraction  $r$  of a light beam which passes from a medium of refractive index  $n_0$  to a medium of index  $n_1$ , viz.,  $\sin i/\sin r = n_1/n_0$ .

**Soliton** - A spatially localized wave in a solid or liquid that can interact strongly with other solitons but will afterwards regain its original form.

**Solubility\*** - A quantity expressing the maximum concentration of some material (the solute) that can exist in another liquid or solid material (the solvent) at thermodynamic equilibrium at specified temperature and pressure. Common measures of solubility include the mass of solute per unit mass of solution (mass fraction), mole fraction of solute, molality, molarity, and others.

**Solubility product constant ( $K_{sp}$ )\*** - The equilibrium constant for the dissolution of a sparsely soluble salt into its constituent ions.

**Space group\*** - A group of symmetry operations (reflections, rotations, etc.) that leave a crystal invariant. A total of 230 space groups have been identified.

**Specific gravity** - Ratio of the mass density of a material to that of water. Since one must specify the temperature of both the sample and the water to have a precisely defined quantity, the use of this term is now discouraged.

**Specific heat** - Heat capacity divided by mass. See Heat capacity.

**Specific quantity** - It is often convenient to express an extensive quantity (e.g., volume, enthalpy, heat capacity, etc.) as the actual value divided by mass. The resulting quantity is called specific volume, specific enthalpy, etc.

**Stacking fault** - An error in the normal sequence of layer growth in a crystal.

**Standard reduction potential ( $E^\circ$ )** - The zero-current potential of a cell in which the specified reduction reaction occurs at the right-hand electrode and the left-hand electrode is the standard hydrogen electrode. Also called Standard electrode potential.

**Stark effect** - The splitting of an energy level of an atom or molecule, and hence a splitting of spectral lines arising from that level, as a result of the application of an external electric field.

**Stoichiometric number ( $\nu$ )** - The number appearing before the symbol for each compound in the equation for a chemical reaction. By convention, it is negative for reactants and positive for products. [2]

**Stokes (St)** - A non-SI unit of kinematic viscosity, equal to  $10^{-4}$  m<sup>2</sup>/s.

**Stokes' law** - The statement, valid under certain conditions, that the viscous force  $F$  experienced by a sphere of radius  $a$  moving at velocity  $v$  in a medium of viscosity  $\eta$  is given by  $F = -6\pi\eta av$ .

**Strain** - The deformation of a body that results from an applied stress.

**Stress** - Force per unit area (pressure) applied to a body. Tensile stress tends to stretch or compress the body in the direction of the applied force. Shear stress results from a tangential force which tends to twist the body.

**Structure factor** - In x-ray crystallography, the sum of the scattering factors of all the atoms in a unit cell, weighted by an appropriate phase factor. The intensity of a given reflection is proportional to the square of the structure factor.

**Superconductor** - A material that experiences a nearly total loss of electrical resistivity below a critical temperature  $T_c$ . The effect can occur in pure metals, alloys, semiconductors, organic compounds, and certain inorganic solids.

**Superfluid** - A fluid with near-zero viscosity and extremely high thermal conductivity. Liquid helium exhibits these properties below 2.186 K (the  $\lambda$  point).

**Surface tension ( $\gamma, \sigma$ )\*** - The force per unit length in the plane of the interface between a liquid and a gas, which resists an increase in the area of that surface. It can also be equated to the surface Gibbs energy per unit area.

**Surfactant** - A substance which lowers the surface tension of the medium in which it is dissolved, and/or the interfacial tension with other phases, and accordingly is positively adsorbed at the liquid-vapor or other interfaces. [3]

**Susceptance ( $B$ )** - Imaginary part of admittance. [1]

**Svedberg** - A non-SI unit of time, used to express sedimentation coefficients, equal to  $10^{-13}$  S



**Tensile strength\*** - In tensile testing, the ratio of maximum load a body can bear before breaking to original cross-sectional area. Also called ultimate strength. [11]

**Tesla (T)\*** - The SI unit of magnetic flux density ( $B$ ), equal to V s/m<sup>2</sup>. [1]



**Thermal conductivity\*** - Rate of heat flow divided by area and by temperature gradient. [1]

**Thermal diffusivity** - Thermal conductivity divided by density and by specific heat capacity at constant pressure. [1]

**Thermal expansion coefficient ( $\alpha$ )\*** - The linear expansion coefficient is defined by  $\alpha = (1/L)(dL/dT)$ ; the volume expansion coefficient by  $\alpha_V = (1/V)(dV/dT)$ . [1]

**Thermodynamic laws** - The foundation of the science of thermodynamics: First law: The internal energy of an isolated system is constant; if energy is supplied to the system in the form of heat  $dq$  and work  $dw$ , then the change in energy  $dU = dq + dw$ . Second law: No process is possible in which the only result is the transfer of heat from a reservoir and its complete conversion to work. Third law: The entropy of a perfect crystal approaches zero as the thermodynamic temperature approaches zero.

**Thermoelectric power** - For a bar of a pure material whose ends are at different temperatures, the potential difference divided by the difference in temperature of the ends. See also Seebeck effect.

**Thomson coefficient ( $\mu$ ,  $\tau$ )** - The heat power developed in the Thomson effect (whereby heat is evolved in a conductor when a current is flowing in the presence of a temperature gradient), divided by the current and the temperature difference. [1]

**Tonne (t)** - An alternative name for megagram (1000 kg). [1]

**Torque ( $T$ )** - For a force  $F$  that produces a torsional motion,  $T = r \times F$ , where  $r$  is a vector from some reference point to the point of application of the force.

**Torr** - A non-SI unit of pressure, equal to 133.322 Pa. The name is generally considered interchangeable with millimeter of mercury.

**Transducer** - Any device that converts a signal from acoustical, optical, or some other form of energy into an electrical signal (or vice versa) while preserving the information content of the original signal.

**Transistor** - A voltage amplifier using controlled electron currents inside a semiconductor.

## U

**Unified atomic mass unit ( $u$ )\*** - A unit of mass used in atomic, molecular, and nuclear science, defined as the mass of one atom of  $^{12}\text{C}$  divided by 12. Its approximate value is  $1.66054 \times 10^{-27}$  kg. [1]

**Universal time ( $tu$ , UT)** - Mean solar time counted from midnight at the Greenwich meridian. Also called Greenwich mean time (GMT). The interval of mean solar time is based on the average, over one year, of the time between successive transits of the sun across the observer's meridian.

## V

**Vacancy** - A missing atom or ion in a crystal lattice.

**Van der Waals' equation\*** - An equation of state for fluids which takes the form:

$$pV_m = RT \left( \frac{1}{V_m - b} - \frac{a}{V_m^2} \right)$$

where  $p$  is pressure,  $V_m$  is molar volume,  $T$  is temperature,  $R$  is the molar gas constant, and  $a$  and  $b$  are characteristic parameters of the substance which describe the effect of attractive and repulsive intermolecular forces, respectively.

**Van der Waals' force** - The weak attractive force between two molecules which arises from electric dipole interactions. It can lead to the formation of stable but weakly bound dimer molecules or clusters.

**Vapor pressure\*** - The pressure of a gas in equilibrium with a liquid (or, in some usage, a solid) at a specified temperature.

**Velocity ( $v$ )** - Rate of change of distance with time.

**Viscosity ( $\eta$ )\*** - The proportionality factor between sheer rate and sheer stress, defined through the equation  $F = \eta A(dv/dx)$ , where  $F$  is the tangential force required to move a planar surface of area  $A$  at velocity  $v$  relative to a parallel surface separated from the first by a distance  $x$ . Sometimes called dynamic or absolute viscosity. The term kinematic viscosity (symbol  $\nu$ ) is defined as  $\eta$  divided by the mass density.

**Volt (V)\*** - The SI unit of electric potential, equal to W/A. [1]

**Volume fraction ( $\phi_j$ )** - Defined as  $V_j/\sum_i V_i$ , where  $V_j$  is the volume of the specified component and the  $V_i$  are the volumes of all the components of a mixture prior to mixing. [2]

## W

**Watt (W)\*** - The SI unit of power, equal to J/s. [1]

**Weight** - That force which, when applied to a body, would give it an acceleration equal to the local acceleration of gravity. [1]

**Work ( $W$ )** - Force multiplied by the displacement in the direction of the force. [1]

**Work function ( $\Phi$ )\*** - The energy difference between an electron at rest at infinity and an electron at the Fermi level in the interior of a substance. It is thus the minimum energy required to remove an electron from the interior of a solid to a point just outside the surface [1]

## X

**X unit (X)** - A unit of length used in x-ray crystallography, equal to approximately  $1.002 \times 10^{-13}$  m.

## Z

**Zeta potential ( $\zeta$ )** - The electric potential at the surface of a colloidal particle relative to the potential in the bulk medium at a long distance. Also called electro-kinetic potential.

## REFERENCES:

- [1] *ISO Standards Handbook 2, Units of Measurement*, International Organization for Standardization, Geneva, 1992.
- [2] *Quantities, Units, and Symbols in Physical Chemistry, Second Edition*, International Union of Pure and Applied Chemistry, Blackwell Scientific Publications, Oxford, 1993.
- [3] *Compendium of Chemical Terminology*, International Union of Pure and Applied Chemistry, Blackwell Scientific Publications, Oxford, 1987.
- [4] *A Guide to IUPAC Nomenclature of Organic Compounds*, International Union of Pure and Applied Chemistry, Blackwell Scientific Publications, Oxford, 1993.
- [5] *Glossary of Class Names of Organic Compounds and Reactive Intermediates Based on Structure, Pure and Applied Chemistry*, 67, 1307, 1995.
- [6] *Compendium of Analytical Nomenclature*, International Union of Pure and Applied Chemistry, Blackwell Scientific Publications, Oxford, 1987.
- [7] *Nomenclature of Inorganic Chemistry*, International Union of Pure and Applied Chemistry, Blackwell Scientific Publications, Oxford, 1990.
- [8] *Glossary of Basic Terms in Polymer Science, Pure and Applied Chemistry*, 68, 2287, 1996.
- [9] *The International Temperature Scale of 1990, Metrologia*, 27, 107, 1990.
- [10] *Compilation of ASTM Standard Definitions*, American Society of Testing and Materials, Philadelphia, 1990.
- [11] *ASM Metals Reference Book*, American Society for Metals, Metals Park, OH, 1983.

### Appendix III – Standard reduction potentials

**Table lists standard reduction potentials,  $E^\circ$  values, at 298.15 K (25°C), and at a pressure of 101.325 kPa (1 atm)**

Chemical reactions	$E^\circ$ (in volts)
$2 \text{H}^+ + 2 \text{e} \rightleftharpoons \text{H}_2$	0.00000
$\text{H}_2 + 2 \text{e} \rightleftharpoons 2 \text{H}^-$	-2.23
$\text{HO}_2 + \text{H}^+ + \text{e} \rightleftharpoons \text{H}_2\text{O}_2$	1.495
$2 \text{H}_2\text{O} + 2 \text{e} \rightleftharpoons \text{H}_2 + 2 \text{OH}^-$	-0.8277
$\text{H}_2\text{O}_2 + 2 \text{H}^+ + 2 \text{e} \rightleftharpoons 2 \text{H}_2\text{O}$	1.776
$\text{O}_2 + 2 \text{H}^+ + 2 \text{e} \rightleftharpoons \text{H}_2\text{O}_2$	0.695
$\text{O}_2 + 4 \text{H}^+ + 4 \text{e} \rightleftharpoons 2 \text{H}_2\text{O}$	1.229
$\text{O}_2 + \text{H}_2\text{O} + 2 \text{e} \rightleftharpoons \text{HO}_2^- + \text{OH}^-$	-0.076
$\text{O}_2 + 2 \text{H}_2\text{O} + 2 \text{e} \rightleftharpoons \text{H}_2\text{O}_2 + 2 \text{OH}^-$	-0.146
$\text{O}_2 + 2 \text{H}_2\text{O} + 4 \text{e} \rightleftharpoons 4 \text{OH}^-$	0.401
$\text{O}_3 + 2 \text{H}^+ + 2 \text{e} \rightleftharpoons \text{O}_2 + \text{H}_2\text{O}$	2.076
$\text{O}_3 + \text{H}_2\text{O} + 2 \text{e} \rightleftharpoons \text{O}_2 + 2 \text{OH}^-$	1.24
$\text{O}(\text{g}) + 2 \text{H}^+ + 2 \text{e} \rightleftharpoons \text{H}_2\text{O}$	2.421
$\text{OH} + \text{e} \rightleftharpoons \text{OH}^-$	2.02
$\text{HO}_2^- + \text{H}_2\text{O} + 2 \text{e} \rightleftharpoons 3 \text{OH}^-$	0.878





---

---

### 5) Doctoral work:

<b>Title of doctoral thesis:</b>	<i>“Studies on synthesis and characterization of Gd doped ceria solid electrolyte”</i>
<b>Research guide:</b>	<b>Dr. (Smt.) L.D. Jadhav,</b> <i>Lecturer, Rajaram College, Kolhapur – 416 004. M.S. INDIA.</i>
<b>Home institute:</b>	<i>Department of Physics,</i> <i>Shivaji University, Kolhapur – 416 004. M.S. INDIA.</i>
<b>Date of Submission:</b>	<i>Submitted in June 2009.</i>

---

### 6) Prospective research interests:

***I wish to continue my research work in material science, specifically in the field of solid oxide fuel cells.***

*During my doctoral work I have got developed lot of interest in the field of solid oxide fuel cells. The experience gained in preparing the materials, specifically for solid oxide fuel cells, using different chemical methods; I would be very much interested to move on my pace of research in the same direction. Thus, I would be very much interested to prepare the oxide materials using low temperature chemical synthesis techniques with potential application in the field of catalysis, solid oxide fuel cells, gas sensors, batteries, etc.*

---

### 7) Hands-on-experience on different techniques:

<b>Material synthesis techniques:</b>	<ul style="list-style-type: none"><li>• <u>Ceramic route (solid-state reaction):</u><ul style="list-style-type: none"><li>○ for preparation of metal oxide bulk samples</li></ul></li><li>• <u>Spray pyrolysis technique:</u><ul style="list-style-type: none"><li>○ for preparation of metal oxide thin films</li></ul></li><li>• <u>Solution combustion: (glycine nitrate process)</u><ul style="list-style-type: none"><li>○ for the preparation of nano-crystalline powders</li></ul></li></ul>
<b>Processing instruments</b>	<ul style="list-style-type: none"><li>• Programmable furnaces,</li></ul>

---

<i>Characterization instruments handled</i>	<ul style="list-style-type: none"> <li>• <i>Optical spectroscope –</i> <ul style="list-style-type: none"> <li>○ <i>Systronics spectrometer -119,</i></li> </ul> </li> <li>• <i>Impedance analyzer –</i> <ul style="list-style-type: none"> <li>○ <i>Solartron-1260 Impedance analyzer,</i></li> <li>○ <i>HP-4284A Precision LCR Meter</i></li> </ul> </li> <li>• <i>Gas Chromatography –</i> <ul style="list-style-type: none"> <li>○ <i>Shimadzu, Japan; GC-2014-ATF,</i></li> </ul> </li> <li>• <i>Scanning electron microscope</i> <ul style="list-style-type: none"> <li>○ <i>JEOL-JSM-6360,</i></li> </ul> </li> <li>• <i>X-ray diffraction</i> <ul style="list-style-type: none"> <li>○ <i>PHILIPS, PW-3710,</i></li> </ul> </li> <li>• <i>Thermo-Gravimetric-Differential Thermal Analysis</i> <ul style="list-style-type: none"> <li>○ <i>Perkin-Elmer TGA-DTA-DSC</i></li> </ul> </li> <li>• <i>Surface profiler</i> <ul style="list-style-type: none"> <li>○ <i>AMBIOS make XP-1</i></li> </ul> </li> </ul>
<i>Characterization tools used (not handled the instruments )</i>	<ul style="list-style-type: none"> <li>• <i>Transmission electron microscope,</i> <ul style="list-style-type: none"> <li>○ <i>PHILIPS, CM-200</i></li> </ul> </li> <li>• <i>Atomic force microscope,</i> <ul style="list-style-type: none"> <li>○ <i>Nanoscope-E, Digital Instruments, USA</i></li> </ul> </li> <li>• <i>FT-IR spectroscope</i> <ul style="list-style-type: none"> <li>○ <i>Perkin-Elmer, FT-IR Spectrum one</i></li> </ul> </li> </ul>

*Nevertheless, I have great interest to get familiar with other instruments required for my research as well as the instrumentation available in the concerned research laboratory.*

## **8) Computer skills:**

<i>Operating systems:</i>	<ul style="list-style-type: none"> <li>• <i>Windows 95/98/2000/XP/VISTA, UNIX*</i></li> </ul>
<i>Applications</i>	<ul style="list-style-type: none"> <li>• <i>MS Office 98/2000/XP/2003/2007, Acrobat Prof. 7.0,</i></li> <li>• <i>Origin Lab 6.0/7.0/8..0*,</i> <ul style="list-style-type: none"> <li>○ <i>for scientific data-analysis and presentation</i></li> </ul> </li> <li>• <i>LabVIEW .8.0*</i> <ul style="list-style-type: none"> <li>○ <i>Graphical programming for virtual instrumentation,</i></li> </ul> </li> <li>• <i>ZView 2.4a</i> <ul style="list-style-type: none"> <li>○ <i>Impedance analysis software,</i></li> </ul> </li> <li>• <i>GCSolution 2.1</i> <ul style="list-style-type: none"> <li>○ <i>Gas Chromatography – data acquisition and analysis</i></li> </ul> </li> </ul>
<i>Languages:</i>	<i>C, C++, Visual C++*</i>
<i>Network security:</i>	<i>Participated in “Ankit Fadia’s Certified Ethical Hacker 2.0” course.</i>

---

## 9) List of publications:

### A. Papers published/accepted/submitted to the cited journals [05+03\*]

1. L. D. Jadhav, **M.G. Chourashiya**, A.P. Jamale, A.U. Chavan, J.Y. Patil, "Synthesis of highly dense  $Ce_{1-x}Gd_xO_{2-x/2}$  ( $x = 0-0.30$ ) solid solutions using nano-crystalline powders and a plausibility of reduction of ceria at higher sintering temperature", Submitted\*
2. **M.G. Chourashiya** and L.D. Jadhav, "Synthesis and characterization of GDC (10%Gd doped Ceria)/GDC and GDC/NiO-GDC structures for intermediate or low temperature solid oxide fuel cells", Submitted\* to Materials Chemistry and Physics
3. **M.G. Chourashiya**, S.R. Bhardwaj and L.D. Jadhav, "Electrochemical impedance and microstructure of dense  $Ce_{1-x}Gd_xO_{2-x/2}$  ceramics prepared through modified thermal treatment", Submitted\*
4. L. D. Jadhav, **M.G. Chourashiya**, K. M. Subhedar, A. K. Tyagi, J. Y. Patil, "Synthesis of nano-crystalline Gd doped Ceria by combustion technique", Journal of Alloys and Compounds, 470, (2009) 383-386.
5. **M. G. Chourashiya**, S. H. Pawar and L.D. Jadhav, "Synthesis and characterization of  $Gd_{0.1}Ce_{0.9}O_{1.95}$  thin films by spray pyrolysis technique", Applied Surface Science, 254 (2008) 3431-3435.
6. **M.G. Chourashiya**, J. Y. Patil, S.H. Pawar and L.D. Jadhav; "Studies on structural, morphological and electrical properties of  $Ce_{1-x}Gd_xO_{2-x/2}$ ", Materials Chemistry and Physics, 109 (2008) 39-44.
7. **M.G. Chourashiya**, S.S. Potdar and L.D. Jadhav; "Structural, morphological and electrical properties of  $Ce_{0.9}Gd_{0.1}O_{1.95}$ ", In International Conference on Advances in Energy Research (ICAER-07), organized by Indian Institute of Technology (IIT), Bombay, India. Vol. 02, **2007**, pp – 247-251.



- 
8. L.D. Jadhav, S.H. Pawar and **M.G. Chourashiya**; “Effect of sintering temperature on structural and electrical properties of gadolinium doped ceria ( $Ce_{0.9}Gd_{0.1}O_{1.95}$ )”, *Bulletin of Material Science*, Vol. 30, April **2007**, 97 – 100.

**B. Papers presented/accepted at National and International conferences Seminars/ Symposia/ workshops [23]**

1. **M.G. Chourashiya** and L.D. Jadhav, “Micro-structural and electrical evaluation of dense  $Ce_{1-x}Gd_xO_{2-x/2}$  ( $x = 0.1, 0.2$  and  $0.3$ ) as solid electrolytes for intermediate temperature solid oxide fuel cells”, in International Workshop on Nanotechnology and Advanced Functional Materials – 2009 (NTAFM-09) organized jointly by Materials Research Society of Pune, NCL Pune and IISER Pune at NCL Pune during 9<sup>th</sup> – 11<sup>th</sup> July **2009**.
2. **M.G. Chourashiya**, L.D. Jadhav, “Fabrication of 10%Gd doped ceria (GDC)/NiO-GDC half-cell for low or intermediate temperature solid oxide fuel cells using spray pyrolysis” in 5<sup>th</sup> International Conference on Materials for Advanced Technologies – 2009 (ICMAT & IUMRS-ICA 2009) organized by Materials Research Society of Singapore at the **Suntec Singapore International Convention & Exhibition Centre, Singapore** during 28 June to 3 July **2009**.
3. **M.G. Chourashiya**, L.D. Jadhav, “Studies on micro-structural and electrical properties of 10%Gd doped ceria films deposited on glass and ceramic substrates” in national Symposium on Nano-materials and their Applications – 2009 (SNMA-09) organized by Department of Electronics, Fergusson college, Pune during 4-6 March **2009**.
4. A.P. Jamale, **M.G. Chourashiya**, L.D. Jadhav, “Synthesis and characterization of 8%Ytria stabilized zirconia (8YSZ) and NiO-8YSZ thin films using spray pyrolysis” in national Symposium on Nano-materials and their Applications – 2009 (SNMA-09) organized by Department of Electronics, Fergusson college, Pune during 4-6 March **2009**.

- 
5. A.P. Jamale, T. Barage, S. Powar, **M.G. Chourashiya**, L.D. Jadhav, “*Synthesis and characterization of 8%Ytria Stabilized Zirconia (8YSZ) and NiO-8YSZ thin films*” in International Conference on NAno-Materials and Applications (ICNAMA-2008) organized by Department of Chemistry and Department of Physics, Shivaji University, Kolhapur during 9-11 December **2008**.
  6. A.U. Chavan, A.G. Chourasiya, **M.G. Chourashiya**, L.D. Jadhav, “*Synthesis and characterization of NiO-10%Gd doped ceria composites*” in International Conference on NAno-Materials and Applications (ICNAMA-2008) organized by Department of Chemistry and Department of Physics, Shivaji University, Kolhapur during 9-11 December **2008**.
  7. J.Y. Patil, R.A. Panaskar, **M.G. Chourashiya**, L.D. Jadhav, “*Structural, morphological and electrical properties of GNP synthesized nano-crystalline  $Ce_{1-x}Gd_xO_{2-x/2}$  ( $x= 0-0.3$ )*”, in International Conference on NAno-Materials and Applications (ICNAMA-2008) organized by Department of Chemistry and Department of Physics, Shivaji University, Kolhapur during 9-11 December **2008**.
  8. **M.G. Chourashiya**, S. Bhardwaj, L.D. Jadhav “*Electrochemical impedance and morphological characterization of GDC (10%Gd doped ceria) / GDC and GDC / NiO-GDC systems*” in International Conference on NAno-Materials and Applications (ICNAMA-2008) organized by Department of Chemistry and Department of Physics, Shivaji University, Kolhapur during 9-11 December **2008**.
  9. **M.G. Chourashiya**, A. Chavan, A. Jamale, S. Bhardwaj, L. D. Jadhav, “*Electrochemical impedance and microstructural studies on  $Ce_{1-x}Gd_xO_{2-x/2}$  ( $x = 0.1, 0.2$  and  $0.3$ ) prepared with optimized sintering temperature*” in International Symposium on Materials Chemistry (ISMC-2008) organized by Chemistry Division, Bhabha Atomic Research Centre, Trombay, Mumbai-400085, INDIA during 2-5, December **2008**.

- 
10. **M.G. Chourashiya**, S. Bhardwaj, L.D. Jadhav, “*Fabrication of half-cell for low or intermediate temperature solid oxide fuel cells using spray pyrolysis technique for its commercial production*” in International Conference on Electrochemical Power Systems (ICEPS-08) organized by the Society for Advancement of Electrochemical Science and Technology (SAEST) held in Thiruvananthapuram, Kerala, India during 26 - 28 November **2008**.
  11. **M.G. Chourashiya**, L.D. Jadhav, “*Studies on synthesis and characterization of Gd doped ceria thin films on Ni-GDC cermets*” in 19th Annual General Meeting Materials Research Society of India 2008 (MRSI-2008) organized jointly with National Institute for Interdisciplinary Science & Technology (NIST), Shree Chitra Tirunal Institute for Medical Sciences & Technology (SCTIMST), and Vikram Sarabhai Space Centre (VSSC), Thiruvananthapuram, India during February, 14-16, **2008**.
  12. **M.G. Chourashiya**, J.Y. Patil, L.D. Jadhav, “*Structural and electrical properties of CGO10 thin films prepared using spray pyrolysis technique*” in 52nd DAE Solid State Physics Symposium 07 (DAE-SSPS-07) at Mysore University, Mysore during 27 – 31st December **2007**.
  13. J.Y. Patil, R.A. Panaskar, **M.G. Chourashiya**, L.D. Jadhav, “*Preparation and characterization of CeO<sub>2</sub>-Gd<sub>2</sub>O<sub>3</sub> solid solutions*” in the International conference on Advanced Materials for Applications (ICAMA-07), organized by and conducted at Department of Physics, Shivaji University, Kolhapur during 15 – 17, November **2007**.
  14. **M.G. Chourashiya**, J.Y. Patil, L.D. Jadhav, “*Spray pyrolysis of Gd doped ceria thin films on ceramic substrate*” in the International conference on Advanced Materials for Applications (ICAMA-07), organized by and conducted at Department of Physics, Shivaji University, Kolhapur during 15 – 17, November **2007**.
  15. **M.G. Chourashiya**, L.D. Jadhav, “*Synthesis of Gd doped ceria thin films using spray pyrolysis technique and its characterization*” in the National

---

Seminar on Recent Advances in Thin film Technology (NS-RATFT-07) organized by and at IITM, Gwalior during 26-27th October, **2007**.

- 16. M.G. Chourashiya**, J. Y. Patil, S. H. Pawar, L.D. Jadhav, “*Spray Pyrolytic Synthesis of Gd<sub>0.1</sub>Ce<sub>0.9</sub>O<sub>1.95</sub> thin films and their characterization*” in the Millennium Energy Summit 2007 (MES-07), organized jointly by Central Glass & Ceramic Research Institute (CGCRI) and Millennium Institute of Energy & Environment Management (MIEEM) during September 27- 29, **2007** at CGCRI, Kolkata.
- 17. M.G. Chourashiya**, S.H. Pawar, L.D. Jadhav, “*Preparation and Characterization of Gd doped ceria in thin film form*”, in 18th Annual General Meeting (AGM) Materials Research Society of India (MRSI) organized by and at NPL, MRSI Delhi Chapter during 11 -14 February **2007**.
- 18. S. S. Potdar, M.G. Chourashiya**, L.D. Jadhav, “*Studies on synthesis and characterization of Ce<sub>0.9</sub>Gd<sub>0.1</sub>O<sub>2</sub>*” in National Seminar on New Horizons in Physics 2007 (NS – NHP – 07) sponsored by UGC & Shivaji University, Kolhapur during 20 – 21 January **2007** at Yeshwantrao Chavan Institute of Sciences (YCIS) College, Satara, Maharashtra.
- 19. L.D. Jadhav\***, S.H. Pawar, **M.G. Chourashiya**, “*Structural and Electrical Properties of Gadolinium doped Ceria*”, in the Eighth International Symposium on Advances in Electrochemical Sciences and Technologies (ISAEST-8) organized by SAEST, CECRI, Karaikudi during 28th – 30th November **2006** at National Institute of Oceanography (NIO), Goa.
- 20. L.D. Jadhav**, S.H. Pawar, **M.G. Chourashiya**, “*Synthesis and Characterization of Gadolinium doped Ceria (GDC) Oxide by Solid State Reaction*”, in National Seminar on Materials for Advanced Technologies (NASMAT-2006), during 23 – 25, January **2006** at Department of Physics, Shivaji University, Kolhapur.

- 
- 21. M.G. Chourashiya**, A.A. Shaikh, K.B. Jadhav, R.S. Hyam, L.D. Jadhav, S.H. Pawar, “*Nano-Sizing of Boron Particles*”, in National Seminar on Materials for Advanced Technologies (NASMAT-2006), during 23 – 25, January **2006** at Department of Physics, Shivaji University, Kolhapur.
- 22. M.G. Chourashiya**, S.H. Pawar, L.D. Jadhav, “*Studies on synthesis and characterization of  $Gd_{0.1}Ce_{0.9}O_{1.95}$  and  $Gd_{0.2}Ce_{0.8}O_{1.9}$* ”, in BRNS, DAE, Government of India sponsored “Discussion Meeting on Materials for Future Energy System”, during 18 – 19, January **2006** at Multipurpose Hall, BARC, TSH, Mumbai.
- 23. M.G. Chourashiya**, V.R. Shinde, T.P. Gujar, C.D Lokhande, “*Low temperature deposition of  $SnO_2$  by SILAR method*”, in 16th Annual General Meeting (AGM) of the Material Research Society of India (MRSI), during February 10 - 12, **2005** at NCL, Pune.
-

---

---

## 10) Prizes / awards / felicitation:

1. Secured prize for **Best Oral Presentation** at national Symposium on Nano-materials and Application – 2009 organized by Fergusson College, Pune
2. Secured **N. G. Jog's, Lt. Col. V. V. Joshi-Best NCC Cadet Prize** winner for the year 2002-2003 among the 80 NCC cadets of Willingdon College, Sangli.
3. The organizing committee of "**7<sup>th</sup> Annual Meet of Shivaji University Physics Student**" felicitated for attending the Summer School Program held at Institute for Plasma Research (IPR), Gandhinagar, Gujarat.
4. Nominated for "**The President of India Medal for General Proficiency, Shivaji University**" for the year 2004-2005.

---

## 11) Teaching/research experience :

### A. Details of previous or present employment:

Name of employer <sup>#</sup>	Post	Salary drawn (pm)	Period of service		Nature of duties
			From	To	
CSIR, New Delhi	CSIR-SRF	Rs. 14000*/-	1/10/08	Till date	Full time researcher
DRDO, New Delhi	SRF	Rs. 14000*/-	21/06/07	30/09/08	
DRDO, New Delhi	JRF	Rs. 12000*/-	21/06/05	20/06/07	

\* As per new appointment orders plus HRA

<sup>#</sup> Place of employment – Dept. of Physics, Shivaji University, Kolhapur

### B. Summer school:

Participated in a summer school organized by **Institute for Plasma Research, Gandhinagar, Gujarat, India** during 7<sup>th</sup> June to 16<sup>th</sup> July 2004.

The project work carried out during the school was to design dc break in co-axial line of RF supply and EM field simulations in designed object using ANSOFT software. The title of project was "Design of broad band coaxial dc-break using ANSOFT-EM simulation software".

---

---

**12) General information:**

<b>Sex</b>	Male
<b>Marital Status</b>	Unmarried
<b>Date of birth</b>	01-JAN-1982
<b>Place of birth</b>	BAHA CHOWKI. MUNGER, BIHAR
<b>Nationality</b>	INDIAN
<b>Present Age</b>	27 Years
<b>Religion – Caste; Category</b>	HINDU – CHOURASIA; OPEN
<b>Mobile No.</b>	+91 9881004949
<b>E-mail Address</b>	<b>chourashiya@gmail.com</b> , mgchourashiya@yahoo.com
<b>Languages Known</b>	Marathi, Hindi and English

---

**13) Details of passport:**

<b>Passport number:</b>	<b>G7816191</b>
<b>Date of issue:</b>	24-MAR-2008
<b>Date of expiry:</b>	23- MAR-2018
<b>Place of issue:</b>	PUNE (M.S., INDIA)

---

**14) DECLARATION:**

*I hereby declare that the above mentioned information are complete and correct to best of my knowledge.*

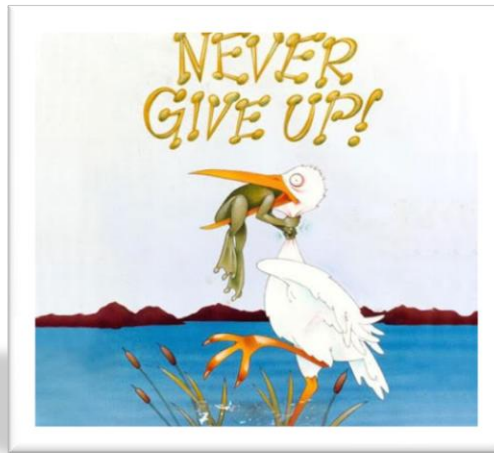
---

**Mr. Muralidhar G. Chourashiya**

**DATE: 18-Aug-2009**







*"The journey of a thousand miles  
begins with a single step."*  
—Chinese proverb



---

***It is the beginning...***





